Lipotoxicity mediates Glutaredoxin 5 deficiency and impaired Fe-S cluster synthesis in β-cells promoting ferroptosis

Inauguraldissertation
zur Erlangung des Grades eines Doktors der Humanbiologie
des Fachbereichs Medizin
der Justus-Liebig-Universität Gießen

vorgelegt von Römer, Axel
aus Heidenheim an der Brenz

Gießen 2025

Aus dem Fachbereich Medizin der Justus-Liebig-Universität Gießen

Medizinische Klinik und Poliklinik III

Endokrinologie, Diabetologie, Stoffwechsel und Ernährungsmedizin

Klinische Forschungseinheit

Gutachter: Prof. Dr. Thomas Linn

Gutachter: PD Dr. Jochen Wiesner

Tag der Disputation: 18.11.2025

Contents

1 Introduction

1.1 Diabetes mellitus

1.1.1 The role of insulin in diabetes mellitus

Diabetes mellitus is a non-communicable disease of the endocrine pancreas whose prevalence has more than doubled over the last 30 years (King et al., 1998). In 2021, this disease posed a health threat to over 537 million adults worldwide (prevalence: 9.8 %) (H. Sun et al., 2022). Additionally, approximately 541 million individuals are at high risk of developing type 2 diabetes due to impaired glucose tolerance. Given that more than one billion people worldwide are classified as obese (Phelps et al., 2024), the number of diabetic patients is expected to rise significantly, potentially reaching 1.3 billion by 2050 (Ong et al., 2023). Most cases of diabetes occur in individuals who are physically inactive and consume an excess of calories, combined with a genetic predisposition to develop insulin resistance (Lagou et al., 2023). The disease is hallmarked by reduced or absent synthesis and action of insulin, impairing blood glucose regulation. Insulin is a hormone produced and secreted by the β-cells of the endocrine pancreas. Further cell types in the pancreas are α-cells producing the insulin antagonist glucagon, δ-cells for production of somatostatin, ε-cells producing ghrelin (Dezaki & Yada, 2022), and γ-cells/pancreatic polypeptide cells (Adams & Blum, 2022). These cells are organized into round clusters known as the islets of Langerhans, with insulin-producing β-cells making up approximately 60 % of the total cell population (Da Silva Xavier, 2018).

1.1.2 Regulation of insulin secretion

β-cells express insulin as precursor protein called preproinsulin, which consists of a signal peptide, an A chain, and a B chain connected by C-peptide (Arunagiri et al., 2024). Upon entry into the endoplasmic reticulum (ER), the signal peptide is cleaved, initiating protein folding. The resulting inactive proinsulin is stored in vesicles within the Golgi apparatus. During secretion, the C-peptide is cleaved, producing active insulin (Derkach et al., 2022). This process requires the activity of the serine protease prohormone convertase (PC1/3 and PC2) and carboxypeptidase E (Meier et al., 2022; Ramzy & Kieffer, 2022). The A chain and B chain are stabilized by three disulfide bridges (Haataja et al., 2016). When blood glucose levels exceed 7 mM (Skelin et al., 2010), glucose enters β-cells via the glucose transporter (GLUT) 1, independently of insulin. By reactions of glycolysis,

adenosine triphosphate (ATP) level rise and close ATP-sensitive potassium channels (Corradi et al., 2023). The resulting rise in potassium depolarizes the cell membrane, opening voltage-dependent calcium channels and allowing calcium influx. This triggers insulin release via exocytosis. Secretion of insulin follows a biphasic pattern with a fast first phase and a sustained second phase (Peng et al., 2024). The first phase involves the release of pre-stored insulin, while the second phase depends on insulin production in response to glucose levels. A subpopulation of β-cells, known as first-responder β-cells, exhibit heightened glucose sensitivity and are crucial for first-phase secretion (Delgadillo-Silva et al., 2024). RNA expression analysis identifies pyridoxamine 5′-phosphate oxidase, the rate-limiting enzyme for active vitamin B6, as a marker for first-responder β-cells in both zebrafish and mouse islets. Transcriptome analysis of the human pancreas further supports the involvement of pyridoxamine 5′-phosphate oxidase in glucose stimulated calcium response. Insulin acts as a ligand for the insulin receptor, triggering its tyrosine kinase activity (E. Choi & Bai, 2023). This leads to the phosphorylation of insulin receptor substrate 1 (IRS1), activation of phosphatidylinositol 3-kinase (PI3K), and protein kinase B (Akt) (Kearney et al., 2021). These downstream pathways initiate the translocation of GLUT4 vesicles to the cell membrane, enabling facilitated glucose uptake in insulin-dependent tissues such as skeletal muscle, adipose tissue, liver, and the heart. Beyond lowering blood glucose, insulin inhibits lipolysis and promotes energy storage in the form of glycogen or triglycerides (Barroso et al., 2024; Czech et al., 2013; Grabner et al., 2021). In diabetes mellitus, β-cell amount and function decline, leading to reduced insulin production, while insulin signaling is impaired by increasing resistance. Abdominal obesity is a major risk factor for diabetes development (Z. Wang et al., 2021).

1.1.3 Classification of diabetes mellitus

Diabetes mellitus is classified based on its etiology into type 1 diabetes, type 2 diabetes, specific types of diabetes due to other causes, and gestational diabetes mellitus (ElSayed et al., 2024). Type 1 diabetes is caused by the autoimmune destruction of β-cells by autoreactive T-cells, leading to an absolute loss of insulin production (W. Tang et al., 2021). Other causes for specific types of diabetes may result from monogenic syndromes, exocrine pancreatic diseases, pancreatectomy, or drug- and chemical-induced diabetes. Gestational diabetes mellitus, diagnosed in 5-14 % of pregnant women, results from hormonal changes during pregnancy and varies significantly by region (Eades et al., 2024;

Muche et al., 2019; Paulo et al., 2021). The majority of diabetes cases, i.e., 95 %, are classified as type 2 diabetes (Ong et al., 2023). Diagnostic criteria for diabetes include glycated hemoglobin (HbA_{1c}) ≥ 6.5 %, fasting plasma glucose ≥ 7 mM, or plasma glucose ≥ 11.1 mM two hours after a 75 g oral glucose tolerance test, or plasma glucose ≥ 11.1 mM accompanying with classic symptoms of hyperglycemia (ElSayed et al., 2024). Prediabetes is diagnosed when insulin sensitivity is impaired but diagnostic criteria for diabetes are not met. Criteria for prediabetes include HbA_{1c} levels of 5.7-6.4 %, fasting plasma glucose levels of 5.6-6.9 mM, or plasma glucose levels of 7.8-11 mM after a 75 g oral glucose tolerance test. Prediabetes progresses to diabetes in approximately 70 % of cases (Nathan et al., 2007).

1.1.4 Symptoms and complications of diabetes mellitus

Elevated blood glucose damages tissues and organs through glycation (Indyk et al., 2021). Initially, small blood vessels are affected, causing microvascular complications such as neuropathy, nephropathy, and retinopathy. Diabetic retinopathy accounts for 2.6 % of global blindness cases (Leasher et al., 2016). Acute hyperglycemia can also cause blurred vision due to lens swelling (Reddy et al., 2022). Excess glucose is excreted via the kidneys, increasing the glomerular filtration rate initially (Vallon & Thomson, 2020), but eventually causing kidney damage and reduced filtration (Tuttle et al., 2023). Glucose's osmotic properties lead to polyuria, which triggers compensatory polydipsia. Nerve damage can result in numbness in the hands and feet, with unnoticed injuries contributing to diabetic foot syndrome (Feldman et al., 2019; D. Lee et al., 2024). Rather unspecific symptoms related to hypoglycemia are weight loss and fatigue (Yaxin Bi et al., 2021). Chronic hyperglycemia generates macrovascular complications increasing the risk of stroke, heart attack, and tissue necrosis. The all-cause mortality, cardiovascular disease mortality, and non-cardiovascular disease, non-cancer mortality are higher with diagnosis of diabetes. On average, diabetes shortens life expectancy by six years (Kaptoge et al., 2023).

1.1.5 Treatments of diabetes mellitus

To mitigate the disease's consequences, treatment begins immediately after diagnosis (Davies et al., 2022). According to the German guidelines (Bundesärztekammer et al., 2023), the foundation of therapy involves non-pharmacological interventions, such as lifestyle modifications, including diet and physical activity. A weight loss improves

glycemic control and can slow progression or prevent manifestation of type 2 diabetes (Lingvay et al., 2022). If necessary, pharmacological treatments include metformin as the first-line medication. Additional therapies involve sodium-glucose cotransporter 2 (SGLT2) inhibitors or glucagon-like peptide-1 (GLP-1) receptor agonists. In advanced stages, exogenous insulin is administered, either as basal or bolus insulin, based on daily carbohydrate intake.

1.2 Lipid metabolism and lipotoxicity

1.2.1 Fatty acid utilization and metabolic flow

The two major risk factors for type 2 diabetes are increasing age and obesity (Bellary et al., 2021). As senescence is inevitable, body weight can be at least partially managed through lifestyle modifications, medical treatments, or surgical interventions. This section focuses on the relationship between obesity, distorted lipid metabolism, and the resulting negative impact on β-cell functionality and insulin sensitivity. Although type 2 diabetes is historically considered a disease of advanced age, the average age of diagnosis has decreased from 52 to 45 years over recent decades, as reported by the NHANES study (Carrillo-Larco et al., 2024; Koopman et al., 2005). Rising obesity rates have contributed to an increased risk of type 2 diabetes in younger populations. Approximately 30 % of overweight individuals develop type 2 diabetes, and 86 % of diabetic patients are overweight (Daousi et al., 2006). The detrimental effects of obesity, mediated by lipid stressors at the cellular level in a pancreatic model, are collectively referred to as lipotoxicity (Y. Lee et al., 1994). Lipotoxicity is broadly defined as the impairment of cellular functions caused by the accumulation of free fatty acids and their intermediates. This phenomenon arises from multifactorial imbalances in the uptake, storage, and utilization of free fatty acids (Nakamura, 2024). Elevated triglyceride levels in diabetic patients result from chronic caloric excess, which degrade to non-esterified free fatty acids by the absence of insulin's antilipolytic effect (Gastaldelli et al., 2017). The precise cause of elevated fatty acid levels remains unclear (Sobczak et al., 2019). Lipid analysis of diabetic patients compared to healthy controls show a 10 % increase in fatty acid concentrations (Sergeant et al., 2016). The predominant free fatty acids in human plasma include oleic acid (37 %), palmitic acid (30 %), stearic acid (10 %), linoleic acid (7 %), and palmitoleic acid (7 %), collectively accounting for over 90 % of total plasma free fatty acids (Quehenberger et al., 2010). These are classified as long-chain fatty acids,

which have a more pronounced detrimental cellular impact compared to short- or medium-chain fatty acids (Plötz et al., 2019). Plasma concentrations of oleic acid and palmitic acid are 80 µM and 63 µM, respectively (Quehenberger et al., 2010). Free fatty acids, particularly those not bound to serum albumin, mediate harmful effects. Their cellular transport is facilitated by G-protein coupled receptor 40 (GPR40), also known as free fatty acid receptor 1 (FFAR1), and cluster of differentiation 36 (CD36), also called fatty acid translocase (FAT). Binding of fatty acids to these transporters depletes cytosolic and mitochondrial calcium stores (S. Xu et al., 2015), which initially enhances insulin secretion (Moon et al., 2020; Usui et al., 2019), but impairs glucose-stimulated insulin secretion and contributes to hyperinsulinemia in diabetes (Fryk et al., 2021). In case of GPR40, the activation of phospholipase C is a contributing factor (H. Yamada et al., 2016). However, sustained calcium depletion necessitates replenishment through sarcoplasmic/endoplasmic reticulum calcium ATPase (SERCA), which is inhibited by free fatty acids (S. Lai et al., 2017). Fatty acid binding to CD36 triggers pro-inflammatory responses (Cifarelli et al., 2021) and increases reactive oxygen species (ROS) levels, which are further amplified by the cyclic GMP-AMP synthase-stimulator of interferon genes (cGAS-STING) pathway (Ma et al., 2023). Once inside the cell, fatty acids have to be activated to acyl-CoA by acyl-CoA synthetase for further processing. Acyl-CoA is transported into the mitochondrial intermembrane space by carnitine palmitoyltransferase (CPT) 1 and into the mitochondrial matrix by CPT2 (Schreurs et al., 2010). CPT1, the key enzyme for lipid metabolism, exchanges the CoA remnant for carnitine to form acyl-carnitine, which is transported across the outer mitochondrial membrane. CPT2 cleaves carnitine to import acyl-CoA into the mitochondrial matrix. Fatty acids serve several essential functions in cells, with energy production through biochemical degradation being one of the most fundamental (Yaney & Corkey, 2003). In the β-oxidation pathway, long-chain acyl-CoA undergoes four enzymatic steps to generate acetyl-CoA, and the reduction equivalents nicotinamide adenine dinucleotide (NADH) and flavin adenine dinucleotide ($FADH_2$). In addition to mitochondrial β-oxidation, peroxisomes also perform β-oxidation, preferentially processing long-chain and very long-chain fatty acids due to the specificity of ATP-binding cassette (ABC) subfamily D transporters (ABCD1, ABCD2, ABCD3) (Morita & Imanaka, 2012). Although the steps of β-oxidation in mitochondria and peroxisomes are similar, the initial dehydrogenation step differs. It is catalyzed by mitochondrial acyl-CoA dehydrogenase (ACAD) or peroxisomal acyl-CoA oxidase (ACOX1) (Ding et al., 2021). In peroxisomes, the reaction

catalyzed by ACOX1 is not coupled to the respiratory chain, resulting in the formation of H_2O_2 and an increase in oxidative distress. Cellular H_2O_2 levels between 1-10 nM support physiological redox signaling via post-translational modifications (Sies & Jones, 2020), a process termed oxidative eustress. Elevated H_2O_2 levels exceeding 100 nM result in oxidative distress, causing molecular damage. Acetyl-CoA derived from β-oxidation or glycolysis enters the Krebs cycle, where it participates in reactions catalyzed by eight enzymes to generate NADH, $FADH_2$, and guanosine-triphosphate (GTP) for ATP production. Among these enzymes are the mitochondrial aconitase (ACO2) and the respiratory chain complex succinate dehydrogenase (SDH), whose dysfunction has been linked to type 2 diabetes (S. Lee et al., 2022). Pyruvate dehydrogenase converts pyruvate to acetyl-CoA, initiating the entry of carbohydrate-derived pyruvate into the Krebs cycle. These reactions require a steady supply of metabolites, which are disrupted by the effects of free fatty acids (S. Srivastava & Chan, 2008). For instance, citrate synthase (CS) activity (Maris et al., 2013) and its associated metabolites, oxaloacetate and citrate, are negatively affected by fatty acids (J. H. Lee et al., 2014), leading to slower enzymatic activity and oxaloacetate accumulation, which may cause an energy deficit (Sumi et al., 2022). Further consequences of a lipotoxic effect are decreased levels of glutamine and subsequently α-ketoglutarate (Lu et al., 2010; X. Zhou et al., 2023), while glutamate is elevated. The tripeptide glutathione, which includes glutamate as a component, is readily oxidized to glutathione disulfide due to fatty acid-induced oxidative distress (Dou et al., 2018), thereby decreasing the activity of antioxidant enzymes that depend on reduced glutathione as a substrate. As central metabolite, pyruvate is strongly influenced by the impact of fatty acids, as the activities of pyruvate carboxylase and the pyruvate dehydrogenase complex are altered (Hasenour et al., 2024). The pyruvate dehydrogenase complex is critical for converting pyruvate into acetyl-CoA for glucose utilization, while pyruvate carboxylase transforms pyruvate into oxaloacetate as part of gluconeogenesis. Impairments in pyruvate carboxylase activity correlate with reduced insulin secretion (Nagaraju & Rajini, 2016). Pyruvate cycling between the mitochondria and cytosol involves the exchange of pyruvate or its intermediates via the pyruvate/malate shuttle, pyruvate/citrate shuttle, or pyruvate/isocitrate shuttle (Rahul et al., 2023). These shuttles depend on the reversible citrate/isocitrate conversion and subsequent reactions involving oxaloacetate. In addition, oxaloacetate is reversible converted to malate and in a second reaction, malate is formed to pyruvate. Impaired pyruvate metabolism negatively affects GLP-1-mediated insulin secretion (Lewandowski et al., 2022). Specifically, disruptions

in the pyruvate/isocitrate shuttle and acetyl-CoA decrease substrate exchange, impairing insulin secretion (Guay et al., 2007). In this case, mitochondrial citrate is transported to the cytosol by citrate carrier for conversion to α-ketoglutarate and NADPH. Cytosolic reduction equivalents and α-ketoglutarate promote glucose-stimulated insulin secretion, which is diminished by inhibited citrate carrier (Menga et al., 2013). These examples illustrate how fatty acid-induced disruptions in metabolic flow impair cellular function, with adverse effects on lipid metabolism and insulin secretion.

1.2.2 Lipotoxicity and respiratory chain complexes

Under physiological conditions, glycolysis and the Krebs cycle fuel energy production by the respiratory chain complexes in the inner mitochondrial membrane, creating a proton gradient used for ATP production. This process relies on electron flow and involves the transfer of protons from the matrix to the intermembrane space through the action of NADH dehydrogenase (complex I) (Abrosimov et al., 2024), SDH (complex II) (S. Lee et al., 2022), cytochrome c reductase (complex III) (Lang et al., 2023), and cytochrome c oxidase (complex IV or COX) (Aharon-Hananel et al., 2022). The energy from protons re-entering the matrix is harnessed by ATP synthase (complex V) to generate ATP (K. Zhang et al., 2022). In detail, complexes I, III, and IV actively translocate protons to the intermembrane space. In complex I, NADH donates electrons, which are transported through a chain of redox centers (Sharma et al., 2009). Among the 45 subunits forming complex I, five are essential for electron transport, including eight iron-sulfur (Fe-S) clusters serving as redox centers (Sheftel et al., 2009). Fe-S clusters are indispensable for electron transport and numerous other proteins critical for molecular and cellular functions, which are discussed in subsequent sections. NADH-derived electrons move sequentially through Fe-S redox centers, from those with lower affinity to those with higher affinity, releasing energy that pumps protons. After reaching the final redox center, electrons are transferred to coenzyme Q, which delivers them to complex III. Complex II, composed of four subunits, cannot translocate protons on its own but enhances the activities of complexes III and IV. Electrons from $FADH_2$ are utilized through three Fe-S clusters within SDH iron-sulfur subunit (SDHB), coupled to the conversion of succinate to fumarate (S. Lee & Annes, 2020). These electrons are also transferred to coenzyme Q, fueling complex III. In complex III, electrons from coenzyme Q pass through two redox centers to reduce cytochrome c. Complex III consists of three redox-active subunits, including one Fe-S cluster in the Rieske iron sulfur

protein (ISP) (Espada et al., 2020). Thus, the respiratory chain requires a total of 12 Fe-S clusters for electron transport. Complex IV, composed of 11 subunits, uses electrons from cytochrome c to reduce oxygen, the final electron acceptor, while further translocating protons. The proton gradient established by these processes drives ATP production by complex V. Protons flow back into the matrix through the F_0 subunit in the inner mitochondrial membrane, inducing a rotational movement (Y. Lai et al., 2023). This rotation facilitates the combination of inorganic phosphate with adenosine diphosphate (ADP) through a conformational change in the water-soluble F_1 subunit located in the matrix. The F_0 and F_1 subunits are connected by the central and peripheral stalk, with the γ subunit of the central stalk playing a pivotal role in conformational changes required for ATP generation. Complex V is composed of 17 individual subunits. Lipotoxicity impacts these processes. For example, reduced expression of the F_1 β subunit, essential as an ATP binding site, hampers ATP production (Mei et al., 2007). Additionally, fatty acid-induced acetylation of complex V, mediated by sirtuin, has been shown to lower its activity (Ciregia et al., 2017).

1.2.3 Lipotoxicity, oxidative distress, and the PPAR pathway

Alongside peroxisomal β-oxidation and CD36 mediated signaling, the activities of complexes I (Read et al., 2021), II (Quinlan et al., 2012), and III (Plecitá-Hlavatá et al., 2020) also generate superoxide and increase ROS levels, which negatively affect cellular functions (Elsner et al., 2011). It is generally assumed that β-cells are particularly vulnerable to oxidative distress due to their lack of mRNA for catalase, low activity of glutathione peroxidase (GPx), and insufficient clearance by superoxide dismutase (Lenzen, 2008). More recent data suggest that other enzymes, such as thioredoxins, contribute to the antioxidant capacity of β-cells (Stancill et al., 2019). To mitigate oxidative distress, uncoupling proteins (UCPs) are activated, reducing ROS at the cost of ATP production. Excess acyl-CoA can induce UCP2, a proton channel in the inner mitochondrial membrane, through interaction with peroxisome proliferator-activated receptors (PPARs) (Y. H. Jung & Bu, 2020; Wan et al., 2010). There are three types, PPARα (Venezia et al., 2021), PPARβ/δ (J. Song et al., 2022), and PPARγ (Mishra et al., 2020), which can bind fatty acids as ligands. Although UCP2 decreases oxidative distress, it also disfavors ATP production, which negatively impacts ATP-dependent insulin secretion (Inoue et al., 2022). Long-chain fatty acids can inhibit the closure of ATP-dependent potassium channels, thereby affecting calcium, attenuating an initial

stimulus for insulin secretion (Bränström et al., 2004). The interaction of acyl-CoA with ATP-dependent potassium channels requires the acyl group, the CoA component, and involvement of protein kinase C (Antollini & Barrantes, 2016). Additionally, fatty acids can activate the mitochondrial permeability transition pore (Taddeo et al., 2020), which degrades the mitochondrial membrane potential and impairs ATP production and insulin secretion (Zhao et al., 2013). Massive induction of the mitochondrial permeability transition pore can also lead to cytochrome c release, triggering the cascade of apoptosis and correlating with necrosis (Bernardi et al., 2023). The promotor of UCP2 contains a sterol regulatory element (SRE) that can be targeted by sterol regulatory element-binding protein (SREBP)-1c, a regulator of fatty acid synthesis (H. Yang et al., 2022). Additionally, hormone-sensitive lipase (HSL) promotes UCP2 in response to free fatty acids (M. Yamada et al., 2022). Thus, fatty acids can induce UCP2 through interactions with HSL, SREBP-1c, or PPARs. Activation of PPARα (Jie Zhang et al., 2021) and PPARγ (J. Zhou et al., 2020) by acyl-CoA is connected to SREBP-1c (Ying Zhang et al., 2022), promoting apoptosis (Rochira et al., 2013), and impairing glucose-stimulated insulin secretion (H. Yang et al., 2022). The translocation of GLUT4 is regulated by PPARα and PPARγ (Loza-Rodríguez et al., 2020), while acyl-CoA esters impair insulin sensitivity via protein kinase C activation (Brandon et al., 2019; Loots et al., 2022). All types of PPARs regulate the expression of peroxisomal ACOX1, the rate-limiting enzyme of peroxisomal β-oxidation (Rakhshandehroo et al., 2010). PPARα promotes triglyceride storage and reduces fatty acid metabolization in the presence of glucose. This interaction, known as the Randle cycle, preserves energy supply by prioritizing glucose oxidation over fat oxidation. However, malonyl-CoA accumulation inhibits CPT1-mediated acyl-CoA transport, impairing lipid metabolism (Prentki et al., 2020). The impaired utilization of acyl-CoA leads to elevated cytosolic concentrations. The activation and accumulation of acyl-CoA appear to be one of the most relevant aspects mediating harmful effects in the context of lipotoxicity, as shown by the inhibition of acyl-CoA synthase (El-Assaad et al., 2003; Maestre et al., 2003; Jin Zhang et al., 2019).

1.2.4 Endoplasmic reticulum stress and apoptosis

A further aspect negatively affected by lipotoxicity is protein biosynthesis. A crucial protein for the functionality of β-cells is pancreatic and duodenal homeobox 1 (PDX1). PDX1 is a transcription factor necessary for endocrine progenitor cells to differentiate into β-cells (Jonsson et al., 1994). The development of the pancreas (Liew et al., 2008)

and islet function (Hui & Perfetti, 2002) also depend on PDX1. As it is required to induce insulin production by activation of the insulin promoter in β-cells, it was initially termed insulin promoter factor 1. While insulin genetically derives from *INS* (human) or *Ins1* and *Ins2* (mouse) (Shiao et al., 2008), insulin correlates with PDX1 (Ebrahim et al., 2022; Weidemann et al., 2024). mRNA levels of insulin are negatively affected by fatty acids (Briaud et al., 2001). Exendin 4, a mimetic of GLP-1 used as diabetes medication, exerts its effect through PDX1 (Ciregia et al., 2015). The central organelle for the maturation of proteins is the ER, which is also impaired by lipotoxicity. The proper folding of proteins involves chaperones and oxidoreductases, with calcium required as a cofactor (Arruda & Hotamisligil, 2015). The processing of proinsulin by PC1/3 is disturbed by palmitic acid (Wen et al., 2023). Protein folding promotes the generation of oxidative distress. Especially forming disulfide bonds by ER oxidoreductin 1 (ERO-1) and protein disulfide isomerase (PDI) creates H_2O_2 (Sharifi et al., 2024). If the protein folding capacity is overwhelmed, ER stress arises, and the unfolded protein response is initiated (Watt et al., 2023). Factors involved in the unfolded protein response include protein kinase R-like ER kinase (PERK), activating transcription factor 6 (ATF6), inositol-requiring enzyme 1 (IRE1), eukaryotic translation initiation factor 2A (eIF2A), C/EBP homologous protein (CHOP), and c-Jun N-terminal kinase (JNK) (I.-R. Jung et al., 2015). The consequences include the accumulation of misfolded proteins and eventually apoptosis, which is caused by fatty acids (Jin et al., 2022; Yuan Zhang et al., 2022). In addition, ceramides are a mechanism of lipotoxicity that induces apoptosis with strong impact, which is restricted to palmitic acid (M. Guo et al., 2024). Palmitoyl-CoA, the activated form of palmitic acid, is a substrate for the de novo synthesis of ceramides. The unfolded protein response increases ceramide production through activation of PERK (McNally et al., 2022). Ceramides negatively affect cell proliferation and differentiation and induce growth arrest and apoptosis (Imierska et al., 2025). Apoptosis is induced by decreased levels of Bcl-2. Furthermore, ceramides mediate increased insulin resistance through protein kinase C (W. Xu et al., 2024), phosphorylation of IRS1 (Sokolowska & Blachnio-Zabielska, 2019), and PDX1 (Maris et al., 2013). IRS1 is negatively regulated by SREBP-1c (Yan Bi et al., 2014). Another regulatory mechanism connected to IRS1 is the PI3K/Akt pathway (Hemmings & Restuccia, 2012). Requirements for the action of insulin include, besides phosphorylation of IRS1, the downstream activation of PI3K and Akt. Akt is activated by tyrosine kinase activity, phosphorylating serine 473 (p-Akt). p-Akt induces translocation of GLUT4 and reduces gluconeogenesis and hepatic glucose output.

Alongside improving insulin sensitivity, p-Akt is favorable for proliferation, protein synthesis, and apoptosis (J.-H. Chang et al., 2020). Further proteins with signaling functions contributing to cell survival include members of the mitogen-activated protein kinase (MAPK) family. Members of this family are extracellular signal-regulated kinases (ERK1, ERK2), JNK, and p38 MAPK. ERK1/2, which are 84 % homologous, are subsequently activated by upstream Raf and MEK1/2 through phosphorylation of threonine 202 and tyrosine 204 (p-ERK1/2) located at the activation loop (Sidarala & Kowluru, 2017). p-ERK1/2 promote proliferation and cellular remodeling, while proteins involved in apoptosis are inactivated. Signals of p-ERK1/2 induced by glucose positively influence insulin secretion and *Ins1* mRNA (Benes et al., 1999). Activation of JNK1 and JNK2, introduced for ER stress, promotes apoptosis and suppresses insulin gene expression involving PDX1 (M. K. Kim et al., 2021). The p38 MAPK is inducible by oxidative distress and promotes apoptosis upon activation. Fatty acids are directly involved in the kinase-related signaling pathways. The dephosphorylation of p-Akt (Y.-C. Chang et al., 2020) and the phosphorylation of JNK is described in diabetic models (I.-R. Jung et al., 2015), disfavoring cellular functions. The lipotoxic effects of accumulating fatty acids harming β-cells are of a multifactorial origin.

1.3 Glutaredoxin and iron-sulfur proteins

1.3.1 Glutaredoxin in the thioredoxin protein family

A potentially underexplored factor that may play a role in the cellular pathologies of diabetes is the mitochondrial protein Glutaredoxin (Glrx) 5. The Glrx system was first described by Arne Holmgren in 1976 as a hydrogen transport system for *Escherichia coli's* ribonucleotide reductase, which included NADPH, glutathione, glutathione reductase, and the newly identified protein Glrx (Holmgren, 1976). Glrxs belong to the thioredoxin protein family. Thioredoxins are small, redox-active proteins with a size of approximately 12 kDa, found across all biological domains (Laurent et al., 1964). They are redox proteins with a CGPC active site motif located at the protein's core, which consists of five β-sheets surrounded by four α-helices (Eklund et al., 1991). Glrxs were originally described as having a further CxxC active site (Martin, 1995; Trnka et al., 2020) and are involved in reducing disulfides and glutathionylated thiols with glutathione as cofactor (Geissel et al., 2024). Based on the number of active site cysteines, Glrxs are classified as either monothiol (CxxS) or dithiol (CxxC).

1.3.2 Classification and overview of glutaredoxins

As investigations revealed discrepancies in the structure of Glrxs with monothiol and dithiol active sites, newer classifications divide them into class I-VI Glrxs (Berndt et al., 2021). Classes III and IV are specific to eukaryotes, while classes V and VI are found in cyanobacteria (Couturier et al., 2009). Classes I and II, however, are ubiquitous across all living organisms. For simpler characterization, most dithiol Glrxs belong to class I and most monothiol Glrxs to class II. In the mammalian genome, the Glrxs include dithiols Glrx1 and isoforms of Glrx2 (mitochondrial Glrx2a, cytosolic/nuclear Glrx2b and Glrx2c), as well as monothiols Glrx3 and Glrx5 (H. Ye et al., 2010). First descriptions of these Glrxs can be found for Glrx1 (Luikenhuis et al., 1998), Glrx2 (Gan, 1992), Glrx3 (Aslund et al., 1994), and Glrx5 (Rodríguez-Manzaneque et al., 1999). To provide an overview about the available research, a literature search in PubMed with Glrxs mentioned in its title by the term (glutaredoxin[Title]) OR ("glrx*"[Title]) OR ("grx"[Title]) reveals 782 articles in June 2024. Regarding human Glrxs, 138 articles are attributed to Glrx1, 84 articles to Glrx2, 63 articles to Glrx3 or its homolog Glrx4, and 48 articles to Glrx5.

There are further Glrxs, associated to other species, which are not present in humans. As orientation, but not as complete list, there are plant Glrxs GrxC1 specific in *Populus trichocarpa* (Y. Feng et al., 2006), GrxC3 in *Manihot esculenta* (X. Guo et al., 2022), GrxC2.1 (Pankaj K. Verma et al., 2016), GrxC2.2 (S. Liu et al., 2019), GrxC7 (Pankaj Kumar Verma et al., 2021), and Grx20 (Ning et al., 2018) in *Oryza sativa*, GrxS25 in *Solanum lycopersicum* (Hou et al., 2019), as well as Grx7, Grx8 (Walters & Escobar, 2016), GrxC2 (Bender et al., 2015), GrxC5 (Couturier et al., 2011), GrxC9 (Herrera-Vásquez et al., 2015), Grxcp (N. Cheng et al., 2006), GrxS8 (Ehrary et al., 2020), GrxS12 (Gama et al., 2008), GrxS13 (La Camera et al., 2011), GrxS14 (Rey et al., 2017), GrxS15 (Moseler et al., 2015), GrxS16 (Hou et al., 2018), GrxS17 (N. Cheng, Liu, et al., 2011), ROXY1, ROXY2 (Xing & Zachgo, 2008), ROXY19 (L.-J. Huang et al., 2016), all described in *Arabidopsis thaliana*. Further non-plant Glrxs are GrxA in *Synechocystis spp.* (Knaff & Sutton, 2013), GrxA1 in *Corynebacterium pseudotuberculosis* (Eberle et al., 2018), GrxC14S in *Escherichia coli* (Bushweller et al., 1992), GrxD (Romsang et al., 2015) found in *Escherichia coli*, *Aspergillus fumigatus*, or *Pseudomonas aeruginosa*, Grx21 in *Caenorhabditis elegans* (Morgan et al., 2010), GrxO2L, and GrxG4L in *Orthopoxvirus vaccinia* (White et al., 2000),

or Grx1p (Håkansson et al., 2006), Grx4p (Peggion et al., 2008), Grx6 (M. Luo et al., 2010), and Grx8 (Eckers et al., 2009) in *Saccharomyces cerevisiae*.

1.3.3 Functional roles of glutaredoxins

Based on their thiol groups, some Glrxs are capable to perform redox reactions. Dithiol Glrxs can function as redox sensors, initiating cellular redox regulation, for example, by altering protein glutathionylation or participating in electron transport in ribonucleotide reductase (Lillig et al., 2005). In contrast, the involvement of monothiol Glrxs in redox signaling is more controversial and debatable (Fernandes et al., 2005; Herrero & de la Torre-Ruiz, 2007; Ogata et al., 2021). Monothiol Glrxs have a more specialized role, particularly in their interactions with Fe-S clusters (Mühlenhoff et al., 2020), which's production is one of the most fundamental properties of mitochondria. Fe-S clusters protect iron from oxidation, a process that became essential after the Earth's atmosphere evolved over one billion years ago (Sheftel, Mason, et al., 2012). The biosynthesis of Fe-S clusters is of high relevance for functionality of proteins, as they are required as cofactors, active site or for structural integrity and stability in Fe-S proteins (Andreini et al., 2017). Disturbances regarding Fe-S clusters can have dramatic impact on fundamental cellular processes, especially for mitochondria (Braymer & Lill, 2017). Previous studies have shown that defects in Glrx5 splicing can disrupt Fe-S cluster homeostasis, leading to mitochondrial dysfunction and the development of diabetes (Camaschella et al., 2007). Moreover, Glrxs are known to be underexpressed in diabetic models (Petry et al., 2017) and in vitro under the influence of fatty acids (Petry et al., 2018), as well as in vivo in high fat diet models (Petry et al., 2022). Given its potential clinical relevance, further investigation into the pathways involving the mitochondrial protein Glrx5 and Fe-S cluster biogenesis is warranted.

Regarding its basic information, Glrx5 is a mitochondrial protein encoded by the nuclear genome (UniProt: Q86SX6 (human) and Q80Y14 (mouse)). The protein is small sized, consisting of 157 (human) or 152 amino acids (mouse), corresponding to a molecular weight of 16.6 (human) or 16.3 kDa (mouse). The first 31 amino acids of both species represent a transit sequence, with the remaining amino acids forming the mature mitochondrial Glrx5 protein, which has a molecular weight of 13.7 (human) or 13.4 kDa (mouse). Despite five replaced amino acids in the transit sequence and five replaced amino acids as well as an additional chain of four amino acids in the mature human

protein sequence, Glrx5 is highly conserved evolutionary (Johansson et al., 2011; Mühlenhoff et al., 2020). The active site CGFS motif is located at amino acids 67-70 (human) or 63-66 (mouse) (Rodríguez-Manzaneque et al., 1999).

1.3.4 Mitochondrial iron-sulfur cluster assembly machinery

Within mitochondria, Glrx5 plays a crucial role in the iron-sulfur cluster assembly (ISC) machinery, which is responsible for synthesizing and transferring Fe-S clusters to target apoproteins. The ISC machinery comprises at least 18 proteins, as described in yeast (Braymer & Lill, 2017). The interplay of the protein network can be divided into three major steps. Articles providing helpful illustrations of how the proteins interact can be found (Ciofi-Baffoni et al., 2018; Stehling et al., 2014).

In the first step, a [2Fe-2S] cluster is assembled by the iron-sulfur cluster assembly protein 1 (Isu1, the human homolog: ISCU2) (Freibert et al., 2021). Inorganic sulfur is therefore released through cysteine desulfurization from a desulfurase complex consisting of nitrogen fixation homolog saccharomyces, iron-sulfur desulfurase, and acyl carrier protein (Nfs1-Isd11-Acp1), binding sulfur to its cysteine (Schulz et al., 2024). The sulfur is presented to cysteine of Isu1 as persulfide. To be further processed, sulfur is reduced by NADPH, yeast adrenodoxin homolog (Yah1, the human homolog: ferredoxin (FDX)) (Sheftel et al., 2010), and adrenodoxin reductase homolog (Arh1, the human homolog: ferredoxin-NADP reductase), while Arh1 delivers electrons to Isu1 (Mühlenhoff, 2003). To supply the ISC with ferrous iron (Fe^{2+}), it is imported into the mitochondria by the transporters mitochondrial RNA-splicing protein (Mrs3 and Mrs4, the human homolog: mitoferrin 1) (Foury & Roganti, 2002). The steps how iron binds to Isu1 are less clarified, but the yeast frataxin homolog (Yfh1, the human homolog: frataxin) could be involved (Gerber et al., 2003). After that, a [2Fe-2S] cluster is assembled at Isu1. In the second step, the cluster is released from Isu1 by stress-seventy subfamily Q protein 1 (Ssq1, the human homolog: Gro-P like protein E protein homolog 75 (GRP75)), J-type accessory chaperone 1 (Jac1, the human homolog: HSC20), Grx5 in yeast, Glrx5 in humans, and mitochondrial Gro-P like protein E (Mge1, the human homolog: suppressor of Ire1 and Lhs1 deletion 1 (SIL1)), which are activated by iron-sulfur assembly proteins (Isa1 and Isa2, the human homolog: ISCA1 and ISCA2). Jac1 binds to the Fe-S-Isu1 complex and further to Ssq1 (Dutkiewicz et al., 2006). By hydrolysis of ATP, there is a conformational change of Ssq1 binding the Fe-S cluster and LPPVK motif of Isu1, releasing Jac1 from

the Fe-S-Isu1 complex (Dutkiewicz et al., 2004). Two molecules of Glrx5 are activated by Isa1 and Isa2 and bind to Ssq1, locating it close to one Fe-S cluster (K.-D. Kim et al., 2010). The cluster binds cysteine sites of two Glrx5 molecules in a reaction depending on glutathione. In a last reaction, Mge1 binds to the Isu1 complex and by phosphorylation of ADP, all factors and proteins are released from Isu1 (Dutkiewicz et al., 2003). The Glrx5 molecules can now transfer its bound Fe-S cluster in the third step to apoproteins. In humans, the Glrx5 supported transfer of clusters is performed by the ATP dependent glucose regulated protein GRP75, iron-sulfur cluster co-chaperone protein (HSCB), and GrpE-like 1 and 2 (GRPEL1/2) (Uhrigshardt et al., 2010). HSCB binds to the ISCU2 bound cluster and is supposed to get into an interaction with Glrx5 by a KKxKK amino acid site at the C terminus (Maio et al., 2014). After a complex with GRP75 is built by HSCB, a conformational change weakens the connection to ISCU2. GRPEL1/2 supports the cluster dissociation from GRP75 to build a complex with two molecules of Glrx5. The dimer in general protects the cluster from an early dissociation if intracellular glutathione is present (Banci et al., 2014). Further descriptions mention an interaction of cluster bound Glrx5 with BolA-like proteins (BOLA1, BOLA3) (Uzarska et al., 2016), in yeast Aim1. A dimer of BOLA1 and BOLA3 could facilitate electron transfer and support transfer of clusters. Glrx5 transfers the bound [2Fe-2S] cluster to apoproteins which probably can directly react with the cluster and bind the sulfur to their amino acids (cysteine, arginine, histidine, or serine). Further relevant factors for cluster insertion into apoproteins could react through the KKxKK site of Glrx5 like SDHAF1 for SDH (Ghezzi et al., 2009) or LYRM7 for ubiquinol-cytochrome c reductase Rieske iron-sulfur polypeptide 1 (UQCRFS1) as part of complex III (Alfattal et al., 2023; Faria et al., 1990). In addition to the [2Fe-2S] clusters, apoproteins also require [4Fe-4S] clusters, whose assembly is less well understood. This process involves several reactions and key factors, including Isa1, Isa2, iron-sulfur cluster assembly factor for biotin synthase and aconitase-like mitochondrial proteins (Iba57), and possibly the NifU-like protein (Nfu1) (Sheftel, Wilbrecht, et al., 2012). Nfu1 is known to bind [4Fe-4S] clusters and insert them into apoproteins (Navarro-Sastre et al., 2011). In humans, Glrx5 assists ISCA1 and ISCA2 in incorporating a [2Fe-2S] cluster, facilitating the formation of a [4Fe-4S] cluster (Cózar-Castellano et al., 2004; Sheftel, Wilbrecht, et al., 2012).

1.3.5 Iron-sulfur cluster export machinery

Once the Fe-S clusters are assembled, they must be exported from the mitochondria to the cytosol. This process is carried out by the ISC export machinery, a smaller protein network involved in transporting Fe-S components (Lill et al., 2015). Although the details of this process are not fully understood (Ferecatu et al., 2014), several key players have been identified. These include the mitochondrial inner membrane ABC transporter Atm1 (the human homolog: ABCB7) (Pandey et al., 2019), as well as the mitochondrial FAD-linked sulfhydryl oxidase Erv1 (the human homolog: augmenter of liver regeneration (ALR)), and the cofactor glutathione (Lange et al., 2001; Ozer et al., 2015). An unidentified Fe-S intermediate derived from the ISC machinery (Pandey et al., 2023) is bound to four glutathione molecules and exported by Atm1 (Srinivasan et al., 2014), whose ATPase activity is stimulated during this process. This enables the Fe-S intermediate to be transferred to the cytosol, a necessary step for further processing of extra-mitochondrial and nuclear Fe-S proteins (Braymer et al., 2024).

1.3.6 Cytosolic iron-sulfur protein assembly machinery

A third protein network, located to the cytosol, completes the complex process of Fe-S cluster synthesis. This network, called the cytosolic iron-sulfur protein assembly (CIA) machinery, consists of 13 known proteins (Ciofi-Baffoni et al., 2018). In humans, the P-loop NTPase and scaffold proteins nucleotide binding protein iron-sulfur cluster assembly factor (NUBP1 and NUBP2, in yeast NBP35 and CFD1), are involved in the assembly of a [4Fe-4S] cluster as tetramer by the $Cx_{13}Cx_2Cx_5C$ motif (N terminus) and $Cx_{18}Cx_2Cx_2C$ motif (C terminus) (Freibert et al., 2017; Stehling et al., 2018). While the sources of the iron and sulfur components are not fully understood, it is hypothesized that the Fe-S intermediate from the ISC export machinery provides the sulfur component. The diflavin reductase NDOR1 (in yeast Top1T722A mutant Hypersensitive (TAH18)) forms a complex with anamorsin to transfer electrons from NADPH to FAD and flavin mononucleotide, eventually passing the electrons to anamorsin (Murataliev et al., 2004). Anamorsin, also known as cytokine induced apoptosis inhibitor 1 (CIAPIN1, in yeast: Dre2), contains two cysteine rich motifs (Cx_8Cx_2CxC and $Cx_2Cx_7Cx_2C$), known as the CIAPIN domain, which are connected by a 51 residues containing linker, to bind a [2Fe-2S] or [4Fe-4S] cluster (Banci et al., 2011). The anamorsin-NDOR1 complex likely delivers electrons to the NUBP1-NUBP2 complex, generating sulfide, similarly to the

role of FDX in mitochondria (Webert et al., 2014). As the Fe-S clusters are assembled, further trafficking in the cytosol is facilitated by BOLA2 (in yeast Fra2) and Glrx3. At least by the type of proteins, this process shows similarities to cluster trafficking in mitochondria. Glrx3 is a cytosolic protein with a molecular weight of 37 kDa, containing a non-redox active thioredoxin domain (Herrero & de la Torre-Ruiz, 2007) and two CGFS Glrx domains (Lillig et al., 2008). Glrx3 was initially described as the protein kinase C-interacting cousin of thioredoxin (PICOT) (Witte et al., 2000). In *Saccharomyces cerevisiae,* there are two homologs Glrx3 and Glrx4 (Fernandes et al., 2005), both of which play a similar role in the maturation of cytosolic and nuclear Fe-S proteins. To transfer CIA-derived clusters, two Glrx3 molecules can dimerize to bind two [2Fe-2S] clusters (Banci et al., 2015). Additionally, it has been shown that two BOLA2 molecules can bind to Glrx3, transferring two [2Fe-2S] clusters as a trimer, a process that has been observed in mammalian cells (Frey et al., 2016), representing an additional way of cluster transfer by Glrx3. The cluster can be transferred to apoanamorsin, likely through a binding site on Glrx3. The ability of Glrx3 to transfer clusters depends on intact mitochondria, a functional ISC and ISC export machinery. It is also suggested that the Fe-S intermediate might serve as a target for Glrx3, which is essential for its transfer activity (Braymer et al., 2024). Interestingly, Glrx3 in yeast does not depend on NBP35 or Dre2. The CDGSH iron-sulfur domain-containing protein 1 (Cisd1), a target for diabetes drugs, may provide an alternative to Glrx3, facilitating Fe-S cluster transfer to apoproteins under conditions of oxidative distress (Colca et al., 2004). The insertion of Fe-S clusters into cytosolic and nuclear target proteins belongs to the late phase of CIA and requires multiple proteins. This process is complex, and many details remain unclear. The proteins CIAO1 (yeast homolog: Cia1) (van Karnebeek et al., 2024), MMS19 (Stehling et al., 2012), and CIA2B form a complex (Stehling et al., 2013), where Fe-S target proteins can locate closely to. The nuclear prelamin A recognition factor-like (NARFL, other name CIAO3, yeast homolog: Nar1) (H. Liu et al., 2023) can bind to this complex and facilitate the uptake of Fe-S cluster through a possible enzymatic activity. In yeast, Nar1 is essential for the maturation of cytosolic and nuclear Fe-S proteins (Urzica et al., 2009). There are more details regarding specific target proteins of the cytosol. CIA2A, as a partner protein of NARFL, could form a complex with CIAO1 to bind a cluster via its cysteine group. The interaction of CIAO1 and CIA2A seems to have an exclusive function for the iron regulatory protein 1 (IRP1) (Stehling et al., 2013), the apo form of which is the cytosolic aconitase (ACO1). Additional data suggest that

NARFL might distribute Fe-S cluster from the NUBP1-NUBP2 complex to CIAO1 and CIA2A. Other factors, such as oral cancer overexpressed 1 (ORAOV1) and Yae1 domain-containing protein 1 (YAE1D1), are also associated with the CIA machinery and are related to ABC sub-family E member 1 (ABCE1) (Paul et al., 2015), which antagonizes the anti-viral action of ribonuclease L. Finally, the radical S-adenosyl methionine domain-containing protein 2 (viperin) (Upadhyay et al., 2017), which is involved in enhancing viral infectivity, has been shown to depend on tryptophan to interact with the cluster-distributing complex.

1.3.7 Overview of iron-sulfur cluster proteins

Fe-S cluster synthesis in both the mitochondria and the cytosol is orchestrated by an interplay of over 30 required proteins, while Glrx5 serves as a central factor in mitochondrial cluster transfer. The protein networks interact with one another, and mitochondrial factors can influence cytosolic and nuclear proteins. Although the majority of ISC and CIA components are known, some remain undiscovered (Ciofi-Baffoni et al., 2018). While there is more information on the steps of ISC, details of the CIA machinery still require further investigation. The Fe-S clusters produced by these processes are crucial for the function of many related proteins. An analysis of the Fe-S proteome has identified 70 genes encoding Fe-S proteins (Andreini et al., 2009), with approximately 61 % of these proteins containing [4Fe-4S] clusters and 39 % containing [2Fe-2S] clusters (Andreini et al., 2016). A rare form, the [3Fe-4S] cluster, is found in a few proteins, such as SDH (Kita et al., 1990), respiratory nitrate reductase 2 β chain (Blasco et al., 1990), fumarate reductase iron-sulfur subunit (Johnson et al., 1988), and glutamate synthase (Filetici et al., 1996). Further examples of mitochondrial proteins that use Fe-S clusters as cofactors with relevance for the recent topic are: the ISC proteins FDX1, FDX2, ferredoxin 1-like (FDX1L), Glrx5, Isa1, Isa2, Isu1, Nfu1, Nfs1, the ISC export machinery transporter ABCB7, the ACO2 as part of Krebs cycle, respiratory chain complex I subunits (NDUFS1, NDUFS7, NDUFS8, NDUFV1, NDUFV2), complex II subunit SDHB, complex III subunit UQCRFS1, and ubiquinol-cytochrome c reductase Rieske iron-sulfur polypeptide 1 pseudogene 1 (UQCRFS1P1) with a predicted association to complex III. For completion, complex I contains two [2Fe-2S] and six [4Fe-4S] clusters, complex II contains each one [2Fe-2S], [4Fe-4S], and [3Fe-4S] cluster, and complex III contains a single [2Fe-2S] cluster (Read et al., 2021). Further examples for outer-mitochondrial proteins include glutamine phosphoribosylpyrophosphate

amidotransferase (GPAT) involved in purine biosynthesis, DNA polymerase subunit δ 1 (PolD1) for DNA repair, the CIA proteins CIAPIN1, Cisd1, NARFL, NUBP1, NUBP2, BOLA1, BOLA2, BOLA3, Glrx3 for cytosolic cluster transfer, Glrx2 for cellular response upon oxidative distress mediated apoptosis, ferrochelatase for inserting iron into protoporphyrin as final step of heme synthesis, and ACO1 with iron regulatory function. Further examples associated to amino acids, and nucleotide metabolism as well as RNA and DNA related processes, underscore the broad impact of Fe-S cluster defects on fundamental cellular functions and their clinical relevance. A case report of a Glrx5 mutation has been linked to disruptions in iron homeostasis and the development of diabetes (Camaschella et al., 2007).

1.4 Iron metabolism and ferroptosis

1.4.1 Physiological iron regulation

There is evidence suggesting a correlation between Glrx5 and iron metabolism, which may contribute to the progression of diabetes. This section explains how cellular iron is regulated, the consequences of dysregulated iron levels, and how Glrx5 may influence this process. Proper regulation of iron levels is critical for all organisms and therefore tightly controlled (Galy et al., 2024). Low iron levels result in cell proliferation arrest and induce cell death due to mitochondrial dysfunction, as iron is essential for electron transfer, redox reactions, and the synthesis of Fe-S clusters (Cui et al., 2019). Additional iron-dependent processes include oxygen transport by hemoglobin and DNA synthesis (Jian Wang & Pantopoulos, 2011). Excessive iron can be harmful, as it promotes the formation of radicals that damage molecules such as DNA, proteins, and cell membranes, potentially triggering cell death. To avoid the harmful effects of aberrant iron levels, cellular iron is regulated by various proteins involved in iron uptake, storage, and export. Dietary iron enters the systemic circulation through enterocytes in the duodenum and jejunum. In the duodenum, the intestinal ferrireductase, duodenal cytochrome B (Dcytb), reduces ferric iron (Fe^{3+}) to ferrous iron (Fe^{2+}) (Sharp, 2007). Ferrous iron is absorbed by enterocytes via the divalent metal transporter 1 (DMT1, synonym SLC11A2), with a potential alternative transporter, ZRT/IRT-like protein 14 (ZIP14) (Coffey & Knutson, 2017). Once inside the enterocyte, ferrous iron is exported by the only known iron exporter, ferroportin (synonym SLC40A1) (Azucenas et al., 2023). Ferrous iron is oxidized by human ferroxidases, ceruloplasmin, and its homolog, hephaestin, converting

it to ferric iron, which is then loaded onto the plasma iron transport protein, transferrin (Helman et al., 2023). Under normal conditions, about one-third of transferrin is bound to a single iron molecule, whereas in pathophysiological conditions such as hemochromatosis, two iron molecules bind, forming diferric transferrin (Fang et al., 2023). Iron-loaded transferrin binds to transferrin receptor (TfR) 1, an isoform of DMT1, on the cell membrane, facilitating iron uptake into the target cell. Another homolog of TfR1, the type II transmembrane glycoprotein TfR2, is expressed primarily in hepatocytes and erythroid cells and has a lower affinity for iron (Silvestri et al., 2014), whereas TfR1 is ubiquitously expressed. After endocytosis and endosomal acidification, iron is released from transferrin, leaving apotransferrin to remain bound to TfR1 (Rizzollo et al., 2021). Six-Transmembrane epithelial antigen of the prostate (STEAP) reduces ferric iron to ferrous iron, allowing it to exit the endosome via DMT1 and distribute to the cytosol or mitochondria (Meng et al., 2022). To prevent the harmful effects of free iron, ferric iron is stored in ferritin. Ferritin is a highly conserved heteropolymer composed of 24 subunits, including ferritin light chain (FTL) and ferritin heavy chain (FTH1) (A. K. Srivastava et al., 2023), with the composition of subunits varying across tissues (Harned et al., 2010). Ferritin can store approximately 4,500 iron atoms, though only about one-third of ferritin is typically loaded (Harrison & Arosio, 1996). FTH1 possesses ferroxidase activity, which is essential for storing oxidized iron. Iron binds to poly(rC)-binding protein 1 (PCBP1), which then interacts with ferritin for storage (Yubo Wang et al., 2023). Mitochondrial ferritin, a specialized homopolymer of the heavy chain with ferroxidase activity, is expressed in metabolically active cells to prevent harmful reactions involving free iron, especially during oxidative distress (Bou-Abdallah et al., 2024). Free iron can also promote apoptosis, inducible by opening of the mitochondrial permeability transition pore, triggering the release of cytochrome c (Rauen et al., 2004), also interacting with fatty acids. To increase cellular iron levels, iron is released from ferritin via the ubiquitin-proteasome system (Din et al., 2024).

To prevent radical reactions from free iron and ensure sufficient iron supply, the regulation of related proteins is crucial. Iron regulation is largely mediated by the Fe-S protein ACO1, as described in the previous chapter. ACO1 is a cytosolic protein composed of four domains, while domains 1 and 2 represent the core protein, and domains 3 and 4 are aligned alongside it (Rouault, 2019). The active site contains a [4Fe-4S] cluster that closes a hydrophilic cavity between the core and domain 3 through a conformational change (Rouault, 2006a). This holostructure enables ACO1 to catalyze

the conversion of citrate to its intermediate cis-aconitate, and further to isocitrate. Residues of all four domains contribute to the catalytic activity. In case of iron depletion, the iron dissociates from the active site of ACO1, leaving a [3Fe-4S] cluster, which inactivates ACO1 (B. Zhang et al., 2013). Increased oxidative distress can also lead to the disassembly of iron from the cluster. After this conformational change, domains 3 and 4 open the cavity to the core protein. The inactive [3Fe-4S] cluster converts the holoprotein ACO1 to its iron regulatory protein form IRP1. The open cavity of IRP1 binds to iron-responsive elements (IREs) in the untranslated regions (UTR) of mRNA, post-transcriptionally regulating the expression of proteins involved in iron homeostasis (Walden et al., 2006). The IRE is characterized by an approximately 30 nucleotide hairpin structure (Addess et al., 1997). At the 3' and 5' end of the sequence is a helical structure forming the lower stem, connected to the upper stem with an unpaired bulged cytosine, providing flexibility. The loop of the hairpin contains a six nucleotide structure with AGU residues at positions 2, 3, and 4 (Addess et al., 1997), which binds to the IRP1 cavity of domains 2 and 3, while the bulged cytosine interacts with a binding site at domain 4. A scheme illustrating the IRE structure (Rouault, 2006b) and interaction with IRP1 (Rouault, 2006a) can be found in the literature. Of note, there is also an iron regulatory protein 2 (IRP2, further known as iron responsive element binding protein 2 or ACO3) (Kerins et al., 2017), sharing 64 % identity to IRP1 (Anderson et al., 2012). Inducible by decreasing iron level, IRP2 binds IRE, but this action is independent from Fe-S cluster (Hentze et al., 2010). Upon replenishment of iron, IRP2 degrades (Terzi et al., 2021). IRP2 is thought to be responsive for special types of IRE, which needs further clarification. The interaction of the IRE with IRP1 regulates the expression of iron-related genes. When the IRE is located closer to the 5'UTR, IRP1 prevents the binding of translation factors, decreasing translation efficiency and transcript levels. Examples of such mRNAs include *FTH1*, *FTL*, and *SLC40A1*. In conditions of iron depletion, IRP1 decreases the levels of ferritin and ferroportin to increase free iron and decrease iron export of the cell. The 3'UTR is susceptible for degradation by endonucleases (Z. D. Zhou & Tan, 2017). Binding of IRE closer to 3'UTR by IRP1 protects mRNA from cleavage and enhances its half-life leading to more transcripts. Examples include *TFRC* (five IRE in UTR) (Lin et al., 2001), and *SLC11A2*. Binding activity of IRP1 increases the transcripts of TfR1 and DMT1, promoting cellular iron uptake. Notably, some proteins, such as TfR2, mitochondrial ferritin, and the ferroportin isoform *Fpn1b*, do not contain IREs (Q. Yang et al., 2020). Additionally, there are further proteins regulated by 5'UTR

IRE like ACO2 (Shen et al., 2023), SDHB (in *Drosophila melanogaster*) (S. Wu et al., 2022), NDUFS1 (Maio et al., 2022), δ aminolevulinate synthase 2 (ALAS2) (B. Wang et al., 2021), hypoxia-inducible factor 2 α (HIF2α) (Duarte et al., 2021), and amyloid precursor protein (Khan et al., 2023). Further proteins with 3'UTR IRE are glycolate oxidase (in mouse) (Kohler et al., 1999), cell division cycle 14A (CDC14A) (Connell et al., 2023), CDC42 binding protein kinase α (CDC42BPA) (Cmejla et al., 2006), and hydroxyacid oxidase 1 (Hao1) (Cmejla et al., 2006). Of note, the Krebs cycle and respiratory chain components ACO2, SDHB, and NDUFS1 are responsive to iron level, but NDUFS1 is not regulated by IRP1 (Lin et al., 2001). In addition to iron regulation, also heme structures are responsive to IRE by ALAS2, which decreases by low available iron (Jing Wang et al., 2022). Heme synthesis by proerythroblasts is divided into eight enzymatic reactions. ALAS2 is catalyzing the first of these reactions to produce aminolevulinic acid which is further processed to protoporphyrin and completed by iron insertion facilitated by the Fe-S protein ferrochelatase. HIF is a transcription factor to strengthen cells against conditions of hypoxia, while its expression is sensitive against oxygen and stabilized by hypoxia (Catrina & Zheng, 2021). HIF-1 and HIF2α are connected to proteins of iron regulation, up regulating TfR1 (Fagundes et al., 2022), ferroportin (Fuhrmann et al., 2020), DMT1, and Dcytb (Q. Xia et al., 2022), and down regulating hepcidin (Yook et al., 2021). Hepcidin is the main regulator of ferroportin, while high levels of hepcidin degrade ferroportin. Further, proteins of glucose metabolism are regulated by HIF, like GLUT1, GLUT2, GLUT3, and hexokinase 1 and 2, potentially influencing glucose-stimulated insulin secretion (K. Cheng et al., 2010). While ACO1/IRP1 regulates cellular iron level during iron depletion, ACO1 activity in its holoenzyme form plays a key role in citrate metabolism. In iron-depleted states, citrate accumulates due to the inactivity of ACO1. High cytosolic citrate levels inhibit fatty acid transport into mitochondria (Iacobazzi & Infantino, 2014). Further, cytosolic citrate is required to transfer an acetyl group by ATP citrate lyase to form acetyl-CoA. Acetyl-CoA can be used to increase lipid synthesis. Mitochondrial citrate is exported to the cytosol by the citrate carrier CIC. The transformation of citrate is recognized as positive for glucose-stimulated insulin secretion, which is explained by pyruvate cycling, where malate, citrate, and isocitrate are involved (G.-F. Zhang et al., 2021). The NADPH produced in this cycling pathway could promote glucose-stimulated insulin secretion. Thus, ACO1 activity links both citrate metabolism and iron regulation, which may be of particular relevance for type 2 diabetes.

1.4.2 Pathology of iron dysregulation

The discovery of the Rat sarcoma (RAS)-selective lethal compound erastin by Brent Stockwell (Dolma et al., 2003) highlighted a new form of cell death distinct from apoptosis, autophagy, or necrosis. Erastin induces cell death through the RAS-RAF-MEK signaling pathway by binding mitochondrial voltage-dependent anion channels (VDAC2 and VDAC3) (Yagoda et al., 2007), increasing TfR1-dependent iron uptake, and decreasing ferritin levels (W. S. Yang & Stockwell, 2008). This process leads to the accumulation of free iron, triggering lipid peroxidation of cell membrane and ultimately ferroptosis, a form of cell death dependent on iron but not on other metals (Dixon et al., 2012). Further research revealed that erastin also inhibits the cystine/glutamate antiporter, system xc^-, leading to cysteine depletion. Cysteine is necessary for the function of GPx4, which contains selenocysteine and cysteine groups (W. S. Yang et al., 2014). Lipid peroxidation in the presence of elevated iron levels overwhelms the antioxidant defense provided by GPx4, resulting in cell death. Impaired mitochondrial remodeling promotes ferroptosis (S. Tang et al., 2024). Pancreatic β-cells, which are highly susceptible to oxidative distress (Lenzen, 2008), may be particularly vulnerable to ferroptosis due to iron-mediated lipid peroxidation, which could impair β-cell function and promote diabetes progression. The first report on impaired islets functionality by ferroptosis inducing agents can be found in 2018 (Bruni et al., 2018). Ferroptosis has been implicated in palmitate-induced insulin resistance (Cui et al., 2019), highlighting the potential role of iron misregulation in metabolic disorders.

1.5 Glutaredoxin-related pathologies

1.5.1 Clinical relevance of Glutaredoxin 5 mutations

Starting in 2007, Camaschella et al. described the first case report linking a Glrx5 mutation to the manifestation of diabetes (Camaschella et al., 2007). In addition to diabetes, the mutation of Glrx5 was initially associated with iron overload, impaired heme synthesis, sideroblastic anemia, hepatosplenomegaly, liver cirrhosis, jaundice, and non-ketotic hyperglycinemia. To date, seven case reports of Glrx5 mutations have been documented, two of which include diabetes as a clinical manifestation (Camaschella et al., 2007; G. Liu et al., 2014). Four patients exhibited features indicative of disrupted Fe-S cluster biogenesis, resulting in uncontrolled iron homeostasis (Camaschella et al., 2007; G. Liu et al., 2014) in addition with defects of mitochondrial Fe-S proteins like ACO2 or

respiratory chain complexes II and III (Daher et al., 2019; W. X. Feng et al., 2021). Daher et al. hypothesized that diabetes did not develop in their reported patient due to the use of iron chelators. Furthermore, the case reports of seven patients refer to nonketotic hyperglycinemia, a neurodegenerative disorder caused by a dysfunctional glycine cleavage system due to a malfunction of lipoate synthesis by the Fe-S protein lipoic acid synthetase (LIAS) (Baker et al., 2014; Camaschella et al., 2007; Chiu et al., 2016; W. X. Feng et al., 2021; Roy Chowdhury et al., 2024). Another report described a mutation in the Glrx and cysteine rich domain containing 1 (GRXCR), computationally linked to Glrx5, which resulted in hearing loss (Mori et al., 2015). A further case of HSCB mutation, a Glrx5-interacting protein, was associated with sideroblastic anemia (Crispin et al., 2020).

1.5.2 Pathophysiological effects of Glutaredoxin 3 disruptions

Unlike Glrx5, no case reports of Glrx3 mutations have been documented. However, knockout studies in mice have shown that Glrx3 deficiency results in embryonic lethality due to severe cardiac developmental abnormalities (Cha et al., 2008; N. Cheng, Zhang, et al., 2011). Evidence also links Glrx3 to metabolic impairments. Similar to Glrx5, Glrx3 deficiency affects the activity of Fe-S proteins such as IRP1 (N. Cheng et al., 2023; H. Xia et al., 2015), disrupting iron homeostasis and hemoglobin maturation (N. Cheng et al., 2023; Haunhorst et al., 2013). Cheng et al. additionally identified a connection between Glrx3 and PolD1, the catalytically active subunit of DNA polymerase δ. This enzyme is essential for DNA replication, particularly on the lagging strand, and for DNA proofreading and repair. Dysfunctions in DNA polymerase δ are linked to various human pathologies (Nicolas et al., 2016). Another link to nucleotide metabolism is seen in the dependency of GPAT on Glrx3 (Haunhorst et al., 2013). GPAT is expressed as an inactive precursor and requires activation through the insertion of a [4Fe-4S] cluster and the Fe-S cluster dependent removal of an N-terminal propeptide (Martelli et al., 2007). It is the key enzyme of purine biosynthesis, catalyzing the first step of activating ribose-5-phosphate by adding an amide group of glutamate to phosphoribosyl-α-pyrophosphate. The observed impairments in IRP1 and GPAT are likely mediated by the interaction between Glrx3 and anamorsin (Ciofi-Baffoni et al., 2018). The yeast homolog Glrx4 exhibits similar effects on cytosolic ribonucleotide reductase (Attarian et al., 2018) and causes cytosolic iron overload, further underscoring the role of Glrx3 in maintaining iron homeostasis (G. Li et al., 2022).

1.6 Objectives of the study

The manifestation of type 2 diabetes mellitus is hallmarked by dysregulations of lipid metabolism. Especially mitochondria are crucial for functionality of β-cells depending on bioenergetics. Mitochondrial dysfunction, emerging from lipotoxicity, is a key driver of type 2 diabetes progression. In addition to known pathways affected by lipid stressors, the mitochondrial protein Glrx5 may represent a novel factor contributing to the etiology of diabetes.

Glrx5 and Fe-S cluster are integral to numerous proteins essential for cellular integrity. Iron-dependent lipid peroxidation of cell membranes provokes cell death and has been associated with diabetes. Disruptions in Glrx5 can lead to altered iron metabolism via ACO1/IRP1, which post-transcriptionally regulates iron-related proteins. Lipotoxicity-induced ferroptosis, mediated by changes in Glrx5 and ACO1/IRP1, could further exacerbate type 2 diabetes progression.

Using pancreatic β-cells this thesis examines whether …

… fatty acids exert a negative effect on Glrx5 and Fe-S cluster proteins.

… fatty acids lead to cellular changes which can be attributed to ferroptosis.

… effects of lipotoxicity and ferroptosis can be prevented in a Glrx5 overexpression model.

2 Material and methods

2.1 Cell models

2.1.1 MIN6 cells (murine)

The 6th subclone of mouse insulinoma (MIN6) cells, kindly provided by Prof. Lenzen of Hannover Medical School, Hannover, Germany (Baltrusch & Lenzen, 2007), were employed in this study. MIN6 cells were originally created from transgenic C57BL/6 mouse insulinoma cells, immortalized via the SV40 T-antigen under the control of the insulin promoter (Miyazaki et al., 1990). These cells exhibited a physiologic glucose response through the expression of glucokinase and liver type GLUT2 (Ishihara et al., 1993). Passages 50-60 were used for experiments. The cells were cultured in an incubator (Thermo Fisher Scientific, Waltham, MA, USA) at 37 °C and 5 % CO_2 in dulbecco's modified eagle's medium (DMEM) with 25 mM glucose and 1 mM Na-pyruvate (Thermo Fisher Scientific, Cat-No: 41966029). The medium was supplemented with 16 % v/v heat-inactivated fetal bovine serum (Biowest, Riverside, MO, USA), 80 U/ml penicillin/streptomycin (Thermo Fisher Scientific), and 50 µM 2-mercaptoethanol (Thermo Fisher Scientific). Culture media were replaced every 2-3 d. When cells reached 70-80 % confluence, they were washed with phosphate-buffered saline (PBS) (Thermo Fisher Scientific) and reseeded into new adherent T175 cell culture flasks (Sarstedt, Nümbrecht, Germany) via trypsinization with 0.05 % trypsin/ethylenediaminetetraacetic acid (EDTA) (Thermo Fisher Scientific). Trypsinized cells were collected in prewarmed cell culture DMEM and centrifuged (290 x g, 4 min, 21 °C) (Hettich, Tuttlingen, Germany). After removing the supernatant, the cell pellet was resuspended in cell culture DMEM. A cell aliquot was stained with Trypan blue (Sigma-Aldrich, St. Louis, MO, USA) to identify dead cells. Viable cells were counted by a Neubauer counting chamber (Brand, Wertheim, Germany). The initial seeding density for new flasks was 25,000 cells/cm^2. Cell numbers were periodically recorded to calculate growth rate and generation time, based on the following formulas:

$$\text{growth rate} = \frac{\ln(\text{cells}_{t1}) - \ln(\text{cells}_{t0})}{t1[\text{d}] - t0[\text{d}]}$$

$$\text{generation time [d]} = \frac{\ln(2)}{\text{growth rate}}$$

2.1.2 EndoC-βH3 cells (human)

As additional cell line, human EndoC-βH3 cells (Human Cell Design, Toulouse, France) at passage 65 were used (Benazra et al., 2015). These cells were derived from progenitor cells using lentiviral gene transfer (Ravassard et al., 2011; Scharfmann et al., 2014). Treatment with 4-hydroxy-tamoxifen (4-OHT) induced Cre-mediated excision of immortalizing transgenes, promoting β-cell characteristics such as insulin secretion and glucose responsiveness. EndoC-βH3 cells were cultured in adherent T75 cell culture flasks precoated with β-COAT (Human Cell Design) dissolved in DMEM supplemented with 100 U/ml penicillin/streptomycin for 1 hour. Cells were maintained at 37 °C and 5 % CO_2 in OPTIβ1 medium (Human Cell Design), which was replaced weekly. Passaging was performed as described for MIN6 cells. The seeding density was 200,000 cells/cm^2. For induction of insulin secretion, EndoC-βH3 cells were exposed to 1 µM 4-OHT (Sigma-Aldrich) dissolved in OPTIβ1 medium for 14 d, with medium refreshed after 7 d. Immortalizing gene excision lasted in total for 14 d.

2.1.3 JetPRIME transfection of MIN6 cells and flow cytometry

Transiently transfected MIN6 cells were created using chemical transfection with jetPRIME kit (Polyplus-transfection SA, Illkirch, France). Plasmids were amplified by DH5α *Escherichia coli* and purified using the NucleoBond Xtra Maxi kit (MACHEREY-NAGEL, Düren, Germany). Sport6-Glrx5 or Su9-GFP plasmids dissolved in TE buffer (Thermo Fisher Scientific) were used (each c = 1 µg/µl). The genetic sequence for the Sport6-Glrx5 vector is provided in the supplement (Supplement 1). To control the transfection of the mitochondrially located Glrx5, GFP was fused to the subunit of complex V. The number of GFP transfected MIN6 cells was determined in an initial optimization experiment via fluorescence-activated cell sorting (FACS) analysis. Therefore, $1.3*10^6$ MIN6 cells were seeded in a T25 flask. After attaching to the flask for 24 h, the GFP plasmid (m = 0, 0.44, 0.88, 1.33, 1.77, and 2.22 µg) was mixed with 120 µl jetPRIME transfection buffer. The mixture was vortexed and spun down for 5 sec to add the jetPRIME transfection reagent (V = 0.88, 0.88, 1.77, 2.66, 3.54, and 4.44 µl). Following manufacturer recommendations, the added volume of reagent should be double compared to the amount of plasmid. For the control transfection without plasmid, 0.88 µl of reagent was used matching the lowest volume of reagent in this experiment. Transfection mixtures were vortexed and spun down for 5 sec again, followed by a resting

time of 15 min at room temperature. Afterwards, each solution was mixed with 3.33 ml prewarmed DMEM containing fetal bovine serum. The media in the flask were replaced by the transfection solutions, while in one additional flask the medium was replaced with regular cell culture DMEM. During the period of transfection, the cells remained in an incubator (37 °C, 5 % CO_2) for 6 h, until the media was removed and changed to regular cell culture DMEM again for 48 h. After completion of 48 h, cells were collected by trypsin/EDTA as described in the previous chapter. After centrifugation (290 x g, 4 min, 4 °C), cells were transferred to a 1.5 ml tube (Sarstedt) with cold PBS (4 °C) and washed once by centrifugation (290 x g, 4 min, 4 °C). After supernatant was removed, the cells were resuspended in cold PBS (4 °C) to achieve a cell density of $1*10^6$ cells/ml. The cell suspension was kept on ice till the analysis by FACS. Non-viable cells were excluded using propidium iodide (c = 1 µg/µl) (Thermo Fisher Scientific) and analyzed by BD FACSCanto II (Becton, Dickinson and Company, Franklin Lakes, NJ, USA). Cells which have been cultured the entire time in regular DMEM were used for setting gates to identify cells by forward and side scatter density. Data were analyzed by BD FACSDiva software (Becton, Dickinson and Company). Subsequent experiments used 1 µg GFP or Glrx5 plasmid and 2 µl reagent in 120 µl buffer per $1*10^6$ MIN6 cells in a T25 flask. The amounts and volumes were adjusted accordingly if other flasks and cell number were used. For experiments in 96 well plates (Greiner Bio-One, Kremsmünster, Austria), plasmid solutions were diluted to 0.1 µg/µl. The respective groups were labelled as GFP+ or Glrx5+. The fluorescence of GFP+ transfected MIN6 cells in the flasks were controlled 24 h after completing the transfection time by a Leica DM IL LED fluorescence microscope (Leica Camera, Wetzlar, Germany).

2.1.4 Preparation of lipotoxic treatment solution

To study lipotoxic effects, oleic acid was added to cell culture medium (Römer et al., 2022). Oleic acid (Enzo Life Sciences, New York, NY, USA) was dissolved in absolute ethanol (Sigma-Aldrich) to prepare stock solutions at 225 mM, 450 mM, and 900 mM. Stock solutions were diluted 1:300 in cell culture DMEM complexed with fatty acid free bovine serum albumin (BSA) (SERVA Electrophoresis, Heidelberg, Germany, Cat-No: 11945) to achieve final concentrations of 0.75 mM, 1.5 mM, and 3 mM. By complexing DMEM with different amounts of BSA (MW_{BSA} = 66,463 g/mol), the final molar oleic acid:BSA ratio was 5:1. Solutions were nitrogen-overlayed (Linde, Dublin, Ireland), and shaken (IKA, Staufen im Breisgau, Germany) overnight in an incubator (37 °C, 5 % CO_2),

sterile-filtered (0.22 µM) and stored as aliquots at -20 °C. Control media contained equivalent BSA and ethanol concentrations. The ethanol concentrations of media were 0.31 %, 0.28 %, and 0.23 %.

2.1.5 Treatment of cellular models

Wildtype MIN6 cells, GFP+ and Glrx5+ transfected MIN6 cells, and wild type EndoC-βH3 cells were used. All methods were tested on wild type and transfected MIN6 cells, while EndoC-βH3 cells were used to give further comparison for ATP levels. For wild type model experiments, the cells were collected by trypsin/EDTA, centrifuged (290 x g, 4 min, 21 °C) and resuspended in cell culture DMEM. As the cell density was determined by trypan blue counting, a defined number of cells was seeded in well plates or cell culture flasks. After attaching for 24 h, the media were changed depending on the assay to either cell culture DMEM, 0 mM control media with matching concentrations of BSA and ethanol, or treatment media with 0.75 mM, 1.5 mM, or 3 mM oleic acid. The treatment times were 24 h, 48 h, or 5 d. In case of 5 d treatment, the media were changed after 0 h (completing attachment), 48 h, and 96 h.

In the transfected model, a defined number of MIN6 cells was seeded in well plates or cell culture flasks. After completing 24 h attachment to the surface, cells were transfected for 6 hours before replacing the medium with treatment media for 48 h.

There were two different experimental setups for analysis of the transfected MIN6 cells regarding biological effects. The first attempt included GFP transfected cells treated with DMEM as visual control of the transfection, and multiple groups of Glrx5 transfected cells to distinguish effects between cells without treatment (DMEM), with 0 mM control treatment (0.3 mM BSA and 0.28 % ethanol) or with different oleic acid concentrations (0.75 mM, 1.5 mM, and 3 mM). In a second setup, GFP+ and Glrx5+ transfected cells were treated either with one concentration of oleic acid or the matching 0 mM control media to distinguish effects between the transfection and oleic acid, with no further comparison to other oleic acid concentrations or treatment with DMEM. After treatment, cells were analyzed or processed like described in subsequent chapters.

2.2 Glrx5+ transfected C57BL/6 mice

All animal research complied with recommendations from the institutional animal welfare officer, the Chair of Animal Welfare of the Justus Liebig University, Giessen, and the Regional Administrative Council of Giessen, the Veterinary Department, under

codes GI 20/11 No. G 56/2018 and No. G 70/2018. Both committees approved the protocol. All experiments were performed in accordance with the German Animal Welfare Law.

C57BL/6 mice were obtained with a heterozygous or homozygous CRISPR/Cas9 knock-in of *Ins2* and *GLRX5* at the ROSA26 locus (Cyagen Biosciences Inc., Santa Clara, CA, USA). Mice were housed in individually ventilated cages in groups of 5 mice at 22 ± 2 °C and a relative humidity of 55 ± 10 %, with a 14:10 h light and dark cycle, and with tap water and standard diet pellet form (Altromin, Lage, Germany) ad libitum. At 20 weeks of age, organs were collected from one wild type, one homozygous, and one heterozygous C57BL/6 mouse. Mice were anesthetized via intraperitoneal injection of 10 % ketamine (Medistar, Ascheberg, Germany) and 2 % xylazine (Ceva, Düsseldorf, Germany) dissolved in 0.9 % NaCl solution by dosage of 0.1 ml per 10 g body weight. After the abdominal wall was excised, the aorta was cut to drain the blood. The small intestine and pancreas were collected, placed in 2 ml cryo vials (Sigma-Aldrich), frozen with liquid nitrogen, and stored at -80 °C. For pancreatic islet isolation, pancreata of three homozygous or heterozygous mice were pooled. To perfuse the excised pancreata, 2.5 mg collagenase B (Roche, Mannheim, Germany), 35 µl HEPES buffer (Biochrom, Berlin, Germany), 10 µl penicillin/streptomycin, 10 µl ciprofloxacin, and 1 µl gentamycin were added to 1 ml of Hank's Balanced Salt Solution (Biochrom). Pancreata were perfused in a petri dish with 4 ml of prepared solution. The pancreata were chopped with a pair of scissors. The organ with collagenase solution was transferred into a 15 ml tube (Sarstedt), vortexed for 15 sec and placed in a shaking water bath at 37 °C for 10 min, with vortexing after 3, 6, and 10 min. Following 10 min incubation, the tube was intensively shaken by hand for 3 min. The digestion was inactivated by cooling the tube on ice and adding 1X Hank's Balanced Salt Solution (4 °C). After centrifugation (375 x g, 3 min, 4 °C), supernatant was discarded. The tube with digested pancreas was filled with 1X TCM-199 pH 7.4 (Thermo Fisher Scientific). Each ml of 1X TCM-199 was supplemented with 50 µl heat inactivated fetal bovine serum, 20 µl HEPES, and 10 µl penicillin/streptomycin. Individual islets were handpicked under a stereomicroscope (Leica Camera) and collected in a petri dish (Sarstedt) with the described 1X TCM-199. At this step, islets of individual organs were pooled in one petri dish. The islets were placed in an incubator (37 °C, ambient CO_2) overnight. By pooling of three mice, 210 islets for homozygous and 240 islets for heterozygous mice were collected. On the following day, the islets were

transferred into a 15 ml tube and centrifuged (375 x g, 3 min, 4 °C). Supernatant was removed and the collected pellet was frozen with liquid nitrogen and stored at -80 °C. Collected organs and islets were further processed for immunoblotting.

2.3 MTT assay

The 3-(4,5-dimethylthiazol-2-yl)-2,5-diphenyltetrazolium bromide (MTT) assay was used to measure cellular reduction potential mediated by dehydrogenase enzymes (Mosmann, 1983) in wild type and transfected MIN6 cells. Seven replicates per group were prepared, with $1*10^4$ MIN6 cells seeded in 150 µl of DMEM in each well of a 96 well plate (Greiner Bio-One). Wells without cells served as blank. Wild type cells were treated for 24 h and 5 d. To account for the increasing effect of BSA on MTT readouts, all corresponding control groups with varying BSA concentrations were included. Treatment time for transfected cells with 1.5 mM oleic acid was 48 h. After treatment, 50 µl of MTT (Abcam, Cambridge, UK), freshly dissolved in PBS (c = 2 mg/ml) and sterile filtered (0.22 µm), was added to each well. The well plate was protected from light and incubated (37 °C, 5 % CO_2) for 4 h, allowing MTT to be converted into formazan crystals by cellular activity. Subsequently, the MTT solution was replaced with 200 µl of dimethyl sulfoxide (DMSO) (Carl Roth, Karlsruhe, Germany) and the plate was shaken (IKA, Staufen im Breisgau, Germany) for 15 min to dissolve the formazan crystals. Optical density (OD) was measured at 570 nm, with background correction at 620 nm, using a photometer (Berthold Technologies, Bad Wildbad, Germany). The OD of blank wells was subtracted from the $OD_{(570\text{-}620\ nm)}$.

2.4 Protein analysis

2.4.1 Pierce BCA and Bradford protein assays

Protein concentrations in samples prepared for enzyme-linked immunosorbent assay (ELISA), immunoblotting, and Fe-S enzyme activity assays were determined using the Pierce BCA Protein Assay Kit (Thermo Fisher Scientific) or the Bradford Protein Assay (Bio-Rad Laboratories, Hercules, CA, USA). Samples were diluted in distilled water to achieve OD values within the BSA standard range (0.1-1.0 mg/ml). For each assay, 10 µl of BSA standard or sample was pipetted in duplicates into a 96 well plate, with blank wells subtracted from the OD values.

The working reagent of Pierce BCA kit was prepared by mixing reagent A and reagent B in a 50:1 ratio. Each well received 200 µl of the working reagent, and the plate was mixed briefly on a plate shaker for few seconds. After incubation at 37 °C (ambient CO_2) for 30 min, the plate was cooled in room temperature for 5 min, and protein concentration was measured at 570 nm. The Pierce BCA Kit was used for samples prepared with detergent-containing buffers, such as 10 % Nonidet P-40 buffer for ELISA preparation. For the Bradford assay, the Bradford dye reagent was diluted by factor five with distilled water, and 200 µl was added to each well. OD was measured photometrically at 600 nm (Bradford, 1976).

2.4.2 ELISA for insulin and Glutaredoxin 5

ELISA was performed to quantify insulin and Glrx5 levels in wild type and transfected MIN6 cells. For transfected cells, $1.5*10^6$ MIN6 cells were seeded in a T25 flask in 3.5 ml DMEM, followed by transfection and treatment with 0 mM or 1.5 mM oleic acid for 48 h. For wild type cells, $4*10^5$ MIN6 cells were seeded in 6 well plates (Greiner Bio-One) with 3 ml DMEM and treated for 24 h. After treatment, 1 ml of culture medium was collected and centrifuged (290 x g, 8 min, 4 °C). The supernatant was stored at -20 °C. The remaining media in the plate or flask were removed and the PBS washed cells were collected by trypsinization. The centrifuged pellet (290 x g, 4 min, 4 °C) was washed once with PBS by centrifugation (290 x g, 4 min, 4 °C). After removing PBS, cells were lysed with 350 µl Nonidet P-40 buffer (10 % aqueous solution, Merck KGaA, Darmstadt, Germany) supplemented with 3 % v/v protease inhibitor cocktail 100X (Thermo Fisher Scientific) within a few seconds. The lysate was vortexed and incubated on ice for 20 min before centrifugation (16,000 x g, 12 min, 4 °C). Supernatants were collected and stored at -20 °C.

Media and lysate samples were diluted to match the standard range for ELISA measurement. Insulin ELISA (Lot-No: 33802, 35241, 35601, DRG Instruments, Marburg, Germany) required dilution factors of 10,000 (DMEM and 0 mM) and 4,000 (0.75 mM, 1.5 mM, 3 mM) for wild type and transfected cell lysate samples, and 1,200 (DMEM and 0 mM) and 500 (0.75 mM, 1.5 mM, 3 mM) for media samples. For Glrx5 ELISA (Lot-No: D04065798, L19062494, Cusabio Technology LLC, Houston, TX, USA), suitable dilution factors for wild type or GFP+ cell lysate samples were 30

(DMEM and 0 mM) and 15 (0.75 mM, 1.5 mM, 3 mM), while the dilution factor of Glrx5+ cells was 45 across all groups.

In order to analyze insulin, 10 µl of standard or diluted medium and lysate samples were added to the antibody-coated 96 well ELISA plate in duplicates, followed by 100 µl of enzyme conjugate and placing the plate on a plate shaker for 2 h. The enzyme conjugate comprised of a peroxidase coupled monoclonal anti-insulin antibody binding to the insulin of the samples. After 2 h of incubation, wells were washed six times with wash buffer to remove all unbound substances. 200 µl TMB was added for 15 min at room temperature, which created a blue color by oxidation initiated by peroxidase and H_2O_2. To stop the peroxidase, 50 µl of a sulfuric acid containing stop solution was added and the OD was measured at 450 nm.

Glrx5 was analyzed by pipetting 100 µl of standard and diluted lysate into the antibody coated plate in duplicates. After 2 h incubation (37 °C, ambient CO_2), samples were removed and 100 µl of biotin solution was added for 1 h (37 °C, ambient CO_2), binding to Glrx5 of the samples. As the biotin solution was removed, wells were washed three times for each 2 min with 200 µl of wash buffer. 100 µl of an avidin solution conjugated with peroxidase was added for 1 h at 37 °C, binding to biotin. Wells were washed five times for each 2 min with 200 µl wash buffer, and 90 µl TMB was added for 20 min, while the plate was protected from light. Peroxidase oxidized TMB, which was stopped by adding 50 µl of sulfuric acid containing stop solution. The OD was measured at 450 nm.

Protein concentration of cell lysates were determined using Pierce BCA assay. For cell lysate, the results of insulin (µg/ml) and Glrx5 (pg/ml) were divided by the lysate protein concentration (mg/ml). For analysis of insulin in collected media, the result of insulin (µg/ml) was multiplied with the media volume used for treatment and then divided by the total protein amount of the lysate sample.

2.4.3 Activities of iron-sulfur enzymes and respiratory chain complexes

2.4.3.1 Cell fractionation

To measure the activity of Fe-S enzymes in MIN6 cells, $3.5*10^6$ cells were seeded in a T75 flask in 15 ml DMEM and allowed to attach overnight. This assay was conducted for wild type cells with 5 d treatment time and transfected cells with 48 h treatment time. After treatment, cells were harvested using trypsin/EDTA as described previously. The collected cells were centrifuged (290 x g, 4 min, 21 °C) in a 15 ml tube. The supernatant was discarded, and cells were washed with PBS, followed by centrifugation (290 x g, 4 min, 21 °C). The PBS was removed, and the cell pellet was resuspended and vortexed in digitonin buffer (25 mM Tris pH 7.4 (Carl Roth), 250 mM sucrose (Carl Roth), 1.5 mM $MgCl_2$ (Sigma-Aldrich), 80 µM digitonin (Sigma-Aldrich), 1 mM phenylmethylsulfonyl fluoride (PMSF) (Sigma-Aldrich)). To minimize differences in protein concentration due to treatment effects, the buffer volume was reduced for groups exposed to harmful treatment. Specifically, 900 µl of digitonin buffer was used for DMEM and control groups, while 600 µl was used for fatty acid treated groups. Digitonin and PMSF were freshly added to the buffer on the day of sample preparation. Cells were incubated with digitonin buffer on ice for 15 min. Following incubation, one-third of total cell lysate was collected as an aliquot. The remaining lysate was centrifuged (16,000 x g, 10 min, 4 °C), and the supernatant was collected as the cytosolic fraction. The pellet was washed with 500 µl of Mito-buffer (25 mM Tris pH 7.4, 250 mM sucrose, 1.5 mM $MgCl_2$) and centrifuged again (16,000 x g, 10 min, 4 °C). The supernatant was discarded, and the organelles-containing pellet was resuspended in either 400 µl (DMEM and control group) or 300 µl (oleic acid group) of Mito-buffer. This suspension represented the mitochondrial fraction. Protein concentrations for all fractions were determined using the Bradford protein assay. Samples were then frozen in liquid nitrogen and stored at -80 °C.

2.4.3.2 Aconitase activity

For enzyme activity assays, the samples of the fractions were pipetted into well plates in triplicates or quadruplicates. Protein amounts used for aconitase were as follows: 10 µg, 15 µg, 20 µg (total lysate) / 5 µg, 7.5 µg, 10 µg (cytosol) / 2.5 µg, 5 µg, 7.5 µg (organelles)

The sample triplicates were pipetted two times (full activity and reference activity) to a 96 well UV plate (Greiner Bio-One). To the reference wells, 235 µl of buffer (100 mM triethanolamine pH 8.0 (Sigma-Aldrich), 1.5 mM $MgCl_2$ (Sigma-Aldrich), 0.1 % Triton X-100 (Merck), 1.25 mM NADP+ (Sigma-Aldrich)) was added. For the maximum enzyme activity, 15 µl/ml cis-aconitate (20 mM) (Sigma-Aldrich) and 5 µl/ml isocitrate dehydrogenase (40 mU/µl) (Sigma-Aldrich) were added to the buffer. The samples for full activity received 235 µl of this substrate-enzyme buffer. The reaction was monitored at 340 nm for 45 min. Briefly explained, aconitase converted cis-aconitate to isocitrate, which oxidized to oxalosuccinate by isocitrate dehydrogenase, while NADP+ was reduced to NADPH, measurable at 340 nm.

The reference measurement at each time point was subtracted from the corresponding OD value of the reaction supplemented with cis-aconitase and isocitrate dehydrogenase. Enzyme activity was calculated during the linear phase of NADPH production using the formula:

$$\frac{activity\ [U]}{protein\ [g]} = \frac{\frac{\Delta E_{340nm}}{\Delta t[min]} * V_{well}[ml]}{d[cm] * \varepsilon_{340nm}[mM^{-1} * cm^{-1}] * V_{sample}[ml] * c_{protein}[g/ml]}$$

ε_{340nm} = 6.22 mM^{-1}*cm^{-1}

2.4.3.3 Succinate dehydrogenase activity

Protein amounts used for mitochondrial fraction were: 2 µg, 3 µg, 4 µg

Samples were pipetted into a 96 well plate like described for aconitase. For full activity, 235 µl of buffer (50 mM Tris/SO_4 pH 7.4, 0.1 mM EDTA (Merck), 70 µM dichlorophenol-indophenol (Merck), 0.1 % Triton X-100, 0.05 mM decylubiquinone (Sigma-Aldrich), 10 µl/ml succinate (20 %) (Sigma-Aldrich)) was added to the wells. As reference measurement, 10 µl/ml of malonate (20 %) (Sigma-Aldrich) was added to the buffer to inhibit SDH. In this assay, SDH reduced dichlorophenol-indophenol, while $FADH_2$ was oxidized to FAD+. The oxidation to FAD+ was measured over 40 min at 600 nm. After the background was subtracted and the maximum substrate turnover was identified, the enzyme activity was calculated with the same formula as introduced for aconitase. ε_{550nm} = 21 mM^{-1}*cm^{-1}

2.4.3.4 Coupled activity of complexes II and III

Protein amounts used for mitochondrial fraction were: 2.5 µg, 5 µg, 7.5 µg

To assess the activity of complex III, a coupled assay of complexes II and III (C2-C3) was performed. Samples were pipetted like described for aconitase. For assessing full activity, 235 µl of buffer (50 mM Tris/SO_4 pH 7.4, 50 µg/ml KCN (Sigma-Aldrich), 50 µg/ml cytochrome c (III) (Sigma-Aldrich), 12.5 µl/ml succinate (20 %)) was added to the wells. As reference measurement, 12.5 µl/ml malonate (20 %) was added to the buffer to inhibit SDH, stopping the reduction of ubichinone to ubihydrochinone, which would be oxidized again by complex III to reduce cytochrome c. The buffer was added to the triplicate of the reference activity. The reduction of cytochrome c was measured for 40 min at 550 nm. The enzyme activity was calculated as previously described. ε_{550nm} = 19.1 $mM^{-1}*cm^{-1}$

2.4.3.5 Cytochrome c oxidase activity

Protein amounts used for mitochondrial fraction were: 0.3 µg, 0.6 µg, 0.9 µg, 1.2 µg

Samples were pipetted into a 96 well plate as quadruplicates. 235 µl of buffer (50 mM MES pH 6.6 (Sigma-Aldrich), 50 mM NaCl (Carl Roth), 1 % BSA, 0.5 mM dodecylmaltoside (Sigma-Aldrich), 8 µM cytochrome c (II) (described in Stehling et al., 2009)) was added, while wells without samples served as background. During the measurement, cytochrome c was oxidized by COX, which was measured for 30 min at 550 nm. After the background was subtracted and the maximum substrate turnover was identified, the enzyme activity was calculated as described for the other enzymes. ε_{600nm} = 19.1 $mM^{-1}*cm^{-1}$

2.4.3.6 Lactate dehydrogenase activity as cytosolic marker

The measurement of lactate dehydrogenase (LDH) was used as marker for the cytosolic fraction. The activity of ACO1 was divided by the activity of LDH. The used protein amounts were: 0.8 µg, 1.2 µg, 1.6 µg (total lysate) / 0.2 µg, 0.4 µg, 0.6 µg (cytosol) / 1.2 µg, 2.4 µg, 3.6 µg (organelles)

After the samples were pipetted in a 96 well plate, 235 µl of buffer (50 mM Tris/HCl pH 7.4, 1 mM EDTA, 0.1 % Triton X-100, 0.75 mM Na-pyruvate (Thermo Fisher Scientific), 15 µl/ml NADH (10 mg/ml) (Sigma-Aldrich)) was added. Wells without

samples were used as background. LDH was converting pyruvate to lactate, while NADH oxidized to NAD+. The oxidation of NADH was measured for 45 min at 340 nm. The enzyme activity was calculated as described. ε_{340nm} = 6.22 $mM^{-1}*cm^{-1}$

2.4.3.7 Citrate synthase activity as mitochondrial marker

The activity of CS was taken as reference for the enzymes of mitochondrial fraction. The activities of all mitochondrial enzymes were divided by the CS activity. The used protein amounts were 1 µg, 1.5 µg, 2 µg (total lysate) / 3 µg, 6 µg, 9 µg (cytosol) / 0.4 µg, 0.8 µg, 1.2 µg (organelles)

All samples were pipetted two times in triplicates in a 96 well plate and 235 µl of buffer (50 mM Tris/HCl pH 8.0, 100 mM NaCl, 0.5 mM 5,5‘-Dithio-bis-(2-nitrobenzoic acid) (DTNB) (Sigma-Aldrich), 0.1 % Triton X-100, 12.5 µl/ml acetyl-CoA (10 mg/ml) (Sigma-Aldrich)) was added to the wells of the reference measurement. 20 µl/ml oxaloacetate (10 mg/ml) (Sigma-Aldrich) was supplemented to the reference buffer and this buffer was added to the remaining samples for full enzyme activity. CS converted oxaloacetate and acetyl-CoA to citrate and CoASH. The CoASH reacted with DTNB to TNB-CoA, which was measured for 40 min at 412 nm. The enzyme activity was calculated as described. ε_{412nm} = 13.3 $mM^{-1}*cm^{-1}$

2.4.4 Immunoblotting

2.4.4.1 Sample preparation MIN6 cells

Protein analysis was conducted via immunoblotting using the sodium dodecyl sulfate polyacrylamide gel electrophoresis (SDS-PAGE) technique. In both the wild type and transfection model, $3.5*10^6$ MIN6 cells were seeded in T75 flasks containing 14 ml of DMEM. After the treatment period, PBS washed cells were collected by trypsin/EDTA subsequently and centrifuged (290 x g, 4 min, 4 °C). The cell pellet was washed with PBS, centrifuged again (290 x g, 4 min, 4 °C), and the supernatant was removed. The dry cell pellet was frozen in liquid nitrogen and stored at -80 °C until further use.

Prior to gel preparation, the cells were thawed and resuspended in distilled water at a ratio of 15 µl per $1*10^6$ cells. A 10-fold diluted aliquot of the sample was analyzed for total protein using the Bradford protein assay. According to the protein concentration, samples were diluted with 4X Laemmli-buffer (0.24 M Tris pH 6.8, 8 % SDS (Sigma-Aldrich),

4.34 M glycerol (Sigma-Aldrich), 0.3 mM bromophenol blue (Merck)), distilled water, and freshly added 5 % 2-mercaptoethanol (Sigma-Aldrich). The samples were boiled at 95 °C for 5 min and stored at -20 °C. Final protein concentrations varied depending on the target protein, typically ranging from 0.75 µg/µl to 3 µg/µl. Loaded sample volume was 20 µl. Higher protein concentrations were used for proteins with weaker signals.

In a separate experiment, MIN6 cell samples were prepared with increasing protein concentrations (c = 0.25, 0.5, 0.75, 1.0, 1.5, 2.0, 2.5, 3.0, and 3.5 µg/µl) to assess signal linearity during immunoblotting. Loaded sample volume was 20 µl. Signals for tubulin and ERK1/2 were quantified, and a linear regression of signal intensity against protein amount was performed. For reliable quantification, signal detection and protein loading amount needed to correlate linearly.

Glrx5+ transfected MIN6 cells were used as a positive control for Glrx5 detection. Recombinant Glrx5 protein (enQuire Bio LLC, Littleton, CO, USA, Cat-No: QP11992) was also used to evaluate antibody reactivity. Recombinant protein supplemented with 0.1 % BSA was diluted to 3.75 ng/µl with distilled water, 4X Laemmli-buffer and 5 % 2-mercaptoethanol, then boiled at 95 °C for 5 min. The recombinant protein's molecular weight, processed by His-tag purification was 18.8 kDa.

2.4.4.2 Sample preparation fractionated MIN6 cells

After measuring Fe-S enzyme activity in fractionated MIN6 cells, the samples were diluted with 4X Laemmli-buffer, Mito-Buffer, and 5 % 2-mercaptoethanol based on protein concentration. The samples were boiled at 95 °C for 5 min.

2.4.4.3 Sample preparation C57BL/6 mice

A PBS lysis buffer (1 nM EDTA, 0.5 % Triton X-100, 5 mM NaF (Sigma-Aldrich), 6 M urea (Sigma-Aldrich), 2.5 mM Na-pyrophosphat (Sigma-Aldrich), 1 mM Na-orthovanadate (Thermo Fisher Scientific), 0.5 % Na-deoxycholate (Sigma-Aldrich), 0.5 % SDS), freshly supplemented with 1.75 µl aprotinin (Roche), 2 µl leupeptin (Sigma-Aldrich), 2 µl pepstatin (Sigma-Aldrich), and 1 µl PMSF per ml of lysis buffer was prepared. Parts of the retrieved organs were chopped with a pair of scissors and placed in 1.5 ml tubes containing 700 µl of lysis buffer. The tissue was homogenized on ice for several minutes using a motor-driven pestle for pellet mixing (VWR International, Radnor, PA, USA). After homogenizing, the solution was transferred to a new tube, and

1.8 ml of lysis buffer was added. Protein concentration was measured by Pierce BCA assay. Isolated islets were resuspended in PBS and analyzed by Pierce BCA assay. Approximately 100 islets yielded 40 µg of protein. Samples for immunoblotting were prepared by mixing with 4X Laemmli-buffer, PBS, and 5 % 2-mercaptoethanol, boiled at 95 °C for 5 min, and stored at -20 °C.

2.4.4.4 Gel electrophoresis, blotting, and immunodetection

A PerfectBlue dual gel system Twin S (VWR International) with 1.5 mm spacers was used to prepare gels for analysis of total lysate samples. A PerfectBlue dual gel system Twin M (VWR International) was used for MIN6 cell fractions. 30 % Acrylamide:N,N'-methylene bisacrylamide solution 29:1 (SERVA Electrophoresis) was used, which polymerized as TEMED (Carl Roth) and APS (10 %) (Sigma-Aldrich) were added to the gel. A resolving gel with a constantly increasing concentration of polyacrylamide (PAA) (6-20 % PAA, 372 mM Tris pH 8.8, 0.1 % SDS) was cast using a gradient maker (von Keutz Labortechnik, Reiskirchen, Germany) and overlayed with distilled water. The resolving gel solidified for approximately 1:15 h, followed by removing the distilled water and pouring the stacking gel (4 % PAA, 84 mM Tris pH 6.8, 0.1 % SDS). As the stacking gel was poured, a 15-well (gel system Twin S) or 20-well (gel system Twin M) comb was placed into the gel. The gel was placed in a fridge in humidified atmosphere to solidify overnight. The comb was removed, and the gel system was filled with running buffer (25 mM Tris pH 8.3, 190 mM glycine (Sigma-Aldrich)), and 20 µl of each sample was loaded. The used protein amounts are indicated in the respective figures. Two different protein standards were used in each gel for visualization of the electrophoresis (used standards: Precision Plus Protein All Blue Prestained Protein Standards (Bio-Rad Laboratories), PageRuler Prestained Protein Ladder (Thermo Fisher Scientific), PageRuler Unstained Broad Range Protein Ladder (Thermo Fisher Scientific), PageRuler Prestained SM0671 (Thermo Fisher Scientific), Protein Test Mixture 6 (SERVA Electrophoresis)). The gel electrophoresis started with 35 mA till the samples reached the resolving gel. The amperage was increased to constantly 60 mA to separate the samples for approximately 2:30 h. After the protein was separated, it was transferred to a nitrocellulose (NC) membrane using a semi-dry protein transfer in an EBU-4000 blotting chamber (C.B.S. Scientific Company, San Diego, CA, USA). To transfer the protein, all layers of 3 mm Whatman chromatography paper (GE Healthcare, Chalfont St Giles, UK), Amershan Protran 0.45 µM NC membrane (Cytiva,

Marlborough, MA, USA) and the gel were thoroughly soaked with transfer buffer (3.425 M ethanol, 20 mM Tris, 150 mM glycine, 0.02 % SDS) and placed on each other avoiding to include air bubbles between the layers. Three layers of 3 mm Whatman chromatography paper were placed in the blotting chamber. The NC membrane and the gel were placed each on top and everything was covered by three layers of 3 mm Whatman chromatography paper. The size of chromatography papers and membranes was 15.5*11.5 cm. Protein transfer occurred at 300 mA for 3:15 h. As the protein transfer was completed, membranes were washed twice (each 10 min) with distilled water and transfer was verified by staining with Ponceau S for 1:30 min (0.2 % Ponceau S, 3 % tricarboxylic acid (SERVA Electrophoresis)). Ponceau S which was not bound to protein was removed with distilled water. The membrane was allowed to dry between two layers of 3 mm Whatman chromatography paper and stored at room temperature. The membrane was labelled at the respective heights of the molecular weight, washed with distilled water for 15 min, washed with TBS-T (20 mM Tris, 150 mM NaCl, 0.1 % Tween 20 (Sigma-Aldrich)) for 15 min and blocked for 2:00 h (1X Roti Block (Carl Roth), 1 % BSA (Sigma-Aldrich), 0.1 % Na-azide (Sigma-Aldrich) in TBS-T). As the blocking step was finished, the membrane was washed twice with TBS-T (each 10 min) and the membrane was cut according to the molecular weight of target antibodies. The TBS-T washed parts of the membrane were incubated with the primary antibody diluted in buffer (0.33X Roti Block, 0.5 % BSA, 0.02 % Na-azide) for 1:30 h. The membrane was washed thrice with TBS-T (each 10 min), followed by incubation with a horseradish peroxidase (HRP) conjugated secondary antibody for 1 h. Dilution buffer for secondary antibody was 0.5 % BSA in TBS-T. In case of weak signals, the incubation with HRP conjugated secondary antibody was replaced by a biotinylated anti-rabbit antibody for 1 h. After washing thrice with TBS-T (each 10 min), the membrane was incubated by a peroxidase coupled avidin biotin complex solution (Vector Laboratories, Newark, CA, United States) diluted in buffer (0.33X Roti Block, 0.5 % BSA, 0.02 % Na-azide) for 1 h. An annotation can be found in the figures, if the avidin biotin complex was used. A list of used antibodies is given in table 1 and table 2. After incubation of secondary antibody or avidin biotin complex, the membrane was washed thrice with TBS-T (each 10 min), and luminescence was detected using ECL Western Blot Detection Reagents (GE Healthcare). Signals were recorded by a Fusion Solo 4M camera (Vilber Lourmat, Eberhardzell, Germany). Exposure time was ranging between 30 sec and 20 min and was defined individually for each protein, before saturation of the signal was reached.

Table 1: Used primary antibodies for immunoblotting, with all available information or reference for non-commercial origin, arranged by molecular weight.

Antigen	**Dilution**	**Observed molecular weight**	**Host**	**Company**	**Catalog number / Lot number**
PolD1	1250	124 kDa	Rabbit polyclonal	Proteintech Group	15646-1-AP
ACO1	1000	98 kDa	Rabbit polyclonal	Proteintech Group	12406-1-AP
ACO2	3000	86 kDa	Rabbit polyclonal	Thermo Fisher Scientific	PA5-29037 XG3643230B
Akt	1000	60 kDa	Rabbit polyclonal	Cell Signaling	9272S 28
phospho-Akt (Ser473)	1000	60 kDa	Rabbit polyclonal	Cell Signaling	9271L 12
GPAT	500	56 kDa	Rabbit	unpublished	
β-III-tubulin [EP1569Y]	10000	52 kDa	Rabbit monoclonal	Abcam	ab52623 GR149555-33
alpha-tubulin	2500	52 kDa	Mouse monoclonal	Sigma	T6199
Tubulin [YL1/2]	10000	52 kDa	Rat monoclonal	Abcam	ab6160 GR3208838-3
Total OXPHOS Complex III (core protein 2) (UQCRC2) [13G12AF12BB11]	250	48 kDa	Mouse monoclonal	Abcam	ab110413
Complex III (core protein 2) (UQCRC2)	2500	48 kDa	Rabbit	By H. Schägger and I. Wittig Unpublished	
Ferrochelatase	1500	45 kDa	Rabbit	By T. Dailey and H. A. Dailey Sheftel et al. 2010 doi: 10.1073/pnas.1004250107	

Table 1 (continued)

Antigen	**Dilution**	**Observed molecular weight**	**Host**	**Company**	**Catalog number / Lot number**
ERK1/2	1000	42 kDa 44 kDa	Rabbit monoclonal	Cell Signaling	4695S 21
phospho-ERK1/2 (Thr202/ Tyr204)	1000	42 kDa 44 kDa	Rabbit monoclonal	Cell Signaling	4376S 18
Glrx3	1500	40 kDa	Rabbit	Haunhorst et al. 2013 doi: 10.1091/mbc.E12-09-0648	
GAPDH	300	38 kDa	Mouse monoclonal	Sigma	MAB374 2521487
PDX1	4000	38 kDa	Rabbit polyclonal	Sigma	Ab3503-I 3442478
VDAC	1750	34 kDa	Rabbit polyclonal	Proteintech Group	55259-1-AP
GFP	1000	27 kDa	Goat polyclonal	antibodies-online Inc.	ABIN1043856 GF160920
Complex III Rieske Fe-S protein (UQCRFS1)	2500	24 kDa	Rabbit	By H. Schägger and I. Wittig. Sheftel et al. 2012 doi: 10.1091/mbc.E11-09-0772	
Total OXPHOS NDUFB8 [20E9DH10C12]	250	22 kDa	Mouse monoclonal	Abcam	ab110413
COX-2	2500	21 kDa	Rabbit	By H. Schägger and I. Wittig. Sheftel et al. 2012 doi: 10.1091/mbc.E11-09-0772	

Table 1 (continued)

Antigen	**Dilution**	**Observed molecular weight**	**Host**	**Company**	**Catalog number / Lot number**
FTL	5000	20 kDa	Rabbit polyclonal	Proteintech Group	10727-1-AP
GPx4	1000	19 kDa	Rabbit polyclonal	Thermo Fisher Scientific	PA5-102521
Glrx5	500	13 kDa	Rabbit polyclonal	Novus Biologicals	Nbp1-89897 000021103
COX-6 A/B	1250	12 kDa	Rabbit	By H. Schägger and I. Wittig. Sheftel et al. 2012 doi: 10.1091/mbc.E11-09-0772	

Table 2: Used secondary antibodies for immunoblotting, with all available information.

Specificity	**Dilution**	**Host**	**Company**	**Catalog number / Lot number**
Goat IgG (H+L), HRP conjugated	10000	Rabbit polyclonal	Rockland Immunochemicals	605-403-B69 21823
Mouse IgG (H+L), HRP conjugated	2500	Goat	Bio-Rad Laboratories	1706516
Mouse IgG (H+L), HRP conjugated	2500	Goat polyclonal	Calbiochem	401253 D00172425
Rabbit IgG (H+L), HRP conjugated	2000	Goat	Bio-Rad Laboratories	1706515 64425247
Rabbit IgG (H+L), HRP conjugated	10000	Goat polyclonal	Jackson ImmunoResearch	111-035-003 149393
Rabbit IgG (H+L), biotinylated	2500	Goat	Vector Laboratories	BA-1000 ZO0329

2.4.4.5 Tricine gel electrophoresis

The detection of proteins with especially low molecular weight was conducted using a tricine-based gel electrophoresis (Schägger, 2006). The principle was comparable to glycine SDS-PAGE. The differences were the compositions of resolving gel (8-16 % PAA, 1.08 M glycerol, 1 M Tris pH 8.9, 0.1 % SDS), stacking gel (6 % PAA, 1 M Tris pH 8.9, 0.1 % SDS), cathode buffer (0.1 M Tris, 0.1 M tricine (Sigma-Aldrich), 0.1 % SDS) and anode buffer (0.1 M Tris pH 8.45, 0.1 % SDS) replacing the running buffer. A Mini-PROTEAN Tetra Handcast System (Bio-Rad Laboratories) was used for gel casting. This method was applied for Glrx5, COX-6 A/B, and UQCRFS1 and is indicated in the figures.

2.4.4.6 Image quantification of immunoblotting signals

Signals by immunoblotting were quantified using Image Studio Lite 5.2.5 (LI-COR, Inc., Lincoln, NE, USA). Images for analysis were selected before signal saturation. Signal areas were marked to determine the intensity given as relative luminescence unit (RLU), after background subtraction. The resulting values of the target protein were divided by a reference protein. To arrange layouts with representative images of the signals, GIMP 2.10.38 (developed by Spencer Kimball, Peter Mattis, and the GIMP Team) was used.

2.5 Mitochondrial respiration

A total of $9*10^5$ MIN6 cells were seeded in 3 ml of DMEM in a T25 flask in order to measure mitochondrial respiration in both the wild type and transfected cells. After the treatment period, the cells were washed with PBS, detached using trypsin/EDTA, centrifuged (290 x g, 4 min, 21 °C), and resuspended in MIR05 buffer (0.5 mM ethylene glycol-bis(β-aminoethyl ether)-N,N,N′,N′-tetraacetic acid (EGTA) (Thermo Fisher Scientific), 3 mM $MgCl_2$, 60 mM K-lactobionate (Sigma-Aldrich), 20 mM taurine (Sigma-Aldrich), 10 mM KH_2PO_4 (Sigma-Aldrich), 20 mM HEPES (Sigma-Aldrich), 110 mM sucrose, 1 mg/ml BSA, pH 7.1)). The cells were counted and diluted with MIR05 to achieve a final cell density of $5*10^5$/ml. An aliquot of the cells was frozen in liquid nitrogen and stored at -80 °C for CS activity analysis as previously described. Respiration measurements were performed using a 2 ml suspension added to the chamber of the Oxygraph-2k (OROBOROS Instruments, Innsbruck, Austria). This system used a silver Clarke electrode and followed the substrate-uncoupler-inhibitor titration (SUIT) protocol

developed by Prof. Gnaiger, University of Innsbruck, Austria. After stabilization of endogenous respiration, digitonin (20 µM) (Honeywell Fluka, Thermo Fisher Scientific) was added to permeabilize the cells. Glutamate (10 mM) (Sigma-Aldrich) and malate (4 mM) (Sigma-Aldrich) were added to activate complex I, yielding leak 1 respiration. Complex I was measured after the addition of ADP (2 mM) (Sigma-Aldrich) to activate complex V, followed by succinate (10 mM) (Sigma-Aldrich) as complex II substrate, to measure the capacity of oxidative phosphorylation (OXPHOS). Maximum electron transfer system (ETS) capacity was determined by uncoupling the proton gradient using stepwise addition with the protonophore FCCP (0.25 µM) (Sigma-Aldrich), until the respiration reached its maximum. Rotenone (25 µM) (Sigma-Aldrich) was used to inhibit complex I and assess uncoupled complex II respiration. Complex V was inhibited by oligomycine (2.5 µM) (Sigma-Aldrich), resulting in leak 2 respiration. Antimycine A (2.5 µM) (Sigma-Aldrich) was added to inhibit complex III and measure residual respiration by non-enzymatic caused electron transfer, which was subtracted as background. TMPD (0.5 mM) (Sigma-Aldrich) and ascorbate (2 mM) (Sigma-Aldrich) were added. TMPD was used as substrate for complex IV, while ascorbate reduced TMPD again. Finally, Na-azide (120 mM) (Sigma-Aldrich) was added to determine complex IV background respiration. Respiration values for all states were recorded as steady-state and normalized to CS activity.

2.6 Cellular ATP analysis

To measure ATP levels of total cell lysate, $2*10^4$ MIN6 cells were seeded in 100 µl of DMEM in a 96 well luminescence plate (Corning Inc., Corning, NY, USA). Seven replicates per group were prepared in each experiment. Further to the analysis of wild type and transfected MIN6 cells, also $4*10^4$ excised EndoC-βH3 cells were used for measuring cellular ATP levels. As described in chapter 2.1.2, the cells were seeded in a β-COAT coated 96 well luminescence plate in 100 µl OPTIβ1 medium, while oleic acid was prepared with OPTIβ1 medium. Treatment duration for EndoC-βH3 cells was 48 h. Control media were prepared for each oleic acid concentration due to variability in albumin content, influencing ATP readouts. At the end of the treatment, plates were equilibrated to room temperature for 15 min in the dark. An ATP standard curve (0.01-5 µM) (PerkinElmer, Waltham, MA, USA) was prepared, and 100 µl was added in duplicate to the plate. 50 µl of a NaOH containing lysis buffer (PerkinElmer) was added to each well and incubated for 5 min. Subsequently, 50 µl of a solution containing

luciferase, luciferin, and co-substrates (PerkinElmer) was added and incubated for 40 min. Luminescence was measured using a Multimode Microplate Reader (BMG LABTECH, Ortenberg, Germany).

2.7 Gene expression analysis

2.7.1 RNA isolation

The effects of oleic acid and transfection on gene expression were assessed using quantitative real-time polymerase chain reaction (qPCR). For oleic acid treatments, $3*10^5$ MIN6 cells were seeded in 3 ml of DMEM in a 6 well plate and treated for 5 d. For transfection experiments, $1.3*10^6$ MIN6 cells were seeded in a T25 flask, transfected with GFP or Glrx5 plasmids, and maintained in DMEM for 48 h.

At the end of the experiment, cells were washed with PBS, lysed in 300 µl RLT buffer (Qiagen, Hilden, Germany) supplemented with 1 % 2-mercaptoethanol (Sigma-Aldrich), collected in a 1.5 ml tube, and stored at -20 °C. RNA was extracted using the RNeasy Mini Kit (Qiagen). Following thawing and vortexing, an equal volume (300 µl) of ethanol (70 %) (Sigma-Aldrich) was added and mixed with the sample. Samples were transferred to spin columns and centrifuged (16,000 x g, 1 min, 21 °C). The columns were washed with 700 µl RW1 buffer and centrifuged (16,000 x g, 1 min, 21 °C), followed by adding 500 µl RPE buffer and centrifugation (16,000 x g, 1 min, 21 °C). 500 µl RPE buffer was added for a second time and the column tubes were centrifuged (16,000 x g, 2 min, 21 °C), followed by dry centrifugation (16,000 x g, 3 min, 21 °C) with open caps. In the final step, 25 µl of RNase free water was added and tubes were centrifuged (16,000 x g, 1 min, 21 °C). The RNA in RNase free water was collected in a fresh 1.5 ml tube. The RNA was quantified using a Nanodrop 1000 spectrophotometer (Thermo Fisher Scientific) at wavelengths of 260 nm and 280 nm. The samples were diluted with RNase free water according to their concentration to prepare 8 µl samples with an RNA concentration of 125 ng/µl in a 0.2 ml tube.

2.7.2 cDNA preparation

To prepare cDNA, 1 µl of amplification grade DNase (Thermo Fisher Scientific) and 1 µl of 10X DNase reaction buffer (Thermo Fisher Scientific) were added to RNA samples. Following a 15 min incubation at 37 °C in a VWRI732-1210 (VWR International), samples cooled down to room temperature and 1 µl of EDTA (25 mM) (Thermo Fisher

Scientific) was added. After quick centrifugation (290 x g, 5 sec, 21 °C), preincubation was performed at 65 °C for 15 min to inactivate DNase. After cooling to 4 °C for 5 min, 9 µl of a mastermix (4 µl 4X strand buffer, 2 µl DTT (0.1 M), 1 µl dNTP (10 mM), 1 µl oligo d(T), 1 µl superscript (all Thermo Fisher Scientific)) was added, and incubated at 50 °C for 50 min, followed by 72 °C for 15 min. Samples cooled down to 4 °C, and were diluted 1:10 with RNase free water and stored at -20 °C.

2.7.3 qPCR

qPCR was conducted using a mastermix (8.5 µl/sample) for each gene (5 µl SYBR green (Bio-Rad Laboratories), 3.2 µl RNase free water, 0.3 µl primer). Forward and reverse primers were mixed 1:1 and further diluted 1:10 with RNase free water. Primers of *Ins2*, *Glrx5*, and *Rpl32* (reference) (all Thermo Fisher Scientific) were used and can be found in table 3.

A volume of 1.5 µl from each sample was pipetted in triplicates into a MicroAmp Fast Optical 96 well reaction plate (Thermo Fisher Scientific) while kept on ice. Negative controls contained 1.5 µl of RNase free water. Subsequently, 8.5 µl of primer mastermix was added to both the samples and the negative controls. The reaction plate was placed in the Step One Plus Real-Time PCR System (Thermo Fisher Scientific) to initiate the cycling process. Samples were first heated to 95 °C for 10 min, followed by 40 cycles of denaturation at 95 °C for 15 sec and annealing/elongation at 60 °C for 1 min. Finally, a melt curve was generated by gradually increasing the temperature from 60 °C to 95 °C in intervals of 1 min. The Ct values for *Rpl32* were subtracted from target genes of interest, and relative gene expression was calculated using the 2^{-dCt} method.

Table 3: Forward and reverse primer sequences for qPCR.

Primer	**Sequence**
Glrx5 fwd	5’-GAAGAAGGACAAGGTGGTGGTCTTC-3’
Glrx5 rev	5’-GCATCTGCAGAAGAATGTCACAGC-3’
Ins2 fwd	5’-GGCTTCTTCTACACACCCATGT-3’
Ins2 rev	5’-AAGGTCTGAAGGTCACCTGCTC-3’
Rpl32 fwd	5’-GGAGAAGGTTCAAGGGCCAG-3’
Rpl32 rev	5’-GCGTTGGGATTGGTGACTCT-3’

2.8 Statistical analysis

Statistical analyses were performed using GraphPad Prism 9.3.1 (GraphPad Software, San Diego, CA, USA). One-way ANOVA with Tukey's multiple comparisons test or a two-sided unpaired t-test was applied as appropriate. Data were represented as mean ± standard deviation (SD). A p-value < 0.05 was considered significant and marked with *. A p-value < 0.01, < 0.001, and < 0.0001 was marked with **, ***, and ****, respectively.

3 Results

3.1 Pre-experiments for characterization of MIN6 cells and animals in applied methods

In addition to the experiments described in the following chapters, more data were collected to evaluate the characteristics of MIN6 cells and animals under different experimental conditions. Experiments without fatty acid treatment were conducted to examine potential influences from substances used in the methods. The data and detailed descriptions are provided in the supplementary materials, offering helpful information to improve understanding of the experimental model.

The generation time of MIN6 cells, cultured in DMEM, was determined to be 3.9 d (Supplement 2). Fatty acid solutions were prepared using 0.23 % to 0.31 % ethanol, which exerted cytotoxic effects at higher concentrations. The effects of ethanol and DMSO, a potential alternative solvent, were evaluated using the MTT assay. Negative effects were observed at ethanol concentrations exceeding 1 % or DMSO concentrations exceeding 4 % (Supplement 3). The albumin used to complex fatty acids was tested for potential interference with the MTT assay, both in the presence and absence of MIN6 cells. Albumin increased the MTT assay readout, both dependently and independently of MIN6 cells. In experiments without cells, albumin constantly increased the MTT readout, whereas this effect peaked at 6 % albumin after 24 h or 3 % albumin after 5 d, if MIN6 cells were included (Supplement 4). Transfection of MIN6 cells was optimized by varying the amount of GFP plasmid to achieve the highest transfection efficiency. The fluorescence signal and percentage of transfected cells were determined via FACS analysis. Transfecting $1.3*10^6$ MIN6 cells with 1.33 µg of GFP plasmid resulted in a maximum transfection rate of 24 % (Supplement 5). The *Glrx5* gene expression in transfected cells was analyzed using qPCR, revealing an approximately 15-fold increase in *Glrx5* gene expression in Glrx5+ transfected cells compared to GFP+ transfected cells (Supplement 6). Initially, detecting Glrx5+ transfected cells via immunoblotting posed challenges. Antibodies from different manufacturers were tested for specificity using transfected cells and recombinant Glrx5 protein. The Novus Biologicals antibody provided reliable results and was selected for further analysis (Supplement 7). Antibodies against ACO1 were evaluated using cytosolic fractions from MIN6 cells. The Proteintech Group antibody showed satisfactory results in the cytosolic fraction and was chosen for

subsequent experiments (Supplement 8). To ensure reliable immunoblotting quantification, the correlation between luminescence signals and the amount of loaded protein was assessed for MIN6 cells using linear regression. Signals from tubulin and ERK1/2 exhibited a linear correlation with protein loading. Normalizing the protein of interest to the control protein resulted in a function without significant slope, essential for accurate interpretation (Supplement 9). The immunoblotting analysis of FTL revealed an increasing trend in control groups. Testing FTL against a concentration series of ethanol showed elevated signals up to 0.6 % ethanol concentration (Supplement 10). In genetically modified Glrx5+ mice, immunoblotting analysis of prepared organs and isolated islets showed variable results. Tubulin loading controls were inconsistent or absent, while GAPDH controls were evenly distributed. PDX1 was undetectable in intestinal and pancreatic samples. Although Glrx5 signals were detectable in transfected MIN6 cells, they were absent in organ samples (Supplement 11).

3.2 MTT

3.2.1 Oleic acid treatment decreases the MTT readout in wild type MIN6 cells after 24 h and 5 d

The conversion of MTT to formazan was used as a measure of cellular activity. After 24 h of treatment, MIN6 cells exposed to all oleic acid concentrations exhibited a decrease in photometric readout compared to their respective controls (0.7034 ± 0.07905 vs. 0.628 ± 0.06031, * $p < 0.05$, at 0.75 mM, Figure 1A; 0.7399 ± 0.09338 vs. 0.6325 ± 0.06924, ** $p < 0.01$, at 1.5 mM, Figure 1B; 0.7153 ± 0.08272 vs. 0.6174 ± 0.06629, ** $p < 0.01$, at 3 mM, Figure 1C, significances determined by t-test to the respective control group). Relative changes were similar across concentrations (-10.7 % at 0.75 mM, -14.5 % at 1.5 mM, -13.7 % at 3 mM). To simulate chronic diabetes conditions, a prolonged treatment duration of 5 d was implemented. The photometric readout was also diminished during this extended period (1.506 ± 0.1443 vs. 1.277 ± 0.1617, ** $p < 0.01$, at 0.75 mM, Figure 2A; 1.509 ± 0.1412 vs. 1.156 ± 0.1741, **** $p < 0.0001$, at 1.5 mM, Figure 2B; 1.336 ± 0.1491 vs. 0.9956 ± 0.1849, **** $p < 0.0001$, at 3 mM, Figure 2C, significances determined by t-test to the respective control group). The relative changes were more pronounced with increased oleic acid concentrations after 5 d (-15.2 % at 0.75 mM, -23.4 % at 1.5 mM, -25.5 % at 3 mM).

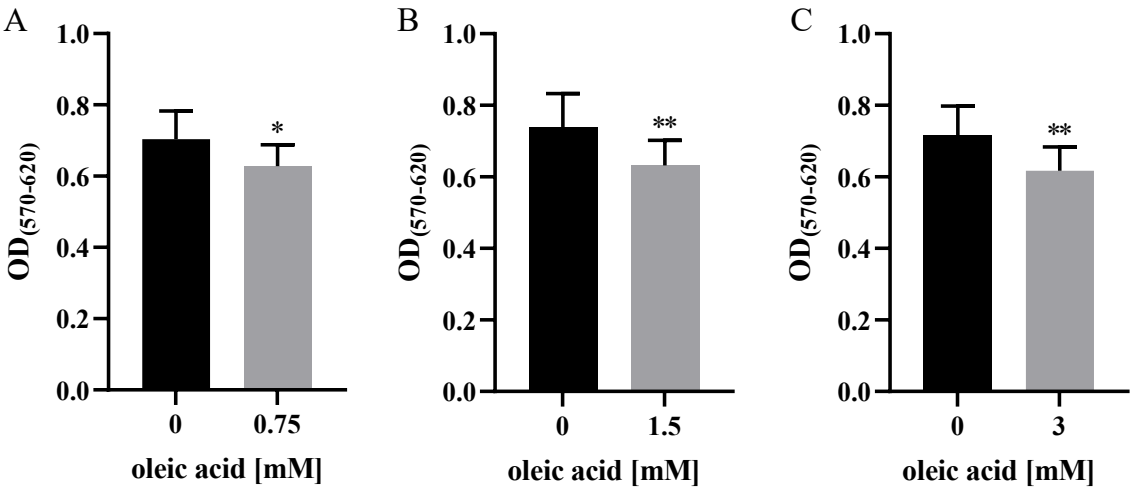

Figure 1: MTT assay results for wild type MIN6 cells treated for 24 h with (A) 0.75 mM, (B) 1.5 mM, and (C) 3 mM oleic acid and their respective controls (n = 10). * $p < 0.05$, ** $p < 0.01$, significances determined by t-test.

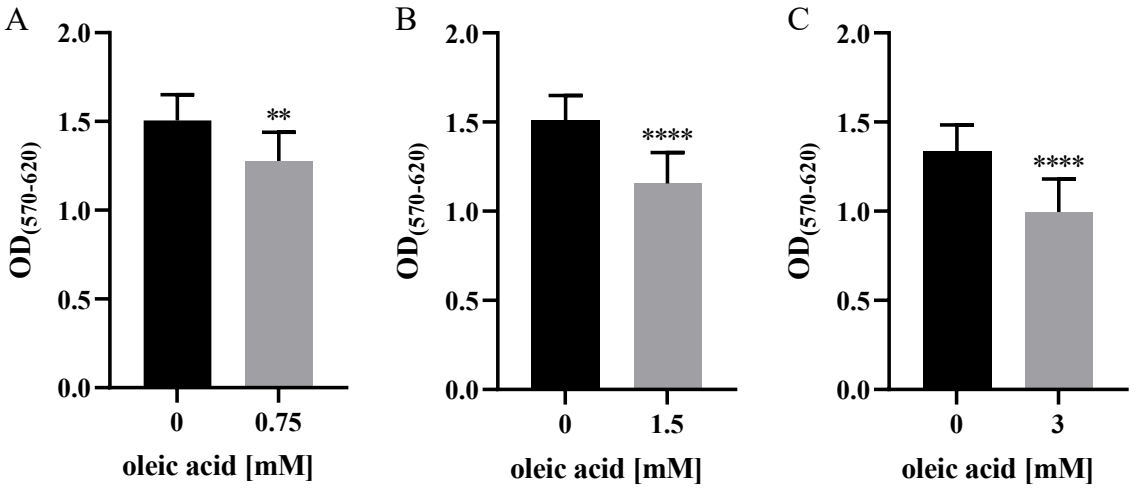

Figure 2: MTT assay results for wild type MIN6 cells treated for 5 d with (A) 0.75 mM, (B) 1.5 mM, and (C) 3 mM oleic acid and their respective controls (n = 12). ** $p < 0.01$, **** $p < 0.0001$, significances determined by t-test.

3.2.2 Transfected MIN6 cells show comparable MTT readout decreases to wild type cells

The impact of 48 h treatment with 1.5 mM oleic acid was assessed in transfected MIN6 cells using the MTT assay. Oleic acid treatment decreased the MTT readout for both GFP+ (0.6968 ± 0.04744 vs. 0.6014 ± 0.05883, * $p < 0.05$, at 1.5 mM for GFP+, Figure 3A, significance determined by t-test to the respective control group) and Glrx5+ transfected cells (0.6963 ± 0.04909 vs. 0.6148 ± 0.06576, * $p < 0.05$, at 1.5 mM for

Glrx5+, Figure 3B, significances determined by t-test to the respective control group). The relative decrease was comparable between the transfected groups (-13.9 % at 1.5 mM for GFP+; -11.7 % at 1.5 mM for Glrx5+).

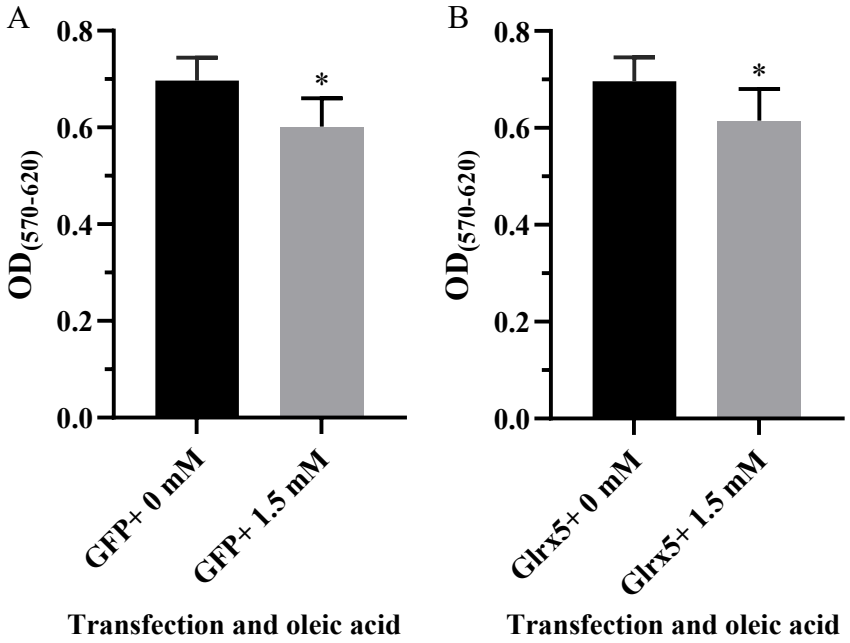

Figure 3: MTT assay results for transfected MIN6 cells treated for 48 h with 1.5 mM oleic acid for (A) GFP+ transfection, and (B) Glrx5+ transfection (n = 6). * $p < 0.05$, significances determined by t-test.

3.3 Slight changes in gene expression detected by qPCR after 5 d oleic acid treatment in wild type MIN6 cells

Despite evidence suggesting that lipid-induced cellular effects were more pronounced at the protein level than genetic level, MIN6 cells were analyzed by qPCR for *Glrx5* and *Ins2* mRNA expression. After 5 d of oleic acid treatment, *Glrx5* mRNA levels, normalized to *Rpl32*, showed a slight but non-significant decrease (1.0 ± 0.09477, with DMEM; 0.8465 ± 0.2626, at 0 mM; 0.8189 ± 0.2638, at 0.75 mM; 0.6628 ± 0.05587, at 1.5 mM; 0.6805 ± 0.1078, at 3 mM, Figure 4A, no significance determined by one-way ANOVA compared to 0 mM). *Ins2* mRNA levels were largely unchanged, except for a significant decrease at 3 mM (1.0 ± 0.07623, with DMEM; 0.9271 ± 0.07402, at 0 mM; 1.045 ± 0.124, at 0.75 mM; 1.041 ± 0.03904, at 1.5 mM; 0.6944 ± 0.05327, * $p < 0.05$, at 3 mM, Figure 4B, significance determined by one-way ANOVA compared to 0 mM).

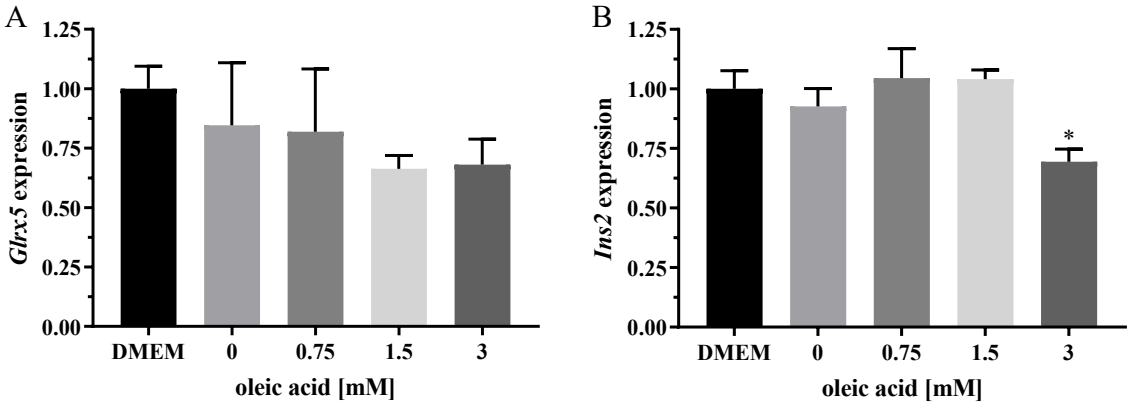

Figure 4: qPCR analysis of gene expression for (A) *Glrx5* mRNA, and (B) *Ins2* mRNA, normalized to *Rpl32* mRNA, in MIN6 cells treated for 5 d with oleic acid (n = 3). * $p < 0.05$, significance by one-way ANOVA compared to 0 mM.

3.4 Protein analysis

3.4.1 Glrx5 and insulin ELISA protein levels decrease after 24 h of oleic acid treatment in wild type MIN6 cells

In addition to qPCR, Glrx5 and insulin protein levels were measured using ELISA. A 24 h treatment with oleic acid led to a significant decrease in Glrx5 levels in the collected cell lysates (1.813 ± 0.4622 ng/mg, at 0 mM; 1.188 ± 0.07773 ng/mg, * $p < 0.05$, at 0.75 mM; 0.8882 ± 0.1702 ng/mg, ** $p < 0.01$, at 1.5 mM; 0.3837 ± 0.07519 ng/mg, **** $p < 0.0001$, at 3 mM, Figure 5, significances determined by one-way ANOVA compared to 0 mM). The relative decrease in Glrx5 levels was concentration-dependent (-34.5 % at 0.75 mM, -51.0 % at 1.5 mM, -78,8 % at 3 mM).

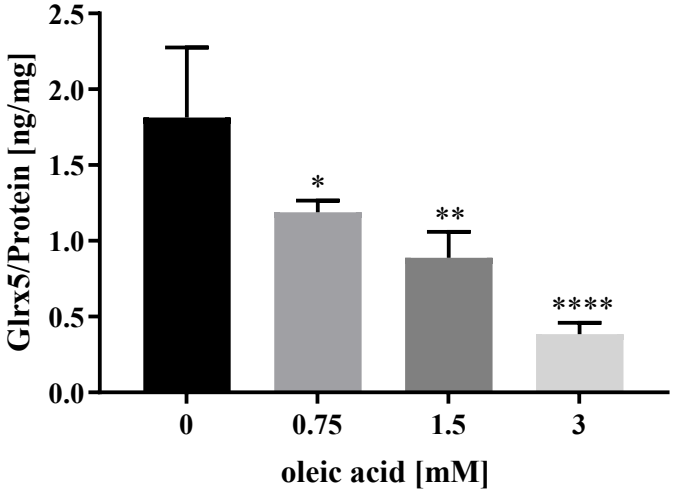

Figure 5: Glrx5 protein levels by ELISA in MIN6 cells treated for 24 h with oleic acid (n = 4). * $p < 0.05$, ** $p < 0.01$, **** $p < 0.0001$, significances by one-way ANOVA compared to 0 mM.

Contrary to the ELISA results, a 5 d treatment with oleic acid did not show significant changes in Glrx5 levels by immunoblotting compared to 0 mM (0.3428 ± 0.2962 RLU, with DMEM; 0.539 ± 0.3393 RLU, at 0 mM; 0.4875 ± 0.1808 RLU, at 0.75 mM; 0.5128 ± 0.234 RLU, at 1.5 mM; 0.5059 ± 0.2428 RLU, at 3 mM, Figure 6A, no significance determined by one-way ANOVA).

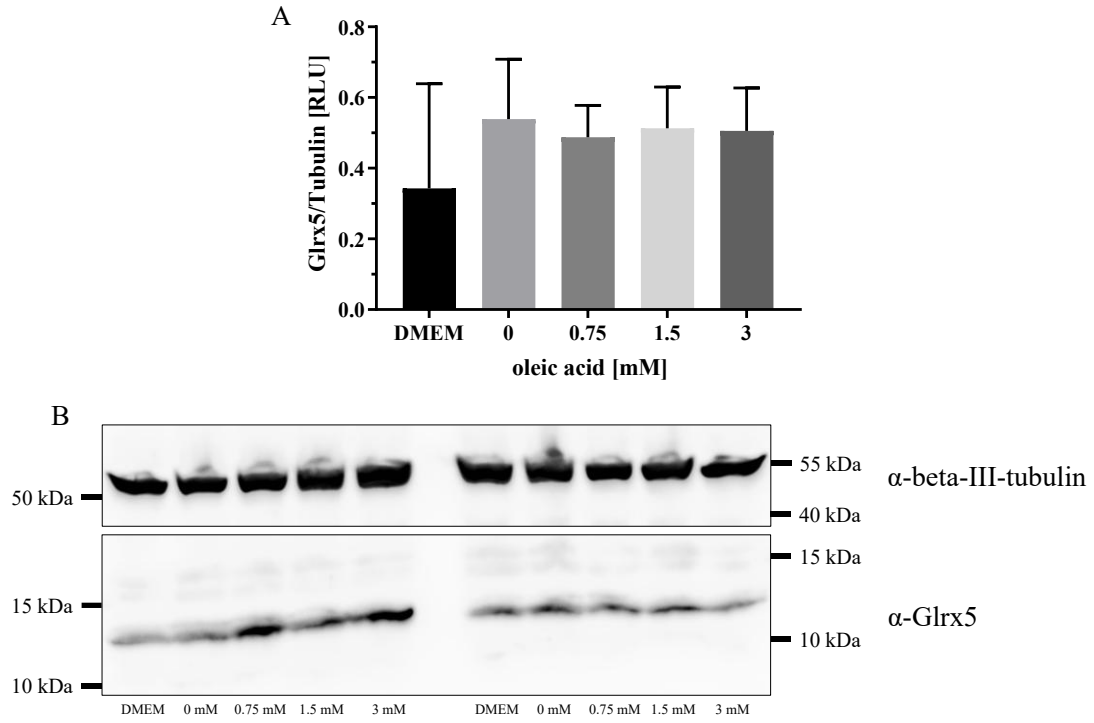

Figure 6: Detection of Glrx5 protein in total lysate of wild type MIN6 cells treated for 5 d with oleic acid via (A) quantification of immunoblotting signals (n = 4). (B) Representative image of two independent experiments with 60 µg protein. Tubulin was the reference protein. No significance by one-way ANOVA.

ELISA analysis of lysates from MIN6 cells treated with oleic acid for 24 h revealed a pronounced decrease in insulin levels at all tested oleic acid concentrations (17.56 ± 3.873 µg/mg, at 0 mM; 4.628 ± 0.3626 µg/mg, **** $p < 0.0001$, at 0.75 mM; 1.811 ± 0.7474 µg/mg, **** $p < 0.0001$, at 1.5 mM; 3.584 ± 0.4195 µg/mg, **** $p < 0.0001$, at 3 mM, Figure 7A, significances determined by one-way ANOVA compared to 0 mM). Relative comparison to 0 mM showed greater changes than those observed by qPCR (-73.6 % at 0.75 mM, -89.7 % at 1.5 mM, -79.6 % at 3 mM).

Similarly, insulin levels in the culture medium were significantly decreased at all concentrations (6.722 ± 1.034 µg/mg, at 0 mM; 1.246 ± 0.1091 µg/mg, **** $p < 0.0001$, at 0.75 mM; 0.9065 ± 0.32 µg/mg, **** $p < 0.0001$, at 1.5 mM; 0.761 ± 0.055 µg/mg,

**** $p < 0.0001$, at 3 mM, Figure 7B, significances determined by one-way ANOVA compared to 0 mM), additionally to strong relative changes (-81.5 % at 0.75 mM, -86.5 % at 1.5 mM, -88.7 % at 3 mM). Compared to lysate results, less insulin was released from the MIN6 cells into the medium.

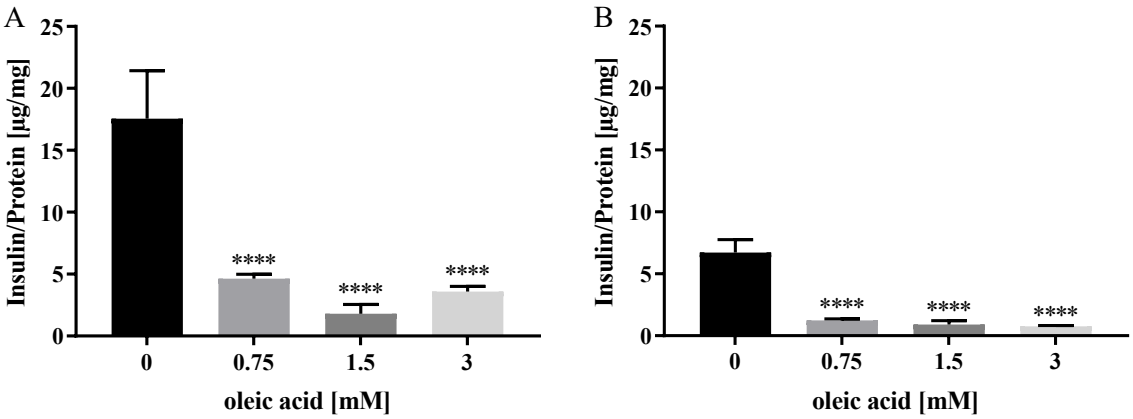

Figure 7: Insulin protein levels by ELISA of wild type MIN6 cells treated for 24 h with oleic acid in (A) cell lysate and (B) media (n = 4). **** $p < 0.0001$, significances by one-way ANOVA compared to 0 mM.

3.4.2 Effects on Glrx5 by ELISA in transfected cells by applying multiple oleic acid concentrations

In Glrx5+ transfected MIN6 cells, ELISA measurements showed a markable increase in Glrx5 levels compared to GFP+ transfected cells. Further comparisons showed a less pronounced decrease by oleic acid concentration than seen in wild type MIN6 cells (11.39 ± 2.005 ng/mg, with DMEM for GFP+; 23.43 ± 3.849 ng/mg, *** $p < 0.001$, with DMEM for Glrx5+; 21.1 ± 3.524 ng/mg, ** $p < 0.01$, at 0 mM for Glrx5+; 14.74 ± 2.488 ng/mg, at 0.75 mM for Glrx5+; 18.75 ± 2.453 ng/mg, * $p < 0.05$, at 1.5 mM for Glrx5+; 18.32 ± 3.034 ng/mg, * $p < 0.05$, at 3 mM for Glrx5+, Figure 8, significances determined by one-way ANOVA compared to GFP+ DMEM). However, no significances were observed between control and oleic acid treated groups within the Glrx5+ transfection group.

Immunoblotting analysis confirmed these findings after 48 h of treatment with oleic acid in transfected MIN6 cells (0.1218 ± 0.02998 RLU, with DMEM for GFP+; 0.7681 ± 0.1281 RLU, *** $p < 0.001$, with DMEM for Glrx5+; 0.9165 ± 0.2055 RLU,

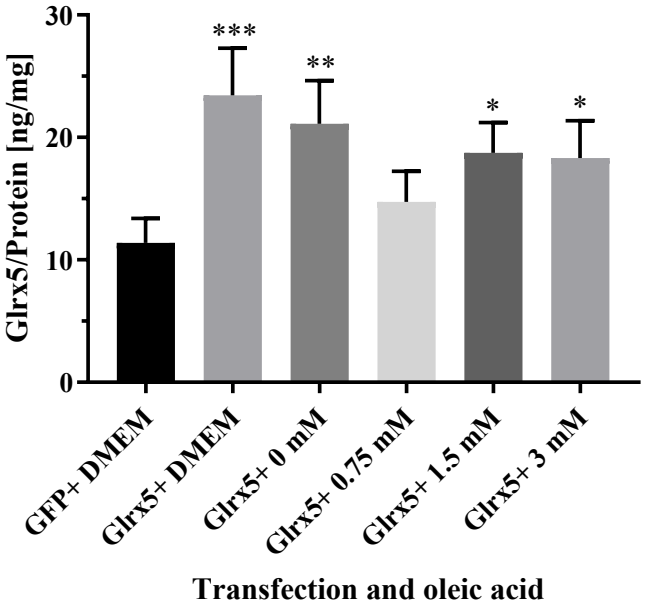

Figure 8: Glrx5 protein levels by ELISA in GFP+ and Glrx5+ transfected MIN6 cells with different treatment groups of oleic acid (n = 4). * $p < 0.05$, ** $p < 0.01$, *** $p < 0.001$, significances by one-way ANOVA compared to GFP+ DMEM.

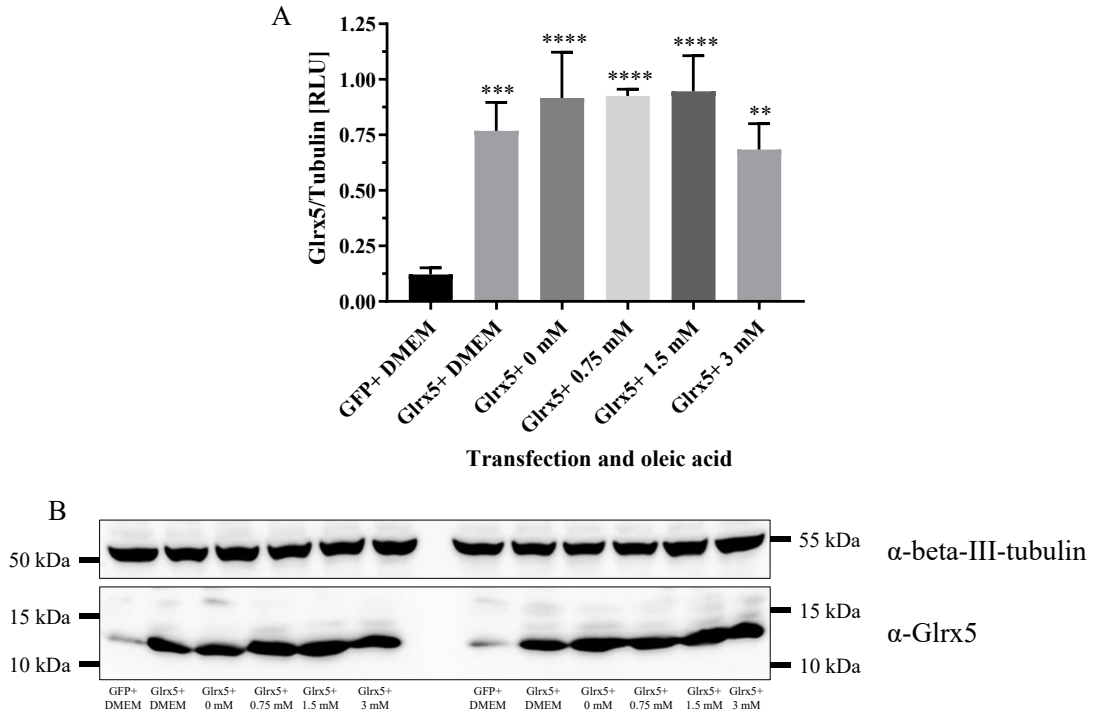

Figure 9: Detection of Glrx5 protein in total lysate of transfected MIN6 cells treated for 48 h with oleic acid via (A) quantification of immunoblotting signals (n = 3). (B) Representative image of two independent experiments with 60 µg protein. Tubulin was the reference protein. ** $p < 0.01$, *** $p < 0.001$, **** $p < 0.0001$, significances by one-way ANOVA compared to GFP+ DMEM.

**** $p < 0.0001$, at 0 mM for Glrx5+; 0.9252 ± 0.03009 RLU, **** $p < 0.0001$, at 0.75 mM for Glrx5+; 0.9463 ± 0.1607 RLU, **** $p < 0.0001$, at 1.5 mM for Glrx5+; 0.6835 ± 0.1167 RLU, ** $p < 0.01$, at 3 mM for Glrx5+, Figure 9A, significances determined by one-way ANOVA compared to GFP+ DMEM). Glrx5+ transfection resulted in a substantial increase in Glrx5 protein levels compared to GFP+ transfected cells. Unlike in wild type cells, no further decrease in ELISA Glrx5 levels were observed with oleic acid treatment in Glrx5+ transfected cells.

3.4.3 Effects on Glrx5 and insulin by ELISA or immunoblotting in transfected cells by applying single oleic acid concentration with respective control

In a separate setup, transfected MIN6 cells were treated with 1.5 mM oleic acid for 48 h, and cell counts were recorded at the end of the experiment. No major differences in cell number were observed between treatment groups or transfection (2.887 ± 0.2477 $*10^6$, at 0 mM for GFP+; 2.581 ± 0.5177 $*10^6$, at 1.5 mM for GFP+; 2.866 ± 0.2613 $*10^6$, at 0 mM for Glrx5+; 3.063 ± 0.7144 $*10^6$, at 1.5 mM for Glrx5+, Figure 10, no significance determined by one-way ANOVA). In this setup, cells grew in T25 cell culture flasks.

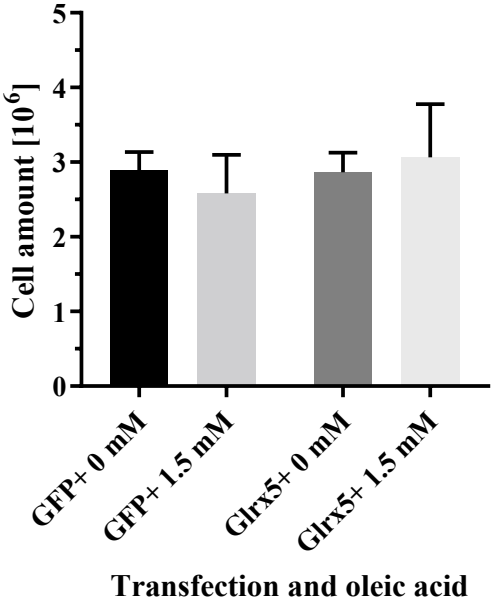

Figure 10: Cell counts of MIN6 cells collected with trypsin/EDTA prior to sample preparation for ELISA (n = 4). Cells were transfected and subsequently treated for 48 h with oleic acid in a T25 flask. No significance by one-way ANOVA.

ELISA analysis of Glrx5 levels showed minimal changes after 48 h of treatment with 1.5 mM oleic acid (10.48 ± 2.697 ng/mg, at 0 mM for GFP+; 8.713 ± 3.216 ng/mg, at 1.5 mM for GFP+; 14.71 ± 3.084 ng/mg, at 0 mM for Glrx5+; 14.1 ± 1.185 ng/mg, at 1.5 mM for Glrx5+, Figure 11, no significance determined by one-way ANOVA). Although Glrx5+ transfection resulted in slightly elevated Glrx5 levels, no further impairment was caused by oleic acid.

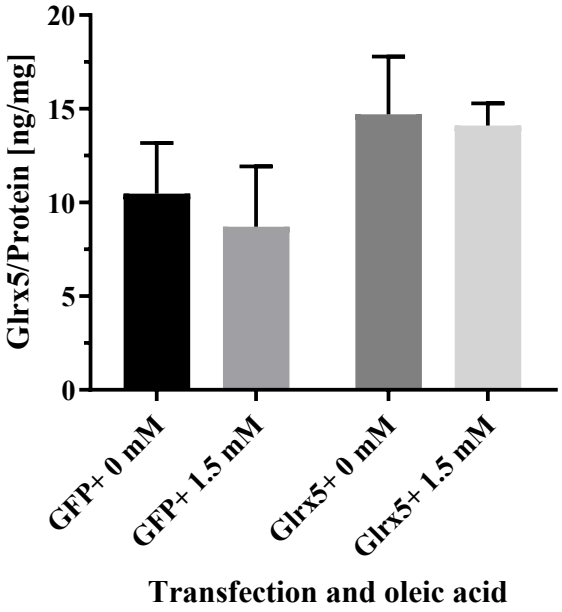

Figure 11: Glrx5 protein levels by ELISA of transfected MIN6 cells treated for 48 h with oleic acid (n = 3-4). No significance by one-way ANOVA.

Immunoblotting analysis of the setup with corresponding GFP+ controls showed a more pronounced increase of Glrx5 compared to ELISA by Glrx5+ transfection (0.05283 ± 0.03129 RLU, at 0 mM for GFP+; 0.07211 ± 0.09279 RLU, at 3 mM for GFP+; 0.2362 ± 0.1092 RLU, at 0 mM for Glrx5+; 0.2081 ± 0.1225 RLU, at 3 mM for Glrx5+, Figure 12A, no significance determined by one-way ANOVA). There was no adverse effect by oleic acid in both transfection groups. GFP was also detected by immunoblotting as further transfection marker. Consistent with previous findings, 3 mM treatment did not significantly alter Glrx5 levels in wild type (Figure 6) or transfected cells (Figure 9).

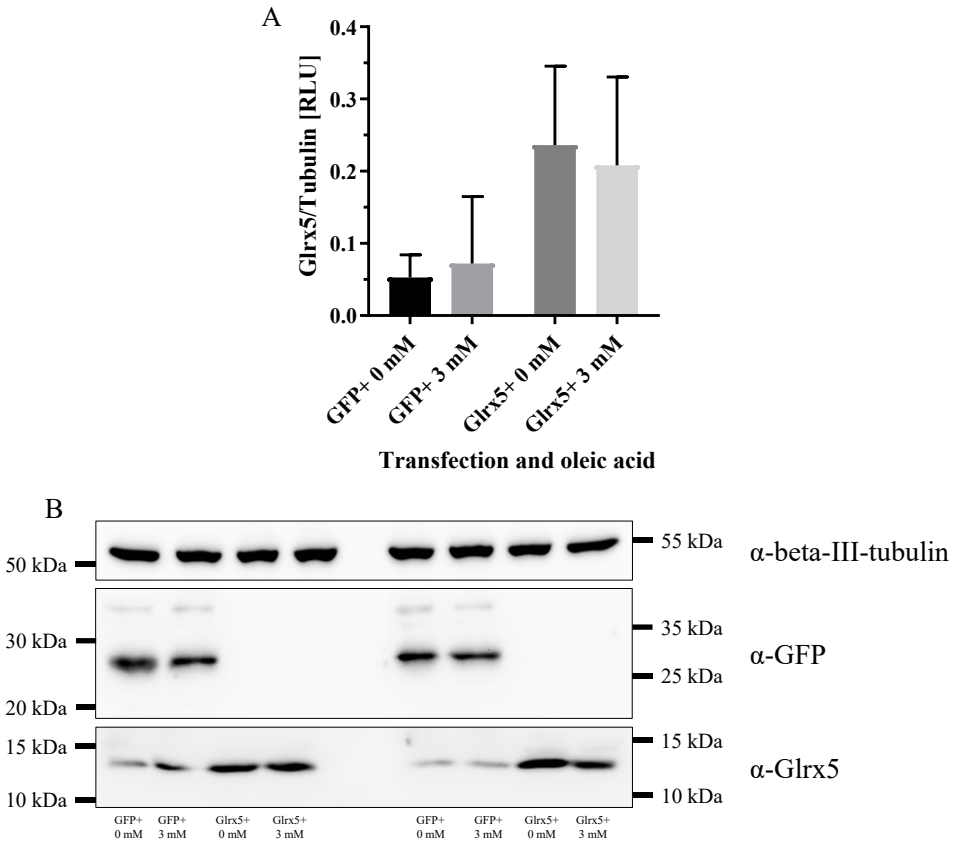

Figure 12: Detection of Glrx5 and GFP in total lysate of transfected MIN6 cells treated for 48 h with oleic acid via (A) quantification of Glrx5 immunoblotting signals (n = 3). (B) Representative image of two independent experiments with 20 µg protein. Tubulin was the reference protein. No significance by one-way ANOVA.

Insulin levels measured by ELISA showed slight decreases in both lysates (40.2 ± 10.98 µg/mg, at 0 mM for GFP+; 31.72 ± 6.457 µg/mg, at 1.5 mM for GFP+; 41.86 ± 14.36 µg/mg, at 0 mM for Glrx5+; 31.21 ± 11.06 µg/mg, at 1.5 mM for Glrx5+, Figure 13A, no significance determined by one-way ANOVA) and culture medium (17.41 ± 9.214 µg/mg, at 0 mM for GFP+; 12.66 ± 3.426 µg/mg, at 1.5 mM for GFP+; 15.30 ± 6.646 µg/mg, at 0 mM for Glrx5+; 11.74 ± 3.83 µg/mg, at 1.5 mM for Glrx5+, Figure 13B, no significance determined by one-way ANOVA). Similar to wild type cells, insulin levels in the medium were lower than in lysates. Overall, the detrimental effects of oleic acid appeared less pronounced in this setup compared to the 5 d treatment in wild type cells, but the recent experiments showed a comparable effect in both transfection groups for Glrx5 and insulin level.

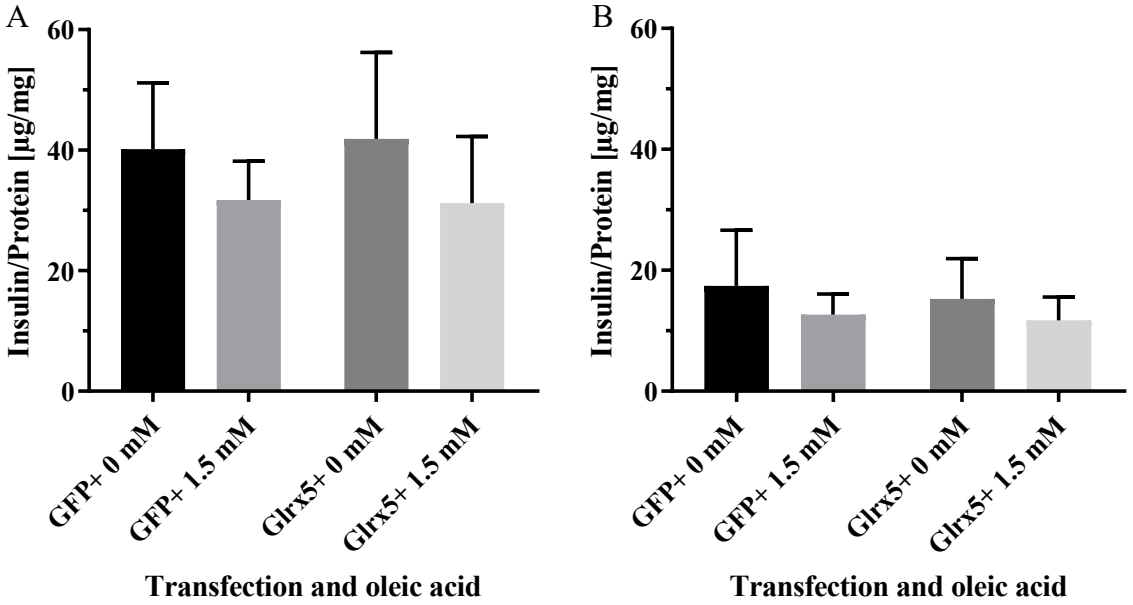

Figure 13: Insulin protein levels by ELISA of transfected MIN6 cells treated for 48 h with oleic acid in (A) cell lysate (n = 3-4) and (B) media (n = 4). No significance by one-way ANOVA.

3.4.4 Cytosolic aconitase activity is impaired after 5 d oleic acid treatment, while other Fe-S enzymes are unchanged in wild type MIN6 cells

Based on the observed changes in Glrx5 protein levels, which were in accordance to insulin levels in wild type cells, the activities of Fe-S cluster dependent enzymes associated with Glrx5 were analyzed. Wild type MIN6 cells treated with varying concentrations of oleic acid for 5 d demonstrated a significant decrease in ACO1 activity (234.5 ± 19.06 mU/mU, with DMEM; 181.0 ± 41.01 mU/mU, at 0 mM; 158.0 ± 17.34 mU/mU, at 0.75 mM; 75.25 ± 26.4 mU/mU, *** $p < 0.001$, at 1.5 mM; 17.77 ± 1.329 mU/mU, **** $p < 0.0001$, at 3 mM, Figure 14A, significances determined by one-way ANOVA compared to 0 mM). In contrast, ACO2 activity showed no significant changes (0.1484 ± 0.03962 mU/mU, with DMEM; 0.1261 ± 0.05516 mU/mU, at 0 mM; 0.1795 ± 0.02716 mU/mU, at 0.75 mM; 0.14 ± 0.03004 mU/mU, at 1.5 mM; 0.1396 ± 0.0329 mU/mU, at 3 mM, Figure 14B, no significance determined by one-way ANOVA compared to 0 mM). ACO1 activity showed greater impairments at higher oleic acid concentrations compared to 0 mM (-12.7 % at 0.75 mM, -58.4 % at 1.5 mM, -90.2 % at 3 mM).

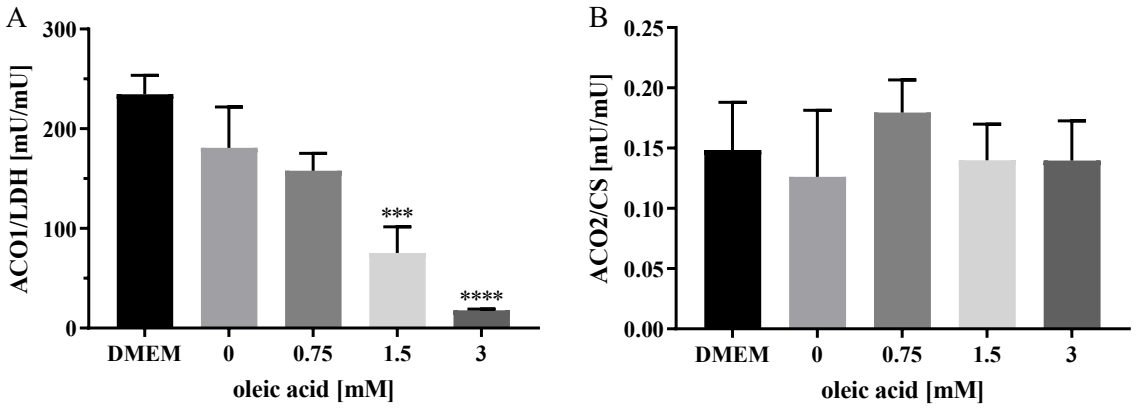

Figure 14: Enzyme activities of (A) ACO1 and (B) ACO2, with respective marker enzymes, in wild type MIN6 cells treated for 5 d with oleic acid (n = 4). *** $p < 0.001$, **** $p < 0.0001$, significances by one-way ANOVA compared to 0 mM.

Further analysis of Fe-S cluster dependent mitochondrial enzymes revealed no significant changes in activity. This included SDH (0.1165 ± 0.04509 mU/mU, with DMEM; 0.1225 ± 0.0284 mU/mU, at 0 mM; 0.1146 ± 0.01693 mU/mU, at 0.75 mM; 0.1124 ± 0.01035 mU/mU, at 1.5 mM; 0.1288 ± 0.03514 mU/mU, at 3 mM, Figure 15A, no significance determined by one-way ANOVA), the C2-C3 complex (0.08356 ± 0.02717 mU/mU, with DMEM; 0.09526 ± 0.01788 mU/mU, at 0 mM; 0.09854 ± 0.01697 mU/mU, at 0.75 mM; 0.0943 ± 0.01595 mU/mU, at 1.5 mM; 0.1056 ± 0.03397 mU/mU, at 3 mM, Figure 15B, no significance determined by one-way ANOVA), and COX (0.9225 ± 0.1896 mU/mU, with DMEM; 1.188 ± 0.2587 mU/mU, at 0 mM; 0.9218 ± 0.1902 mU/mU, at 0.75 mM; 0.9754 ± 0.2605 mU/mU, at 1.5 mM; 0.779 ± 0.1069 mU/mU, at 3 mM, Figure 15C, no significance determined by one-way ANOVA).

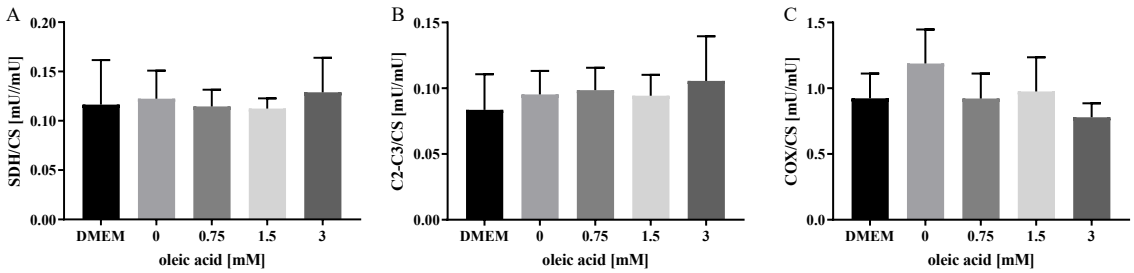

Figure 15: Enzyme activities of (A) SDH, (B) C2-C3, and (C) COX, compared to mitochondrial marker CS in wild type MIN6 cells treated for 5 d with oleic acid (n = 4). No significance by one-way ANOVA.

The efficiency of cellular fractionation was monitored by measuring CS activity, which should predominantly remain in the organelles containing fraction, with minimal leakage into the cytosolic fraction. CS activity detected in the cytosolic fraction was low (3.968 ± 1.386 mU/mg, with DMEM; 5.755 ± 3.414 mU/mg, at 0 mM; 5.45 ± 2.342 mU/mg, at 0.75 mM; 6.46 ± 2.738 mU/mg, at 1.5 mM; 9.245 ± 3.483 mU/mg, at 3 mM, Figure 16A, no significance determined by one-way ANOVA) and the majority of CS activity was retained in the organelles containing fraction (509.5 ± 89.98 mU/mg, with DMEM; 447.4 ± 62.86 mU/mg, at 0 mM; 367.3 ± 97.41 mU/mg, at 0.75 mM; 368.1 ± 67.82 mU/mg, at 1.5 mM; 314.8 ± 81.44 mU/mg, at 3 mM, Figure 16B, no significance determined by one-way ANOVA). Notably, CS activity in the cytosolic fraction increased, while activity in the organelles containing fraction decreased with higher oleic acid concentrations.

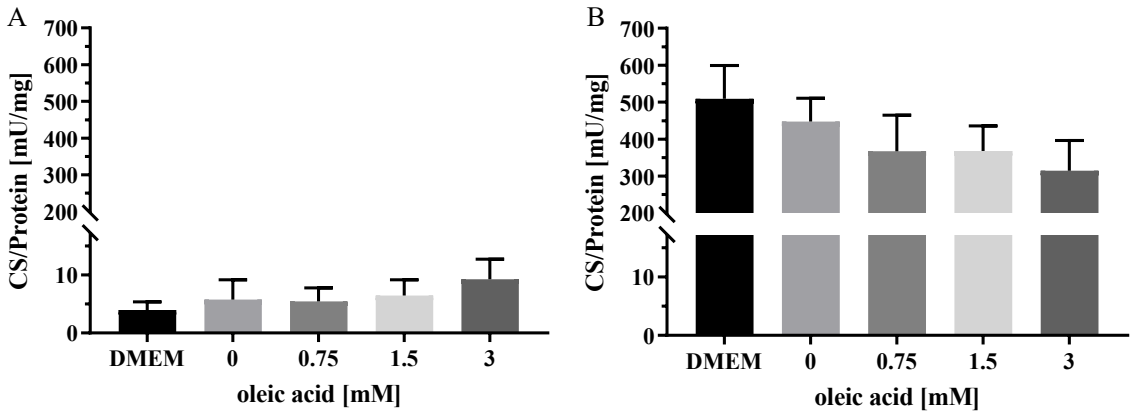

Figure 16: CS enzyme activities in (A) the cytosolic fraction and (B) the organelles containing fraction of wild type MIN6 cells treated for 5 d with oleic acid (n = 4). No significance by one-way ANOVA.

The fractionation quality was further confirmed through immunoblotting. Protein markers for cytosolic tubulin and mitochondrial ACO2 (Figure 17) or MIA40 (not shown) demonstrated appropriate localization. One out of four independent experiments is shown in Figure 17. Tubulin was detected exclusively in the cytosolic fraction (left), whereas ACO2 remained in the organelles containing fraction (right).

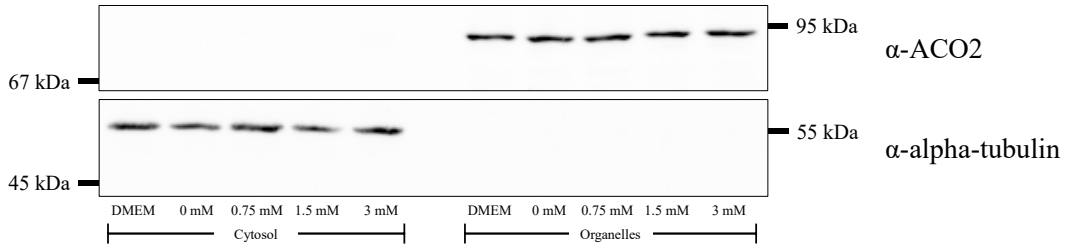

Figure 17: Distribution of tubulin or ACO2 in the cytosolic (left) and organelles containing fractions (right) of wild type MIN6 cells treated for 5 d with oleic acid. Representative image of one independent experiment of MIN6 cells used for analysis of Fe-S enzyme activities with 40 µg protein.

3.4.5 Transfected MIN6 cells show only moderate effects on Fe-S enzymes after 48 h with a concentration series of oleic acid

Transfected MIN6 cells treated with increasing concentrations of oleic acid for 48 h showed decreasing levels of ACO1 (111.1 ± 21.81 mU/mU, with DMEM for GFP+; 130.1 ± 14.36 mU/mU, with DMEM for Glrx5+; 139.5 ± 24.21 mU/mU, at 0 mM for Glrx5+; 96.0 ± 11.2 mU/mU, at 0.75 mM for Glrx5+; 83.43 ± 18.38 mU/mU, at 1.5 mM for Glrx5+; 92.57 ± 36.39 mU/mU, at 3 mM for Glrx5+, Figure 18A, no significance determined by one-way ANOVA compared to Glrx5+ 0 mM). For the first time, a slight decrease in ACO2 activity was observed, although it was not statistically significant (0.167 ± 0.01852 mU/mU, with DMEM for GFP+; 0.2013 ± 0.04119 mU/mU, with DMEM for Glrx5+; 0.1793 ± 0.01721 mU/mU, at 0 mM for Glrx5+; 0.1757 ± 0.01914 mU/mU, at 0.75 mM for Glrx5+; 0.1453 ± 0.02098 mU/mU, at 1.5 mM for Glrx5+; 0.122 ± 0.01735 mU/mU, at 3 mM for Glrx5+, Figure 18B, no significance determined by one-way ANOVA compared to Glrx5+ 0 mM). ACO1 protein levels, assessed by immunoblotting, followed a pattern consistent with enzyme activity. Minor lowering effects were observed with increased oleic acid concentrations, alongside an initial increase in GFP+ transfected cells compared to Glrx5+ cells (0.5154 ± 0.1877 RLU, with DMEM for GFP+; 0.7901 ± 0.4484 RLU, with DMEM for Glrx5+; 0.6929 ± 0.3696 RLU, at 0 mM for Glrx5+; 0.7622 ± 0.441 RLU, at 0.75 mM for Glrx5+; 0.6078 ± 0.2578 RLU, at 1.5 mM for Glrx5+; 0.5406 ± 0.2665 RLU, at 3 mM for Glrx5+, Figure 19A, no significance determined by one-way ANOVA).

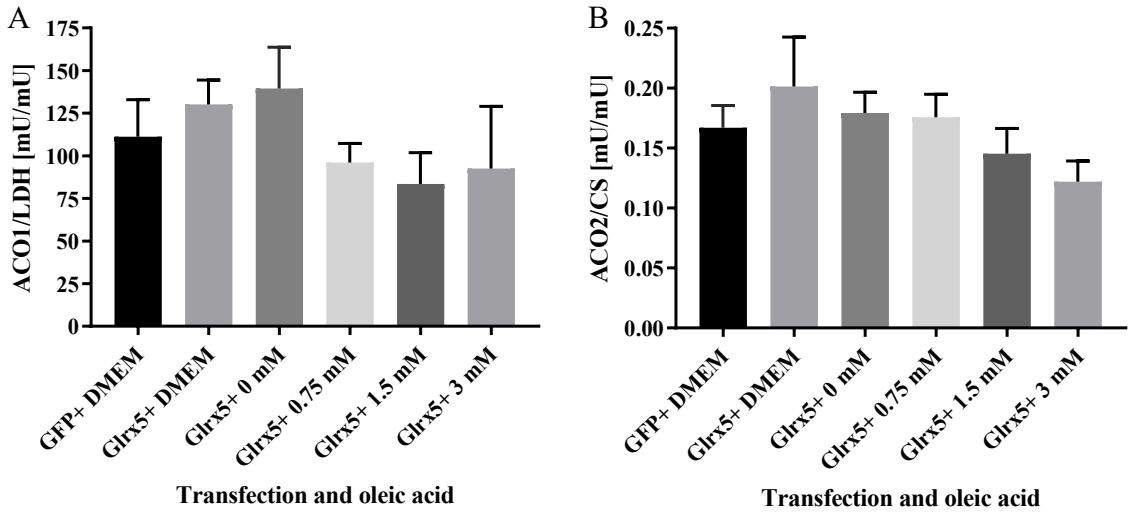

Figure 18: Enzyme activities of (A) ACO1 and (B) ACO2, with respective marker enzymes, in transfected MIN6 cells treated for 48 h with oleic acid (n = 3). No significance by one-way ANOVA.

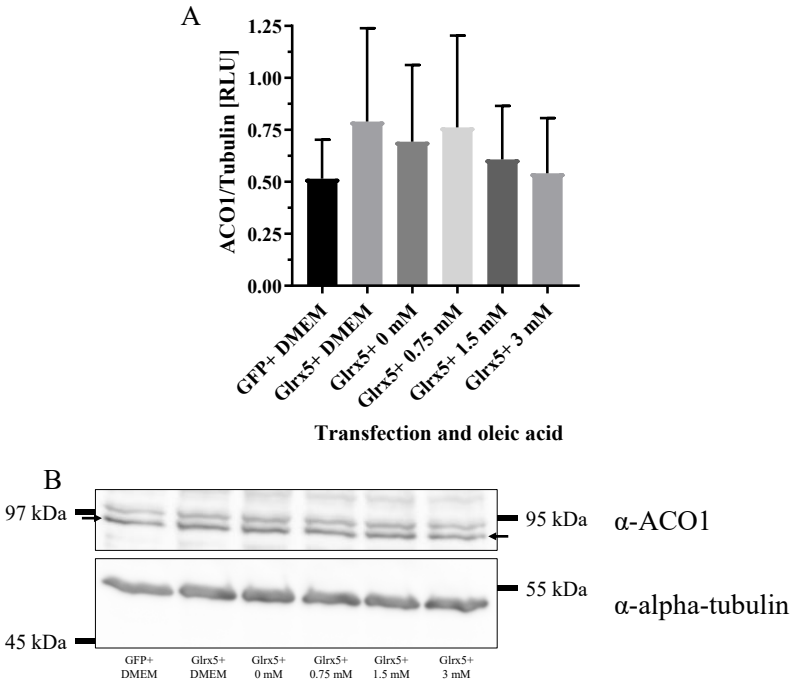

Figure 19: Detection of ACO1 in the cytosol of transfected MIN6 cells treated for 48 h with oleic acid via (A) quantification of immunoblotting signals (n = 3). (B) Representative image of one independent experiment of MIN6 cells used for analysis of Fe-S enzyme activities with 40 µg protein. Tubulin was the reference protein. No significance by one-way ANOVA.

Analysis of additional Fe-S enzymes revealed no significant changes for SDH across the treatment groups (0.0623 ± 0.004464 mU/mU, with DMEM for GFP+; 0.0708 ± 0.009741 mU/mU, with DMEM for Glrx5+; 0.0739 ± 0.01768 mU/mU, at 0 mM for Glrx5+; 0.0621 ± 0.006223 mU/mU, at 0.75 mM for Glrx5+; 0.06153 ± 0.004285 mU/mU, at 1.5 mM for Glrx5+; 0.0605 ± 0.02077 mU/mU, at 3 mM for Glrx5+, Figure 20A, no significance determined by one-way ANOVA compared to Glrx5+ 0 mM). The C2-C3 activity showed a decreasing trend toward with increased oleic acid concentration, though this was not statistically significant (0.08207 ± 0.01634 mU/mU, with DMEM for GFP+; 0.0928 ± 0.02409 mU/mU, with DMEM for Glrx5+; 0.0868 ± 0.0214 mU/mU, at 0 mM for Glrx5+; 0.06303 ± 0.01628 mU/mU, at 0.75 mM for Glrx5+; 0.05907 ± 0.003842 mU/mU, at 1.5 mM for Glrx5+; 0.06047 ± 0.0184 mU/mU, at 3 mM for Glrx5+, Figure 20B, no significance determined by one-way ANOVA compared to Glrx5+ 0 mM), while COX remained unchanged across all conditions (0.5703 ± 0.1221 mU/mU, with DMEM for GFP+; 0.5713 ± 0.1482 mU/mU, with DMEM for Glrx5+; 0.56 ± 0.1038 mU/mU, at 0 mM for Glrx5+; 0.6753 ± 0.1772 mU/mU, at 0.75 mM for Glrx5+; 0.654 ± 0.1348 mU/mU, at 1.5 mM for Glrx5+; 0.5537 ± 0.1913 mU/mU, at 3 mM for Glrx5+, Figure 20C, no significance determined by one-way ANOVA compared to Glrx5+ 0 mM).

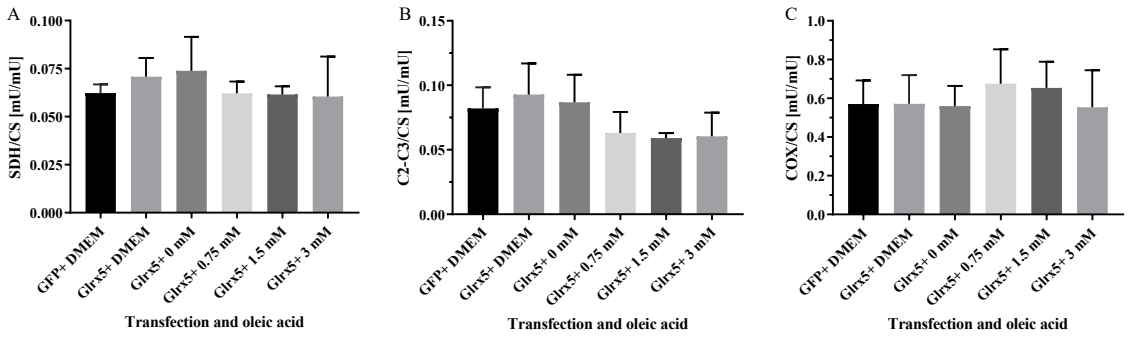

Figure 20: Enzyme activities of (A) SDH, (B) C2-C3, and (C) COX compared to mitochondrial marker CS in transfected MIN6 cells treated for 48 h with oleic acid (n = 3). No significance by one-way ANOVA.

CS activity was comparable to that of wild type cells, with low activity in the cytosolic fraction (7.867 ± 0.8501 mU/mg, with DMEM for GFP+; 6.673 ± 1.488 mU/mg, with DMEM for Glrx5+; 6.03 ± 1.553 mU/mg, at 0 mM for Glrx5+; 7.42 ± 1.178 mU/mg, at 0.75 mM for Glrx5+; 8.52 ± 0.4279 mU/mg, at 1.5 mM for Glrx5+; 11.11 ± 1.259 mU/mg, ** $p < 0.01$, at 3 mM for Glrx5+, Figure 21A, significance determined by

one-way ANOVA compared to Glrx5+ 0 mM) and the majority of activity remaining in the organelles containing fraction (422.3 ± 120.4 mU/mg, with DMEM for GFP+; 384.0 ± 126.1 mU/mg, with DMEM for Glrx5+; 368.3 ± 63.11 mU/mg, at 0 mM for Glrx5+; 356.7 ± 57.64 mU/mg, at 0.75 mM for Glrx5+; 415.7 ± 35.22 mU/mg, at 1.5 mM for Glrx5+; 386.0 ± 43.09 mU/mg, at 3 mM for Glrx5+, Figure 21B, no significance determined by one-way ANOVA compared to Glrx5+ 0 mM). Also, the activity of the cytosolic fraction seemed to increase by oleic acid treatment in this setup.

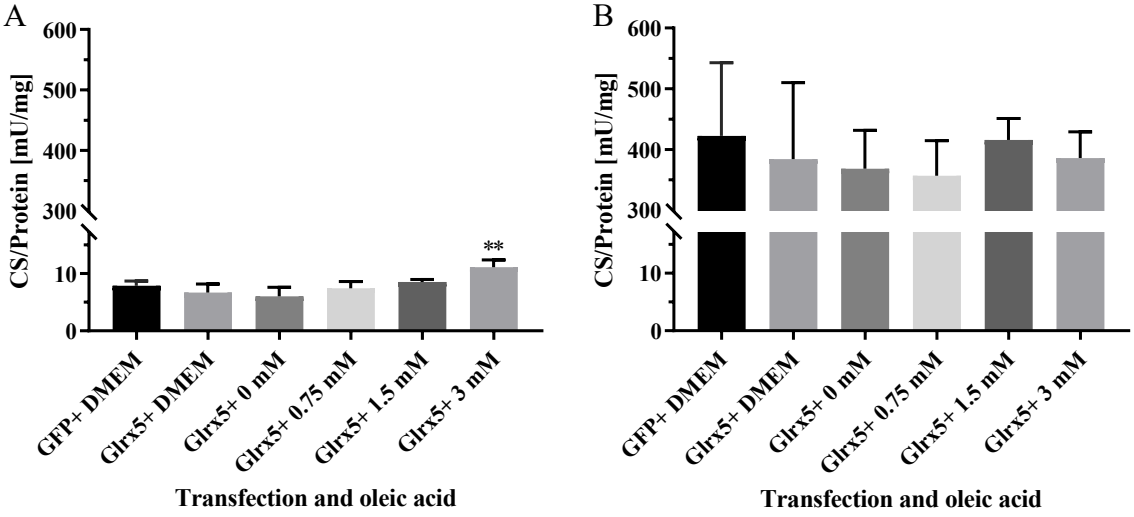

Figure 21: CS enzyme activities in (A) the cytosolic fraction, and (B) the organelles containing fraction of transfected MIN6 cells treated for 5 d with oleic acid (n = 3). ** $p < 0.01$, significance by one-way ANOVA compared to Glrx5+ 0 mM.

The distribution of marker proteins and GFP transfection was verified by immunoblotting. Strong signals were detected for mitochondrial ACO2 and GFP in the organelles fraction (right), and for cytosolic GPAT in the cytosolic fraction (left) (Figure 22). Representative results from one of three replicates are shown in Figure 22. Furthermore, the presence of Glrx5 was confirmed in the organelles fraction via immunoblotting, with a stronger signal observed in Glrx5+ transfected cells compared to GFP+ transfected cells (Figure 23). Representative results from one of three replicates are shown in Figure 23.

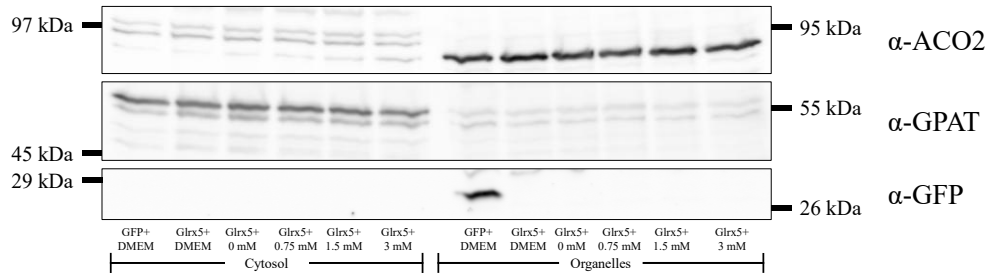

Figure 22: Distribution of GPAT, ACO2 and GFP in the cytosolic (left) or organelles containing fractions (right) of transfected MIN6 cells treated for 48 h with oleic acid. Representative image of one independent experiment of MIN6 cells used for analysis of Fe-S enzyme activities with 40 µg protein. Detection of GFP was enhanced by avidin biotin complex.

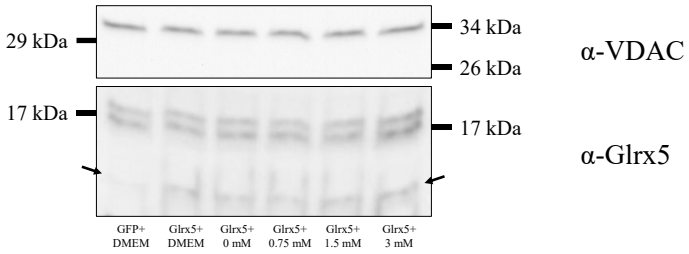

Figure 23: Detection of Glrx5 in organelles of transfected MIN6 cells treated for 48 h with oleic acid. Representative image of one independent experiment of MIN6 cells used for analysis of Fe-S enzyme activities analyzed by tricin SDS-PAGE with 20 µg protein. Detection of Glrx5 was enhanced by avidin biotin complex. VDAC was the reference protein.

3.4.6 Cytosolic aconitase activity is decreased independently of Glrx5 transfection, while mitochondrial Fe-S enzymes are unaffected by oleic acid or transfection

To confirm the results from the initial setup with transfected cells, further samples were analyzed, including an individual GFP+ control group and treatment with 3 mM oleic acid for 48 h. The highest oleic acid concentration was chosen to maximize the likelihood of detecting noticeable differences. Evaluation of cell counts after the treatment period revealed a reduction in cell numbers in response to oleic acid treatment (3.906 ± 1.231 $*10^6$, at 0 mM for GFP+; 1.588 ± 0.1561 $*10^6$, * $p < 0.05$, at 3 mM for GFP+; 3.838 ± 1.309 $*10^6$, at 0 mM for Glrx5+; 1.669 ± 0.4754 $*10^6$, * $p < 0.05$, at 3 mM for Glrx5+, Figure 24, significances determined by one-way ANOVA compared to 0 mM). Unlike the findings shown in Figure 10, this experiment demonstrated a clear effect of oleic acid on cell numbers. Cells were treated in a T75 flask for this setup.

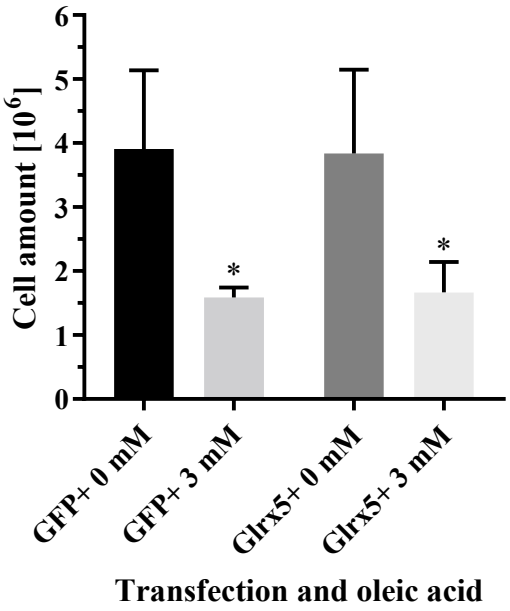

Figure 24: Cell counts of MIN6 cells collected with trypsin/EDTA prior to sample preparation for Fe-S enzyme analysis (n = 4). Cells were transfected and subsequently treated for 48 h with oleic acid in a T75 flask. * $p < 0.05$, significances determined by one-way ANOVA compared to 0 mM.

Consistent with observations in wild type cells, transfected MIN6 cells exhibited decreased ACO1 activity (171.2 ± 31.12 mU/mU, at 0 mM for GFP+; 108.8 ± 14.57 mU/mU, * $p < 0.05$, at 3 mM for GFP+; 158.3 ± 33.88 mU/mU, at 0 mM for Glrx5+; 99.83 ± 20.81 mU/mU, * $p < 0.05$, at 3 mM for Glrx5+, Figure 25A, significances determined by one-way ANOVA compared to 0 mM), while ACO2 remained unchanged across all groups (0.2443 ± 0.01242 mU/mU, at 0 mM for GFP+; 0.264 ± 0.03184 mU/mU, at 3 mM for GFP+; 0.241 ± 0.01431 mU/mU, at 0 mM for Glrx5+; 0.2403 ± 0.0246 mU/mU, at 3 mM for Glrx5+, Figure 25B, significances determined by one-way ANOVA compared to 0 mM). These findings aligned with previous results for ACO1 activity and demonstrated that ACO2 activity was unaffected by transfection or oleic acid treatment, consistent with wild type cells (Figure 14B). The previously observed changes in ACO2 activity in transfected samples (Figure 18B) were not replicated.

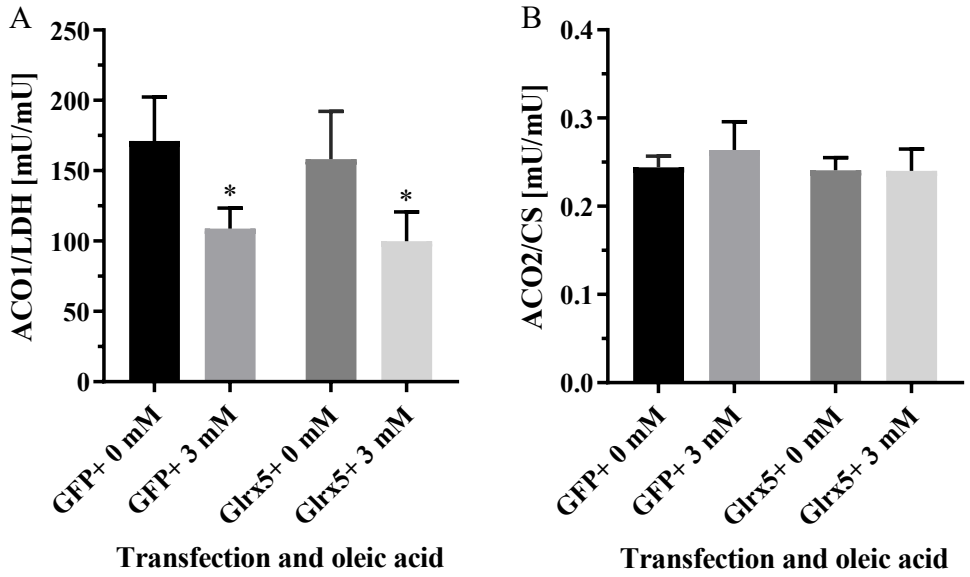

Figure 25: Enzyme activities of (A) ACO1 and (B) ACO2 in transfected MIN6 cells treated for 48 h with oleic acid (n = 4). * $p < 0.05$, significances by one-way ANOVA compared to 0 mM.

Immunoblotting revealed no differences in ACO1 protein levels between transfection and treatment groups, despite changes in enzyme activity (1.999 ± 0.3615 RLU, at 0 mM for GFP+; 2.069 ± 0.3702 RLU, at 3 mM for GFP+; 2.29 ± 0.6974 RLU, at 0 mM for Glrx5+; 1.989 ± 0.8773 RLU, at 3 mM for Glrx5+, Figure 26A, no significances determined by one-way ANOVA), while ACO2 signals appeared elevated with transfection and treatment, but the changes were not significant (3.318 ± 1.183 RLU, at 0 mM for GFP+; 3.676 ± 1.91 RLU, at 3 mM for GFP+; 4.44 ± 1.777 RLU, at 0 mM for Glrx5+; 5.393 ± 1.902 RLU, at 3 mM for Glrx5+, Figure 27A, no significances determined by one-way ANOVA).

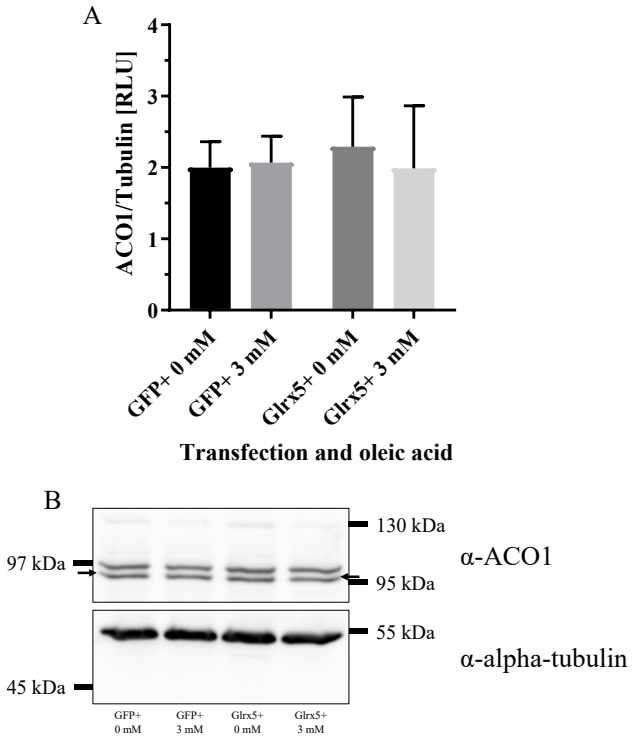

Figure 26: Detection of ACO1 in the cytosol of transfected MIN6 cells treated for 48 h with oleic acid via (A) quantification of immunoblotting signals (n = 4). (B) Representative image of one independent experiment of MIN6 cells used for analysis of Fe-S enzyme activities with 40 µg protein. Tubulin was the reference protein. No significance by one-way ANOVA.

Further analysis of Fe-S enzymes revealed no significant changes in activity. SDH activity remained stable across all groups (0.05403 ± 0.007407 mU/mU, at 0 mM for GFP+; 0.0634 ± 0.003753 mU/mU, at 3 mM for GFP+; 0.05895 ± 0.004388 mU/mU, at 0 mM for Glrx5+; 0.06023 ± 0.006516 mU/mU, at 3 mM for Glrx5+, Figure 28A, no significance determined by one-way ANOVA). Similarly, COX activity was unaffected by transfection or oleic acid treatment (0.4312 ± 0.1047 mU/mU, at 0 mM for GFP+; 0.4849 ± 0.1524 mU/mU, at 3 mM for GFP+; 0.4391 ± 0.1093 mU/mU, at 0 mM for Glrx5+; 0.4617 ± 0.1606 mU/mU, at 3 mM for Glrx5+, Figure 28B, no significance determined by one-way ANOVA).

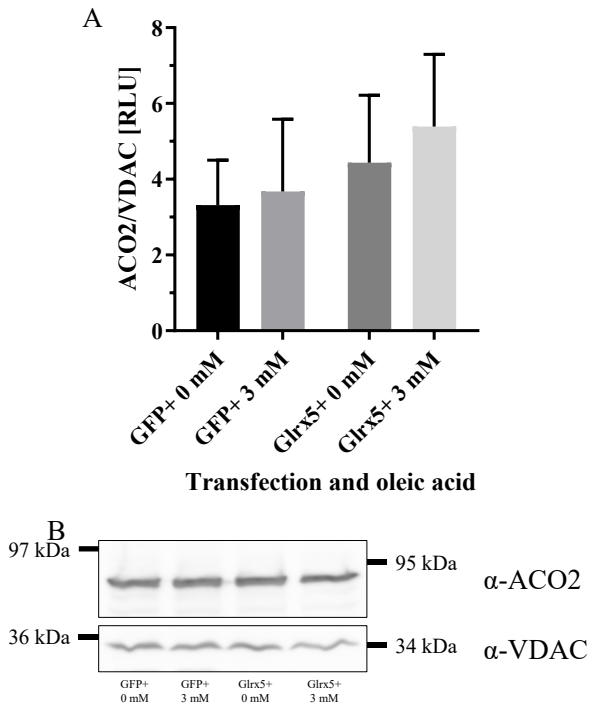

Figure 27: Detection of ACO2 in the organelles fraction of transfected MIN6 cells treated for 48 h with oleic acid via (A) quantification of immunoblotting signals (n = 4). (B) Representative image of one independent experiment of MIN6 cells used for analysis of Fe-S enzyme activities with 40 µg protein. VDAC was the reference protein. No significance by one-way ANOVA.

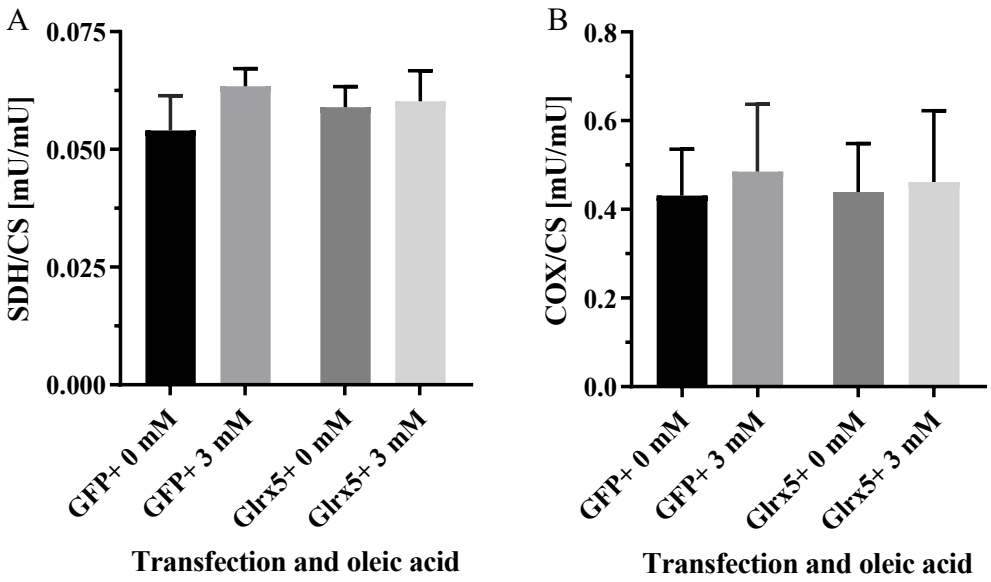

Figure 28: Enzyme activities of (A) SDH and (B) COX, compared to mitochondrial marker CS in transfected MIN6 cells treated for 48 h with oleic acid (n = 4). No significance by one-way ANOVA.

Immunoblotting signals of COX subunits were detected without major changes. COX-2 levels slightly increased with oleic acid (1.468 ± 0.5032 RLU, at 0 mM for GFP+; 1.843 ± 0.4564 RLU, at 3 mM for GFP+; 1.694 ± 0.3649 RLU, at 0 mM for Glrx5+; 1.919 ± 0.4885 RLU, at 3 mM for Glrx5+, Figure 29A, no significance determined by one-way ANOVA). COX-6 A/B levels remained unchanged (2.142 ± 0.7201 RLU, at 0 mM for GFP+; 2.702 ± 1.161 RLU, at 3 mM for GFP+; 2.478 ± 0.8975 RLU, at 0 mM for Glrx5+; 2.564 ± 0.726 RLU, at 3 mM for Glrx5+, Figure 30A, no significance determined by one-way ANOVA).

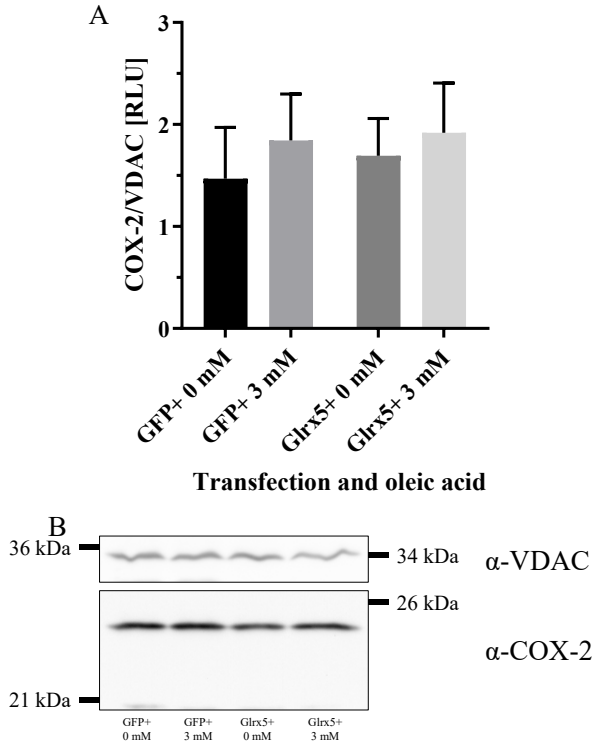

Figure 29: Detection of COX-2 in the organelles fraction of transfected MIN6 cells treated for 48 h with oleic acid via (A) quantification of immunoblotting signals (n = 4). (B) Representative image of one independent experiment of MIN6 cells used for analysis of Fe-S enzyme activities with 40 µg protein. VDAC was the reference protein. No significance by one-way ANOVA.

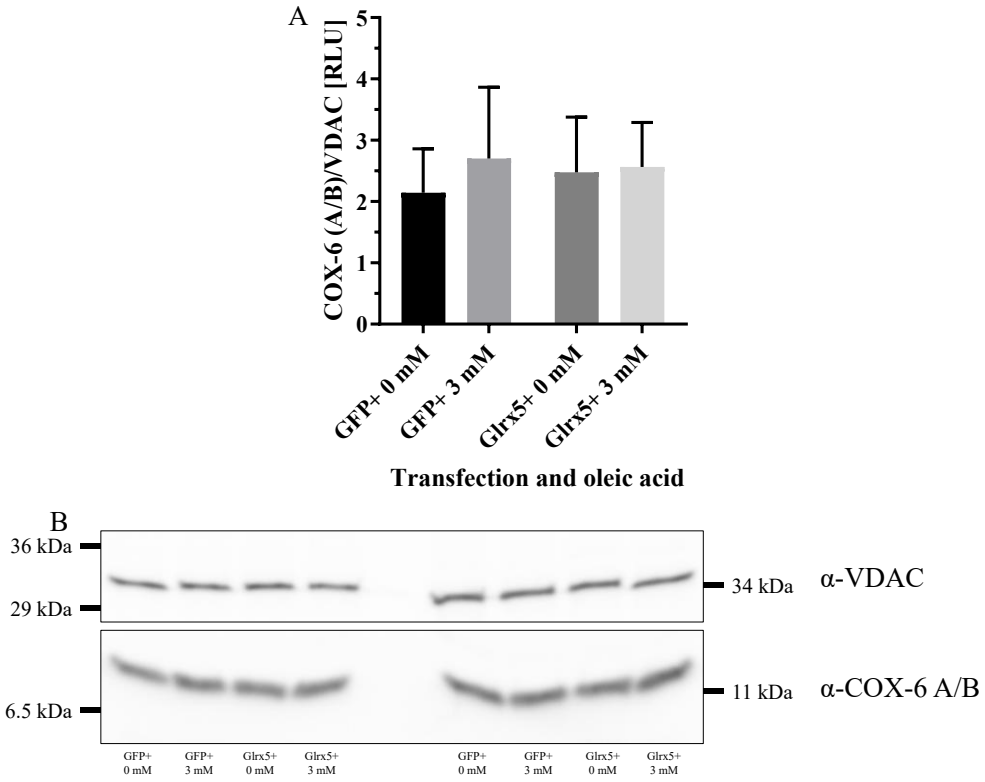

Figure 30: Detection of COX-6 A/B in the organelles fraction of transfected MIN6 cells treated for 48 h with oleic acid via (A) quantification of immunoblotting signals (n = 4). (B) Representative image of two independent experiments of MIN6 cells used for analysis of Fe-S enzyme activities analyzed by tricin SDS-PAGE with 20 µg protein. VDAC was the reference protein. No significance by one-way ANOVA.

Analysis of CS activity revealed a low activity in cytosolic fraction (9.484 ± 1.522 mU/mg, at 0 mM for GFP+; 17.63 ± 2.678 mU/mg, *** $p < 0.001$, at 3 mM for GFP+; 9.266 ± 0.7015 mU/mg, at 0 mM for Glrx5+; 15.32 ± 2.325 mU/mg, ** $p < 0.01$, at 3 mM for Glrx5+, Figure 31A, significances determined by one-way ANOVA compared to 0 mM), compared to high activity in organelles containing fraction (289.3 ± 37.52 mU/mg, at 0 mM for GFP+; 239.4 ± 20.12 mU/mg, at 3 mM for GFP+; 289.2 ± 62.57 mU/mg, at 0 mM for Glrx5+; 251.7 ± 8.814 mU/mg, at 3 mM for Glrx5+, Figure 31B, no significance determined by one-way ANOVA). Similar to the previous samples, oleic acid treatment resulted in increased activity in the cytosolic fraction and decreased activity in the organelles containing fraction.

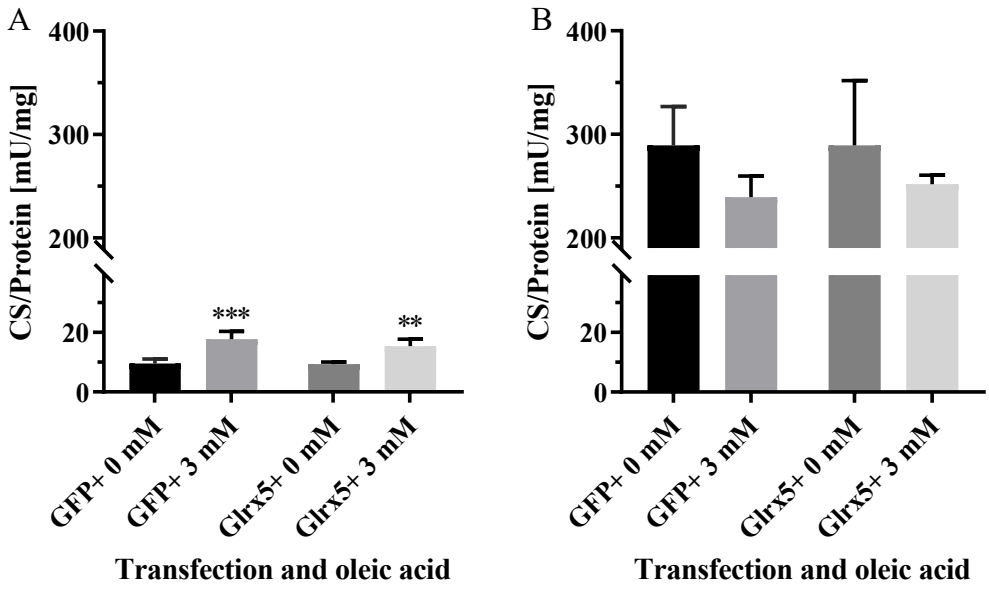

Figure 31: CS enzyme activities in (A) the cytosolic fraction, and (B) the organelles containing fraction of transfected MIN6 cells treated for 48 h with oleic acid (n = 4). ** $p < 0.01$, *** $p < 0.001$, significances by one-way ANOVA compared to 0 mM.

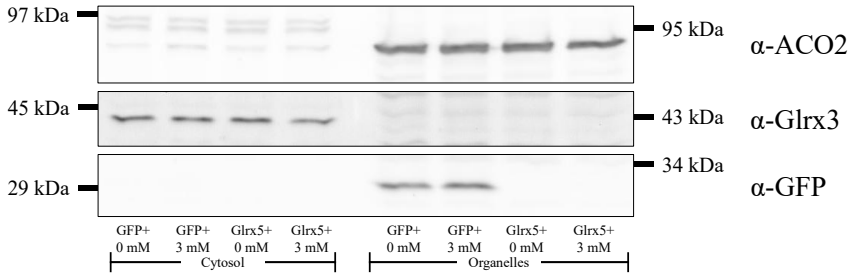

Figure 32: Distribution of ACO2, Glrx3, and GFP in the cytosolic (left) and organelles containing fractions (right) of transfected MIN6 cells treated for 48 h with oleic acid. Representative image of one independent experiment of MIN6 cells used for analysis of Fe-S enzyme activities with 40 µg protein. Detection of Glrx3 and GFP was enhanced by avidin biotin complex.

Immunoblotting confirmed the distribution of cytosolic and mitochondrial proteins, as well as GFP transfection. Strong signals for mitochondrial ACO2 and GFP (right) and cytosolic Glrx3 (left) were detected (Figure 32). Glrx5+ transfection was also confirmed and quantified. Glrx5+ cells exhibited higher Glrx5 signals compared to GFP+ cells (0.1239 ± 0.06159 RLU, at 0 mM for GFP+; 0.09436 ± 0.03881 RLU, at 3 mM for GFP+; 0.4756 ± 0.08245 RLU, *** $p < 0.001$, at 0 mM for Glrx5+; 0.4581 ± 0.1225 RLU,

*** $p < 0.001$, at 3 mM for Glrx5+, Figure 33A, significances determined by one-way ANOVA compared to GFP+). No differences in Glrx5 levels were observed between treatment groups.

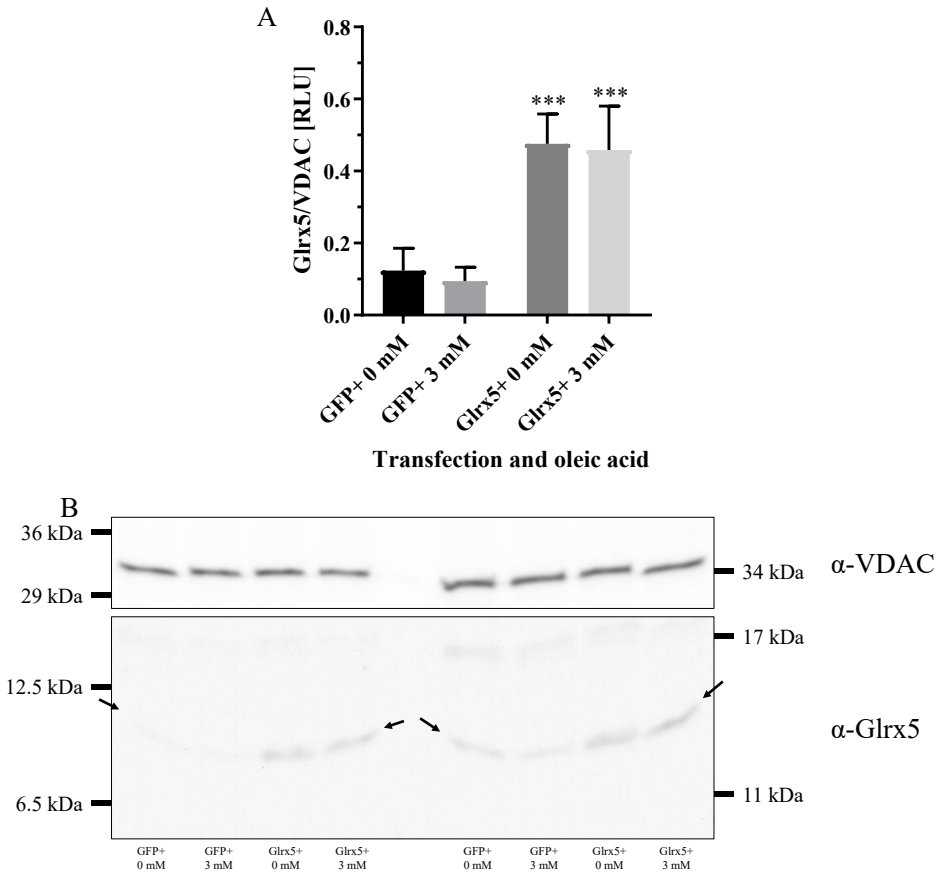

Figure 33: Detection of Glrx5 in the organelles fraction of transfected MIN6 cells treated for 48 h with oleic acid via (A) quantification of immunoblotting signals (n = 4). (B) Representative image of two independent experiments of MIN6 cells used for analysis of Fe-S enzyme activities analyzed by tricin SDS-PAGE with 20 µg protein. Detection of Glrx5 was enhanced by avidin biotin complex. VDAC was the reference protein. Significances by one-way ANOVA compared to GFP+.

3.4.7 Respirometry of wild type MIN6 cells is decreased after 5 d treatment with 0.75 mM oleic acid

The previously analyzed Fe-S proteins, SDH and COX, are involved in the mitochondrial respiratory chain. Therefore, the mitochondrial respiration of MIN6 cells treated for 5 d with 0.75 mM oleic acid was analyzed using high resolution respirometry. Following the titration protocol, no remarkable differences were observed in endogenous respiration (1525 ± 358.9 pmol/s*U_{CS} vs. 1379 ± 255.8 pmol/s*U_{CS}, no significance determined by

t-test, Figure 34A), permeabilized respiration (66.75 ± 45.96 pmol/s*U_{CS} vs. 20.73 ± 16.31 pmol/s*U_{CS}, * $p < 0.05$, significance determined by t-test, Figure 34B), leak 1 (246.1 ± 46.67 pmol/s*U_{CS} vs. 218.3 ± 37.53 pmol/s*U_{CS}, no significance determined by t-test, Figure 34C), or complex I (885.3 ± 245.3 pmol/s*U_{CS} vs. 890.7 ± 247.0 pmol/s*U_{CS}, no significance determined by t-test, Figure 34D). Upon titration of succinate, a decrease in respiration was observed in cells treated with oleic acid for OXPHOS (3643 ± 413.0 pmol/s*U_{CS} vs. 2712 ± 308.1 pmol/s*U_{CS}, **** $p < 0.0001$, significance determined by t-test, Figure 34E), ETS (3516 ± 366.7 pmol/s*U_{CS} vs. 2579 ± 273.4 pmol/s*U_{CS}, **** $p < 0.0001$, significance determined by t-test, Figure 34F), complex II (3073 ± 387.2 pmol/s*U_{CS} vs. 2003 ± 224.3 pmol/s*U_{CS}, **** $p < 0.0001$, significance determined by t-test, Figure 34G), leak 2 (1685 ± 306.6 pmol/s*U_{CS} vs. 1209 ± 201.8 pmol/s*U_{CS}, *** $p < 0.001$, significance determined by t-test, Figure 34H), and complex IV (2717 ± 434.9 pmol/s*U_{CS} vs. 1826 ± 268.3 pmol/s*U_{CS}, **** $p < 0.0001$, significance determined by t-test, Figure 34I).

In contrast to respirometry findings for complex I, immunoblotting of the complex I subunit NDUFB8 revealed decreased signals after 5 d of oleic acid treatment (1.014 ± 0.1046 RLU, with DMEM; 1.053 ± 0.08569 RLU, at 0 mM; 1.092± 0.05009 RLU, at 0.75 mM; 0.6583 ± 0.02754 RLU, *** $p < 0.001$, at 1.5 mM; 0.7234 ± 0.01586 RLU, *** $p < 0.001$, at 3 mM, Figure 35, significances determined by one-way ANOVA compared to 0 mM).

3.4.8 Respirometry of transfected MIN6 cells is decreased after 48 h treatment with 3 mM oleic acid

To further investigate the effects on Fe-S cluster containing respiratory chain complexes, transfected MIN6 cells were treated with oleic acid for 48 h. The cell count at the end of the experiment was determined. Consistent with observations from 1.5 mM treatment in transfected ELISA samples (Figure 10), no changes in cell amount were noted after 48 h of treatment with 3 mM (1.709 ± 0.3581 *10^6, at 0 mM for GFP+; 1.625 ± 0.5417 *10^6, at 3 mM for GFP+; 1.784 ± 0.5016 *10^6, at 0 mM for Glrx5+; 1.638 ± 0.505 *10^6, at 3 mM for Glrx5+, Figure 36, no significance determined by one-way ANOVA). Like ELISA samples, the MIN6 cells used for respirometry were cultured in T25 flasks.

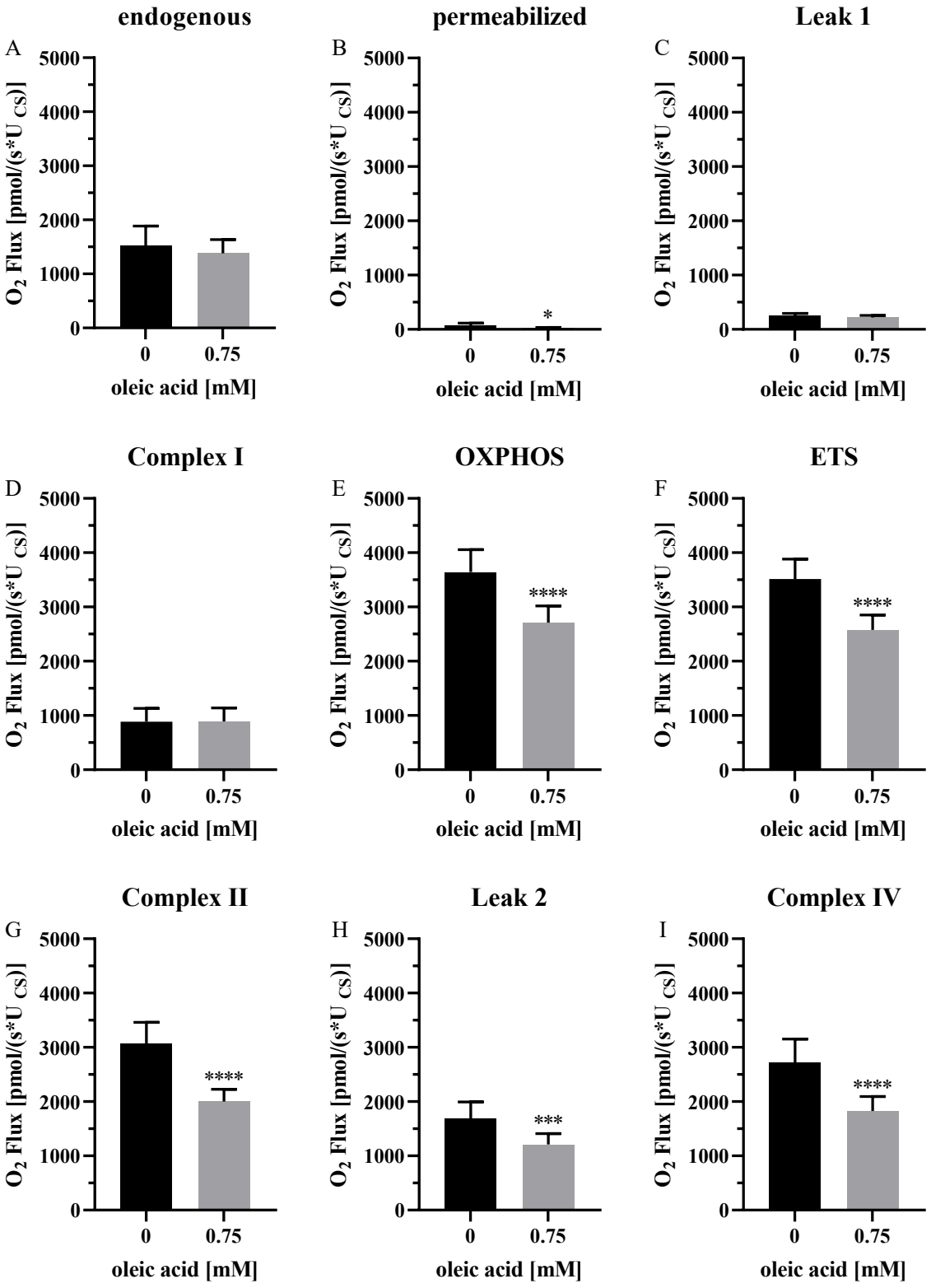

Figure 34: Respirometry analysis of wild type MIN6 cells treated for 5 d with 0.75 mM oleic acid. (A) endogenous respiration (n = 11-12), (B) permeabilized respiration (n = 6-8), (C) leak 1 (n = 11-12), (D) complex I (n = 11-12), (E) OXPHOS (n = 11-12), (F) ETS (n = 11-12), (G) complex II (n = 11-12), (H) leak 2 (n = 11-12), and (I) complex IV (n = 11-12). * $p < 0.05$, *** $p < 0.001$, **** $p < 0.0001$, significances determined by t-test.

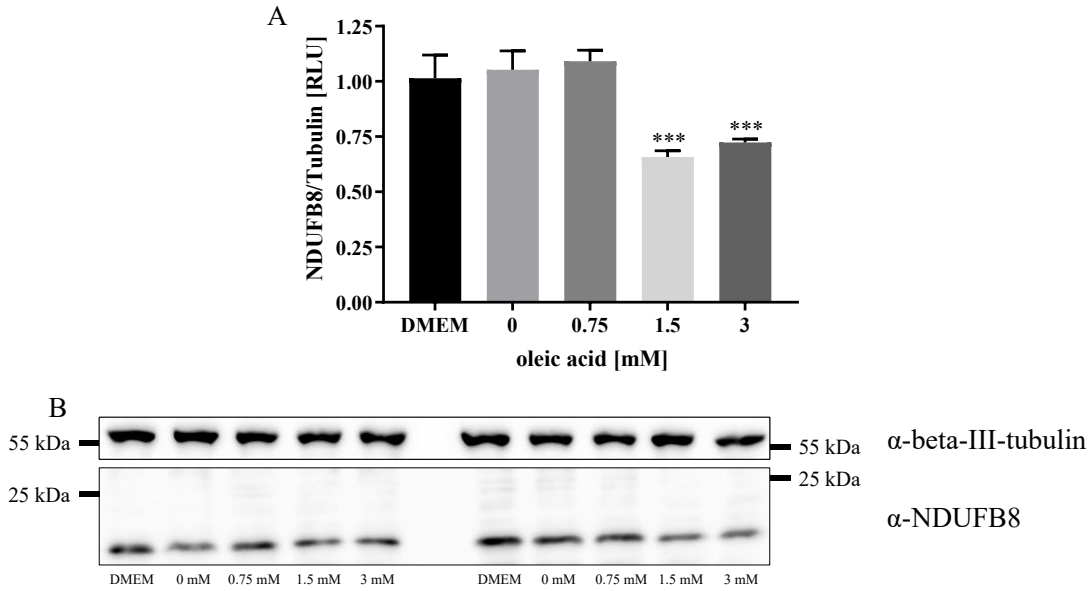

Figure 35: Detection of the complex I subunit NDUFB8 in total lysates of wild type MIN6 cells treated for 5 d with oleic acid via (A) quantification of immunoblotting signals (n = 3). (B) Representative image of two independent experiments with 15 µg protein. Tubulin was the reference protein. *** $p < 0.001$, significances by one-way ANOVA compared to 0 mM.

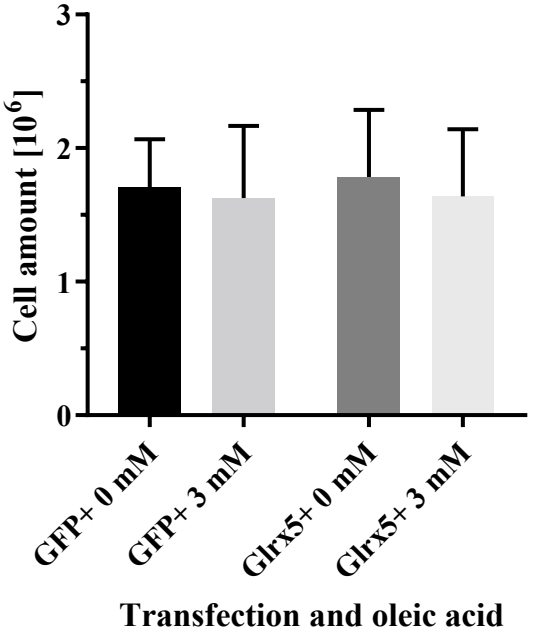

Figure 36: Cell counts of transfected MIN6 cells collected with trypsin/EDTA prior to sample preparation for respirometry (n = 8). Cells were transfected and subsequently treated for 48 h with oleic acid in a T25 flask. No significance by one-way ANOVA.

Endogenous respiration (1443 ± 252.2 pmol/s*U_{CS}, at 0 mM for GFP+; 1416 ± 249.9 pmol/s*U_{CS}, at 3 mM for GFP+; 1516 ± 360.4 pmol/s*U_{CS}, at 0 mM for Glrx5+; 1548 ± 322.7 pmol/s*U_{CS}, at 3 mM for Glrx5+, Figure 37A, no significance determined by one-way ANOVA), and permeabilized respiration (143.7 ± 90.38 pmol/s*U_{CS}, at 0 mM for GFP+; 74.67 ± 42.95 pmol/s*U_{CS}, at 3 mM for GFP+; 69.01 ± 19.41 pmol/s*U_{CS}, at 0 mM for Glrx5+; 33.29 ± 5.66 pmol/s*U_{CS}, at 3 mM for Glrx5+, Figure 37B, no significance determined by one-way ANOVA) were unaffected by transfection and treatment. Small changes in leak 1 were observed (567.5 ± 180.4 pmol/s*U_{CS}, at 0 mM for GFP+; 318.4 ± 135.9 pmol/s*U_{CS}, at 3 mM for GFP+; 475.3 ± 200.0 pmol/s*U_{CS}, at 0 mM for Glrx5+; 291.1 ± 185.0 pmol/s*U_{CS}, at 3 mM for Glrx5+, Figure 37C, no significance determined by one-way ANOVA). Starting with ADP titration, a decrease in respiration was observed throughout the measurement by oleic acid treatment for complex I (792.5 ± 234.0 pmol/s*U_{CS}, at 0 mM for GFP+; 321.3 ± 198.1 pmol/s*U_{CS}, * $p < 0.05$, at 3 mM for GFP+; 748.3 ± 386.6 pmol/s*U_{CS}, at 0 mM for Glrx5+; 261.5 ± 235.7 pmol/s*U_{CS}, * $p < 0.05$, at 3 mM for Glrx5+, Figure 37D, significances determined by one-way ANOVA compared to 0 mM), OXPHOS (2578 ± 657.8 pmol/s*U_{CS}, at 0 mM for GFP+; 1072 ± 326.2 pmol/s*U_{CS}, ** $p < 0.01$, at 3 mM for GFP+; 2700 ± 961.8 pmol/s*U_{CS}, at 0 mM for Glrx5+; 1051 ± 584.6 pmol/s*U_{CS}, *** $p < 0.001$, at 3 mM for Glrx5+, Figure 37E, significances determined by one-way ANOVA compared to 0 mM), ETS (2890 ± 968.7 pmol/s*U_{CS}, at 0 mM for GFP+; 1268 ± 630.3 pmol/s*U_{CS}, ** $p < 0.01$, at 3 mM for GFP+; 3106 ± 1124 pmol/s*U_{CS}, at 0 mM for Glrx5+; 1214 ± 578.5 pmol/s*U_{CS}, *** $p < 0.001$, at 3 mM for Glrx5+, Figure 37F, significances determined by one-way ANOVA compared to 0 mM), complex II (1900 ± 739.1 pmol/s*U_{CS}, at 0 mM for GFP+; 799.9 ± 357.3 pmol/s*U_{CS}, ** $p < 0.01$, at 3 mM for GFP+; 2104 ± 656.7 pmol/s*U_{CS}, at 0 mM for Glrx5+; 813.3 ± 383.2 pmol/s*U_{CS}, *** $p < 0.001$, at 3 mM for Glrx5+, Figure 37G, significances determined by one-way ANOVA compared to 0 mM), leak 2 (1942 ± 695.9 pmol/s*U_{CS}, at 0 mM for GFP+; 745.8 ± 373.0 pmol/s*U_{CS}, ** $p < 0.01$, at 3 mM for GFP+; 2084 ± 635.2 pmol/s*U_{CS}, at 0 mM for Glrx5+; 824.5 ± 389.6 pmol/s*U_{CS}, *** $p < 0.001$, at 3 mM for Glrx5+, Figure 37H, significances determined by one-way ANOVA compared to 0 mM), and complex IV (4038 ± 931.1 pmol/s*U_{CS}, at 0 mM for GFP+; 2013 ± 548.4 pmol/s*U_{CS}, *** $p < 0.001$, at 3 mM for GFP+; 3836 ± 825.4 pmol/s*U_{CS}, at 0 mM for Glrx5+; 1979 ± 531.4 pmol/s*U_{CS}, **** $p < 0.0001$, at 3 mM for Glrx5+, Figure 37I, significances determined by one-way ANOVA compared to 0 mM).

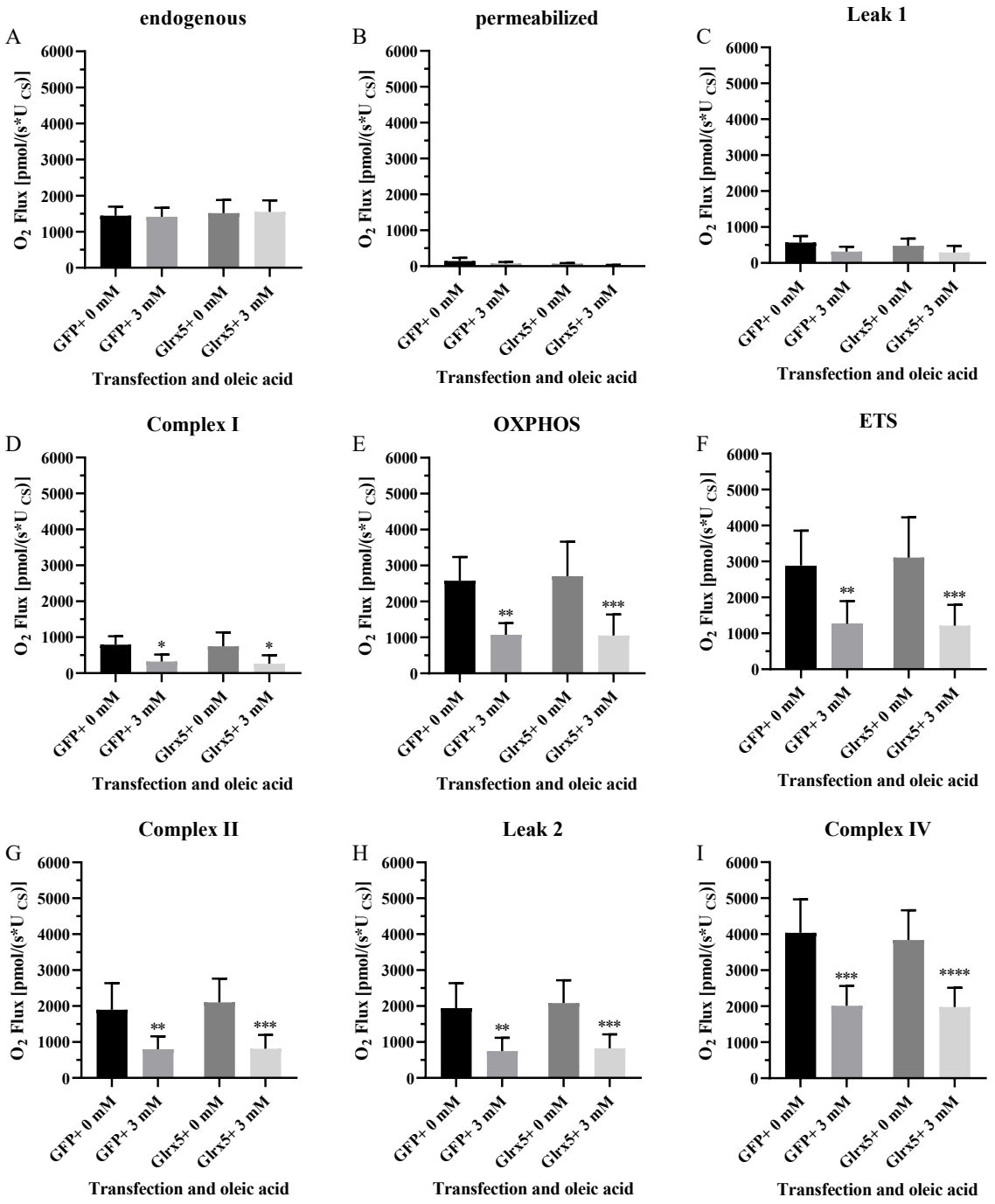

Figure 37: Respirometry analysis of transfected MIN6 cells treated for 48 h with 3 mM oleic acid. (A) endogenous respiration (n = 8), (B) permeabilized respiration (n = 3-6), (C) leak 1 (n = 6-8), (D) complex I (n = 6-8), (E) OXPHOS (n = 7-8), (F) ETS (n = 7-8), (G) complex II (n = 7-8), (H) leak 2 (n = 7-8), and (I) complex IV (n = 7-8). * $p < 0.05$, ** $p < 0.01$, *** $p < 0.001$, **** $p < 0.0001$, significances by one-way ANOVA compared to 0 mM.

3.4.9 Cellular ATP levels are elevated in both the wild type and transfected MIN6 cells after oleic acid treatment

As mitochondrial respiration is the primary source of biochemical energy, ATP levels in wild type MIN6 cells were measured after 5 d of treatment with oleic acid. All oleic acid concentrations resulted in higher ATP levels (63.93 ± 13.86 % vs. 100 ± 33.2 %, ** $p < 0.01$, at 0.75 mM, Figure 38A; 51.85 ± 18.45 % vs. 100 ± 19.22 %, **** $p < 0.0001$, at 1.5 mM, Figure 38B; 48.5 ± 11.23 % vs. 100 ± 15.81 %, **** $p < 0.0001$, at 3 mM, Figure 38C, significances determined by t-test to the respective control group). The magnitude of differences compared to the control group increased with higher oleic acid concentrations (-36.1 % at 0.75 mM, -48.2 % at 1.5 mM, -51.5 % at 3 mM).

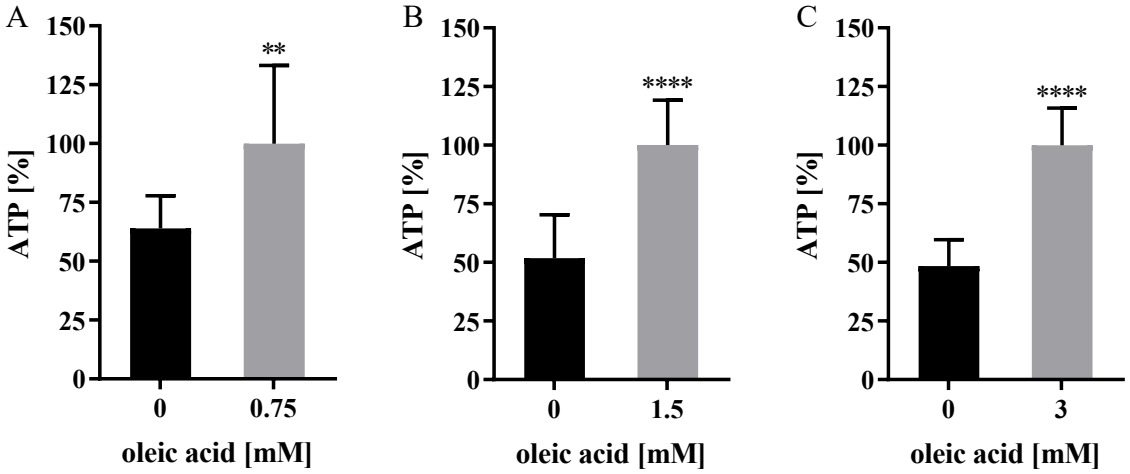

Figure 38: ATP levels in MIN6 cells treated for 5 d with (A) 0.75 mM, (B) 1.5 mM, and (C) 3 mM oleic acid and their respective controls (n = 12). ** $p < 0.01$, **** $p < 0.0001$, significances determined by t-test.

To assess the effect of treatment duration, ATP levels were measured in wild type MIN6 cells at 24 h intervals up to 96 h. Elevated ATP levels were observed at all time points compared to the control group. ATP levels were higher after 24 h (69.17 ± 17.84 % vs. 100 ± 19.72 %, * $p < 0.05$, at 0.75 mM; 54.55 ± 19.32 % vs. 100 ± 20.52 %, ** $p < 0.01$, at 1.5 mM; 43.47 ± 12.76 % vs. 100 ± 32.52 %, ** $p < 0.01$, at 3 mM, Figure 39A, significances determined by t-test to the respective control group), 48 h (84.35 ± 28.08 % vs. 100 ± 29.64 %, at 0.75 mM; 57.99 ± 24.23 % vs. 100 ± 24.57 %, * $p < 0.05$, at 1.5 mM; 61.35 ± 18.63 % vs. 100 ± 40.71 %, at 3 mM, Figure 39B, significance determined by t-test to the respective control group), 72 h (79.01 ± 27.08 % vs. 100 ± 45.66 %, at

0.75 mM; 59.59 ± 40.39 % vs. 100 ± 62.45 %, at 1.5 mM; 54.33 ± 21.81 % vs. 100 ± 54.95 %, at 3 mM, Figure 39C, no significance determined by t-test to the respective control group), and 96 h (77.12 ± 23.94 % vs. 100 ± 30.72 %, at 0.75 mM; 64.16 ± 19.12 % vs. 100 ± 47.73 %, at 1.5 mM; 63.38 ± 24.72 % vs. 100 ± 54.41 %, at 3 mM, Figure 39D, no significance determined by t-test to the respective control group). Like observed in Figure 38, greater differences between treatment group and control group were observed with increased oleic acid concentration.

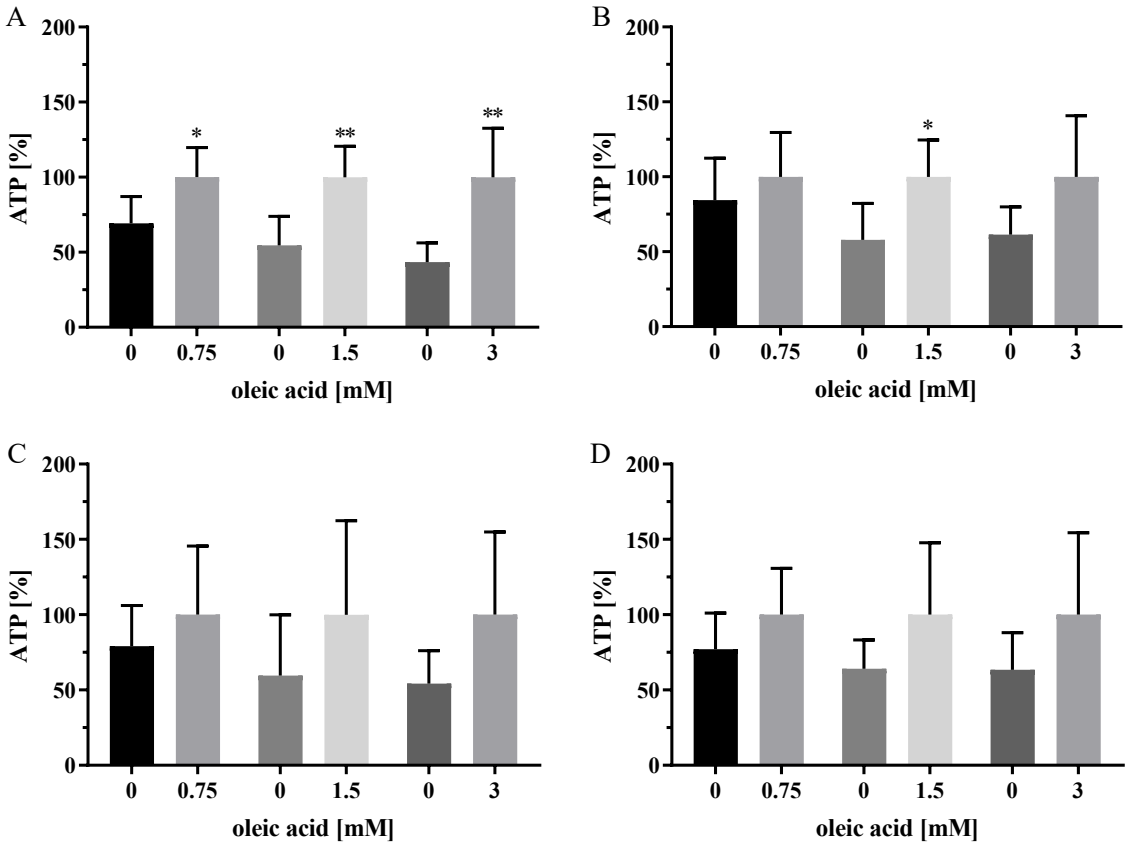

Figure 39: ATP levels of MIN6 cells measured at 24 h intervals after (A) 24 h, (B) 48 h, (C) 72 h, or (D) 96 h treatment with 0.75 mM, 1.5 mM, and 3 mM oleic acid and their respective control groups (n = 6). * $p < 0.05$, ** $p < 0.01$, comparison of treatment to respective control group by t-test.

Consistent with wild type cells, the treatment of transfected cells revealed higher ATP levels with oleic acid treatment (2.358 ± 0.509 µM, at 0 mM for GFP+; 3.767 ± 0.9429 µM, * $p < 0.05$, at 1.5 mM for GFP+; 2.209 ± 0.5071 µM, at 0 mM for Glrx5+; 3.795 ± 0.8329 µM, * $p < 0.05$, at 1.5 mM for Glrx5+, Figure 40, significances determined by one-way ANOVA compared to 0 mM). There was no difference between the transfection groups.

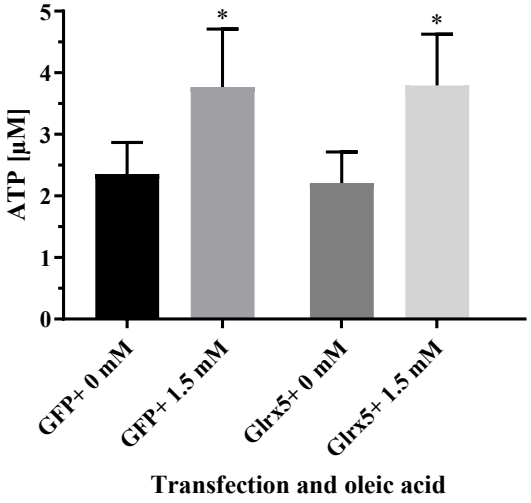

Figure 40: ATP levels in transfected MIN6 cells treated for 48 h with 1.5 mM oleic acid (n = 5). * $p < 0.05$, significances by one-way ANOVA compared to 0 mM.

3.4.10 ATP levels in EndoC-βH3 cells are higher by oleic acid

ATP levels were measured in EndoC-βH3 cells after 48 h of oleic acid treatment. Similar to murine MIN6 cells, oleic acid increased ATP levels (60.49 ± 16.97 % vs. 100 ± 25.49 %, * $p < 0.05$, at 0.75 mM, Figure 41A; 55.27 ± 10.34 % vs. 100 ± 25.47 %, ** $p < 0.01$, at 1.5 mM, Figure 41B; 39.16 ± 11.43 % vs. 100 ± 19.48 %, **** $p < 0.0001$, at 3 mM, Figure 41C, significances determined by t-test to the respective control group). The differences between treatment and control groups became more pronounced with increased oleic acid concentrations.

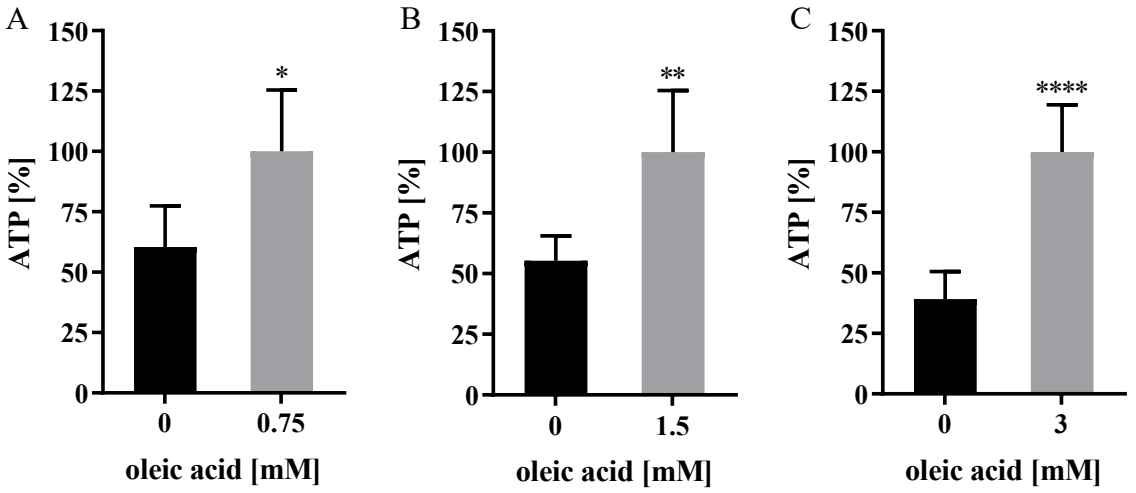

Figure 41: ATP levels in EndoC-βH3 cells treated for 48 h with (A) 0.75 mM, (B) 1.5 mM, and (C) 3 mM oleic acid and their respective controls (n = 6). * $p < 0.05$, ** $p < 0.01$, **** $p < 0.0001$, significances determined by t-test.

3.4.11 Immunosignals of complex III core protein 2 and Rieske remain unchanged after oleic acid treatment

In addition to mitochondrial Fe-S cluster proteins, immunoblotting was conducted to evaluate signals for complex III subunit core protein 2 (UQCRC2), which was not directly assessed by enzyme activity or respirometry. In wild type MIN6 cells, oleic acid treatment

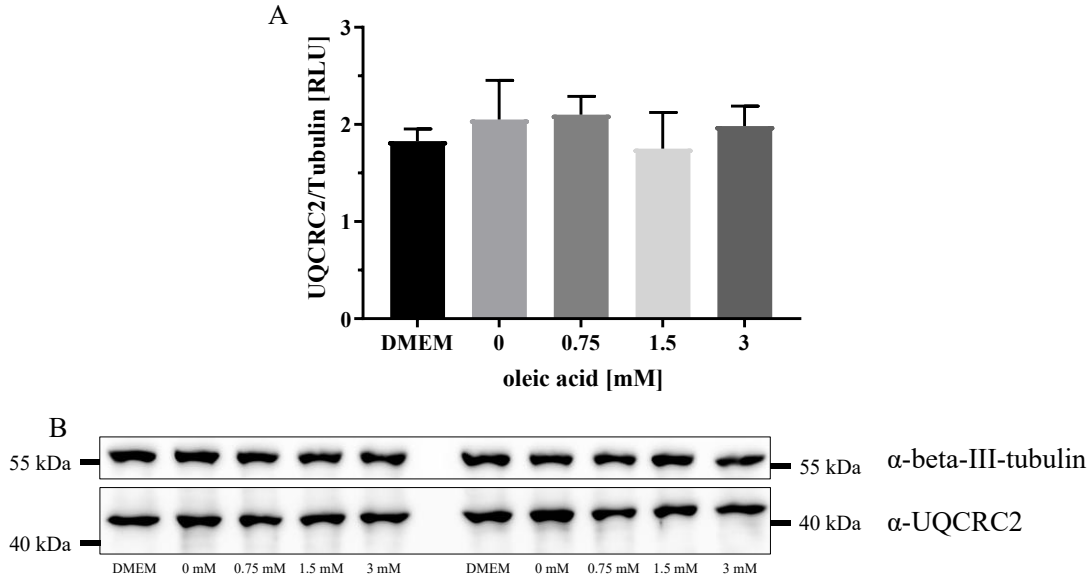

Figure 42: Detection of UQCRC2 in total lysate of wild type MIN6 cells treated for 5 d with oleic acid via (A) quantification of immunoblotting signals (n = 4). (B) Representative image of two independent experiments with 15 µg protein. Tubulin was the reference protein. No significance by one-way ANOVA.

did not alter UQCRC2 (1.828 ± 0.1262 RLU, with DMEM; 2.05 ± 0.4047 RLU, at 0 mM; 2.1 ± 0.1887 RLU, at 0.75 mM; 1.752 ± 0.3718 RLU, at 1.5 mM; 1.984 ± 0.2039 RLU, at 3 mM, Figure 42A, no significance determined by one-way ANOVA), which was consistent with transfected MIN6 cells after 48 h of treatment (4.564 ± 1.98 RLU, at 0 mM for GFP+; 4.677 ± 2.524 RLU, at 3 mM for GFP+; 4.475 ± 1.938 RLU, at 0 mM for Glrx5+; 5.771 ± 2.148 RLU, at 3 mM for Glrx5+, Figure 43A, no significance determined by one-way ANOVA).

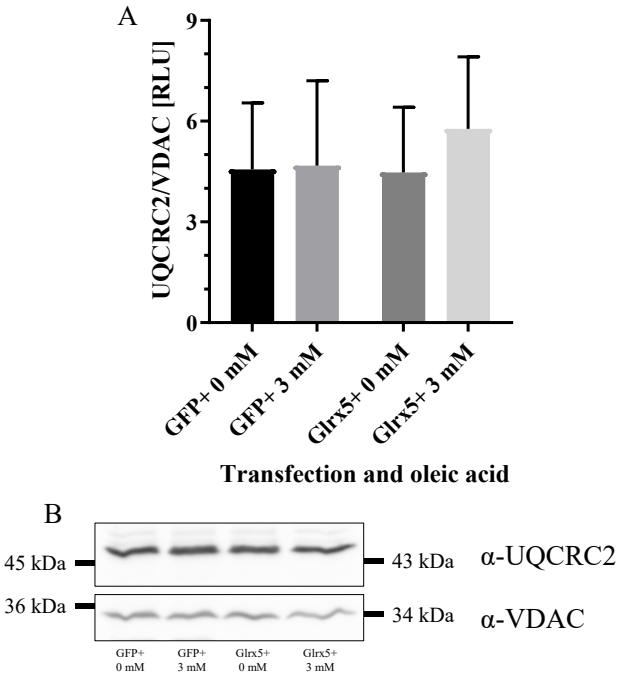

Figure 43: Detection of UQCRC2 in organelles of transfected MIN6 cells treated for 48 h with oleic acid via (A) quantification of immunoblotting signals (n = 4). (B) Representative image of one independent experiment of MIN6 cells used for analysis of Fe-S enzyme activities with 40 µg protein. VDAC was the reference protein. No significance by one-way ANOVA.

Also, UQCRFS1 signals were unaffected via oleic acid in the transfection model (0.8775 ± 0.2691 RLU, at 0 mM for GFP+; 1.001 ± 0.1468 RLU, at 3 mM for GFP+; 0.9736 ± 0.1118 RLU, at 0 mM for Glrx5+; 0.86 ± 0.1916 RLU, at 3 mM for Glrx5+, Figure 44A, no significance determined by one-way ANOVA).

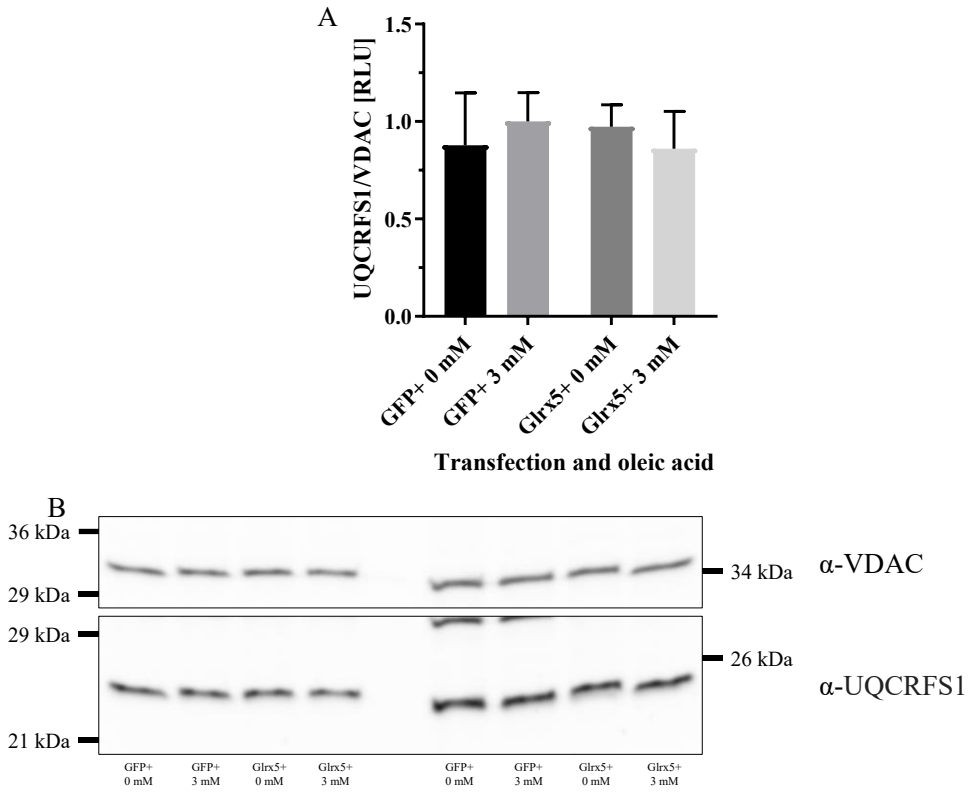

Figure 44: Detection of UQCRFS1 in organelles of transfected MIN6 cells treated for 48 h with oleic acid via (A) quantification of immunoblotting signals (n = 4). (B) Representative image of two independent experiments of MIN6 cells used for analysis of Fe-S enzyme activities analyzed by tricin SDS-PAGE with 20 µg protein. VDAC was the reference protein. No significance by one-way ANOVA.

3.4.12 Oleic acid treatment affects outer mitochondrial proteins PolD1, GPAT, and Glrx3

Given the observed change in Glrx5 ELISA level and the impaired ACO1 activity, additional outer mitochondrial Fe-S cluster proteins were analyzed via immunoblotting. Initial analyses revealed weaker signals for PolD1 with oleic acid treatment of wild type cells, while densitometry analysis was not differing between the groups (0.2443 ± 0.1237 RLU, with DMEM; 0.2757 ± 0.1194 RLU, at 0 mM; 0.2399 ± 0.1134 RLU, at 0.75 mM; 0.2211 ± 0.03761 RLU, at 1.5 mM; 0.2186 ± 0.06698 RLU, at 3 mM, Figure 45A, no significance determined by one-way ANOVA).

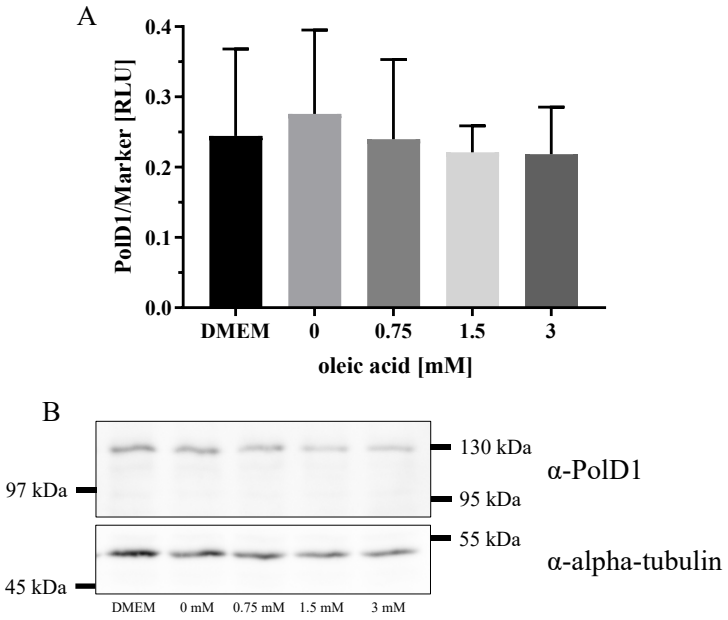

Figure 45: Detection of PolD1 in cytosol of wild type MIN6 cells treated for 5 d with oleic acid via (A) quantification of immunoblotting signals (n = 3). (B) Representative image of one independent experiment of MIN6 cells used for analysis of Fe-S enzyme activities with 40 µg protein. Tubulin was the reference protein. No significance by one-way ANOVA.

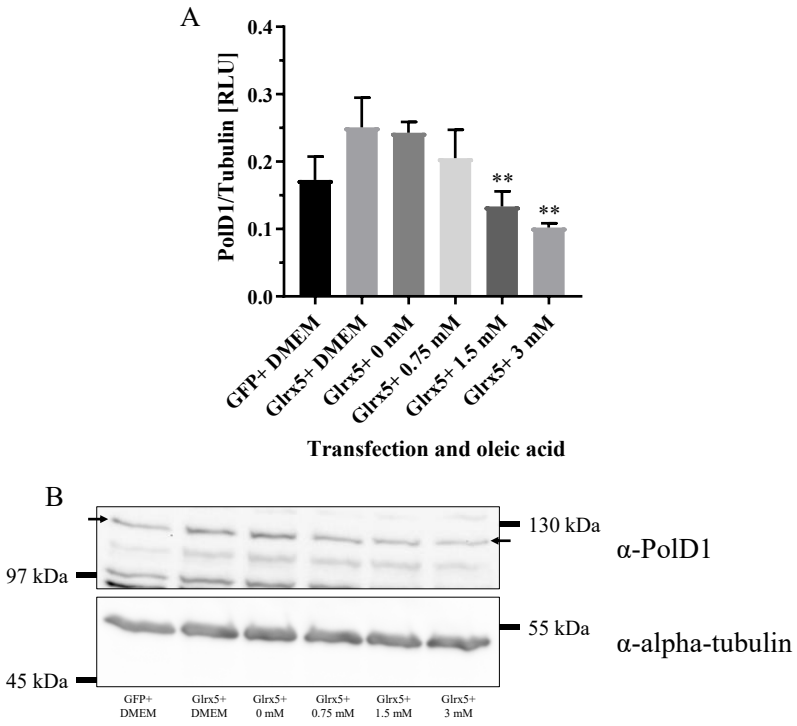

Figure 46: Detection of PolD1 in the cytosol of transfected MIN6 cells treated for 5 d with oleic acid via by (A) quantification of immunoblotting signals (n = 3). (B) Representative image of one independent experiment of MIN6 cells used for analysis of Fe-S enzyme activities with 40 µg protein. Tubulin was the reference protein. ** $p < 0.01$, significances by one-way ANOVA compared to Glrx5+ 0 mM.

In transfected MIN6 cells, Glrx5+ transfection initially showed a trend toward increased PolD1 signal compared to GFP+ transfection, though this increase was not statistically significant. Additionally, oleic acid treatment resulted in a notable decrease in PolD1 signal at higher concentrations (0.1729 ± 0.03462 RLU, with DMEM for GFP+; 0.2509 ± 0.04394 RLU, with DMEM for Glrx5+; 0.243 ± 0.01572 RLU, at 0 mM for Glrx5+; 0.205 ± 0.04226 RLU, at 0.75 mM for Glrx5+; 0.1335 ± 0.02242 RLU, ** $p < 0.01$, at 1.5 mM for Glrx5+; 0.1022 ± 0.006328 RLU, ** $p < 0.01$, at 3 mM for Glrx5+, Figure 46A, significances determined by one-way ANOVA compared to Glrx5+ 0 mM). These findings were further validated in experiments using the respective GFP+ control transfection. Treatment with 3 mM oleic acid for 48 h decreased PolD1 immunoblotting signals, regardless of the transfection group (0.3018 ± 0.06914 RLU, at 0 mM for GFP+; 0.1708 ± 0.0428 RLU, * $p < 0.05$, at 3 mM for GFP+; 0.3196 ± 0.05798 RLU, at 0 mM for Glrx5+; 0.1711 ± 0.07277 RLU, * $p < 0.05$, at 3 mM for Glrx5+, Figure 47A, significances determined by one-way ANOVA compared to 0 mM).

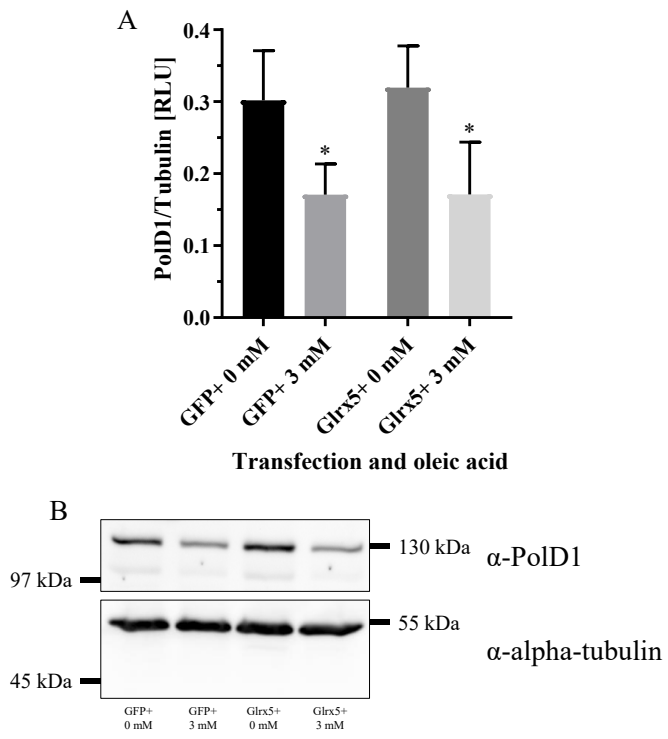

Figure 47: Detection of PolD1 in the cytosol of transfected MIN6 cells treated for 5 d with oleic acid via (A) quantification of immunoblotting signals (n = 4). (B) Representative image of one independent experiment of MIN6 cells used for analysis of Fe-S enzyme activities with 40 µg protein. Tubulin was the reference protein. * $p < 0.05$, significances by one-way ANOVA compared to 0 mM.

Immunoblotting of GPAT resulted in a dose-dependent decrease in signal intensity with increased oleic acid concentrations in wild type MIN6 cells (1.179 ± 0.0697 RLU, with DMEM; 1.277 ± 0.09513 RLU, at 0 mM; 1.171 ± 0.141 RLU, at 0.75 mM; 1.023 ± 0.2142 RLU, at 1.5 mM; 0.7905 ± 0.1208 RLU, ** $p < 0.01$, at 3 mM, Figure 48A, significance determined by one-way ANOVA compared to 0 mM). In transfected MIN6 cells, GPAT signals also decreased with oleic acid treatment, though this was not significant (0.9195 ± 0.1109 RLU, with DMEM for GFP+; 0.7736 ± 0.1389 RLU, with DMEM for Glrx5+; 0.7804 ± 0.08089 RLU, at 0 mM for Glrx5+; 0.7819 ± 0.1284 RLU, at 0.75 mM for Glrx5+; 0.601 ± 0.1267 RLU, at 1.5 mM for Glrx5+; 0.5718 ± 0.04415 RLU, at 3 mM for Glrx5+, Figure 49A, no significance determined by one-way ANOVA).

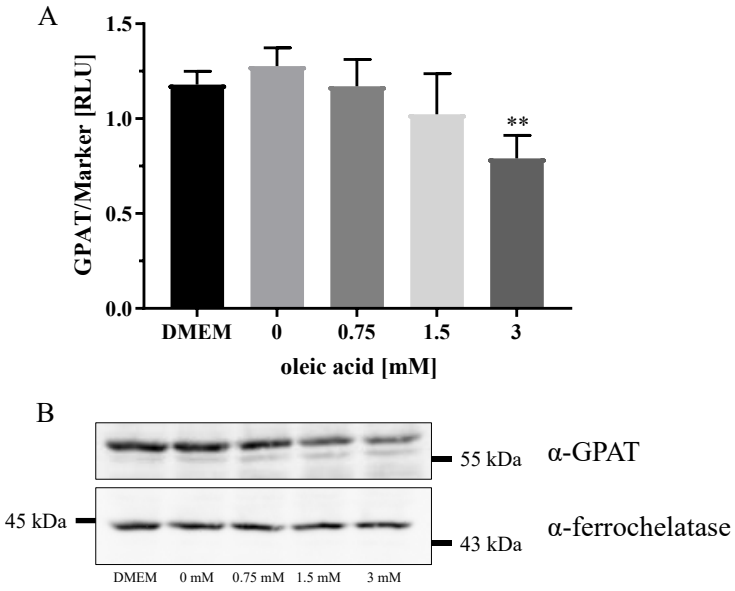

Figure 48: Detection of GPAT in the cytosol of wild type MIN6 cells treated for 5 d with oleic acid via (A) quantification of immunoblotting signals (n = 3). (B) Representative image of one independent experiment of MIN6 cells used for analysis of Fe-S enzyme activities with 40 µg protein. Ferrochelatase was the reference protein. ** $p < 0.01$, significance by one-way ANOVA compared to 0 mM.

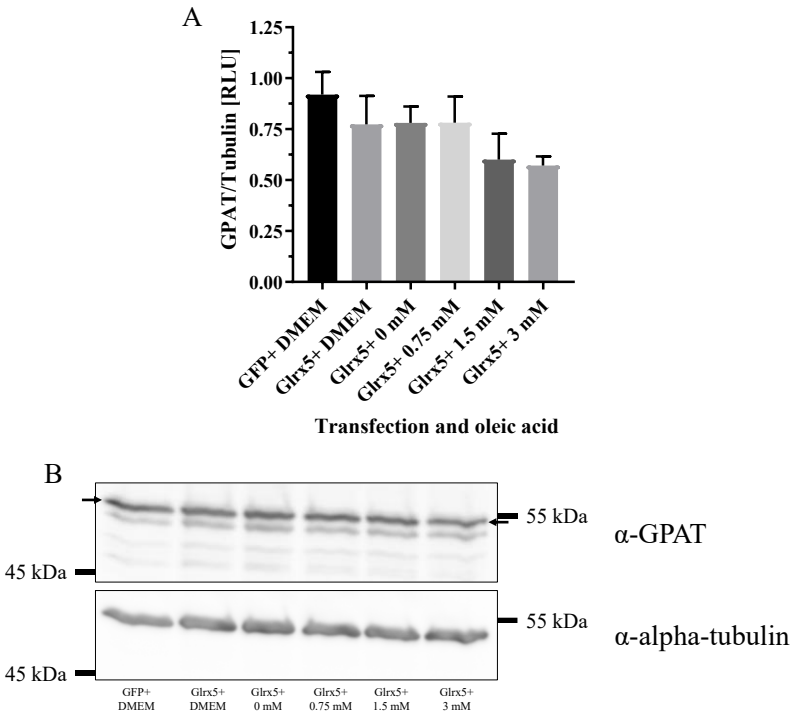

Figure 49: Detection of GPAT in the cytosol of transfected MIN6 cells treated for 48 h with oleic acid via (A) quantification of immunoblotting signals (n = 3). (B) Representative image of one independent experiment of MIN6 cells used for analysis of Fe-S enzyme activities with 40 µg protein. Tubulin was the reference protein. No significance by one-way ANOVA.

Further analysis of respective GFP+ controls revealed no clear changes in GPAT signals after 48 h of treatment (2.979 ± 1.952 RLU, at 0 mM for GFP+; 2.334 ± 1.788 RLU, at 3 mM for GFP+; 2.614 ± 1.87 RLU, at 0 mM for Glrx5+; 2.42 ± 1.36 RLU, at 3 mM for Glrx5+, Figure 50A, no significance determined by one-way ANOVA). These results did not confirm the decreases indicated in earlier experiments, leaving the effect of oleic acid on GPAT unclear.

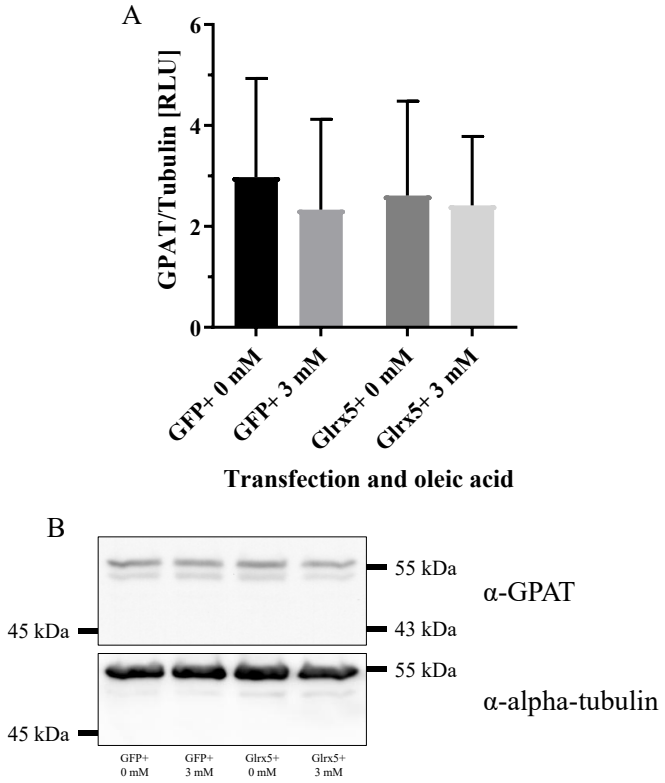

Figure 50: Detection of GPAT in the cytosol of transfected MIN6 cells treated for 48 h with oleic acid via (A) quantification of immunoblotting signals (n = 4). (B) Representative image of one independent experiment of MIN6 cells used for analysis of Fe-S enzyme activities with 40 µg protein. Tubulin was the reference protein. No significance by one-way ANOVA.

Cytosolic Glrx3 analysis revealed an effect of oleic acid treatment in transfected MIN6 cells (0.292 ± 0.05408 RLU, at 0 mM for GFP+; 0.244 ± 0.04545 RLU, at 3 mM for GFP+; 0.383 ± 0.08244 RLU, at 0 mM for Glrx5+; 0.2413 ± 0.06458 RLU, * $p < 0.05$, at 3 mM for Glrx5+, Figure 51A, significance determined by one-way ANOVA compared to Glrx5+ 0 mM). Immunoblotting images indicated a clear decrease in Glrx3 levels with 3 mM oleic acid treatment. Additionally, Glrx5+ transfection appeared to enhance Glrx3 protein levels compared to GFP+ transfection. The connection between Glrx5+ transfection and Glrx3 protein level remains uncertain.

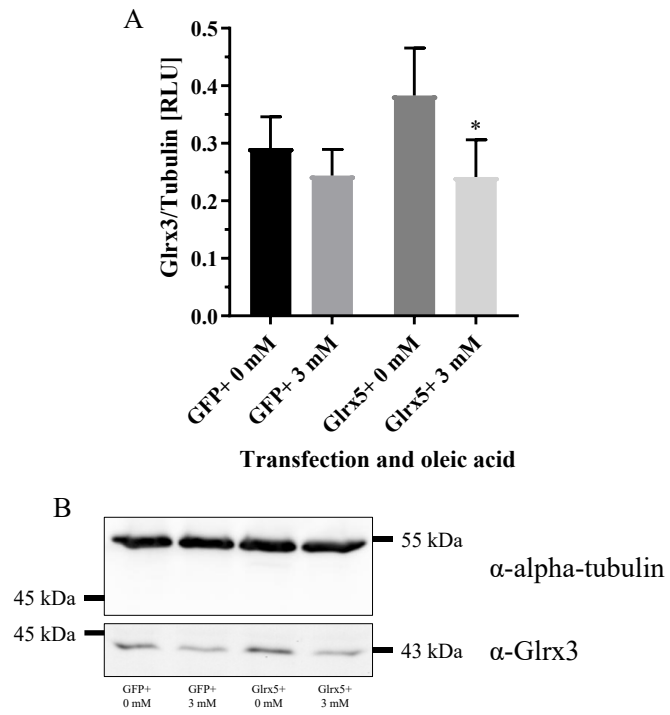

Figure 51: Detection of Glrx3 in the cytosol of transfected MIN6 cells treated for 48 h with oleic acid via (A) quantification of immunoblotting signals (n = 4). (B) Representative image of one independent experiment of MIN6 cells used for analysis of Fe-S enzyme activities with 40 µg protein. Detection of Glrx3 was enhanced by avidin biotin complex. Tubulin was the reference protein. * $p < 0.05$, significance by one-way ANOVA compared to Glrx5+ 0 mM.

3.4.13 Ferritin light chain levels decrease after oleic acid treatment, while GPx4 levels remain unchanged

Based on the results of decreased Glrx5 protein and ACO1 activity, further proteins associated with iron regulation and ferroptosis were analyzed. Immunoblotting consistently showed a significant increase in FTL signal in the 0 mM control group compared to the DMEM group. Oleic acid treatment decreased FTL levels relative to the 0 mM group in a dose-dependent manner (0.3075 ± 0.08793 RLU, with DMEM; 0.6627 ± 0.2497 RLU, at 0 mM; 0.2969 ± 0.1146 RLU, * $p < 0.05$, at 0.75 mM; 0.1849 ± 0.05363 RLU, ** $p < 0.01$, at 1.5 mM; 0.1247 ± 0.07376 RLU, *** $p < 0.001$, at 3 mM, Figure 52A, significances determined by one-way ANOVA compared to 0 mM).

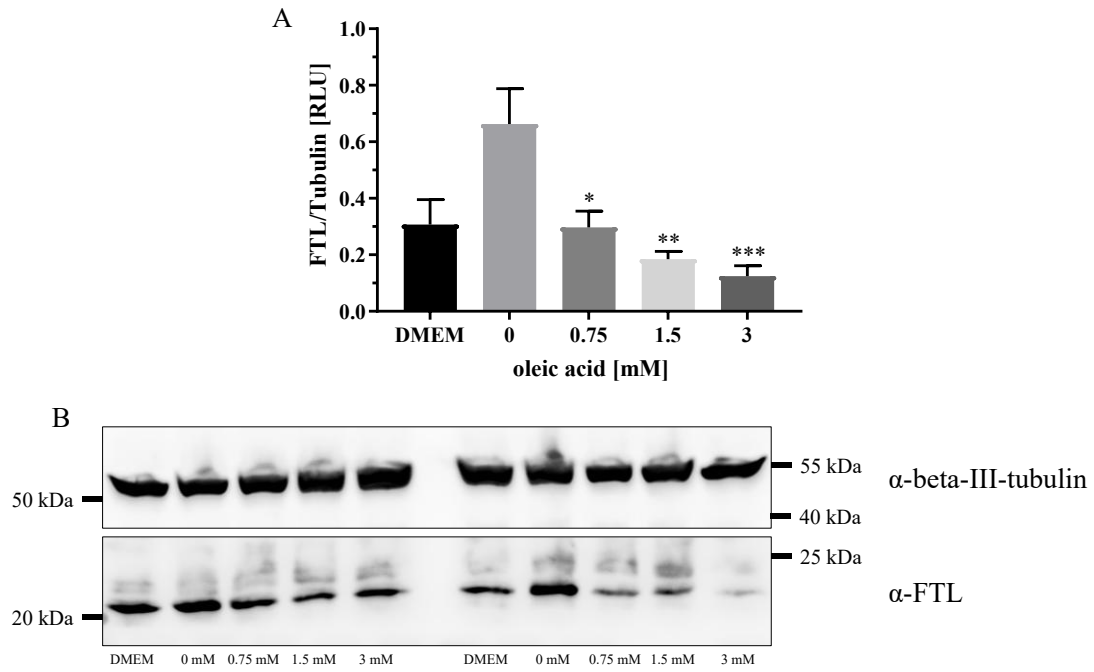

Figure 52: Detection of FTL in total lysate of wild type MIN6 cells treated for 5 d with oleic acid via (A) quantification of immunoblotting signals (n = 4). (B) Representative image of two independent experiments with 60 µg protein. Tubulin was the reference protein. * $p < 0.05$, ** $p < 0.01$, *** $p < 0.001$, significance by one-way ANOVA compared to 0 mM.

Treatment of the transfected model confirmed the effect of wild type cells, as the control treatment was increasing FTL compared to DMEM, and oleic acid further decreased the signal relative to the control (0.3941 ± 0.04456 RLU, with DMEM for GFP+; 0.2682 ± 0.07359 RLU, with DMEM for Glrx5+; 0.7985 ± 0.2273 RLU, at 0 mM for Glrx5+; 0.2368 ± 0.08396 RLU, **** $p < 0.0001$, at 0.75 mM for Glrx5+; 0.2574 ± 0.01816 RLU, **** $p < 0.0001$, at 1.5 mM for Glrx5+; 0.315 ± 0.02427 RLU, **** $p < 0.0001$, at 3 mM for Glrx5+, Figure 53A, significances determined by one-way ANOVA compared to Glrx5+ 0 mM). The comparison of GFP+ DMEM and Glrx5+ DMEM exhibited no difference in FTL protein levels.

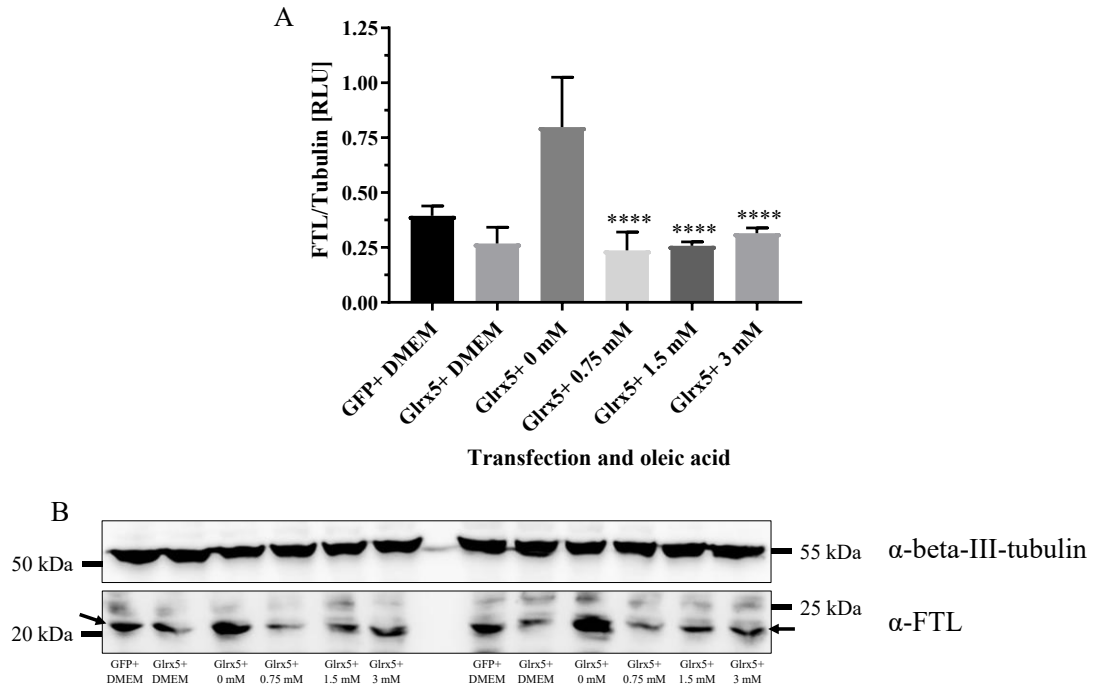

Figure 53: Detection of FTL in total lysate of transfected MIN6 cells treated for 48 h with oleic acid via (A) quantification of immunoblotting signals (n = 4). (B) Representative image of two independent experiments with 60 µg protein. Tubulin was the reference protein. **** $p < 0.0001$, significance by one-way ANOVA compared to Glrx5+ 0 mM.

The cell count of transfected samples used for immunoblotting relate to the following figures. A strong impact in cell number after 48 h of oleic acid treatment in T75 flasks was observed ($3.881 \pm 1.006 * 10^6$, at 0 mM for GFP+; $1.556 \pm 0.4185 * 10^6$, ** $p < 0.01$, at 3 mM for GFP+; $4.169 \pm 0.9001 * 10^6$, at 0 mM for Glrx5+; $1.513 \pm 0.2773 * 10^6$, ** $p < 0.01$, at 3 mM for Glrx5+, Figure 54, significances determined by one-way ANOVA compared to 0 mM). Taking together the data of cell counts, a decreasing effect was observable with 3 mM oleic acid treatment in T75 flasks (Fe-S enzyme activity and immunoblotting), whereas treatment with 1.5 mM or 3 mM oleic acid in T25 flasks (ELISA and respirometry) had no impact on cell count. Overall, there was no difference between the transfection groups.

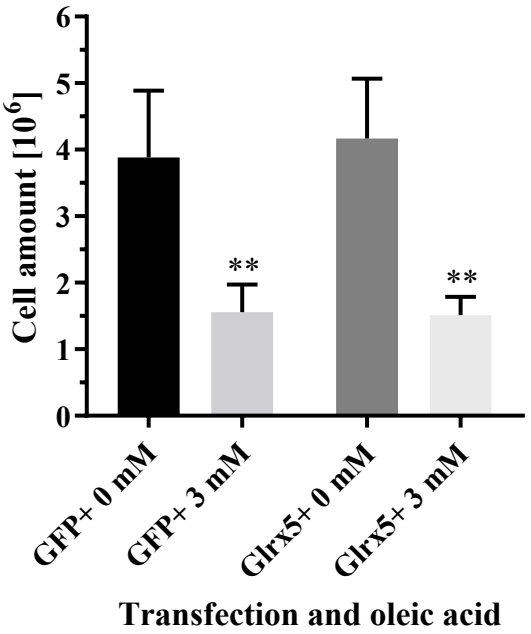

Figure 54: Cell counts of transfected MIN6 cells collected with trypsin/EDTA prior to sample preparation for immunoblotting (n = 4). Cells were transfected and subsequently treated for 48 h with oleic acid in a T75 flask. ** $p < 0.01$, significance by one-way ANOVA compared to 0 mM.

In the transfection model with respective GFP+ control, FTL signals decreased with 3 mM oleic acid (0.1586 ± 0.07443 RLU, at 0 mM for GFP+; 0.01121 ± 0.006838 RLU, * $p < 0.05$, at 3 mM for GFP+; 0.1495 ± 0.08685 RLU, at 0 mM for Glrx5+; 0.02341 ± 0.02643 RLU, * $p < 0.05$, at 3 mM for Glrx5+, Figure 55A, significances determined by one-way ANOVA compared to 0 mM). The signal of FTL by oleic acid was nearly absent compared to the previous figures. No differences were detected between the transfection groups.

Further analysis of GPx4, a lipid peroxide detoxifying enzyme, appeared to decrease following oleic acid treatment, without significance (0.1528 ± 0.05336 RLU, with DMEM; 0.1654 ± 0.07064 RLU, at 0 mM; 0.2198 ± 0.0921 RLU, at 0.75 mM; 0.1682 ± 0.05686 RLU, at 1.5 mM; 0.1015 ± 0.04337 RLU, at 3 mM, Figure 56A, no significance determined by one-way ANOVA).

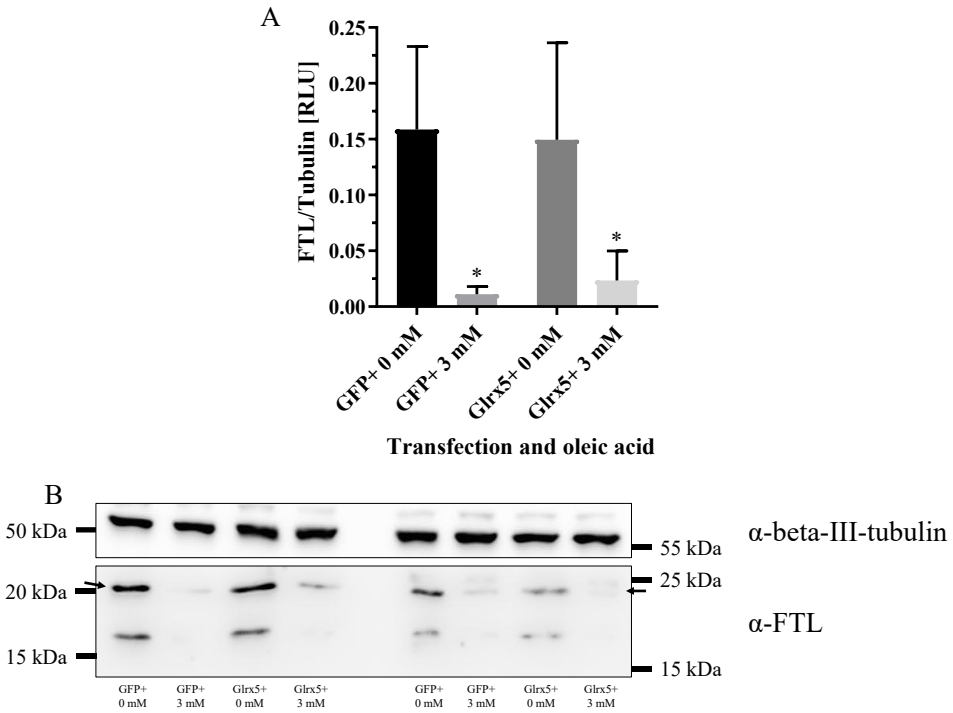

Figure 55: Detection of FTL in total lysate of transfected MIN6 cells treated for 48 h with oleic acid via (A) quantification of immunoblotting signals (n = 4). (B) Representative image of two independent experiments with 15 µg protein. Tubulin was the reference protein. * $p < 0.05$, significance by one-way ANOVA compared to 0 mM.

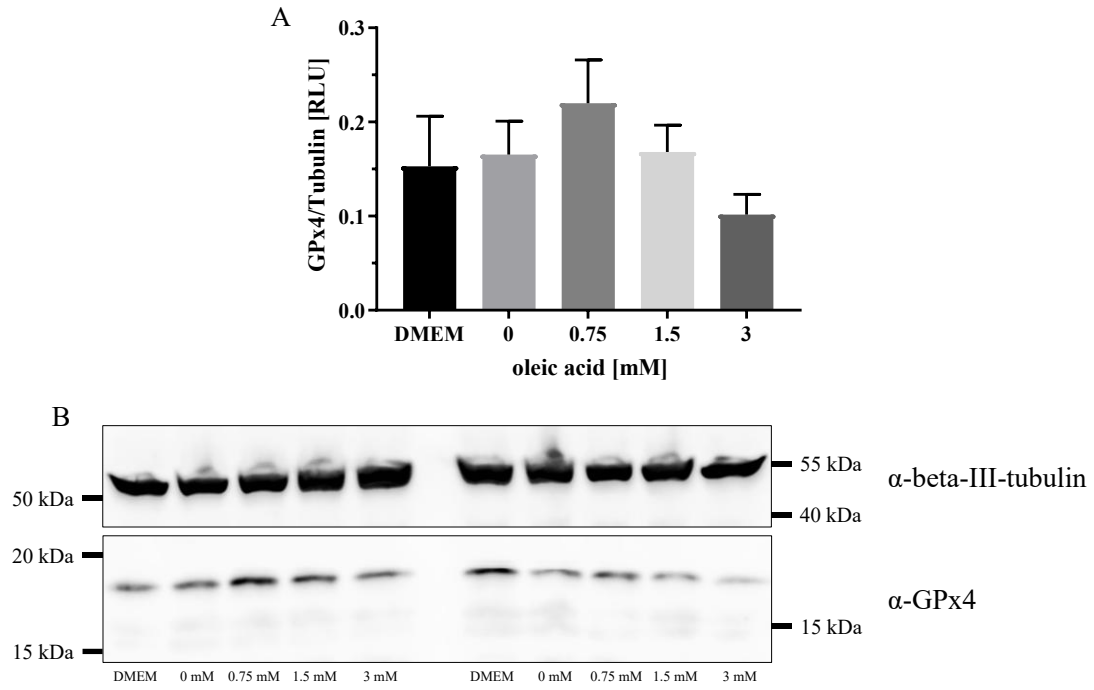

Figure 56: Detection of GPx4 in total lysate of wild type MIN6 cells treated for 5 d with oleic acid via (A) quantification of immunoblotting signals (n = 4). (B) Representative image of two independent experiments with 60 µg protein. Tubulin was the reference protein. No significance by one-way ANOVA.

The interpretation of immunoblotting signals in the transfection model remained inconclusive for oleic acid treatment. The differences between oleic acid and control were not strongly pronounced, and the deviations were greater compared to wild type cells (0.2929 ± 0.07141 RLU, with DMEM for GFP+; 0.2569 ± 0.112 RLU, with DMEM for Glrx5+; 0.1399 ± 0.1282 RLU, at 0 mM for Glrx5+; 0.2194 ± 0.1535 RLU, at 0.75 mM for Glrx5+; 0.2006 ± 0.1812 RLU, at 1.5 mM for Glrx5+; 0.1361 ± 0.08997 RLU, at 3 mM for Glrx5+, Figure 57A, no significance determined by one-way ANOVA).

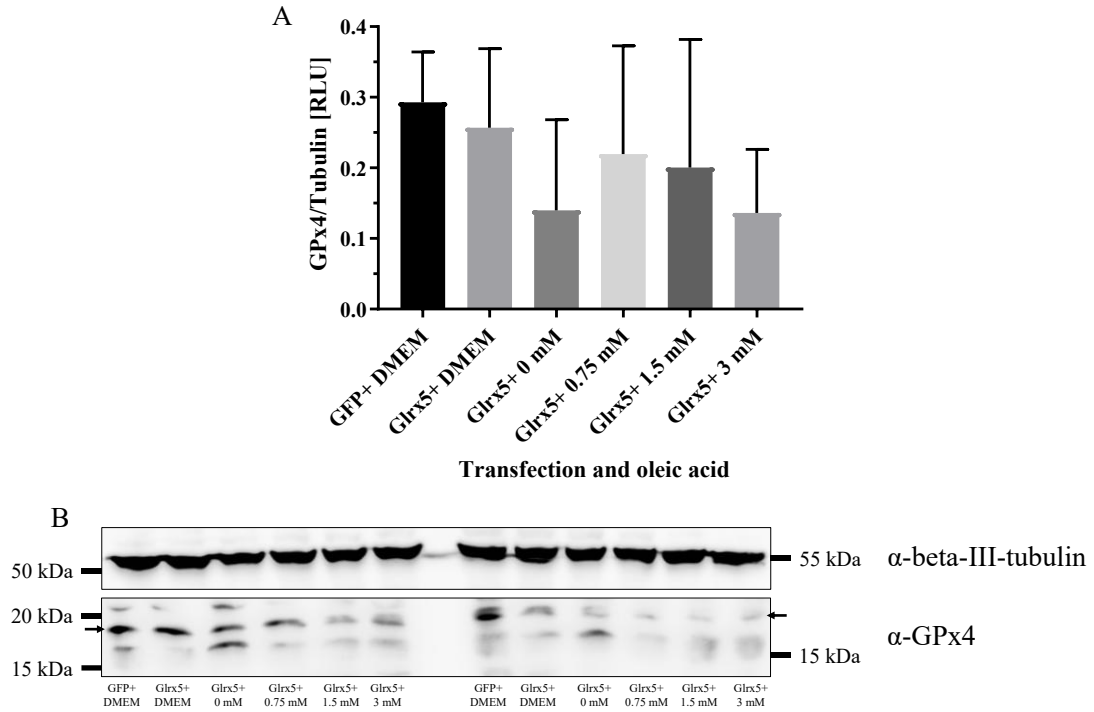

Figure 57: Detection of GPx4 in total lysate of transfected MIN6 cells treated for 48 h with oleic acid via (A) quantification of immunoblotting signals (n = 4). (B) Representative image of two independent experiments with 60 µg protein. Tubulin was the reference protein. No significance by one-way ANOVA.

Similarly, in the additional transfection model, no differences were observed due to transfection or treatment (0.04321 ± 0.01624 RLU, at 0 mM for GFP+; 0.02947 ± 0.03466 RLU, at 3 mM for GFP+; 0.04115 ± 0.04053 RLU, at 0 mM for Glrx5+; 0.03754 ± 0.02021 RLU, at 3 mM for Glrx5+, Figure 58A, no significance determined by one-way ANOVA). Thus, an effect similar to that observed in wild type cells could not be confirmed.

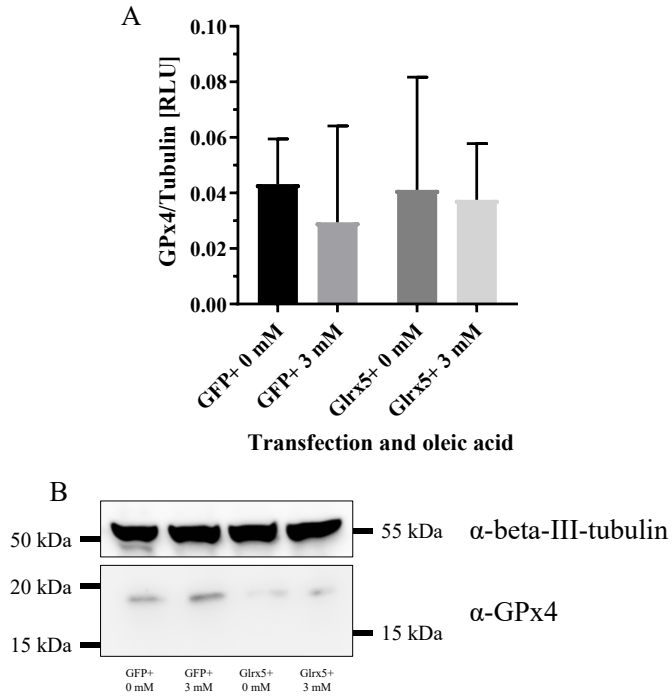

Figure 58: Detection of GPx4 in total lysate of transfected MIN6 cells treated for 48 h with oleic acid via (A) quantification of immunoblotting signals (n = 3). (B) Representative image of one independent experiment with 60 µg protein. Tubulin was the reference protein. No significance by one-way ANOVA.

3.4.14 Oleic acid treatment alters proteins unrelated to Fe-S clusters, such as PDX1 and p-ERK1/2, while p-Akt signals remain weak

Proteins unrelated to Fe-S clusters but relevant to diabetes and cellular function were analyzed by immunoblotting. In wild type MIN6 cells, oleic acid decreased PDX1 levels (0.936 ± 0.1667 RLU, with DMEM; 0.9222 ± 0.1396 RLU, at 0 mM; 0.7074 ± 0.1387 RLU, at 0.75 mM; 0.63 ± 0.1681 RLU, at 1.5 mM; 0.5133 ± 0.1286 RLU, * $p < 0.05$, at 3 mM, Figure 59A, significance determined by one-way ANOVA compared to 0 mM).

Similarly, in transfected cells with multiple oleic acid concentrations, PDX1 levels decreased with 3 mM treatment, showing no effect of the transfection itself (1.221 ± 0.387 RLU, with DMEM for GFP+; 1.113 ± 0.3803 RLU, with DMEM for Glrx5+; 1.432 ± 0.4669 RLU, at 0 mM for Glrx5+; 1.217 ± 0.5367 RLU, at 0.75 mM for Glrx5+; 1.297 ± 0.1203 RLU, at 1.5 mM for Glrx5+; 0.5312 ± 0.2434 RLU, * $p < 0.05$, at 3 mM for

Glrx5+, Figure 60A, significance determined by one-way ANOVA compared to Glrx5+ 0 mM).

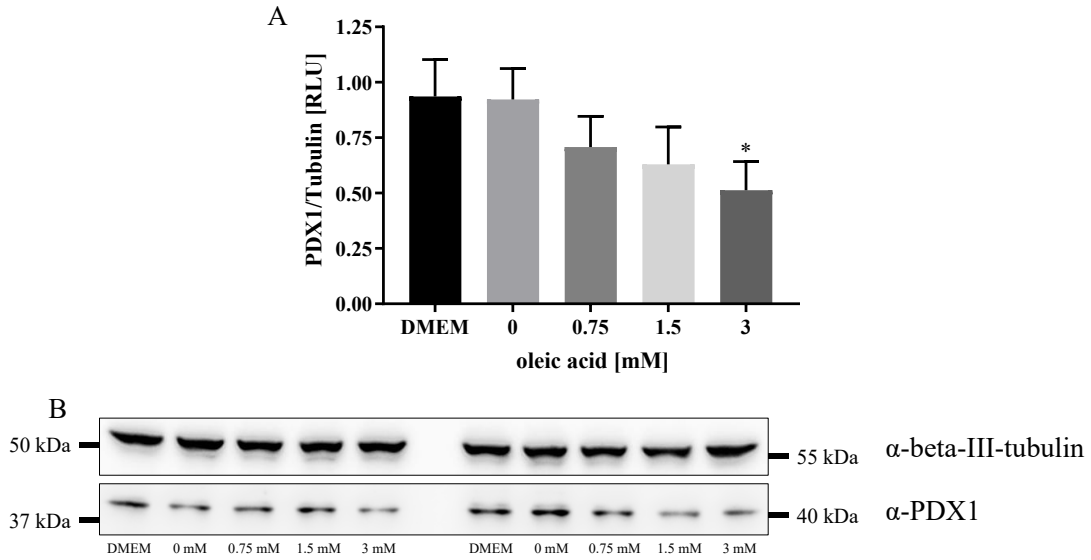

Figure 59: Detection of PDX1 in total lysate of wild type MIN6 cells treated for 5 d with oleic acid via (A) quantification of immunoblotting signals (n = 4). (B) Representative image of two independent experiments with 15 µg protein. Tubulin was the reference protein. * $p < 0.05$, significance by one-way ANOVA compared to 0 mM.

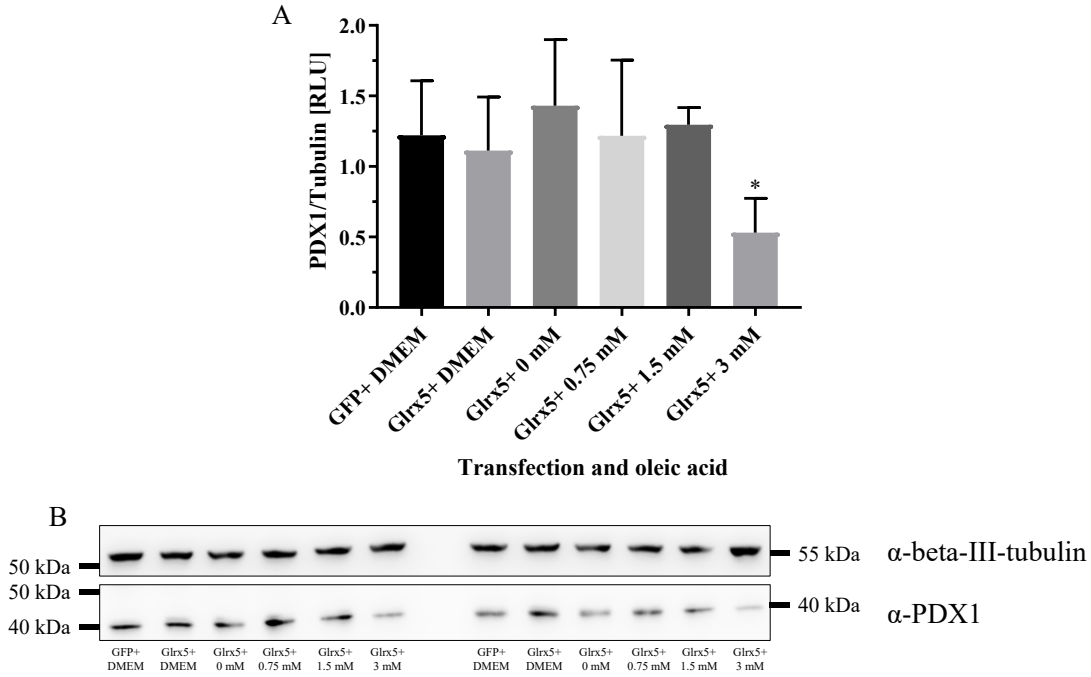

Figure 60: Detection of PDX1 in total lysate of transfected MIN6 cells treated for 48 h with oleic acid via (A) quantification of immunoblotting signals (n = 4). (B) Representative image of two independent experiments with 15 µg protein. Tubulin was the reference protein. * $p < 0.05$, significance by one-way ANOVA compared to Glrx5+ 0 mM.

Analysis of PDX1 for transfected cells for GFP+ control revealed decreased signals with 3 mM oleic acid (0.2457 ± 0.0358 RLU, at 0 mM for GFP+; 0.1258 ± 0.03291 RLU, * $p < 0.05$, at 3 mM for GFP+; 0.2045 ± 0.07034 RLU, at 0 mM for Glrx5+; 0.06723 ± 0.02453 RLU, * $p < 0.05$, at 3 mM for Glrx5+, Figure 61A, significances determined by one-way ANOVA compared to 0 mM). It was not clear, if there were further differences by Glrx5+ resulting in a decreased signal, as the previous detection showed no difference by GFP+ transfection.

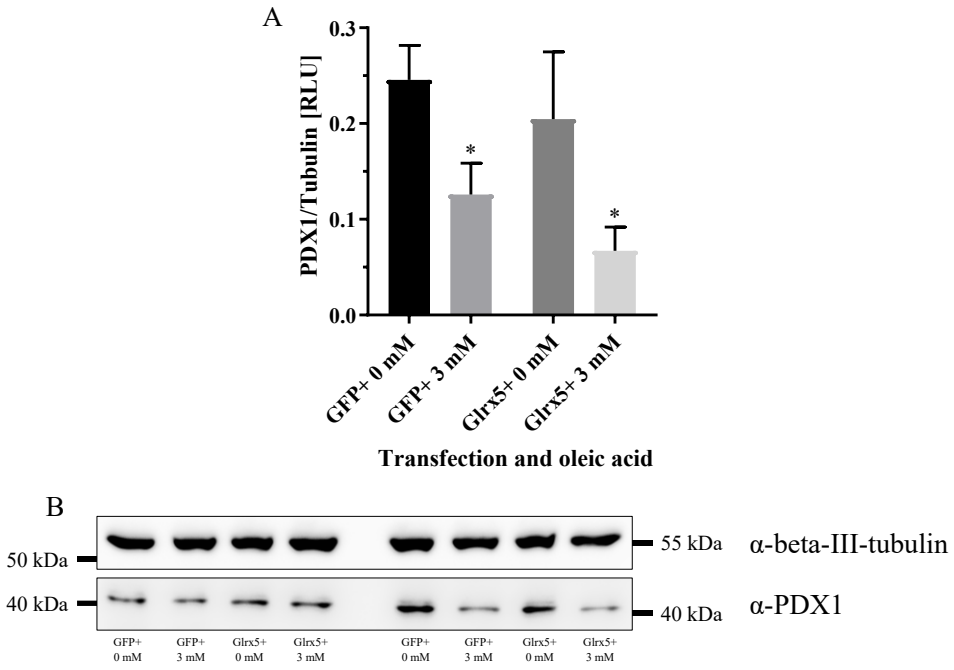

Figure 61: Detection of PDX1 in total lysate of transfected MIN6 cells treated for 48 h with oleic acid via (A) quantification of immunoblotting signals (n = 3). (B) Representative image of two independent experiments with 20 µg protein. Tubulin was the reference protein. * $p < 0.05$, significance by one-way ANOVA compared to 0 mM.

By using antibodies against the phosphorylated and non-phosphorylated form of ERK1/2, a decreased signal for p-ERK1/2 was detected by oleic acid treatment in wild type MIN6 cells, without affecting total ERK1/2 levels (0.1685 ± 0.0834 RLU, with DMEM; 0.1866 ± 0.05755 RLU, at 0 mM; 0.04173 ± 0.02842 RLU, ** $p < 0.01$, at 0.75 mM; 0.02873 ± 0.01518 RLU, ** $p < 0.01$, at 1.5 mM; 0.0335 ± 0.02409 RLU, ** $p < 0.01$, at 3 mM, Figure 62A, significances determined by one-way ANOVA compared to 0 mM). The effect was strong for all oleic acid concentrations.

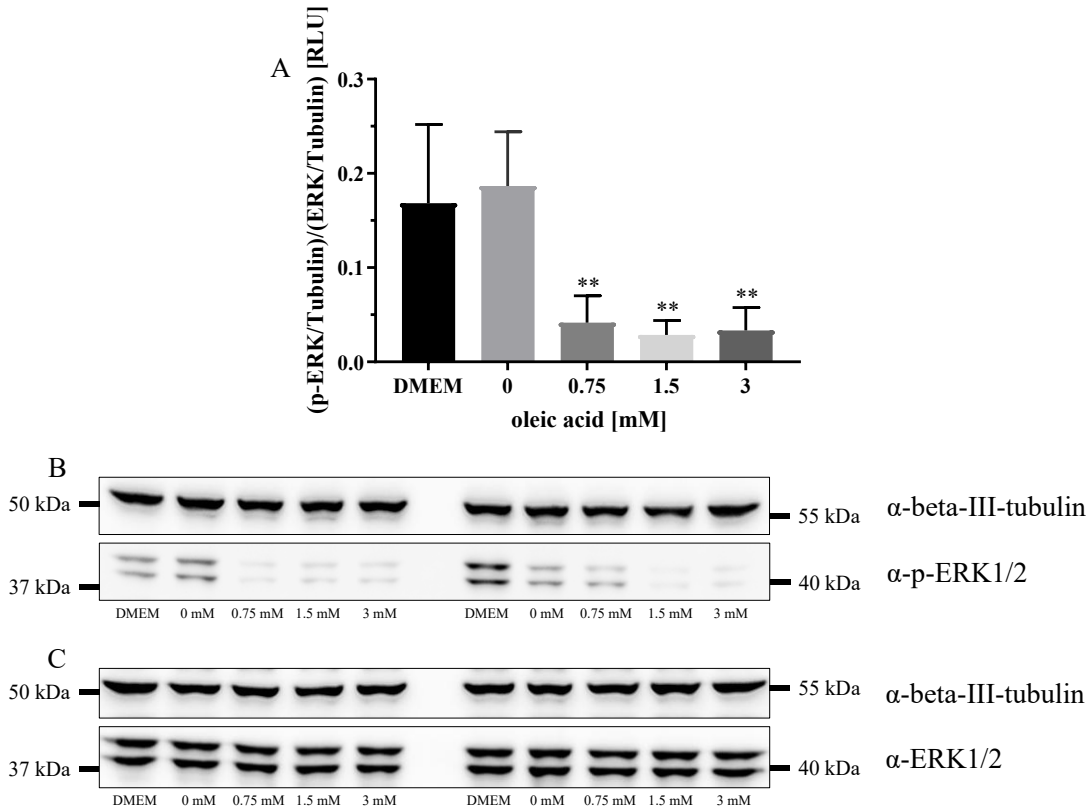

Figure 62: Detection of p-ERK1/2 and total ERK1/2 in total lysate of wild type MIN6 cells treated for 5 d with oleic acid via (A) quantification of immunoblotting signals (n = 4). Ratio of phosphorylated to total ERK1/2 was calculated. Representative image of two independent experiments with 15 µg protein against (B) p-ERK1/2 and (C) total ERK1/2. Tubulin was the reference protein. ** $p < 0.01$, significance by one-way ANOVA compared to 0 mM.

Analysis of the transfection model revealed decreased p-ERK1/2 signals with 3 mM of oleic acid treatment, without further differences due to the transfection groups (0.3729 ± 0.07371 RLU, at 0 mM for GFP+; 0.1564 ± 0.06398 RLU, * $p < 0.05$, at 3 mM for GFP+; 0.4496 ± 0.1744 RLU, at 0 mM for Glrx5+; 0.1286 ± 0.0421 RLU, ** $p < 0.01$, at 3 mM for Glrx5+, Figure 63A, significances determined by one-way ANOVA compared to 0 mM).

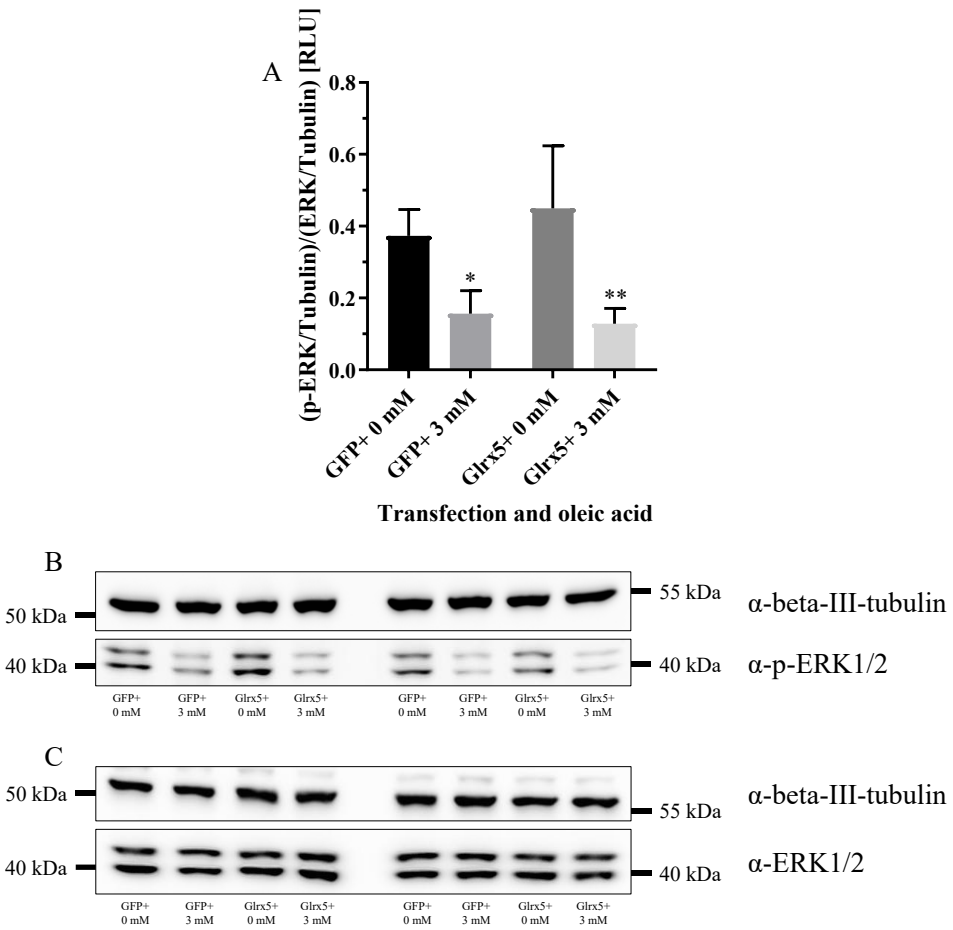

Figure 63: Detection of p-ERK1/2 and total ERK1/2 in total lysate of transfected MIN6 cells treated for 48 h with oleic acid via (A) quantification of immunoblotting signals (n = 4). Ratio of phosphorylated to total ERK1/2 was calculated. Representative image of two independent experiments with 15 µg protein against (B) p-ERK1/2 and (C) total ERK1/2. Tubulin was the reference protein. * $p < 0.05$, ** $p < 0.01$, significance by one-way ANOVA compared to 0 mM.

Akt was detected as further protein with activation by phosphorylation. In contrast, p-Akt signals were weak and unchanged by oleic acid treatment. Calculation of p-Akt resulted in a declined signal, remaining non-significant (0.01989 ± 0.005973 RLU, with DMEM; 0.0228 ± 0.009394 RLU, at 0 mM; 0.02302 ± 0.005851 RLU, at 0.75 mM; 0.01988 ± 0.004468 RLU, at 1.5 mM; 0.01342 ± 0.003504 RLU, at 3 mM, Figure 64A, no significance determined by one-way ANOVA).

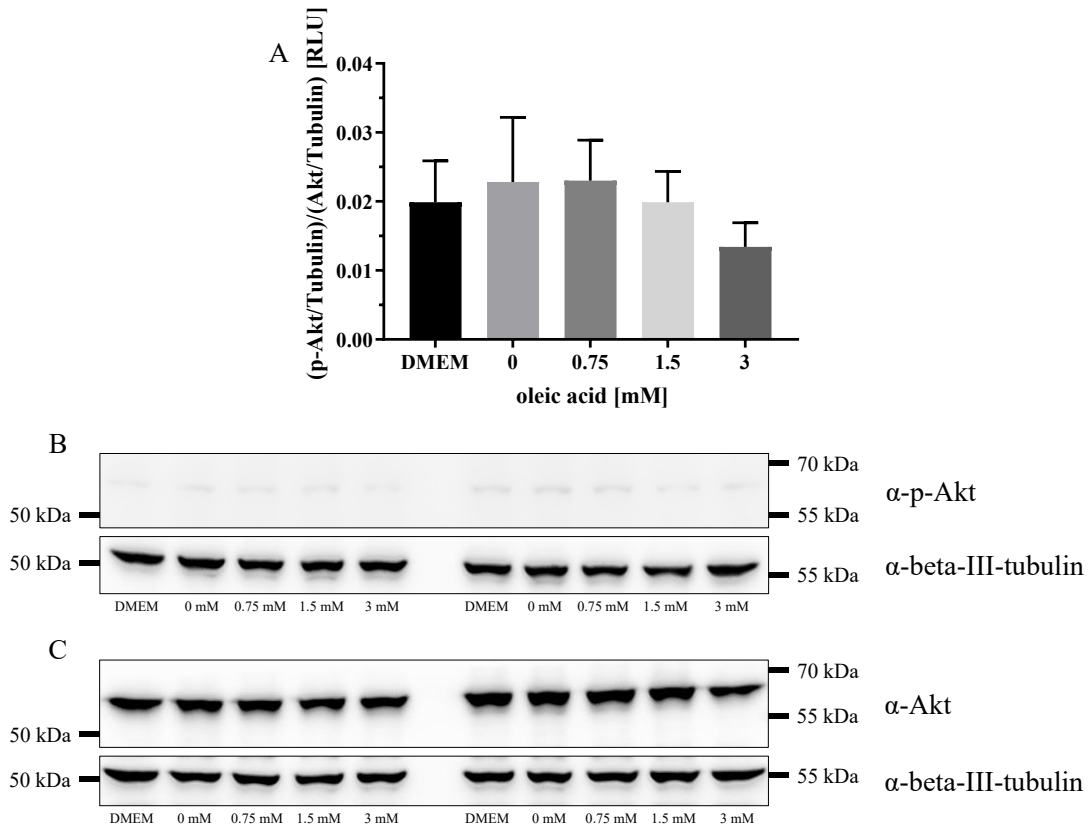

Figure 64: Detection of p-Akt and total Akt in total lysate of wild type MIN6 cells treated for 5 d with oleic acid via (A) quantification of immunoblotting signals (n = 4). Ratio of phosphorylated to total Akt was calculated. Representative image of two independent experiments with 15 µg protein against (B) p-Akt and (C) total Akt. Tubulin was the reference protein. No significance by one-way ANOVA.

For complementary measurements with transfected cells, the detection of p-Akt was waived, as the signal remained nearly undetectable. Analysis of total Akt showed an equal signal across all samples (1.208 ± 0.1104 RLU, at 0 mM for GFP+; 1.148 ± 0.05393 RLU, at 3 mM for GFP+; 1.117 ± 0.1151 RLU, at 0 mM for Glrx5+; 1.254 ± 0.166 RLU, at 3 mM for Glrx5+, Figure 65A, no significance determined by one-way ANOVA). Consistent with wild type cells, oleic acid treatment had no impact on total Akt.

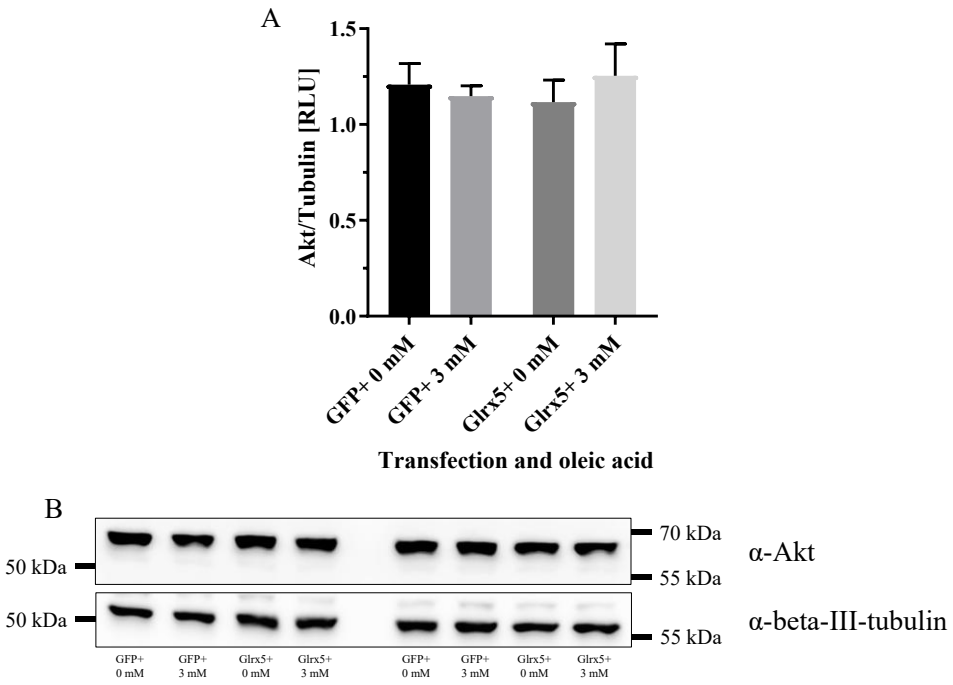

Figure 65: Detection of total Akt in total lysate of transfected MIN6 cells treated for 48 h with oleic acid via (A) quantification of immunoblotting signals (n = 4). (B) Representative image of two independent experiments with 15 µg protein. Tubulin was the reference protein. No significance by one-way ANOVA.

These findings revealed how oleic acid influenced mitochondrial function, Fe-S cluster associated proteins, and iron metabolism, alongside key signaling pathways in pancreatic β-cells. They provide a foundation for further exploration of the cellular mechanisms underlying β-cell dysfunction and their integration into the broader context of diabetes research.

4 Discussion

4.1 Decreased redox potential under lipotoxic treatment

To investigate the impact of oleic acid on general cellular oxidoreductase activity, the widely used MTT assay was employed. The results showed a modest decrease in OD after 24 h (Figure 1) and 48 h (Figure 3) treatment, without evidence of a dose-dependent effect. More pronounced effects were observed after 5 d of treatment, following a dose-dependent pattern with a maximum decrease of -25.5 % (Figure 2). The assay indicated no induction of cell death, as treatment with all oleic acid concentrations was not harmful to cellular function. Reactions contributing to MTT reduction predominantly originated from glycolysis and the ER and depended on cofactors such as NADH and NADPH (Bernas & Dobrucki, 2002; Berridge et al., 2005; Berridge & Tan, 1993). These findings suggested that oleic acid was thereby suitable for mimicking lipotoxic effects and for evaluating further cellular parameters. Based on literature, a decrease greater than -50 % would be considered severely cytotoxic, referring to IC_{50} threshold (Tolosa et al., 2015). Although all treatment durations demonstrated detrimental effects, longer treatment times elicited a more pronounced and reproducible response. In transfected cells, 48 h treatment resulted in a modest decrease comparable to 24 h treatment with 1.5 mM oleic acid in wild type cells. The behavior of MIN6 cells upon fatty acid treatment was not altered by transfection, and absolute values of OD remained within a comparable range to those observed in wild type cells after 24 h treatment. Thus, the method of chemical transfection with the chosen plasmids created a cellular model without any indication of altered responses to lipid stressors. Additionally, Glrx5 expression did not provide a beneficial effect on MIN6 cells. To fully interpret the results, it is important to consider the mechanisms measured by the MTT assay. The assay was initially described for measuring cell survival and proliferation depending on the activity of living cells and excluding dead cells (Mosmann, 1983), as dehydrogenase enzymes of active mitochondria were assumed to reduce MTT (Yuanbin Liu, 1999; Yuanbin Liu et al., 1997). Consequently, higher formazan production correlated with greater energy metabolism. However, while the assay has been used to assess cell proliferation, proliferation is not a requirement for the assay. The idea of Tim Mosmann was to establish an assay which was not influenced by culture medium, but the results of the supplement indicated a big impact of added albumin on MTT readouts (Supplement Figure 3), which was also described in literature (Funk et

al., 2007; K. T. Huang et al., 2004). Like demonstrated, formazan production can occur in the absence of cells under certain experimental setups (Supplement Figure 4). Mosmann's original protocol used 5-10 % fetal bovine serum, which contained albumin, a component with variable natural concentrations (Zheng et al., 2006). This effect had to be carefully controlled especially in experiments using albumin complexed fatty acids. Recent studies suggested that the majority of the MTT signal originated from non-mitochondrial sources (Aitken et al., 2020). While some articles generalized MTT results as measures of cell viability (Kumar et al., 2018), such interpretations are often unsubstantiated (Ghasemi et al., 2021). It is preferable to report MTT results as OD values and to use complementary methods, such as TUNEL assay or FACS with 7-AAD, propidium iodide, or annexin V staining, for assessing viability.

4.2 Impacts on insulin secretion and β-cell identity

In contrast to the mild impairments observed in the MTT assay, ELISA measurements of insulin revealed a significant decrease in both the cell lysates and culture media of wild type cells. This approximately -80 % decrease in insulin was unexpected given the moderate effects seen in the MTT assay and was negative in the context of type 2 diabetes. The results suggested that lipotoxic stress severely impaired β-cell insulin production and secretion (Z. Song et al., 2019), potentially contributing to chronic hyperglycemia and its associated clinical complications. *Ins2* qPCR results showed a moderate decrease only at the highest oleic acid concentration (-30 %), while mRNA levels in other treatment groups remained unchanged (Figure 4B). This suggested that post-transcriptional regulation likely drove the observed changes in insulin protein level. For instance, treatments with 0.75 mM and 1.5 mM oleic acid altered insulin levels without corresponding transcriptional changes. The decline in insulin mRNA could be attributed to decreased PDX1 protein levels, which were significantly affected at 3 mM oleic acid, while also the lower concentrations showed weaker signals by immunoblotting of the wild type model (Figure 59). The critical role of PDX1 in maintaining β-cell function and identity is well-established (Olson et al., 1995). Loss of PDX1 signal was considered detrimental to the functionality of β-cells, and can even lead to their dedifferentiation, highlighting its importance in stress response (Gao et al., 2014). PDX1 is a factor of central importance for β-cells, which's reactivity points to severe stressors on protein level (Fujimoto & Polonsky, 2009). Alternative explanations for post-transcriptional changes could involve microRNAs and RNA-binding proteins (Pérez-García et al., 2022).

RNA-binding protein HuD (C. Kim et al., 2016), or DEAD-Box Helicase 1 (DDX1) inducible by 500 µM palmitic acid (Zonghong Li et al., 2018) modified transcription and translation of insulin. Secretion of insulin was changed under influence of CUG-binding protein 1 (CUGBP1), suppressing cyclic adenosine monophosphate (cAMP) levels (Zhai et al., 2016), RNA Binding Fox-1 Homolog 1 and 2 (Rbfox1 and Rbfox2) (Juan-Mateu et al., 2017), or miR-9, by altered sirtuin 1 expression (Ramachandran et al., 2011). Alternative splicing of genes required for exocytosis served also an explanation (Moss et al., 2023). Additionally, miR-15a, targeting UCP2, increased ATP levels from the respiratory chain, while high ATP/ADP ratios were a factor initiating insulin secretion (L.-L. Sun et al., 2011). If the recent MIN6 experiments were extended to the transfection model, oleic acid treatment produced weaker effects on released insulin (Figure 13). There was no distinct difference between the respective transfection groups and there was no positive impact by the Glrx5 transfection. Notably, experiments conducted later in the study showed milder lipotoxic effects, potentially reflecting improved cell culture handling techniques. All insulin measurements were performed under non-stimulated conditions with a constant high glucose concentration (25 mM), reflecting standard culture conditions for MIN6 cells (Miyazaki et al., 1990). Thereby, the results did not reflect stimulated secretion of insulin. In theory, treatment with cytotoxic properties could potentially have increased cell rupture and led to release of insulin into the medium. However, this was not observed in the recent experiments. Generally, glucose concentration was a decisive parameter for lipotoxic effects, as higher glucose concentrations made it more likely to detect negative outcomes from fatty acid treatment (Maris et al., 2013; Saitoh et al., 2010). This relationship can be explained, for instance, by the interactions between glucose and lipid metabolism for rate limiting substrates and feedback inhibition like the Randle cycle with malonyl-CoA (Yoon et al., 2021). Lipid stressors may also had a greater impact on an active and metabolically challenged state compared to cells in resting phases (Köhnke et al., 1993). The interplay between glucose and lipid stressors is commonly referred to as glucolipotoxicity (Roduit et al., 2000). A positive impact on insulin levels would be particularly relevant for clinical applications. However, the observed results for insulin and PDX1 in MIN6 cells remained unaffected by the transfection. So far, no connections have been described between PDX1 and Glrxs.

4.3 Post-translational modifications of signaling pathways

Further lipotoxicity targets independent from Glrx5 and Fe-S clusters included kinase signaling pathways such as ERK1/2 and Akt. Oleic acid treatment resulted in a substantial decrease in p-ERK1/2 levels, while total ERK1/2 remained unchanged (Figures 62, 63). These effects were consistent across wild type and transfected cells, with no dose-dependent differences observed on p-ERK1/2 signals. Dephosphorylation of proteins is another form of post-translational modification. Blunted p-ERK1/2 signaling was considered detrimental, as it can impair cell survival, proliferation and cytoskeletal remodeling (Hu & Lin, 2024). ERK1/2 was activated by growth factor-stimulated phosphorylation, acting on downstream processes, including ribosomal S6 kinase family of proteins (Cronin et al., 2021). It was likely that fatty acids could thereby negatively affect cell cycle. Impaired MIN6 cell survival was assessed using an ERK2 siRNA model, which downregulated ERK1/2 and also led to altered p-CREB protein levels (Costes et al., 2006). The glucose-dependent insulin transcription was decreased in MIN6 cells by inhibiting p-ERK1/2, highlighting the significant role of p-ERK1/2 in insulin secretion (Benes et al., 1999). No differences in behavior were observed between wild type and transfected cells, and Glrx5 transfection had no positive effect. In contrast to p-ERK1/2, signals of p-Akt were weak (Figure 64) and did not show clear changes with oleic acid treatment. As consequence, p-Akt signals were not further assessed in the transfected model. By information of the literature, decreased p-Akt levels were negative for insulin secretion, as Akt was a downstream factor of the insulin receptor (Y. B. Kim et al., 1999). Akt was phosphorylated by upstream kinases upon binding to PIP3 produced by PI3k, which was stimulated by insulin (Coffer et al., 1998). Elevated levels of oxidative distress were reported to hydroxylate insulin, lowering the affinity to the insulin receptor (Montes-Cortes et al., 2010). Further, p-Akt was positive for proliferation and survival (Hart & Vogt, 2011). It was possible to increase p-Akt of MIN6 cells in experimental setups by exogenous insulin stimulation (Tam et al., 2023). It is worth noting that MIN6 cells, often considered insulin-resistant (K. Cheng et al., 2012), may have inherently weak p-Akt signals due to culture conditions with a constant high glucose concentration. For reference, the glucose concentration of DMEM used for regular MIN6 culture was 25 mM (450 mg/dl), which was comparable to levels observed in patients in the emergency department for unrecognized or uncontrolled diabetes (Crilly et al., 2018). It was doubtful whether the weak p-Akt changes in the wild type model would had a

relevant impact on the insulin sensitivity of the cells. Furthermore, it was noteworthy that the treatment conditions had no effect on Akt signals. Data from an associated project indicated that treatment with comparable concentrations of palmitic acid decreased Akt signals by up to -40 % in immunoblotting (by Kim Kühne, unpublished). This effect was not observed for oleic acid. Therefore, it could be possible that this effect was differentiating if saturated or unsaturated fatty acids were applied. In general, saturated fatty acids were considered as more lipotoxic (W. Liu et al., 2024). Especially palmitic acid can induce apoptosis by formation of ceramides (Fretts et al., 2021), also initiating ferroptosis (M. Guo et al., 2024). Decreased Akt levels were described in the literature as an approach to sensitize chemo resistant cancer cells (A.-R. Choi et al., 2014). This was shown by treatment with salinomycin. The authors were debating if changes of Akt were mediated by altered Akt mRNA levels, Akt protein stability, or Akt protein translation. Loss of Akt would be considered as negative for MIN6 cells. The current experiments showed no differences in p-ERK1/2, ERK1/2, or Akt signals between wild type and transfected cells, with no protective effect from Glrx5 transfection on p-ERK1/2 signals.

4.4 Glutaredoxin 5 and iron-sulfur cluster

4.4.1 Aspects inside mitochondria

4.4.1.1 Glutaredoxin 5 in MIN6 cells and their molecular biological adjustment

Similar to *Ins2* qPCR results, *Glrx5* mRNA expression was diminished following treatment with 3 mM oleic acid compared to the control (*Ins2*: -25 %, *Glrx5*: -20 %), which has not reached significance in this experiment (Figure 4). Due to the high standard deviations, it would be highly speculative to conclude that fatty acids affect the genetic regulation of Glrx5. Based on data of an associated project, changes in *Glrx5* qPCR of -50 % were observable in MIN6 cells upon treatment with 3 mM oleic acid (Kreimer, 2024). This suggested that further genetic analysis under lipotoxic conditions could reveal a stronger influence at a genetic level. In contrast, Glrx5 protein levels assessed via ELISA showed a significant decrease across all oleic acid concentrations (Figure 5). This effect appeared dose-dependent and was consistent with immunohistological findings in pancreatic islets of db/db mice (Petry et al., 2017, 2018). The oleic acid induced decrease of Glrx5 could not be confirmed by immunoblotting (Figure 6).

It is important to note that immunoblotting, while offering higher specificity, may has limitations in quantification compared to more sensitive methods like ELISA. Immunocytochemical analysis of Glrx5 in MIN6 cells could provide additional clarity. The biological effect of Glrx5 deficits varied across systems, with non-erythroid cells being more resilient to impairments, unless particularly reliant on heme structures (Camaschella et al., 2007). Characterization of transfected MIN6 cells showed a dramatic 15-fold increase in *Glrx5* mRNA expression, as demonstrated in the supplementary material (Supplement Figure 6). This increase was confirmed by both ELISA and immunoblotting across both transfection setups (Figures 8, 9, 11, 12). Unlike the wild type model, both methods provided consistent results for Glrx5 expression following transfection, lending credibility to the data. No biological alterations were detected following Glrx5 overexpression. Notably, there were discrepancies between the genetic and protein levels, as the induced gene expression from transfection was greater than the protein levels observed through ELISA or immunoblotting. This underscored the necessity to thoroughly validate the model and exercise caution when drawing conclusions from gene expression to protein levels without additional measurements. Furthermore, the interpretation relied heavily on the transfection rate of 24 %, reported in the supplement (Supplement Table 1), which was inconsistent with the observed changes at both the gene and protein levels. The FACS measurement provided the first opportunity for single-cell-level detection. In contrast, other methods such as MTT, ELISA, qPCR, and immunoblotting reflected an average of transfected and non-transfected cells, which had relevant implications for interpretation. Future experiments could focus on additional single-cell analyses, such as immunocytochemistry, to explore correlations in cellular subpopulations based on Glrx5 levels.

4.4.1.2 Mitochondrial iron-sulfur proteins of energy metabolism remain unaffected

The primary focus of this project was to investigate the correlation between lipotoxic stress and Fe-S cluster related factors, potentially influenced by Glrx5 deficiencies. Analyses of isolated mitochondrial Fe-S enzyme activities (ACO2, SDH, C2-C3) and COX activity in the wild type model revealed no changes following oleic acid treatment (Figures 14B, 15). Observations in transfection models corroborated these results (Figures 20, 25B, 28). Minor apparent changes on enzyme activities (Figures 15C, 18B,

20B) were biologically insignificant when all experiments were considered collectively. This outcome was unexpected given the initial hypothesis, as SDH activity is considered a sensitive parameter for Fe-S cluster deficiencies (X. Wang et al., 2022). These findings suggested that a pronounced Glrx5 defect, as inferred from Glrx5 immunoblotting, was unlikely. Immunoblotting of the second transfection model supported the enzyme activity results, showing unchanged signals for ACO2 (Figure 27), and UQCRFS1 (Figure 44). Non Fe-S proteins, such as COX-2 (Figure 29), COX-6 A/B (Figure 30), and UQCRC2 (Figure 43) were also unaffected. Literature indicated that long noncoding RNAs related to UQCRFS1 and UQCRC2 were differentially expressed in a type 2 diabetes liver transcriptome analysis, with UQCRC2 being strongly correlated with type 2 diabetes (X. Lan et al., 2022). Additionally, UQCRC2 protein levels in primary adipocytes increased under treatment with canagliflozin (X. Yang et al., 2020). A crucial step in determining cytosolic and mitochondrial protein distribution was digitonin-based cell fractionation, which was effective and did not compromise interpretability. The chosen digitonin concentration allowed adequate separation of cytosolic fractions from organelles while preserving mitochondrial integrity. This was confirmed by low CS activity (Figures 16, 21, 31) and weak signals of soluble mitochondrial proteins, such as ACO2, in the cytosol (Figures 17, 22, 32). Fraction separation was further validated by minimal cytosolic proteins signals, such as GPAT or Glrx3, in organelles fractions. The distribution of proteins targeted by transfection was plausible (Figures 22, 23, 32, 33).

4.4.1.3 Functional respiratory analysis reacts on oleic acid

In contrast to isolated enzyme activities, respirometry showed decreased oxygen consumption of single states upon oleic acid treatment (Figure 34). This was particularly evident when substrates activating all respiratory chain complexes were added, and impaired respiration persisted throughout the measurements. Similar effects were observed in transfection models, where decreased respiration was measurable upon complex V activation, even without complex II involvement (Figure 37). Transfection itself did not influence this effect. While complex I respiration remained consistent in wild type cells, oleic acid treatment significantly decreased NDUFB8 signals. NDUFB8 is a non Fe-S cluster and non-catalytically subunit of complex I (Y. Li et al., 2021). NDUFB8, together with six other proteins, is part of the ND5 subunit. The subunits ND2, ND4, and ND5 build the proton translocation module requiring 34 subunits or assembly factors (Signes & Fernandez-Vizarra, 2018). NDUFB8 was reactive to high fat diets in

Alzheimer's disease models, an effect mediated by PPARγ activity and PPARγ coactivator 1α (Palomera-Avalos et al., 2017). Resveratrol treatment reversed this effect, likely through improved mitochondrial fusion. Notably, Fe-S cluster subunits NDUFS4 (Mise et al., 2024) and NDUFS8 (Flotyńska et al., 2022) correlated with diabetes susceptibility and insulin sensitivity.

4.4.1.4 ATP utilization is restricted independent of complex V

ATP levels in MIN6 cells were lower in control groups and remained higher in treated cells (Figure 38), despite higher oxidative phosphorylation respiration in controls. Two potential explanations could account for this observation. Firstly, the elevated ATP levels might resulted from increased ATP synthesis via oleic acid degradation. Secondly, the higher ATP levels could reflect a decrease in ATP-consuming processes induced by oleic acid. The first explanation has limitations, as it was unlikely that ATP levels would be elevated despite diminished oxidative phosphorylation respiration. Given that mitochondrial processes account for 98 % of cellular ATP production (L. Jiang et al., 2010), it was more plausible that oleic acid treatment impaired ATP-consuming pathways. This interpretation was supported by a review discussing similar mechanisms (Buttgereit & Brand, 1995). Most ATP in cells is required for protein and RNA/DNA synthesis, followed by substrate oxidation and cycling of sodium and calcium, all of which were disrupted by lipotoxicity (An et al., 2021; Arruda & Hotamisligil, 2015; Bays, 2013; Engin, 2024; Good & Stoffers, 2020). Also insulin synthesis and secretion was consuming a lot of ATP (Y. Tang et al., 2024). The ATP differences increased depending on the oleic acid concentration, as confirmed by 24 h interval measurements in MIN6 cells (Figure 39). Additionally, data from an associated project indicated that the absolute ATP readouts of MIN6 cells were lower in the control groups compared to those cultured with DMEM. The presence of BSA in the control groups was identified as a significant factor that greatly diminished ATP-dependent luminescence (-66 % at 0.15 mM, -84 % at 0.3 mM, -92 % at 0.6 mM, by Kim Kühne, unpublished). Luminescence spectral analysis ruled out quenching as the cause. Because of limited space in 96 well plates, standards with adjusted BSA concentrations were not included for all treatment groups, necessitating the use of relative ATP values (Figures 38, 39, 41). In transfection models, absolute ATP levels could be measured with single oleic acid concentrations (Figure 40). Elevated ATP levels were consistent with respirometry data. Decreased respiration likely reflected allosteric inhibition of complex IV by ATP phosphorylation (Arnold &

Kadenbach, 1997), a rate-limiting step in the respiratory chain (Ramzan et al., 2020). Like seen in transfection model, the respiration was decreased as complex V was activated, which included complex IV activity. As ATP levels of the treated cells remained higher, the respiration reflected complex IV inhibition, which was apparent for all following stages of respiration, always including complex IV participation. If this effect was taken into account, it was plausible that there would be no difference within the single mitochondrial respiratory states and no fatty acid mediated defect of the respiratory chain (Chance & Williams, 1955). This inhibition was specific to respirometry and not observed in isolated Fe-S enzyme activity measurements (Figures 15C, 20C, 28B). In contrast to respirometry, the enzyme activity was assessed detached from the functional respiratory chain and ATP inhibition. This highlighted again the necessity for extensive analyses covering genetic level, protein level, and functional assessment. Premature conclusions with missing evaluations can mislead, like demonstrated for Glrx5 transfection and FACS analysis, or the discrepancy between mitochondrial proteins and mitochondrial respiration, or the mitochondrial respiration and ATP synthesis. As respirometry follow-up experiment, it would be possible to exclude the ATP inhibition effect by titrating hexokinase for irreversible dephosphorylation of complex IV (Gouspillou et al., 2011) or performing measurements with excess exogenous ATP. The transfection was not affecting the behavior of MIN6 cells upon treatment and Glrx5 transfection had no effect compared to GFP transfection. Similar ATP changes were observed in EndoC-βH3 cells, suggesting diminished ATP-consuming pathways as a likely explanation in human models as well. Literature does not indicate differences between fatty acid treatment effects in murine and human models.

4.4.2 Outer-mitochondrial factors connected to iron-sulfur clusters

4.4.2.1 Cytosolic aconitase and iron regulation

Although many mitochondrial Fe-S cluster related factors were unaffected by oleic acid, notable effects were observed outside the mitochondria. One of the most significant change was the alteration in ACO1 activity, in contrast to the unaffected ACO2 activity. This was clearly evident in both the wild type and the Glrx5 overexpressing MIN6 cells treated with 3 mM of oleic acid (Figures 14A, 25A), whereas ACO1 activity remained unchanged in transfected cells treated with lower concentrations (Figure 18A). In general,

treatment duration exceeding 5 d was more likely to induce definite changes compared to 48 h treatments. Measurements revealed strong impairments in ACO1 activity, while immunoblotting signals for ACO1 protein remained unchanged by oleic acid (Figure 26). This inactivation of ACO1, despite steady protein levels, may be explained by a loss of its Fe-S cluster, which activated its iron regulatory function (Oskarsson et al., 2020). Such activation could lead to uncontrolled iron regulation and ferroptosis, as demonstrated in yeast with inhibited *GRX5* expression (Rodríguez-Manzaneque et al., 2002). The evaluation of the literature revealed a lack of comparable studies in diabetic models. In recent experiments, ACO1 activity appeared independent of Glrx5 transfection, contrary to the available literature (Camaschella et al., 2007; Rodríguez-Manzaneque et al., 2002). Additional discrepancies with the literature included impaired SDH (Rodríguez-Manzaneque et al., 2002) or ACO2 activity (Camaschella et al., 2007) in yeast and zebrafish, which were not observed in MIN6 cells (Figures 14B, 15A). All experiments were conducted under normoxic conditions, but testing Glrx5 protein levels and ACO1 activity under hypoxic conditions could provide further insights. It could be possible that ACO1 activity remained unaffected upon fatty acid treatment, making oxygen and oxidation necessary factors in human skeletal muscle cells (Cui et al., 2019). However, ACO2, known to be highly sensitive to oxidative distress in HeLa cells (Ferecatu et al., 2014), was unaffected in MIN6 cells. These results suggested that the observed effect on ACO1 activity was unlikely to be caused by Glrx5.

4.4.2.2 Potential mechanisms beyond Glutaredoxin 5 in cytosolic aconitase regulation

A comparison with the literature provided alternative explanations for changes in ACO1/IRP1 unrelated to lipotoxicity. For example, the outer mitochondrial membrane protein Cisd1 transported Fe-S clusters to cytosolic proteins (Camponeschi et al., 2017; Golinelli-Cohen et al., 2016; Lipper et al., 2015) and restored IRP1 activity under oxidative distress (Ferecatu et al., 2014), as demonstrated in *Drosophila melanogaster* (Huynh et al., 2019). Additionally, connections to the glycolytic enzyme enolase, which catalyzed the conversion of 2-phosphoglycerate to phosphoenolpyruvate, have been described. Enolase 1 (He et al., 2023; T. Zhang et al., 2022) and enolase 3 (Arenbaoligao et al., 2023) degraded IRP1. Human genome analyses revealed correlations between IRP1 and genes such as DMT1 (Weijiao et al., 2021) and ACSL4 (J. Zhu et al., 2022). ACSL4, a long-chain fatty acid CoA ligase 4, preferentially converted arachidonic acid to

arachidonoyl-CoA. Ferroptosis regulating agents, including erastin (Yao et al., 2021) and dihydroorotate dehydrogenase, essential for pyrimidine nucleotide synthesis, have been linked to IRP1 in mice (W. Zhang et al., 2022). The mediator of ERBB2-driven cell motility 1 (MEMO1) showed correlations to TfR2, mitoferrin, and IRP1 (Dolgova et al., 2024), or the effects were mediated by glutamate dependent ion channel N-methyl d-aspartate receptor (H.-P. Cheng et al., 2023). ISC maturation factors such as Nbp35 and Nar1 were also required for ACO1 assembly in yeast (Stehling et al., 2018). Ferroptosis may be independent of IRP1 and instead mediated by IRP2 (Terzi et al., 2021), or influenced by NF-κB activity in glioblastoma (Y. Lan et al., 2023). Post-translational modifications, including phosphorylation, also regulated the functions of IRP1 (Brown et al., 1998) and IRP2 (Schalinske & Eisenstein, 1996). Opposed to the gathered data, most literature focused on genetic ACO1 regulation and its role in iron regulation, with limited studies addressing its activity as basis for ferroptosis (Daher et al., 2019; Ferecatu et al., 2014; Tan et al., 2016). A common aim in these studies was the induction of cellular iron overload and ferroptosis to sensitize chemotherapy-resistant cancer cells, directly caused by IRP1 (Cai et al., 2023; Y. Lan et al., 2023; Rah et al., 2024; Yao et al., 2021). For example, inhibiting *GLRX5* in colorectal cancer cells induced ferroptosis (J. Lee et al., 2020). Stearoyl-CoA desaturase 1 has been associated with potentiation of cancer therapy (H. Luo et al., 2022) and decreased ferroptosis (Kato et al., 2020; H. Luo et al., 2022; Yinu Wang et al., 2024; T. Wu et al., 2023; Xiao et al., 2023; X. Xie et al., 2023; L. Xu et al., 2024; Z. Ye et al., 2022). Stearoyl-CoA desaturase 1 converted saturated fatty acids to unsaturated fatty acids like palmitic to palmitoleic acid, and stearic to oleic acid. Based on this literature, unsaturated fatty acids, including oleic acid, were considered to suppress ferroptosis.

4.4.2.3 The experimental setup affects results for ferroptosis research

It has to be mentioned, that the experimental setups of studies reporting beneficial effects of unsaturated fatty acids differed from the MIN6 experiments, where oleic acid was used to mimic obesity-related pathophysiology. Comparing the treatment, it was remarkable that applied oleic acid concentration of articles stating positive effects remained low. The concentrations were 12.5-50 µM (Mann et al., 2024), 20 µM (Cotticelli et al., 2020), 62-125 µM (Yusuf et al., 2020), 80 µM (Kato et al., 2020; Z. Ye et al., 2022), 100 µM (H. Luo et al., 2022; L. Xu et al., 2024), 200 µM (Yinu Wang et al., 2024), 250 µM

(J. Xu et al., 2023), 400 µM (X. Xie et al., 2023), or 500 µM (Y. Xie et al., 2022). Few articles stated ferroptosis enhancing effects by oleic acid, and some of the applied concentrations tended to be higher as opposed to the previous references. They were 60 µM (Liao et al., 2022), 200 µM oleic acid plus 100 µM palmitic acid (Y. Yang et al., 2020; M. Zhu et al., 2023), 600 µM oleic acid (Altomare et al., 2022), or 600 µM oleic acid plus 1 µg/ml lipopolysaccharide (Z. Jiang et al., 2023). After reviewing the available literature on lipotoxic effects on mitochondria in cell models, the conclusion was reached that beneficial effects of fatty acids were mostly observed when applied at low concentrations (Römer et al., 2021). The choice of fatty acid concentration in cellular models was critical, as it significantly impacted experimental outcomes. Suitable fatty acid concentrations commonly used in cell models were around 0.5-2.0 mM (Mir et al., 2015; Wehinger et al., 2015). Analysis of total free fatty acids revealed 1.5-3.0 mM in the blood of a high fat diet mouse model (Petry et al., 2022). To assess the impact of a fatty acid treatment, the amount of unbound fatty acid was considered as more decisive parameter (Cnop et al., 2001). The equilibrium model of 0.5 mM oleic acid or palmitic acid bound to 1 % BSA detected only low amounts of unbound fatty acid with 47 nM or 27 nM. In the current MIN6 protocol, 0.5 mM fatty acid with a molar 5:1 ratio resulted in 0.66 % BSA. This information could be transferred that the MIN6 protocol would result in higher nanomolar levels of unbound oleic acid. Plasma fatty acid levels in diabetic patients were only slightly changed, with a 10 % increase compared to healthy individuals (Sergeant et al., 2016). Arguing about transferability of fatty acid concentrations was difficult due to a heterogeneity of the literature. Like previously described for the impact on ferroptosis, the results varied strongly and supported pathways promoting and inhibiting ferroptosis. Also there was evidence for a beneficial association between oleic acid and a decreased risk of diabetes (Yuan & Larsson, 2020), and an unfavorable association of plasma fatty acids as diabetogenic indicator increasing blood glucose and HbA_{1c} (E. A. Yu et al., 2018). While pathways promoting lipotoxicity were described extensively herein, there were also explanations for beneficial effects (Chen et al., 2020; Zheng Li et al., 2020; Zhao et al., 2013). Positive effects were frequently described after fatty acid treatment with low concentrations and within few hours. While under these conditions, negative consequences omit, and insulin secretion was promoted by improved lipid metabolism activating PPARγ or PPARγ coactivator 1 α (Oropeza et al., 2015), increased GPR40 mediated calcium influx and relieved oxidative distress by UCP2 induction (Ježek et al., 2015), or provided ATP for insulin secretion by

β-oxidation (Green et al., 2009). This highlighted the confusing and partially contradicting evidence towards fatty acid mediated effects, which can only be solved by rigorous protocols.

4.4.2.4 Iron regulation in β-cells

If ACO1 activity was altered by oleic acid, dysregulation of the iron metabolism may occur, leading to an increase in cellular free iron through upregulation of TfR1 and DMT1 and suppressing ferritin and ferroportin (Ouyang et al., 2023). β-cells and MIN6 cells (Mao et al., 2017; Shu et al., 2019) generally expressed all of the relevant iron-regulating proteins, including TfR1, ferritin, ferroportin, DMT1, and hepcidin (Ikeda et al., 2020; Kimita et al., 2024). Hepcidin expression was also suppressed by p-Akt (Mleczko-Sanecka et al., 2014), which increased ferroportin levels. Thus, low levels of p-Akt could theoretically have decreased iron export via ferroportin. Levels of TfR1, ferritin, and DMT1 were higher in β-cells compared to α-cells, likely due to increased iron demand for cellular activity (Berthault et al., 2020). However, the increased expression of iron import proteins rendered these cells more susceptible to iron overload (Koch et al., 2003). Increased iron levels were predictive for type 2 diabetes and ferritin was elevated to compensate for higher serum iron in patients (Altamura et al., 2017; Bonfils et al., 2015).

4.4.2.5 Implications for ferroptosis research in diabetes models

In MIN6 cells, treatment with oleic acid significantly decreased FTL protein levels (Figures 52, 53, 55), which would be in accordance to IRP1 regulation promoting free iron. Ferritin degradation under oxidative distress has been demonstrated in a high fat diet model in rats (Meli et al., 2013). This free iron constituted the labile iron pool, which participated in detrimental reactions, including the formation of lipid peroxides with cell membranes. Excessive lipid peroxides can cause cell death if GPx4-mediated detoxification was overwhelmed. Immunoblotting for GPx4 revealed ambiguities. While the clearest signals were observed in wild type MIN6 cells, GPx4 levels appeared to decrease with increased oleic acid concentration (Figure 56), suggesting a diminished antioxidant defense in already stressed β-cells (Xue et al., 2023). Lipid peroxide accumulation would be plausible, but data interpretation was impeded in the first transfection model by cross-reactivity and high standard deviations (Figure 57). Although the mean values suggested a similar pattern of oleic treatment, the results were inconclusive. Signals from the second transfection model were weak, and no clear effect

of oleic acid was observed (Figure 58). The literature reported unchanged GPx4 levels after oleic acid treatment, which was considered to confer protection against ferroptosis (Magtanong et al., 2019). These findings added a controversial dimension to the role of unsaturated fatty acids in ferroptosis. For example, monounsaturated fatty acids like oleic acid may counteracted lipid peroxidation in cell membranes, unlike polyunsaturated fatty acids. This protective effect selectively inhibited ferroptosis-related cell death induced by erastin, dependent on oleic acid activation by ACSL3. Considering all MIN6 experiments, the results for GPx4 remained elusive. Genetic analyses could further investigate ferroptosis mechanisms. For instance, qPCR could assess iron-regulating protein-related RNA levels to determine ACO1's influence. RNA band-shift assays could evaluate RNA-binding activity of IRP (Meli et al., 2013). In the recent project, protein levels were assessed as relevant factor eventually affecting cellular phenotype. Further experiments should measure intracellular iron and lipid peroxides using selective fluorescence dyes (Nishizawa et al., 2020; Yan Zhang et al., 2023). Such studies could elucidate whether ferritin downregulation was due to decreased intracellular iron or increased mitochondrial iron leading to lipid peroxide formation. Additionally, GPx4's antioxidative capacity could be examined using specific inhibitors such as erastin (Shao et al., 2022), or ML162 and RSL3, which indirectly inhibit thioredoxin reductase 1 (Cheff et al., 2023). The current data suggested that ferritin-mediated changes in iron storage could negatively impact β-cells. Further experiments could explore the consequences of intracellular iron shifts for lipid peroxide formation. Nuclear factor erythroid-2-related factor 2 (Nrf2), which regulated GPx4 and ferritin via SLC7A11, the subunit of system xc^-, may also were involved (Anandhan et al., 2023). Other factors, such as Kelch-like ECH-associated protein 1 (KEAP1), HECT and RLD domain containing E3 ubiquitin protein ligase 2 (HERC2), vesicle associated membrane protein 8 (VAMP8), and nuclear receptor co-activator 4 (NCOA4), were implicated in this axis, which has been proposed to sensitize cancer cells to chemotherapy via ferroptosis (Cai et al., 2023; Duarte et al., 2021). GPx4-independent pathways of ferroptosis also warrant investigation.

4.4.2.6 Methodological considerations for analysis of iron metabolism

The FTL results (Figures 52, 53) showed a significant increase in the control group compared to the DMEM group. This effect was likely caused by ethanol, consistent with reports in HepG2 cells treated with 300 mM ethanol (Moirand et al., 1995). In the MIN6

protocol, ethanol concentrations in treatment solutions were approximately 70 mM, indicating that ethanol in fatty acid control solutions affected protein blotting results for iron metabolism. This highlighted the importance of standardized protocols. Evaluation of all assay results indicated no severe damaging effect of ethanol to the cells. This would be expected for concentrations over 1 %, confirmed by MTT assays (Supplement Figure 2). By using different stock solutions for fatty acid treatment, the ethanol concentration was differing from 0.23 % to 0.31 %. Regarding transferability, it should be considered once that this was equivalent to 2.3-3.1 ‰ over a 5 d time period. To unify ethanol percentages in future experiments, oleic acid could be dissolved in water-diluted ethanol. If further experiments should be performed, this would be recommended to eliminate multiple ethanol percentages as disturbing factor. For the recent experimental setup, absolute ethanol would be used to prepare 900 mM oleic acid, whereas 83.4 vol% ethanol would be used for 450 mM, and 77.1 vol% ethanol for 225 mM, resulting in a final ethanol concentration of 0.23 % across all groups. Regarding this project, the differing ethanol was not considered as severe confounder. Despite its weaker adverse effect on cells, it was not recommended to use DMSO as alternative, as the solubility of different fatty acids was differing between the solvents, giving the example by manufacturer information (Cayman Chemical, Item No. 10006627 and 90260) especially for palmitic acid with a solubility in DMSO (20 mg/ml) only a fifth compared to oleic acid (> 100 mg/ml). Ethanol ensured comparable conditions for different fatty acids. Ferritin and IRP1 were known to respond to cell density, which may influenced ferroptosis (Yan et al., 2024). Higher cell density inhibited proliferation, decreasing iron uptake and utilization (Pourcelot et al., 2015). In theory, it could be possible that control cells had a higher proliferation rate reaching early confluence compared to oleic acid treated cells. A cellular response could be an increase of ferritin by control cells because of restricted proliferation (Yan et al., 2024). But it has to be considered that in the recent experiment it was unknown if oleic acid decreased cell numbers per plate by enhanced apoptosis or by decreased proliferation. In the first case, the remaining cells would have required iron and low levels of ferritin, while in the second case, no iron would be required and ferritin was elevated. Apart from theory, the explanation of ferritin reactivity upon cell density was not plausible for the recent experiments. The difference of ferritin between DMEM and control group disagreed with an effect by cell density, because the control group did not had an effect on cell amount in experiments compared to DMEM. The cell number was assessed by an associated project after 5 d, starting with $3*10^5$ cells

in a T25 flask, culturing MIN6 cells with DMEM, control treatment, or 1.5 mM oleic acid or palmitic acid (7.75 ± 2.36 *10^5, with DMEM; 6.15 ± 1.44 *10^5, at 0 mM; 3.94 ± 1.61 *10^5, at 1.5 mM oleic acid; 3.88 ± 1.14 *10^5, at 1.5 mM palmitic acid, n = 5, by Kim Kühne, unpublished). Impairing effects on cell confluence were suspected only at 3 mM oleic acid, which would increase ferritin levels depending on cell density. By comparing the gathered information, it was unlikely that FTL changes were caused by cell density. Counting MIN6 cells prior to sample preparation, revealed an unexpected effect upon fatty acid treatment, affecting cell numbers differently depending on flask size. In T25 flasks, cell count remained stable after treatment with 1.5 mM or 3 mM oleic acid (Figures 10, 36), while T75 flasks showed a decrease (Figures 24, 54). An explanation could be the ratio of growing area to edges of the flask, as cell density and volume of treatment media was adjusted to the flask size. Cells in smaller flasks tended to cluster in the center, possibly creating a denser network that offered protection against treatment media. This phenomenon was observed incidentally and could be systematically studied but was not considered a confounding factor in the current analysis. In summary, cell number was not predictive of the outcome for the analyzed parameters. While cell numbers of the T25 flask were unchanged, respiration was differing at 3 mM treatment (Figure 37). In contrast, the Fe-S enzyme activities were decreased for ACO1 or unchanged for ACO2, SDH, or COX (Figures 25, 28), while cell numbers were differing following oleic acid treatment.

4.4.2.7 The relevance of Glutaredoxin 5 transfection for iron metabolism

The observed effects on cell count and ferroptosis-related analyses, such as FTL immunoblotting, remained unchanged following Glrx5 transfection. Considering the limited transfection efficiency, future experiments at the single-cell level would be highly informative. For instance, correlating Glrx5 expression with altered targets like ACO1 or FTL through double-labeling cells with specific antibodies using immunocytochemistry could provide valuable insights. This approach would help determine whether transfected cells with individual elevated Glrx5 levels exhibited positive transfection effects that were obscured in the current experiments, which reflected the mean response of both the transfected and non-transfected MIN6 cells. Beyond the presented results, previous studies have demonstrated the relationship between Glrx5 and iron regulation in fungi (Tamayo et al., 2016), plants (S. Zhou et al., 2024), and a stem cell model (Yanting Liu

et al., 2024), alongside case reports earlier mentioned (Daher et al., 2019; H. Ye et al., 2010). In the MIN6 model, a novel finding was that changes in ACO1 activity and FTL levels occurred with oleic acid treatment alone. Given that EndoC-βH3 cells exhibited similar ATP level responses to MIN6 cells (Figure 41), it would be informative to replicate the described effects in EndoC-βH3 cells. Investigating ACO1 activity, as well as ACO1 and FTL protein levels, would offer significant insights into the transferability of ferroptosis-related findings to a human model.

4.4.2.8 Further potential iron-sulfur proteins as targets in lipotoxicity research

While the project primarily focused on mitochondrial and ferroptosis-related proteins, additional data from MIN6 cells revealed changes in cytosolic Fe-S cluster proteins. Notably, PolD1 and GPAT, associated with DNA and purine biosynthesis, and Glrx3, involved in cytosolic Fe-S cluster transfer, responded to oleic acid treatment. PolD1, in particular, showed a pronounced response in the transfection models (Figures 46, 47), whereas this effect was weaker in the wild type model, even with extended treatment duration (Figure 45). The absence of a pronounced effect in wild type cells remained unexplained. Information to mutational changes of PolD1 have been linked to mandibular hypoplasia, deafness, progeroid features, and lipodystrophy (MDPL) syndrome, with occasional reports of diabetes correlating with hypertriglyceridemia (Reinier et al., 2015; Sasaki et al., 2018; L. R. Wang et al., 2018; L. Zhou et al., 2022). Reviews suggested connections to diabetes, possibly mediated by progeria and disruptions in glycolysis and the Krebs cycle (Nicolas et al., 2016; Vatier et al., 2013). In contrast, GPAT exhibited decreased immunoblotting signals with increased oleic acid concentrations in the wild type model (Figure 48). However, this finding was inconsistent and could not be replicated in the transfection models (Figures 49, 50). No prior studies have linked GPAT to diabetes. So far, the reactivities of PolD1 and GPAT inducible by fatty acids or a connection to lipotoxicity were not described. Since the effects were convincing by immunoblotting, these proteins should be included as further possible targets in the field of lipotoxicity, which needed more data to prove an involvement. These findings added two further Fe-S cluster proteins, PolD1 and GPAT, to the list of candidates responsive to Fe-S cluster deficiency (Martelli et al., 2007; Netz et al., 2012). Notably, these effects were independent of Glrx5 transfection. Given that other Fe-S proteins were unaffected

by fatty acid treatment, this supported the hypothesis that Glrx5 did not mediate the observed impairments. Overall, the effects induced by oleic acid were highly selective.

4.4.2.9 Glutaredoxin 3 as additional extra-mitochondrial iron-sulfur cluster distributing protein

The cytosolic effects of oleic acid treatment highlighted the potential relevance of Glrx3, a cytosolic Fe-S cluster transfer factor (Camponeschi et al., 2020). Immunoblotting revealed weaker Glrx3 signals in the transfection model by oleic acid (Figure 51). Considering previous findings (Petry et al., 2017), both Glrx3 and its homolog Glrx4 should be evaluated as potential contributors to the pathogenesis of type 2 diabetes. A minor adjustment to the current hypothesis could position cytosolic Glrx3 as a meaningful factor in lipotoxicity, rather than mitochondrial Glrx5. Additionally, pathways related to Fe-S clusters could still be explored. The involvement of Glrx3/Glrx4 in lipotoxicity and ferroptosis was supported by literature. Transcriptome analysis in high fat fed mice identified Glrx3 as a protective factor against heart failure (N. Cheng et al., 2021). A shift in redox balance was suggested as underlying factor. Glrx3 functionality, dependent on intact mitochondria, was linked to IRP1 and GPAT (Braymer et al., 2024; Haunhorst et al., 2013), potentially mediated by anamorsin (Ciofi-Baffoni et al., 2018). The GPAT effect was dependent on CIA factors NUBP1 and NARFL (Ferecatu et al., 2014). Interactions between Glrx3/Glrx4 and iron regulation were demonstrated in various species, including mice (N. Cheng et al., 2023), zebrafish (Haunhorst et al., 2013), fungi (Alkafeef et al., 2020; Attarian et al., 2018; McCotter et al., 2023; D. Zhang et al., 2017), yeast (Jbel et al., 2011; K.-D. Kim et al., 2011; Ojeda et al., 2006), and bacteria (H. Xia et al., 2015). The CCAAT-binding factor complex, involving its subunit protein Php4, was shown to interact with Glrx4 under low-iron conditions in *Schizosaccharomyces pombe* (Mercier & Labbé, 2009; Vachon et al., 2012). Other Glrxs, such as monothiols GrxS17 in *Arabidopsis thaliana* (N. Cheng et al., 2020; H. Yu et al., 2017) or GrxD in *Aspergillus fumigatus* (Misslinger et al., 2019), were also implicated as Fe-S cluster factors. Dithiol Glrx2 connected to redox balance, but independent from Fe-S cluster, was involved in iron regulation shown in *Saccharomyces cerevisiae* (McDonagh et al., 2011) or a dopaminergic cell model (D. W. Lee et al., 2009). The obtained data identified several Fe-S cluster related proteins in MIN6 cells responding to oleic acid treatment independently of Glrx5. These findings provided new opportunities for research into type 2 diabetes and suggested a broader scope for future investigations.

4.5 Relevance of the topic

The impairment of cellular functions by lipid stressors, collectively known as lipotoxicity, is a major factor in the progression of type 2 diabetes. Despite over 30 years of research on the underlying pathways, type 2 diabetes remains a persistent disease with a steadily increasing incidence. Therefore, additional research to identify new therapeutic approaches and targets is essential for improving treatment. Starting in 2018 (Wenz et al., 2018), ferroptosis has been identified as a contributing factor in type 2 diabetes progression (Miao et al., 2023), compromising β-cell function through increased oxidative burden caused by free iron and lipid peroxides. Impairments in Glrx5 have been proposed as a potential mediator, initiating dysregulated iron metabolism through its connection with Fe-S clusters and IRP1, as evidenced by case reports (Camaschella et al., 2007; Daher et al., 2019; G. Liu et al., 2014). The synthesis of Fe-S clusters is among the most fundamental cellular functions required by numerous proteins (Rouault & Tong, 2005). Furthermore, impaired Glrx5 promotes mitochondrial dysfunction. Glrxs have been shown to be negatively affected by lipotoxicity in diabetic models (Petry et al., 2018). Given their crucial role in cellular and mitochondrial metabolism, this project aimed to expand the current knowledge of lipotoxic effects, with a particular focus on Glrx5, mitochondria, and ferroptosis.

4.6 Summary of experiments

The previous sections elucidated the effects of oleic acid on MIN6 and EndoC-βH3 cells which were further investigated in genetically altered Glrx5 overexpressing MIN6 cells. Overall, oleic acid treatment had detrimental effects on cellular characteristics or remained in some experiments neutral. The experiments with biologically negative changes included MTT, qPCR for *Ins2*, ELISA for Glrx5 and insulin in the wild type model, ACO1 activity, respirometry with ATP levels, and immunoblotting signals for PolD1, GPAT, NDUFB8, FTL, PDX1, and p-ERK1/2. A further experiment with a potential negative impact was immunoblotting for Glrx3, but data interpretation was in general difficult and not strikingly convincing. None of the effects were altered by Glrx5 transfection. In contrast, several experiments showed no change after oleic acid treatment, including qPCR for *Glrx5*, immunoblotting for Glrx5 in the wild type model, ELISA and immunoblotting for Glrx5 in the transfected model, all Fe-S enzyme activities except for ACO1, and immunoblotting for ACO1, ACO2, COX-2, COX-6 A/B, UQCRC2,

UQCRFS1, ERK1/2, and Akt. Experiments with weak or unobservable effects included insulin ELISA in the transfected model and immunoblotting signals for GPx4 and p-Akt.

4.7 Study limitations

While many experiments provided valuable insights into Fe-S clusters in a diabetes model, some limitations should be noted. Establishing a stable Glrx5 transfected model with high transfection efficiency would greatly enhance data interpretation. Moreover, the use of a knockdown or knockout model could clarify the results. Stable transfection could be achieved through electroporation or lentiviral transduction. A stable model would allow for extended treatment times, facilitating the identification of affected proteins. Experiments that would benefit from longer treatment durations include Glrx5 and insulin ELISA, as well as immunoblotting for GPAT, Glrx3, and GPx4. The current transfection rate, as detected by FACS analysis, was 24 %, which means the experiments reflected the average of transfected and non-transfected cells. Single-cell analysis using immunocytochemistry would allow for a more precise correlation of target proteins with Glrx5, which would enhance knowledge. Similarly, measurements of free iron in individual cells and genetic regulation of IRP1-associated proteins would complement the results for FTL signals. These experiments highlighted the heterogeneity of the analyzed parameters. Although only a small portion of cells were transfected with Glrx5, a clear signal by immunoblotting and a massive induction by qPCR were observed. Insights into mitochondrial respiration also varied depending on whether isolated enzymes or functional mitochondria were analyzed. These results encouraged for extensive analysis to provide a comprehensive interpretation. Not all proteins could be addressed that detailed, and broader approaches could further elucidate the system. Despite the transfection limitations, the establishment of transfected MIN6 cells was successful, and their basic cellular behavior was comparable to wild type MIN6 cells. The transferability of results from cell culture to patients remained limited. Increasing sample sizes would increase meaningfulness of almost every experiment, though valuable insights were obtained even with low replication numbers. This underscores the profound cellular impact of oleic acid, as evidenced by ACO1 activity and immunoblotting signals for PolD1, FTL, PDX1, and p-ERK1/2. While MIN6 cells served as a reliable model for Fe-S cluster and mitochondrial analyses, the C57BL/6 Glrx5 knock-in model left most questions unanswered. The knock-in of Glrx5 could not be confirmed by immunoblotting. Further challenges included the identification of suitable reference proteins.

β-III-tubulin posed great difficulties for detection, while YL1/2 tubulin was visible in various organs. Organ and islet preparation showed reasonable results, as evidenced by GAPDH control. Notably, the ability to directly blot islets presented an intriguing opportunity for diabetes research. Immunoblotting images of pancreatic islets were rarely found in the literature. Although isolated islets could be used, the need for large numbers of animals for pooling islets limited extended studies. Ethical considerations regarding animal research further restricted the feasibility of more extensive experiments.

4.8 Reviewing study objectives and conclusion

The analysis of MIN6 cells under lipotoxic conditions showed an impaired metabolism, including compromised insulin synthesis. While mitochondrial dysfunction was a well described contributor to the progression of type 2 diabetes (Samuel & Shulman, 2019), many mitochondrial factors in MIN6 cells remained unaffected. The observed changes in respiration were likely due to ATP-dependent inhibition rather than a general mitochondrial defect. In contrast, outer-mitochondrial targets, such as ACO1, FTL, PolD1, GPAT, p-ERK1/2, and PDX1, showed more pronounced sensitivity to lipotoxicity. The changes in ACO1 activity and FTL expression suggested a ferroptosis-related pattern. The consequences of dysregulated iron regulation due to lipotoxic treatment should be explored in further experiments. Although valuable insights were gained from MIN6 and EndoC-βH3 cell models, the questions related to C57BL/6 Glrx5 knock-in mice remained unanswered. In summary, oleic acid negatively affected selective Fe-S proteins in MIN6 cells, but Glrx5 transfection did not offer protective effects in the experiments. It was unlikely that the observed effects were due to a Glrx5-mediated Fe-S cluster defect. An alternative hypothesis could involve the cytosolic monothiol Glrx3, which presented a promising target for further hypotheses. Knowledge was gained on Fe-S cluster related factors and changes in iron regulation, which may play a pivotal role in metabolic dysfunction and type 2 diabetes. This could pave the way for further projects expanding the information regarding the fascinating section of Fe-S clusters and lipotoxicity.

Abstract

Glutaredoxin 5 (Glrx5), a key carrier protein for iron-sulfur clusters within the mitochondrial iron-sulfur cluster assembly machinery, may represent a relevant mechanism contributing to the development of type 2 diabetes under lipotoxic stress. Impairments in iron-sulfur clusters can lead to mitochondrial dysfunction and dysregulated iron homeostasis, triggering iron-dependent peroxidation of cell membranes and β-cell decay (ferroptosis). Such disruptions in mitochondrial integrity can have profound consequences on cellular metabolism and survival. Treatment of wild type and Glrx5-modified MIN6 cells with oleic acid revealed a detrimental shift in NADH dependent redox potential, as assessed by MTT analysis. Protein analysis showed diminished levels of intracellular insulin and Glrx5, along with decreased *Ins2* gene expression, while *Glrx5* gene expression remained unchanged, suggesting post-transcriptional regulatory mechanisms. Among iron-sulfur proteins upon oleic acid treatment, cytosolic aconitase activity was attenuated, accompanied by lower protein levels of PolD1 and GPAT. In contrast, mitochondrial aconitase activity, respiratory chain complexes II, III, and IV, and immunoblot signals of cytosolic aconitase, mitochondrial aconitase, UQCRC2, UQCRFS1, COX-2, and COX-6 A/B remained unaffected, highlighting a selective vulnerability to lipotoxic stress. Additional proteins unrelated to Glrx5, such as p-ERK1/2, PDX1, NDUFB8 and the iron-storage protein ferritin light chain, were negatively impacted by oleic acid treatment, further emphasizing the complex regulatory network involved in iron metabolism. Functional impairments in mitochondrial respiration and ATP levels were detected. All observed effects were not reversed by Glrx5 transfection, indicating that Glrx5 may not be the major factor for lipotoxic pathophysiology. Similarly, oleic acid treatment of human EndoC-βH3 cells mirrored the ATP level response seen in MIN6 cells, reinforcing the potential relevance of these findings for human β-cell physiology. The attenuation of cytosolic aconitase activity, despite unchanged immunoblot signals, could be caused by a loss of the iron-sulfur cluster. This could disrupt iron regulation, as indicated by ferritin levels. The findings highlight the response of selected iron-sulfur proteins to lipotoxic stress, suggesting their potential role in the pathogenesis of type 2 diabetes. Further experimental exploration of lipotoxicity-related mechanisms and their impact on mitochondrial and cytosolic iron-sulfur proteins is essential for understanding the development and potential therapeutic targets of type 2 diabetes.

Zusammenfassung

Glutaredoxin 5 (Glrx5), ein zentrales Transportprotein innerhalb der mitochondrialen Eisen-Schwefel Cluster Assemblierungsmaschinerie, könnte ein relevanter Mechanismus sein, der unter lipotoxischem Stress zur Entstehung von Typ 2 Diabetes beiträgt. Störungen der Eisen-Schwefel Cluster können mitochondriale Dysfunktion und eine gestörte Eisenregulation verursachen, wodurch eisenabhängige Peroxidationen von Zellmembranen β-Zell Verlust (Ferroptose) hervorrufen könnten. Die Behandlung von Wildtyp und Glrx5-genmodifizierten MIN6 Zellen mit Ölsäure führte zu einer nachteiligen Veränderung des NADH vermittelten Redoxpotentials, gemessen durch MTT Reduktion. Die Proteinanalyse zeigte verminderte Mengen an intrazellulärem Insulin und Glrx5, sowie eine abgeschwächte *Ins2* Genexpression, während die *Glrx5* Genexpression unverändert blieb, was auf post-transkriptionelle Regulations-mechanismen hindeuten könnte. Bei den Eisen-Schwefel Proteinen wurde eine herabgesetzte Aktivität der cytosolischen Aconitase sowie eine geringere Proteinexpression von PolD1 und GPAT festgestellt. Die Aktivitäten der mitochondrialen Aconitase, der Atmungskettenkomplexe II, III und IV sowie die Immunoblot Signale der cytosolischen Aconitase, mitochondrialen Aconitase, UQCRC2, UQCRFS1, COX-2 und COX-6 A/B waren nicht beeinträchtigt, wodurch eine selektive Anfälligkeit gegenüber lipotoxischem Stress gezeigt wurde. Weitere, nicht mit Glrx5 assoziierte Proteine, wie p-ERK1/2, PDX1, NDUFB8 und das Eisenspeicherprotein Ferritin (leichte Kette) wurden durch Ölsäure negativ beeinflusst, was die komplexe Regulation des Eisenstoffwechsels verdeutlicht. Funktionelle Beeinträchtigungen der mitochondrialen Atmung und des intrazellulären ATPs wurden detektiert. Alle beobachteten Effekte wurden nicht durch die Glrx5-Transfektion aufgehoben, wobei Glrx5 eine untergeordnete Bedeutung in der Pathophysiologie der Lipotoxizität zukommen könnte. Eine vergleichbare Reaktion der ATP Spiegel wurde in humanen EndoC-βH3 Zellen beobachtet, womit die Relevanz der Ergebnisse für die menschliche β-Zell Physiologie untermauert wird. Die eingeschränkte Aktivität der cytosolischen Aconitase trotz unveränderter Immunoblot Signale könnte durch den Verlust des Eisen-Schwefel Clusters erklärt werden, welche eine gestörte Eisenregulation zur Folge haben könnte, wie durch Ferritin gezeigt wurde. Die Ergebnisse deuten darauf hin, dass ausgewählte Eisen-Schwefel Proteine auf lipotoxischen Stress reagieren, und in weiterführenden Studien für die Pathogenese des Typ 2 Diabetes von Bedeutung sein könnten. Das Verständnis weiterer Mechanismen, die mit Lipotoxizität in Verbindung stehen, sowie deren Auswirkungen auf mitochondriale und cytosolische Eisen-Schwefel-Enzyme ist entscheidend für die Erforschung der Diabetes Pathogenese und potenzieller therapeutischer Zielstrukturen.

References

Abrosimov, R., Baeken, M. W., Hauf, S., Wittig, I., Hajieva, P., Perrone, C. E., & Moosmann, B. (2024). Mitochondrial complex I inhibition triggers NAD+-independent glucose oxidation via successive NADPH formation, “futile” fatty acid cycling, and FADH2 oxidation. *GeroScience*, *46*(4), 3635–3658. https://doi.org/10.1007/s11357-023-01059-y

Adams, M. T., & Blum, B. (2022). Determinants and dynamics of pancreatic islet architecture. *Islets*, *14*(1), 82–100. https://doi.org/10.1080/19382014.2022.2030649

Addess, K. J., Basilion, J. P., Klausner, R. D., Rouault, T. A., & Pardi, A. (1997). Structure and dynamics of the iron responsive element RNA: implications for binding of the RNA by iron regulatory binding proteins. *Journal of Molecular Biology*, *274*(1), 72–83. https://doi.org/10.1006/jmbi.1997.1377

Aharon-Hananel, G., Romero-Afrima, L., Saada, A., Mantzur, C., Raz, I., & Weksler-Zangen, S. (2022). Cytochrome c Oxidase Activity as a Metabolic Regulator in Pancreatic Beta-Cells. *Cells*, *11*(6), 929. https://doi.org/10.3390/cells11060929

Aitken, R. J., Gregoratos, D., Kutzera, L., Towney, E., Lin, M., Wilkins, A., & Gibb, Z. (2020). Patterns of MTT reduction in mammalian spermatozoa. *Reproduction*, *160*(3), 431–445. https://doi.org/10.1530/REP-20-0205

Alfattal, R., Alfarhan, M., Algaith, A. M., Albash, B., Elshafie, R. M., Alshammari, A., et al. (2023). LYRM7-associated mitochondrial complex III deficiency with non-cavitating leukoencephalopathy and stroke-like episodes. *American Journal of Medical Genetics Part A*, *191*(5), 1401–1411. https://doi.org/10.1002/ajmg.a.63143

Alkafeef, S. S., Lane, S., Yu, C., Zhou, T., Solis, N. V., Filler, S. G., et al. (2020). Proteomic profiling of the monothiol glutaredoxin Grx3 reveals its global role in the regulation of iron dependent processes. *PLOS Genetics*, *16*(6), e1008881. https://doi.org/10.1371/journal.pgen.1008881

Altamura, S., Kopf, S., Schmidt, J., Müdder, K., da Silva, A. R., Nawroth, P., & Muckenthaler, M. U. (2017). Uncoupled iron homeostasis in type 2 diabetes mellitus. *Journal of Molecular Medicine*, *95*(12), 1387–1398. https://doi.org/10.1007/s00109-017-1596-3

Altomare, A. A., Aiello, G., Garcia, J. L., Garrone, G., Zoanni, B., Carini, M., et al. (2022). Protein Profiling of a Cellular Model of NAFLD by Advanced Bioanalytical Approaches. *International Journal of Molecular Sciences*, *23*(16), 9025. https://doi.org/10.3390/ijms23169025

An, Y. A., Chen, S., Deng, Y., Wang, Z. V., Funcke, J.-B., Shah, M., et al. (2021). The mitochondrial dicarboxylate carrier prevents hepatic lipotoxicity by inhibiting white adipocyte lipolysis. *Journal of Hepatology*, *75*(2), 387–399. https://doi.org/10.1016/j.jhep.2021.03.006

Anandhan, A., Dodson, M., Shakya, A., Chen, J., Liu, P., Wei, Y., et al. (2023). NRF2 controls iron homeostasis and ferroptosis through HERC2 and VAMP8. *Science Advances*, *9*(5). https://doi.org/10.1126/sciadv.ade9585

Anderson, C. P., Shen, M., Eisenstein, R. S., & Leibold, E. A. (2012). Mammalian iron metabolism and its control by iron regulatory proteins. *Biochimica et Biophysica Acta (BBA) - Molecular Cell Research*, *1823*(9), 1468–1483. https://doi.org/10.1016/j.bbamcr.2012.05.010

Andreini, C., Bertini, I., & Rosato, A. (2009). Metalloproteomes: A Bioinformatic Approach. *Accounts of Chemical Research*, *42*(10), 1471–1479. https://doi.org/10.1021/ar900015x

Andreini, C., Banci, L., & Rosato, A. (2016). Exploiting Bacterial Operons To Illuminate Human Iron–Sulfur Proteins. *Journal of Proteome Research*, *15*(4), 1308–1322. https://doi.org/10.1021/acs.jproteome.6b00045

Andreini, C., Rosato, A., & Banci, L. (2017). The relationship between environmental dioxygen and iron-sulfur proteins explored at the genome level. *PLoS ONE*, *12*(1), e0171279. https://doi.org/10.1371/journal.pone.0171279

Antollini, S. S., & Barrantes, F. J. (2016). Fatty Acid Regulation of Voltage- and Ligand-Gated Ion Channel Function. *Frontiers in Physiology*, *7*(NOV), 573. https://doi.org/10.3389/fphys.2016.00573

Arenbaoligao, Guo, X., Xiong, J., Zhang, S., Yang, Y., Chen, D., & Xie, Y. (2023). Kumatakenin inhibited iron-ferroptosis in epithelial cells from colitis mice by regulating the Eno3-IRP1-axis. *Frontiers in Pharmacology*, *14*, 1127931. https://doi.org/10.3389/fphar.2023.1127931

Arnold, S., & Kadenbach, B. (1997). Cell Respiration is Controlled by ATP, an Allosteric Inhibitor of Cytochrome- c Oxidase. *European Journal of Biochemistry*, *249*(1), 350–354. https://doi.org/10.1111/j.1432-1033.1997.t01-1-00350.x

Arruda, A. P., & Hotamisligil, G. S. (2015). Calcium Homeostasis and Organelle Function in the Pathogenesis of Obesity and Diabetes. *Cell Metabolism*, *22*(3), 381–397. https://doi.org/10.1016/j.cmet.2015.06.010

Arunagiri, A., Alam, M., Haataja, L., Draz, H., Alasad, B., Samy, P., et al. (2024). Proinsulin folding and trafficking defects trigger a common pathological disturbance of endoplasmic reticulum homeostasis. *Protein Science*, *33*(4), e4949. https://doi.org/10.1002/pro.4949

Aslund, F., Ehn, B., Miranda-Vizuete, A., Pueyo, C., & Holmgren, A. (1994). Two additional glutaredoxins exist in Escherichia coli: glutaredoxin 3 is a hydrogen donor for ribonucleotide reductase in a thioredoxin/glutaredoxin 1 double mutant. *Proceedings of the National Academy of Sciences*, *91*(21), 9813–9817. https://doi.org/10.1073/pnas.91.21.9813

Attarian, R., Hu, G., Sánchez-León, E., Caza, M., Croll, D., Do, E., et al. (2018). The Monothiol Glutaredoxin Grx4 Regulates Iron Homeostasis and Virulence in Cryptococcus neoformans. *MBio*, *9*(6). https://doi.org/10.1128/mBio.02377-18

Azucenas, C. R., Ruwe, T. A., Bonamer, J. P., Qiao, B., Ganz, T., Jormakka, M., et al. (2023). Comparative analysis of the functional properties of human and mouse ferroportin. *American Journal of Physiology-Cell Physiology*, *324*(5), C1110–C1118. https://doi.org/10.1152/ajpcell.00063.2023

Baker, P. R., Friederich, M. W., Swanson, M. A., Shaikh, T., Bhattacharya, K., Scharer, G. H., et al. (2014). Variant non ketotic hyperglycinemia is caused by mutations in LIAS, BOLA3 and the novel gene GLRX5. *Brain*, *137*(2), 366–379. https://doi.org/10.1093/brain/awt328

Baltrusch, S., & Lenzen, S. (2007). Novel insights into the regulation of the bound and diffusible glucokinase in MIN6 β-cells. *Diabetes*, *56*(5), 1305–1315. https://doi.org/10.2337/db06-0894

Banci, L., Bertini, I., Ciofi-Baffoni, S., Boscaro, F., Chatzi, A., Mikolajczyk, M., et al. (2011). Anamorsin Is a [2Fe-2S] Cluster-Containing Substrate of the Mia40-Dependent Mitochondrial Protein Trapping Machinery. *Chemistry & Biology*, *18*(6), 794–804. https://doi.org/10.1016/j.chembiol.2011.03.015

Banci, L., Brancaccio, D., Ciofi-Baffoni, S., Del Conte, R., Gadepalli, R., Mikolajczyk, M., et al. (2014). [2Fe-2S] cluster transfer in iron–sulfur protein biogenesis. *Proceedings of the National Academy of Sciences*, *111*(17), 6203–6208. https://doi.org/10.1073/pnas.1400102111

Banci, L., Camponeschi, F., Ciofi-Baffoni, S., & Muzzioli, R. (2015). Elucidating the Molecular Function of Human BOLA2 in GRX3-Dependent Anamorsin Maturation Pathway. *Journal of the American Chemical Society*, *137*(51), 16133–16143. https://doi.org/10.1021/jacs.5b10592

Barroso, E., Jurado-Aguilar, J., Wahli, W., Palomer, X., & Vázquez-Carrera, M. (2024). Increased hepatic gluconeogenesis and type 2 diabetes mellitus. *Trends in Endocrinology & Metabolism*, *35*(12), 1062–1077. https://doi.org/10.1016/j.tem.2024.05.006

Bays, H. (2013). Sodium Glucose Co-transporter Type 2 (SGLT2) Inhibitors: Targeting the Kidney to Improve Glycemic Control in Diabetes Mellitus. *Diabetes Therapy*, *4*(2), 195–220. https://doi.org/10.1007/s13300-013-0042-y

Bellary, S., Kyrou, I., Brown, J. E., & Bailey, C. J. (2021). Type 2 diabetes mellitus in older adults: clinical considerations and management. *Nature Reviews Endocrinology*, *17*(9), 534–548. https://doi.org/10.1038/s41574-021-00512-2

Benazra, M., Lecomte, M.-J., Colace, C., Müller, A., Machado, C., Pechberty, S., et al. (2015). A human beta cell line with drug inducible excision of immortalizing transgenes. *Molecular Metabolism*, *4*(12), 916–925. https://doi.org/10.1016/j.molmet.2015.09.008

Bender, K. W., Wang, X., Cheng, G. B., Kim, H. S., Zielinski, R. E., & Huber, S. C. (2015). Glutaredoxin AtGRXC2 catalyses inhibitory glutathionylation of Arabidopsis BRI1-associated receptor-like kinase 1 (BAK1) in vitro. *The Biochemical Journal*, *467*(3), 399–413. https://doi.org/10.1042/BJ20141403

Benes, C., Poitout, V., Marie, J.-C., Martin-Perez, J., Roisin, M.-P., & Fagard, R. (1999). Mode of regulation of the extracellular signal-regulated kinases in the pancreatic β-cell line MIN6 and their implication in the regulation of insulin gene transcription. *Biochemical Journal*, *340*(1), 219–225. https://doi.org/10.1042/0264-6021:3400219

Bernardi, P., Gerle, C., Halestrap, A. P., Jonas, E. A., Karch, J., Mnatsakanyan, N., et al. (2023). Identity, structure, and function of the mitochondrial permeability transition pore: controversies, consensus, recent advances, and future directions. *Cell Death & Differentiation*, *30*(8), 1869–1885. https://doi.org/10.1038/s41418-023-01187-0

Bernas, T., & Dobrucki, J. (2002). Mitochondrial and nonmitochondrial reduction of MTT: Interaction of MTT with TMRE, JC-1, and NAO mitochondrial fluorescent probes. *Cytometry*, *47*(4), 236–242. https://doi.org/10.1002/cyto.10080

Berndt, C., Christ, L., Rouhier, N., & Mühlenhoff, U. (2021). Glutaredoxins with iron-sulphur clusters in eukaryotes - Structure, function and impact on disease. *Biochimica et Biophysica Acta (BBA) - Bioenergetics*, *1862*(1), 148317. https://doi.org/10.1016/j.bbabio.2020.148317

Berridge, M. V., & Tan, A. S. (1993). Characterization of the Cellular Reduction of 3-(4,5-dimethylthiazol-2-yl)-2,5-diphenyltetrazolium bromide (MTT): Subcellular Localization, Substrate Dependence, and Involvement of Mitochondrial Electron Transport in MTT Reduction. *Archives of Biochemistry and Biophysics*, *303*(2), 474–482. https://doi.org/10.1006/abbi.1993.1311

Berridge, M. V., Herst, P. M., & Tan, A. S. (2005). Tetrazolium dyes as tools in cell biology: New insights into their cellular reduction. *Biotechnology Annual Review*, *11*, 127–152. https://doi.org/10.1016/S1387-2656(05)11004-7

Berthault, C., Staels, W., & Scharfmann, R. (2020). Purification of pancreatic endocrine subsets reveals increased iron metabolism in beta cells. *Molecular Metabolism*, *42*, 101060. https://doi.org/10.1016/j.molmet.2020.101060

Bi, Yan, Wu, W., Shi, J., Liang, H., Yin, W., Chen, Y., et al. (2014). Role for sterol regulatory element binding protein-1c activation in mediating skeletal muscle insulin resistance via repression of rat insulin receptor substrate-1 transcription. *Diabetologia*, *57*(3), 592–602. https://doi.org/10.1007/S00125-013-3136-1

Bi, Yaxin, Zhang, L., Li, X., Kan, Y., Li, S., Zou, Y., et al. (2021). Contributing factors of fatigue in patients with type 2 diabetes: A systematic review. *Psychoneuroendocrinology*, *130*, 105280. https://doi.org/10.1016/j.psyneuen.2021.105280

Blasco, F., Iobbi, C., Ratouchniak, J., Bonnefoy, V., & Chippaux, M. (1990). Nitrate reductases of Escherichia coli: Sequence of the second nitrate reductase and comparison with that encoded by the narGHJI operon. *Molecular and General Genetics MGG*, *222*(1), 104–111. https://doi.org/10.1007/BF00283030

Bonfils, L., Ellervik, C., Friedrich, N., Linneberg, A., Sandholt, C. H., Jørgensen, M. E., et al. (2015). Fasting serum levels of ferritin are associated with impaired pancreatic beta cell function and decreased insulin sensitivity: a population-based study. *Diabetologia*, *58*(3), 523–533. https://doi.org/10.1007/S00125-014-3469-4

Bou-Abdallah, F., Fish, J., Terashi, G., Zhang, Y., Kihara, D., & Arosio, P. (2024). Unveiling the stochastic nature of human heteropolymer ferritin self-assembly mechanism. *Protein Science*, *33*(8), e5104. https://doi.org/10.1002/PRO.5104

Bradford, M. M. (1976). A rapid and sensitive method for the quantitation of microgram quantities of protein utilizing the principle of protein-dye binding. *Analytical Biochemistry*, *72*(1–2), 248–254. https://doi.org/10.1016/0003-2697(76)90527-3

Brandon, A. E., Liao, B. M., Diakanastasis, B., Parker, B. L., Raddatz, K., McManus, S. A., et al. (2019). Protein Kinase C Epsilon Deletion in Adipose Tissue, but Not in Liver, Improves Glucose Tolerance. *Cell Metabolism*, *29*(1), 183-191.e7. https://doi.org/10.1016/j.cmet.2018.09.013

Bränström, R., Aspinwall, C. A., Välimäki, S., Östensson, C. G., Tibell, A., Eckhard, M., et al. (2004). Long-Chain CoA esters activate human pancreatic beta-cell KATP channels: Potential role in Type 2 diabetes. *Diabetologia*, *47*(2), 277–283. https://doi.org/10.1007/s00125-003-1299-x

Braymer, J. J., & Lill, R. (2017). Iron–sulfur cluster biogenesis and trafficking in mitochondria. *Journal of Biological Chemistry*, *292*(31), 12754–12763. https://doi.org/10.1074/jbc.R117.787101

Braymer, J. J., Stehling, O., Stümpfig, M., Rösser, R., Spantgar, F., Blinn, C. M., et al. (2024). Requirements for the biogenesis of [2Fe-2S] proteins in the human and yeast cytosol. *Proceedings of the National Academy of Sciences*, *121*(21), e2400740121. https://doi.org/10.1073/pnas.2400740121

Briaud, I., Harmon, J. S., Kelpe, C. L., Segu, V. B. G., & Poitout, V. (2001). Lipotoxicity of the pancreatic β-cell is associated with glucose-dependent esterification of fatty acids into neutral lipids. *Diabetes*, *50*(2), 315–321. https://doi.org/10.2337/diabetes.50.2.315

Brown, N. M., Anderson, S. A., Steffen, D. W., Carpenter, T. B., Kennedy, M. C., Walden, W. E., & Eisenstein, R. S. (1998). Novel role of phosphorylation in Fe–S cluster stability revealed by phosphomimetic mutations at Ser-138 of iron regulatory protein 1. *Proceedings of the National Academy of Sciences*, *95*(26), 15235–15240. https://doi.org/10.1073/pnas.95.26.15235

Bruni, A., Pepper, A. R., Pawlick, R. L., Gala-Lopez, B., Gamble, A. F., Kin, T., et al. (2018). Ferroptosis-inducing agents compromise in vitro human islet viability and function. *Cell Death & Disease*, *9*(6), 595. https://doi.org/10.1038/s41419-018-0506-0

Bundesärztekammer, Kassenärztliche Bundesvereinigung, & Arbeitsgemeinschaft der Wissenschaftlichen Medizinischen Fachgesellschaften. (2023). Nationale Versorgungs Leitlinie Typ-2-Diabetes - Langfassung Version 3.0. https://doi.org/10.6101/AZQ/000503

Bushweller, J. H., Aaslund, F., Wuethrich, K., & Holmgren, A. (1992). Structural and functional characterization of the mutant Escherichia coli glutaredoxin (C14→S) and its mixed disulfide with glutathione. *Biochemistry*, *31*(38), 9288–9293. https://doi.org/10.1021/bi00153a023

Buttgereit, F., & Brand, M. D. (1995). A hierarchy of ATP-consuming processes in mammalian cells. *Biochemical Journal*, *312*(1), 163–167. https://doi.org/10.1042/bj3120163

Cai, S., Ding, Z., Liu, X., & Zeng, J. (2023). Trabectedin induces ferroptosis via regulation of HIF-1α/IRP1/TFR1 and Keap1/Nrf2/GPX4 axis in non-small cell lung cancer cells. *Chemico-Biological Interactions*, *369*, 110262. https://doi.org/10.1016/j.cbi.2022.110262

Camaschella, C., Campanella, A., De Falco, L., Boschetto, L., Merlini, R., Silvestri, L., et al. (2007). The human counterpart of zebrafish shiraz shows sideroblastic-like microcytic anemia and iron overload. *Blood*, *110*(4), 1353–1358. https://doi.org/10.1182/blood-2007-02-072520

La Camera, S., L'Haridon, F., Astier, J., Zander, M., Abou-Mansour, E., Page, G., et al. (2011). The glutaredoxin ATGRXS13 is required to facilitate Botrytis cinerea infection of Arabidopsis thaliana plants. *The Plant Journal*, *68*(3), 507–519. https://doi.org/10.1111/j.1365-313X.2011.04706.x

Camponeschi, F., Ciofi-Baffoni, S., & Banci, L. (2017). Anamorsin/Ndor1 Complex Reduces [2Fe–2S]-MitoNEET via a Transient Protein–Protein Interaction. *Journal of the American Chemical Society*, *139*(28), 9479–9482. https://doi.org/10.1021/jacs.7b05003

Camponeschi, F., Prusty, N. R., Heider, S. A. E., Ciofi-Baffoni, S., & Banci, L. (2020). GLRX3 Acts as a [2Fe–2S] Cluster Chaperone in the Cytosolic Iron–Sulfur Assembly Machinery Transferring [2Fe–2S] Clusters to NUBP1. *Journal of the American Chemical Society*, *142*(24), 10794–10805. https://doi.org/10.1021/jacs.0c02266

Carrillo-Larco, R. M., Guzman-Vilca, W. C., Xu, X., & Bernabe-Ortiz, A. (2024). Mean age and body mass index at type 2 diabetes diagnosis: Pooled analysis of 56 health surveys across income groups and world regions. *Diabetic Medicine*, *41*(2). https://doi.org/10.1111/dme.15174

Catrina, S.-B., & Zheng, X. (2021). Hypoxia and hypoxia-inducible factors in diabetes and its complications. *Diabetologia*, *64*(4), 709–716. https://doi.org/10.1007/s00125-021-05380-z

Cha, H., Kim, J. M., Oh, J. G., Jeong, M. H., Park, C. S., Park, J., et al. (2008). PICOT is a critical regulator of cardiac hypertrophy and cardiomyocyte contractility. *Journal of Molecular and Cellular Cardiology*, *45*(6), 796–803. https://doi.org/10.1016/j.yjmcc.2008.09.124

Chance, B., & Williams, G. R. (1955). Respiratory enzymes in oxidative phosphorylation. III. The steady state. *Journal of Biological Chemistry*, *217*(1), 409–427. https://doi.org/10.1016/S0021-9258(19)57191-5

Chang, J.-H., Jin, M.-M., & Liu, J.-T. (2020). Dexmedetomidine pretreatment protects the heart against apoptosis in ischemia/reperfusion injury in diabetic rats by activating PI3K/Akt signaling in vivo and in vitro. *Biomedicine & Pharmacotherapy*, *127*, 110188. https://doi.org/10.1016/j.biopha.2020.110188

Chang, Y.-C., Lin, C.-W., Chang, Y.-S., Chen, P.-H., Li, C.-Y., Wu, W.-C., & Kao, Y.-H. (2020). Monounsaturated oleic acid modulates autophagy flux and upregulates angiogenic factor production in human retinal pigment epithelial ARPE-19 cells. *Life Sciences*, *259*, 118391. https://doi.org/10.1016/j.lfs.2020.118391

Cheff, D. M., Huang, C., Scholzen, K. C., Gencheva, R., Ronzetti, M. H., Cheng, Q., et al. (2023). The ferroptosis inducing compounds RSL3 and ML162 are not direct inhibitors of GPX4 but of TXNRD1. *Redox Biology*, *62*, 102703. https://doi.org/10.1016/j.redox.2023.102703

Chen, Y., Ren, Q., Zhou, Z., Deng, L., Hu, L., Zhang, L., & Li, Z. (2020). HWL-088, a new potent free fatty acid receptor 1 (FFAR1) agonist, improves glucolipid metabolism and acts additively with metformin in ob/ob diabetic mice. *British Journal of Pharmacology*, *177*(10), 2286–2302. https://doi.org/10.1111/bph.14980

Cheng, H.-P., Feng, D., Li, X., Gao, L., Qiu, Y., Liang, X., et al. (2023). NMDA receptor activation induces damage of alveolar type II cells and lung fibrogenesis through ferroptosis. *Biochimica et Biophysica Acta (BBA) - Molecular Cell Research*, *1870*(7), 119535. https://doi.org/10.1016/j.bbamcr.2023.119535

Cheng, K., Ho, K., Stokes, R., Scott, C., Lau, S. M., Hawthorne, W. J., et al. (2010). Hypoxia-inducible factor-1α regulates β cell function in mouse and human islets. *Journal of Clinical Investigation*, *120*(6), 2171–2183. https://doi.org/10.1172/JCI35846

Cheng, K., de lghingaro-Augusto, V., Nolan, C. J., Turner, N., Hallahan, N., Andrikopoulos, S., & Gunton, J. E. (2012). High passage MIN6 cells have impaired insulin secretion with impaired glucose and lipid oxidation. *PLoS ONE*, *7*(7). https://doi.org/10.1371/journal.pone.0040868

Cheng, N., Liu, J.-Z., Brock, A., Nelson, R. S., & Hirschi, K. D. (2006). AtGRXcp, an Arabidopsis Chloroplastic Glutaredoxin, Is Critical for Protection against Protein Oxidative Damage. *Journal of Biological Chemistry*, *281*(36), 26280–26288. https://doi.org/10.1074/jbc.M601354200

Cheng, N., Zhang, W., Chen, W., Jin, J., Cui, X., Butte, N. F., et al. (2011). A mammalian monothiol glutaredoxin, Grx3, is critical for cell cycle progression during embryogenesis. *The FEBS Journal*, *278*(14), 2525–2539. https://doi.org/10.1111/j.1742-4658.2011.08178.x

Cheng, N., Liu, J.-Z., Liu, X., Wu, Q., Thompson, S. M., Lin, J., et al. (2011). Arabidopsis Monothiol Glutaredoxin, AtGRXS17, Is Critical for Temperature-dependent Postembryonic Growth and Development via Modulating Auxin Response. *Journal of Biological Chemistry*, *286*(23), 20398–20406. https://doi.org/10.1074/jbc.M110.201707

Cheng, N., Yu, H., Rao, X., Park, S., Connolly, E. L., Hirschi, K. D., & Nakata, P. A. (2020). Alteration of iron responsive gene expression in Arabidopsis glutaredoxin S17 loss of function plants with or without iron stress. *Plant Signaling & Behavior*, *15*(6), 1758455. https://doi.org/10.1080/15592324.2020.1758455

Cheng, N., Mo, Q., Donelson, J., Wang, L., Breton, G., Rodney, G. G., et al. (2021). Crucial Role of Mammalian Glutaredoxin 3 in Cardiac Energy Metabolism in Diet-induced Obese Mice Revealed by Transcriptome Analysis. *International Journal of Biological Sciences*, *17*(11), 2871–2883. https://doi.org/10.7150/IJBS.60263

Cheng, N., Donelson, J., Breton, G., & Nakata, P. A. (2023). Liver specific disruption of Glutaredoxin 3 leads to iron accumulation and impaired cellular iron homeostasis. *Biochemical and Biophysical Research Communications*, *649*, 39–46. https://doi.org/10.1016/j.bbrc.2023.01.095

Chiu, C. F., Lin, J. L., Lin, J. J., Tseng, M. H., Lo, F. S., & Chiang, M. C. (2016). Nonketotic Hyperglycinemia of Infants in Taiwan. *Pediatrics and Neonatology*, *57*(5), 420–426. https://doi.org/10.1016/j.pedneo.2015.10.008

Choi, A.-R., Kim, J.-H., & Yoon, S. (2014). Sensitization of Cancer Cells through Reduction of Total Akt and Downregulation of Salinomycin-Induced pAkt, pGSk3 β, pTSC2, and p4EBP1 by Cotreatment with MK-2206. *BioMed Research International*, *2014*(1), 1–8. https://doi.org/10.1155/2014/295760

Choi, E., & Bai, X.-C. (2023). The Activation Mechanism of the Insulin Receptor: A Structural Perspective. *Annual Review of Biochemistry*, *92*(1), 247–272. https://doi.org/10.1146/annurev-biochem-052521-033250

Cifarelli, V., Appak-Baskoy, S., Peche, V. S., Kluzak, A., Shew, T., Narendran, R., et al. (2021). Visceral obesity and insulin resistance associate with CD36 deletion in lymphatic endothelial cells. *Nature Communications*, *12*(1), 3350. https://doi.org/10.1038/s41467-021-23808-3

Ciofi-Baffoni, S., Nasta, V., & Banci, L. (2018). Protein networks in the maturation of human iron–sulfur proteins. *Metallomics*, *10*(1), 49–72. https://doi.org/10.1039/C7MT00269F

Ciregia, F., Giusti, L., Ronci, M., Bugliani, M., Piga, I., Pieroni, L., et al. (2015). Glucagon-like peptide 1 protects INS-1E mitochondria against palmitate-mediated beta-cell dysfunction: A proteomic study. *Molecular BioSystems*, *11*(6), 1696–1707. https://doi.org/10.1039/c5mb00022j

Ciregia, F., Bugliani, M., Ronci, M., Giusti, L., Boldrini, C., Mazzoni, M. R., et al. (2017). Palmitate-induced lipotoxicity alters acetylation of multiple proteins in clonal β cells and human pancreatic islets. *Scientific Reports*, *7*(1), 13445. https://doi.org/10.1038/s41598-017-13908-w

Cmejla, R., Petrak, J., & Cmejlova, J. (2006). A novel iron responsive element in the 3′UTR of human MRCKα. *Biochemical and Biophysical Research Communications*, *341*(1), 158–166. https://doi.org/10.1016/j.bbrc.2005.12.155

Cnop, M., Hannaert, J. C., Hoorens, A., Eizirik, D. L., & Pipeleers, D. G. (2001). Inverse Relationship between Cytotoxicity of Free Fatty Acids in Pancreatic Islet Cells and Cellular Triglyceride Accumulation. *Diabetes*, *50*(8), 1771–1777. https://doi.org/10.2337/diabetes.50.8.1771

Coffer, P. J., Jin, J., & Woodgett, J. R. (1998). Protein kinase B (c-Akt): a multifunctional mediator of phosphatidylinositol 3-kinase activation. *Biochemical Journal*, *335*(1), 1–13. https://doi.org/10.1042/BJ3350001

Coffey, R., & Knutson, M. D. (2017). The plasma membrane metal-ion transporter ZIP14 contributes to nontransferrin-bound iron uptake by human β-cells. *American Journal of Physiology-Cell Physiology*, *312*(2), C169–C175. https://doi.org/10.1152/ajpcell.00116.2016

Colca, J. R., McDonald, W. G., Waldon, D. J., Leone, J. W., Lull, J. M., Bannow, C. A., et al. (2004). Identification of a novel mitochondrial protein ("mitoNEET") cross-linked specifically by a thiazolidinedione photoprobe. *American Journal of Physiology-Endocrinology and Metabolism*, *286*(2), E252–E260. https://doi.org/10.1152/ajpendo.00424.2003

Connell, G. J., Abasiri, I. M., & Chaney, E. H. (2023). A temporal difference in the stabilization of two mRNAs with a 3′ iron-responsive element during iron deficiency. *RNA*, *29*(8), 1117–1125. https://doi.org/10.1261/rna.079665.123

Corradi, J., Thompson, B., Fletcher, P. A., Bertram, R., Sherman, A. S., & Satin, L. S. (2023). KATP channel activity and slow oscillations in pancreatic beta cells are regulated by mitochondrial ATP production. *The Journal of Physiology*, *601*(24), 5655–5667. https://doi.org/10.1113/JP284982

Costes, S., Broca, C., Bertrand, G., Lajoix, A. D., Bataille, D., Bockaert, J., & Dalle, S. (2006). ERK1/2 control phosphorylation and protein level of cAMP-responsive element-binding protein: a key role in glucose-mediated pancreatic beta-cell survival. *Diabetes*, *55*(8), 2220–2230. https://doi.org/10.2337/DB05-1618

Cotticelli, M. G., Forestieri, R., Xia, S., Joyasawal, S., Lee, T., Xu, K., et al. (2020). Identification of a Novel Oleic Acid Analog with Protective Effects in Multiple Cellular Models of Friedreich Ataxia. *ACS Chemical Neuroscience*, *11*(17), 2535–2542. https://doi.org/10.1021/acschemneuro.0c00323

Couturier, J., Jacquot, J.-P., & Rouhier, N. (2009). Evolution and diversity of glutaredoxins in photosynthetic organisms. *Cellular and Molecular Life Sciences*, *66*(15), 2539–2557. https://doi.org/10.1007/s00018-009-0054-y

Couturier, J., Ströher, E., Albetel, A. N., Roret, T., Muthuramalingam, M., Tarrago, L., et al. (2011). Arabidopsis Chloroplastic Glutaredoxin C5 as a Model to Explore Molecular Determinants for Iron-Sulfur Cluster Binding into Glutaredoxins. *Journal of Biological Chemistry*, *286*(31), 27515–27527. https://doi.org/10.1074/JBC.M111.228726

Cózar-Castellano, I., del Valle Machargo, M., Trujillo, E., Arteaga, M. F., González, T., Martín-Vasallo, P., & Avila, J. (2004). hIscA: a protein implicated in the biogenesis of iron–sulfur clusters. *Biochimica et Biophysica Acta (BBA) - Proteins and Proteomics*, *1700*(2), 179–188. https://doi.org/10.1016/j.bbapap.2004.05.004

Crilly, C. J., Allen, A. J., Amato, T. M., Tiberio, A., Schulman, R. C., & Silverman, R. A. (2018). Evaluating the Emergency Department Observation Unit for the management of hyperglycemia in adults. *The American Journal of Emergency Medicine*, *36*(11), 1975–1979. https://doi.org/10.1016/J.AJEM.2018.02.027

Crispin, A., Guo, C., Chen, C., Campagna, D. R., Schmidt, P. J., Lichtenstein, D., et al. (2020). Mutations in the iron-sulfur cluster biogenesis protein HSCB cause congenital sideroblastic anemia. *The Journal of Clinical Investigation*, *130*(10), 5245–5256. https://doi.org/10.1172/JCI135479

Cronin, R., Brooke, G. N., & Prischi, F. (2021). The role of the p90 ribosomal S6 kinase family in prostate cancer progression and therapy resistance. *Oncogene*, *40*(22), 3775–3785. https://doi.org/10.1038/s41388-021-01810-9

Cui, R., Choi, S. E., Kim, T. H., Lee, H. J., Lee, S. J., Kang, Y., et al. (2019). Iron overload by transferrin receptor protein 1 regulation plays an important role in palmitate-induced insulin resistance in human skeletal muscle cells. *The FASEB Journal*, *33*(2), 1771–1786. https://doi.org/10.1096/FJ.201800448R

Czech, M. P., Tencerova, M., Pedersen, D. J., & Aouadi, M. (2013). Insulin signalling mechanisms for triacylglycerol storage. *Diabetologia*, *56*(5), 949–964. https://doi.org/10.1007/s00125-013-2869-1

Daher, R., Mansouri, A., Martelli, A., Bayart, S., Manceau, H., Callebaut, I., et al. (2019). GLRX5 mutations impair heme biosynthetic enzymes ALA synthase 2 and ferrochelatase in Human congenital sideroblastic anemia. *Molecular Genetics and Metabolism*, *128*(3), 342–351. https://doi.org/10.1016/j.ymgme.2018.12.012

Daousi, C., Casson, I. F., Gill, G. V., MacFarlane, I. A., Wilding, J. P. H., & Pinkney, J. H. (2006). Prevalence of obesity in type 2 diabetes in secondary care: Association with cardiovascular risk factors. *Postgraduate Medical Journal*, *82*(966), 280–284. https://doi.org/10.1136/pmj.2005.039032

Davies, M. J., Aroda, V. R., Collins, B. S., Gabbay, R. A., Green, J., Maruthur, N. M., et al. (2022). Management of Hyperglycemia in Type 2 Diabetes, 2022. A Consensus Report by the American Diabetes Association (ADA) and the European Association for the Study of Diabetes (EASD). *Diabetes Care*, *45*(11), 2753–2786. https://doi.org/10.2337/dci22-0034

Delgadillo-Silva, L. F., Tasöz, E., Singh, S. P., Chawla, P., Georgiadou, E., Gompf, A., et al. (2024). Optogenetic β cell interrogation in vivo reveals a functional hierarchy directing the Ca 2+ response to glucose supported by vitamin B6. *Science Advances*, *10*(26), eado4513. https://doi.org/10.1126/sciadv.ado4513

Derkach, K. V., Bakhtyukov, A. A., Basova, N. E., Zorina, I. I., & Shpakov, A. O. (2022). The Restorative Effect of Combined Insulin and C-Peptide Intranasal Administration on Hormonal Status and Hypothalamic Signaling in the Male Rat Model of Severe Short-Term Streptozotocin-Induced Diabetes. *Journal of Evolutionary Biochemistry and Physiology*, *58*(3), 677–691. https://doi.org/10.1134/S002209302203005X

Dezaki, K., & Yada, T. (2022). Status of ghrelin as an islet hormone and paracrine/autocrine regulator of insulin secretion. *Peptides*, *148*, 170681. https://doi.org/10.1016/j.peptides.2021.170681

Din, M. A. U., Lin, Y., Wang, N., Wang, B., & Mao, F. (2024). Ferroptosis and the ubiquitin-proteasome system: exploring treatment targets in cancer. *Frontiers in Pharmacology*, *15*, 1383203. https://doi.org/10.3389/fphar.2024.1383203

Ding, L., Sun, W., Balaz, M., He, A., Klug, M., Wieland, S., et al. (2021). Peroxisomal β-oxidation acts as a sensor for intracellular fatty acids and regulates lipolysis. *Nature Metabolism*, *3*(12), 1648–1661. https://doi.org/10.1038/s42255-021-00489-2

Dixon, S. J., Lemberg, K. M., Lamprecht, M. R., Skouta, R., Zaitsev, E. M., Gleason, C. E., et al. (2012). Ferroptosis: An iron-dependent form of nonapoptotic cell death. *Cell*, *149*(5), 1060–1072. https://doi.org/10.1016/j.cell.2012.03.042

Dolgova, N., Uhlemann, E.-M. E., Boniecki, M. T., Vizeacoumar, F. S., Ara, A., Nouri, P., et al. (2024). MEMO1 binds iron and modulates iron homeostasis in cancer cells. *ELife*, *13*. https://doi.org/10.7554/eLife.86354

Dolma, S., Lessnick, S. L., Hahn, W. C., & Stockwell, B. R. (2003). Identification of genotype-selective antitumor agents using synthetic lethal chemical screening in engineered human tumor cells. *Cancer Cell*, *3*(3), 285–296. https://doi.org/10.1016/S1535-6108(03)00050-3

Dou, X., Li, S., Hu, L., Ding, L., Ma, Y., Ma, W., et al. (2018). Glutathione disulfide sensitizes hepatocytes to TNFα-mediated cytotoxicity via IKK-β S-glutathionylation: a potential mechanism underlying non-alcoholic fatty liver disease. *Experimental & Molecular Medicine*, *50*(4), 1–16. https://doi.org/10.1038/s12276-017-0013-x

Duarte, T. L., Talbot, N. P., & Drakesmith, H. (2021). NRF2 and Hypoxia-Inducible Factors: Key Players in the Redox Control of Systemic Iron Homeostasis. *Antioxidants & Redox Signaling*, *35*(6), 433–452. https://doi.org/10.1089/ars.2020.8148

Dutkiewicz, R., Schilke, B., Knieszner, H., Walter, W., Craig, E. A., & Marszalek, J. (2003). Ssq1, a mitochondrial Hsp70 involved in iron-sulfur (Fe/S) center biogenesis. Similarities to and differences from its bacterial counterpart. *The Journal of Biological Chemistry*, *278*(32), 29719–29727. https://doi.org/10.1074/JBC.M303527200

Dutkiewicz, R., Schilke, B., Cheng, S., Knieszner, H., Craig, E. A., & Marszalek, J. (2004). Sequence-specific interaction between mitochondrial Fe-S scaffold protein Isu and Hsp70 Ssq1 is essential for their in vivo function. *The Journal of Biological Chemistry*, *279*(28), 29167–29174. https://doi.org/10.1074/JBC.M402947200

Dutkiewicz, R., Marszalek, J., Schilke, B., Craig, E. A., Lill, R., & Mühlenhoff, U. (2006). The Hsp70 Chaperone Ssq1p Is Dispensable for Iron-Sulfur Cluster Formation on the Scaffold Protein Isu1p. *Journal of Biological Chemistry*, *281*(12), 7801–7808. https://doi.org/10.1074/JBC.M513301200

Eades, C. E., Burrows, K. A., Andreeva, R., Stansfield, D. R., & Evans, J. M. M. (2024). Prevalence of gestational diabetes in the United States and Canada: a systematic review and meta-analysis. *BMC Pregnancy and Childbirth*, *24*(1), 204. https://doi.org/10.1186/s12884-024-06378-2

Eberle, R. J., Kawai, L. A., de Moraes, F. R., Tasic, L., Arni, R. K., & Coronado, M. A. (2018). Biochemical and biophysical characterization of a mycoredoxin protein glutaredoxin A1 from Corynebacterium pseudotuberculosis. *International Journal of Biological Macromolecules*, *107*(Pt B), 1999–2007. https://doi.org/10.1016/j.ijbiomac.2017.10.063

Ebrahim, N., Shakirova, K., & Dashinimaev, E. (2022). PDX1 is the cornerstone of pancreatic β-cell functions and identity. *Frontiers in Molecular Biosciences*, *9*, 1091757. https://doi.org/10.3389/fmolb.2022.1091757

Eckers, E., Bien, M., Stroobant, V., Herrmann, J. M., & Deponte, M. (2009). Biochemical characterization of dithiol glutaredoxin 8 from saccharomyces cerevisiae: The catalytic redox mechanism redux. *Biochemistry*, *48*(6), 1410–1423. https://doi.org/10.1021/bi801859b

Ehrary, A., Rosas, M., Carpinelli, S., Davalos, O., Cowling, C., Fernandez, F., & Escobar, M. (2020). Glutaredoxin AtGRXS8 represses transcriptional and developmental responses to nitrate in Arabidopsis thaliana roots. *Plant Direct*, *4*(6), e00227. https://doi.org/10.1002/pld3.227

Eklund, H., Gleason, F. K., & Holmgren, A. (1991). Structural and functional relations among thioredoxins of different species. *Proteins: Structure, Function, and Bioinformatics*, *11*(1), 13–28. https://doi.org/10.1002/prot.340110103

El-Assaad, W., Buteau, J., Peyot, M. L., Nolan, C., Roduit, R., Hardy, S., et al. (2003). Saturated fatty acids synergize with elevated glucose to cause pancreatic β-cell death. *Endocrinology*, *144*(9), 4154–4163. https://doi.org/10.1210/en.2003-0410

ElSayed, N. A., Aleppo, G., Bannuru, R. R., Bruemmer, D., Collins, B. S., Ekhlaspour, L., et al. (2024). 2. Diagnosis and Classification of Diabetes: Standards of Care in Diabetes—2024. *Diabetes Care*, *47*(Suppl 1), S20–S42. https://doi.org/10.2337/dc24-S002

Elsner, M., Gehrmann, W., & Lenzen, S. (2011). Peroxisome-generated hydrogen peroxide as important mediator of lipotoxicity in insulin-producing cells. *Diabetes*, *60*(1), 200–208. https://doi.org/10.2337/db09-1401

Engin, A. (2024). Lipid Storage, Lipolysis, and Lipotoxicity in Obesity. In *Advances in experimental medicine and biology* (Vol. 1460, pp. 97–129). Springer, Cham. https://doi.org/10.1007/978-3-031-63657-8_4

Espada, L., Dakhovnik, A., Chaudhari, P., Martirosyan, A., Miek, L., Poliezhaieva, T., et al. (2020). Loss of metabolic plasticity underlies metformin toxicity in aged Caenorhabditis elegans. *Nature Metabolism*, *2*(11), 1316–1331. https://doi.org/10.1038/s42255-020-00307-1

Fagundes, R. R., Bourgonje, A. R., Hu, S., Barbieri, R., Jansen, B. H., Sinnema, N., et al. (2022). HIF1α-Dependent Induction of TFRC by a Combination of Intestinal Inflammation and Systemic Iron Deficiency in Inflammatory Bowel Disease. *Frontiers in Physiology*, *13*, 889091. https://doi.org/10.3389/fphys.2022.889091

Fang, X., Ardehali, H., Min, J., & Wang, F. (2023). The molecular and metabolic landscape of iron and ferroptosis in cardiovascular disease. *Nature Reviews Cardiology*, *20*(1), 7–23. https://doi.org/10.1038/s41569-022-00735-4

Faria, J. L., Berberan-Santos, M., & Prieto, M. J. E. (1990). A comment on the localization of cyanine dye binding to brush-border membranes by the fluorescence quenching of n-(9-anthroyloxy) fatty acid probes. *Biochimica et Biophysica Acta (BBA) - Biomembranes*, *1026*(1), 133–134. https://doi.org/10.1016/0005-2736(90)90343-M

Feldman, E. L., Callaghan, B. C., Pop-Busui, R., Zochodne, D. W., Wright, D. E., Bennett, D. L., et al. (2019). Diabetic neuropathy. *Nature Reviews Disease Primers*, *5*(1), 41. https://doi.org/10.1038/s41572-019-0092-1

Feng, W. X., Zhuo, X. W., Liu, Z. M., Li, J. W., Zhang, W. H., Wu, Y., et al. (2021). Case Report: A Variant Non-ketotic Hyperglycinemia With GLRX5 Mutations: Manifestation of Deficiency of Activities of the Respiratory Chain Enzymes. *Frontiers in Genetics*, *12*, 605778. https://doi.org/10.3389/fgene.2021.605778

Feng, Y., Zhong, N., Rouhier, N., Hase, T., Kusunoki, M., Jacquot, J.-P., et al. (2006). Structural Insight into Poplar Glutaredoxin C1 with a Bridging Iron−Sulfur Cluster at the Active Site. *Biochemistry*, *45*(26), 7998–8008. https://doi.org/10.1021/bi060444t

Ferecatu, I., Gonçalves, S., Golinelli-Cohen, M. P., Clémancey, M., Martelli, A., Riquier, S., et al. (2014). The diabetes drug target MitoNEET governs a novel trafficking pathway to rebuild an Fe-S cluster into cytosolic aconitase/iron regulatory protein 1. *The Journal of Biological Chemistry*, *289*(41), 28070–28086. https://doi.org/10.1074/JBC.M114.548438

Fernandes, A. P., Fladvad, M., Berndt, C., Andrésen, C., Lillig, C. H., Neubauer, P., et al. (2005). A novel monothiol glutaredoxin (Grx4) from Escherichia coli can serve as a substrate for thioredoxin reductase. *The Journal of Biological Chemistry*, *280*(26), 24544–24552. https://doi.org/10.1074/JBC.M500678200

Filetici, P., Martegani, M. P., Valenzuela, L., González, A., & Ballario, P. (1996). Sequence of the GLT1 gene from Saccharomyces cerevisiae reveals the domain structure of yeast glutamate synthase. *Yeast*, *12*(13), 1359–1366. https://doi.org/10.1002/(SICI)1097-0061(199610)12:13<1359::AID-YEA3>3.0.CO;2-5

Flotyńska, J., Klause, D., Kulecki, M., Cieluch, A., Chomicka-Pawlak, R., Zozulińska-Ziółkiewicz, D., & Uruska, A. (2022). Higher NADH Dehydrogenase [Ubiquinone] Iron–Sulfur Protein 8 (NDUFS8) Serum Levels Correlate with Better Insulin Sensitivity in Type 1 Diabetes. *Current Issues in Molecular Biology*, *44*(9), 3872–3883. https://doi.org/10.3390/cimb44090266

Foury, F., & Roganti, T. (2002). Deletion of the Mitochondrial Carrier Genes MRS3 andMRS4 Suppresses Mitochondrial Iron Accumulation in a Yeast Frataxin-deficient Strain. *Journal of Biological Chemistry*, *277*(27), 24475–24483. https://doi.org/10.1074/JBC.M111789200

Freibert, S.-A., Goldberg, A. V., Hacker, C., Molik, S., Dean, P., Williams, T. A., et al. (2017). Evolutionary conservation and in vitro reconstitution of microsporidian iron–sulfur cluster biosynthesis. *Nature Communications*, *8*(1), 13932. https://doi.org/10.1038/ncomms13932

Freibert, S.-A., Boniecki, M. T., Stümpfig, C., Schulz, V., Krapoth, N., Winge, D. R., et al. (2021). N-terminal tyrosine of ISCU2 triggers [2Fe-2S] cluster synthesis by ISCU2 dimerization. *Nature Communications*, *12*(1), 6902. https://doi.org/10.1038/s41467-021-27122-w

Fretts, A. M., Jensen, P. N., Hoofnagle, A. N., McKnight, B., Howard, B. V., Umans, J., et al. (2021). Plasma ceramides containing saturated fatty acids are associated with risk of type 2 diabetes. *Journal of Lipid Research*, *62*, 100119. https://doi.org/10.1016/j.jlr.2021.100119

Frey, A. G., Palenchar, D. J., Wildemann, J. D., & Philpott, C. C. (2016). A Glutaredoxin·BolA Complex Serves as an Iron-Sulfur Cluster Chaperone for the Cytosolic Cluster Assembly Machinery. *The Journal of Biological Chemistry*, *291*(43), 22344–22356. https://doi.org/10.1074/JBC.M116.744946

Fryk, E., Olausson, J., Mossberg, K., Strindberg, L., Schmelz, M., Brogren, H., et al. (2021). Hyperinsulinemia and insulin resistance in the obese may develop as part of a homeostatic response to elevated free fatty acids: A mechanistic case-control and a population-based cohort study. *EBioMedicine*, *65*, 103264. https://doi.org/10.1016/j.ebiom.2021.103264

Fuhrmann, D. C., Mondorf, A., Beifuß, J., Jung, M., & Brüne, B. (2020). Hypoxia inhibits ferritinophagy, increases mitochondrial ferritin, and protects from ferroptosis. *Redox Biology*, *36*, 101670. https://doi.org/10.1016/j.redox.2020.101670

Fujimoto, K., & Polonsky, K. S. (2009). Pdx1 and other factors that regulate pancreatic β-cell survival. *Diabetes, Obesity and Metabolism*, *11*(s4), 30–37. https://doi.org/10.1111/j.1463-1326.2009.01121.x

Funk, D., Schrenk, H.-H., & Frei, E. (2007). Serum albumin leads to false-positive results in the XTT and the MTT assay. *BioTechniques*, *43*(2), 178–186. https://doi.org/10.2144/000112528

Galy, B., Conrad, M., & Muckenthaler, M. (2024). Mechanisms controlling cellular and systemic iron homeostasis. *Nature Reviews Molecular Cell Biology*, *25*(2), 133–155. https://doi.org/10.1038/s41580-023-00648-1

Gama, F., Bréhélin, C., Gelhaye, E., Meyer, Y., Jacquot, J. P., Rey, P., & Rouhier, N. (2008). Functional analysis and expression characteristics of chloroplastic Prx IIE. *Physiologia Plantarum*, *133*(3), 599–610. https://doi.org/10.1111/J.1399-3054.2008.01097.X

Gan, Z.-R. (1992). Cloning and sequencing of a gene encoding yeast thioltransferase. *Biochemical and Biophysical Research Communications*, *187*(2), 949–955. https://doi.org/10.1016/0006-291X(92)91289-3

Gao, T., McKenna, B., Li, C., Reichert, M., Nguyen, J., Singh, T., et al. (2014). Pdx1 Maintains β Cell Identity and Function by Repressing an α Cell Program. *Cell Metabolism*, *19*(2), 259–271. https://doi.org/10.1016/j.cmet.2013.12.002

Gastaldelli, A., Gaggini, M., & DeFronzo, R. A. (2017). Role of Adipose Tissue Insulin Resistance in the Natural History of Type 2 Diabetes: Results From the San Antonio Metabolism Study. *Diabetes*, *66*(4), 815–822. https://doi.org/10.2337/DB16-1167

Geissel, F., Lang, L., Husemann, B., Morgan, B., & Deponte, M. (2024). Deciphering the mechanism of glutaredoxin-catalyzed roGFP2 redox sensing reveals a ternary complex with glutathione for protein disulfide reduction. *Nature Communications*, *15*(1), 1733. https://doi.org/10.1038/s41467-024-45808-9

Gerber, J., Mühlenhoff, U., & Lill, R. (2003). An interaction between frataxin and Isu1/Nfs1 that is crucial for Fe/S cluster synthesis on Isu1. *EMBO Reports*, *4*(9), 906–911. https://doi.org/10.1038/sj.embor.embor918

Ghasemi, M., Turnbull, T., Sebastian, S., & Kempson, I. (2021). The MTT assay: Utility, limitations, pitfalls, and interpretation in bulk and single-cell analysis. *International Journal of Molecular Sciences*, *22*(23), 12827. https://doi.org/10.3390/IJMS222312827/S1

Ghezzi, D., Goffrini, P., Uziel, G., Horvath, R., Klopstock, T., Lochmüller, H., et al. (2009). SDHAF1, encoding a LYR complex-II specific assembly factor, is mutated in SDH-defective infantile leukoencephalopathy. *Nature Genetics*, *41*(6), 654–656. https://doi.org/10.1038/NG.378

Golinelli-Cohen, M. P., Lescop, E., Mons, C., Gonçalves, S., Clémancey, M., Santolini, J., et al. (2016). Redox Control of the Human Iron-Sulfur Repair Protein MitoNEET Activity via Its Iron-Sulfur Cluster. *The Journal of Biological Chemistry*, *291*(14), 7583–7593. https://doi.org/10.1074/JBC.M115.711218

Good, A. L., & Stoffers, D. A. (2020). Stress-Induced Translational Regulation Mediated by RNA Binding Proteins: Key Links to β-Cell Failure in Diabetes. *Diabetes*, *69*(4), 499–507. https://doi.org/10.2337/DBI18-0068

Gouspillou, G., Rouland, R., Calmettes, G., Deschodt-Arsac, V., Franconi, J.-M., Bourdel-Marchasson, I., & Diolez, P. (2011). Accurate Determination of the Oxidative Phosphorylation Affinity for ADP in Isolated Mitochondria. *PLoS ONE*, *6*(6), e20709. https://doi.org/10.1371/journal.pone.0020709

Grabner, G. F., Xie, H., Schweiger, M., & Zechner, R. (2021). Lipolysis: cellular mechanisms for lipid mobilization from fat stores. *Nature Metabolism*, *3*(11), 1445–1465. https://doi.org/10.1038/s42255-021-00493-6

Green, C. D., Jump, D. B., & Olson, L. K. (2009). Elevated insulin secretion from liver X receptor-activated pancreatic β-cells involves increased de novo lipid synthesis and triacylglyceride turnover. *Endocrinology*, *150*(6), 2637–2645. https://doi.org/10.1210/en.2008-1039

Guay, C., Madiraju, S. R. M., Aumais, A., Joly, É., & Prentki, M. (2007). A role for ATP-citrate lyase, malic enzyme, and pyruvate/citrate cycling in glucose-induced insulin secretion. *Journal of Biological Chemistry*, *282*(49), 35657–35665. https://doi.org/10.1074/jbc.M707294200

Guo, M., Huang, X., Zhang, J., Huang, Y., Tang, Y., Wen, H., et al. (2024). Palmitic acid induces β-cell ferroptosis by activating ceramide signaling pathway. *Experimental Cell Research*, *440*(2), 114134. https://doi.org/10.1016/j.yexcr.2024.114134

Guo, X., Yu, X., Xu, Z., Zhao, P., Zou, L., Li, W., et al. (2022). CC-type glutaredoxin, MeGRXC3, associates with catalases and negatively regulates drought tolerance in cassava (Manihot esculenta Crantz). *Plant Biotechnology Journal*, *20*(12), 2389–2405. https://doi.org/10.1111/PBI.13920

Haataja, L., Manickam, N., Soliman, A., Tsai, B., Liu, M., & Arvan, P. (2016). Disulfide Mispairing During Proinsulin Folding in the Endoplasmic Reticulum. *Diabetes*, *65*(4), 1050–1060. https://doi.org/10.2337/db15-1345

Håkansson, K. O., Østergaard, H., & Winther, J. R. (2006). Crystallization of mutant forms of glutaredoxin Grx1p from yeast. *Acta Crystallographica Section F Structural Biology and Crystallization Communications*, *62*(9), 920–922. https://doi.org/10.1107/S1744309106031216

Harned, J., Ferrell, J., Lall, M. M., Fleisher, L. N., Nagar, S., Goralska, M., & Christine McGahan, M. (2010). Altered Ferritin Subunit Composition: Change in Iron Metabolism in Lens Epithelial Cells and Downstream Effects on Glutathione Levels and VEGF Secretion. *Investigative Ophthalmology & Visual Science*, *51*(9), 4437–4446. https://doi.org/10.1167/IOVS.09-3861

Harrison, P. M., & Arosio, P. (1996). The ferritins: molecular properties, iron storage function and cellular regulation. *Biochimica et Biophysica Acta (BBA) - Bioenergetics*, *1275*(3), 161–203. https://doi.org/10.1016/0005-2728(96)00022-9

Hart, J. R., & Vogt, P. K. (2011). Phosphorylation of AKT: a Mutational Analysis. *Oncotarget*, *2*(6), 467–476. https://doi.org/10.18632/oncotarget.293

Hasenour, C. M., Banerjee, D. R., & Young, J. D. (2024). Metabolic Fluxes in the Renal Cortex Are Dysregulated In Vivo in Response to High-Fat Diet. *Diabetes*, *73*(6), 903–908. https://doi.org/10.2337/DB23-0710

Haunhorst, P., Hanschmann, E.-M., Bräutigam, L., Stehling, O., Hoffmann, B., Mühlenhoff, U., et al. (2013). Crucial function of vertebrate glutaredoxin 3 (PICOT) in iron homeostasis and hemoglobin maturation. *Molecular Biology of the Cell*, *24*(12), 1895–1903. https://doi.org/10.1091/mbc.e12-09-0648

He, X., Zhang, J., Gong, M., Gu, Y., Dong, B., Pang, X., et al. (2023). Identification of potential ferroptosis-associated biomarkers in rheumatoid arthritis. *Frontiers in Immunology*, *14*, 1197275. https://doi.org/10.3389/fimmu.2023.1197275

Helman, S. L., Zhou, J., Fuqua, B. K., Lu, Y., Collins, J. F., Chen, H., et al. (2023). The biology of mammalian multi-copper ferroxidases. *BioMetals*, *36*(2), 263–281. https://doi.org/10.1007/s10534-022-00370-z

Hemmings, B. A., & Restuccia, D. F. (2012). PI3K-PKB/Akt Pathway. *Cold Spring Harbor Perspectives in Biology*, *4*(9), a011189–a011189. https://doi.org/10.1101/cshperspect.a011189

Hentze, M. W., Muckenthaler, M. U., Galy, B., & Camaschella, C. (2010). Two to Tango: Regulation of Mammalian Iron Metabolism. *Cell*, *142*(1), 24–38. https://doi.org/10.1016/j.cell.2010.06.028

Herrera-Vásquez, A., Carvallo, L., Blanco, F., Tobar, M., Villarroel-Candia, E., Vicente-Carbajosa, J., et al. (2015). Transcriptional Control of Glutaredoxin GRXC9 Expression by a Salicylic Acid-Dependent and NPR1-Independent Pathway in Arabidopsis. *Plant Molecular Biology Reporter*, *33*(3), 624. https://doi.org/10.1007/S11105-014-0782-5

Herrero, E., & de la Torre-Ruiz, M. A. (2007). Monothiol glutaredoxins: a common domain for multiple functions. *Cellular and Molecular Life Sciences*, *64*(12), 1518–1530. https://doi.org/10.1007/s00018-007-6554-8

Holmgren, A. (1976). Hydrogen donor system for Escherichia coli ribonucleoside-diphosphate reductase dependent upon glutathione. *Proceedings of the National Academy of Sciences*, *73*(7), 2275–2279. https://doi.org/10.1073/pnas.73.7.2275

Hou, J., Zhang, Q., Zhou, Y., Ahammed, G. J., Zhou, Y., Yu, J., et al. (2018). Glutaredoxin GRXS16 mediates brassinosteroid-induced apoplastic H2O2 production to promote pesticide metabolism in tomato. *Environmental Pollution*, *240*, 227–234. https://doi.org/10.1016/j.envpol.2018.04.120

Hou, J., Sun, Q., Li, J., Ahammed, G. J., Yu, J., Fang, H., & Xia, X. (2019). Glutaredoxin S25 and its interacting TGACG motif-binding factor TGA2 mediate brassinosteroid-induced chlorothalonil metabolism in tomato plants. *Environmental Pollution*, *255*(Pt 2), 113256. https://doi.org/10.1016/j.envpol.2019.113256

Hu, F., & Lin, C. (2024). TRPM2 knockdown attenuates myocardial apoptosis and promotes autophagy in HFD/STZ-induced diabetic mice via regulating the MEK/ERK and mTORC1 signaling pathway. *Molecular and Cellular Biochemistry*, *479*(12), 3307–3328. https://doi.org/10.1007/s11010-024-04926-0

Huang, K. T., Chen, Y. H., & Walker, A. M. (2004). Inaccuracies in MTS assays: Major distorting effects of medium, serum albumin, and fatty acids. *BioTechniques*, *37*(3), 406–412. https://doi.org/10.2144/04373st05

Huang, L.-J., Li, N., Thurow, C., Wirtz, M., Hell, R., & Gatz, C. (2016). Ectopically expressed glutaredoxin ROXY19 negatively regulates the detoxification pathway in Arabidopsis thaliana. *BMC Plant Biology*, *16*(1), 200. https://doi.org/10.1186/s12870-016-0886-1

Hui, H., & Perfetti, R. (2002). Pancreas duodenum homeobox-1 regulates pancreas development during embryogenesis and islet cell function in adulthood. *European Journal of Endocrinology*, *146*(2), 129–141. https://doi.org/10.1530/EJE.0.1460129

Huynh, N., Ou, Q., Cox, P., Lill, R., & King-Jones, K. (2019). Glycogen branching enzyme controls cellular iron homeostasis via Iron Regulatory Protein 1 and mitoNEET. *Nature Communications*, *10*(1), 5463. https://doi.org/10.1038/s41467-019-13237-8

Iacobazzi, V., & Infantino, V. (2014). Citrate – new functions for an old metabolite. *Biological Chemistry*, *395*(4), 387–399. https://doi.org/10.1515/hsz-2013-0271

Ikeda, Y., Watanabe, H., Shiuchi, T., Hamano, H., Horinouchi, Y., Imanishi, M., et al. (2020). Deletion of H-ferritin in macrophages alleviates obesity and diabetes induced by high-fat diet in mice. *Diabetologia*, *63*(8), 1588–1602. https://doi.org/10.1007/S00125-020-05153-0

Imierska, M., Zabielski, P., Roszczyc-Owsiejczuk, K., Pogodzińska, K., & Błachnio-Zabielska, A. (2025). Impact of reduced hepatic ceramide levels in high-fat diet mice on glucose metabolism. *The Journal of Nutritional Biochemistry*, *135*, 109785. https://doi.org/10.1016/j.jnutbio.2024.109785

Indyk, D., Bronowicka-Szydełko, A., Gamian, A., & Kuzan, A. (2021). Advanced glycation end products and their receptors in serum of patients with type 2 diabetes. *Scientific Reports*, *11*(1), 13264. https://doi.org/10.1038/s41598-021-92630-0

Inoue, R., Tsuno, T., Togashi, Y., Okuyama, T., Sato, A., Nishiyama, K., et al. (2022). Uncoupling protein 2 and aldolase B impact insulin release by modulating mitochondrial function and Ca2+ release from the ER. *IScience*, *25*(7), 104603. https://doi.org/10.1016/j.isci.2022.104603

Ishihara, H., Asano, T., Tsukuda, K., Katagiri, H., Inukai, K., Anai, M., et al. (1993). Pancreatic beta cell line MIN6 exhibits characteristics of glucose metabolism and glucose-stimulated insulin secretion similar to those of normal islets. *Diabetologia*, *36*(11), 1139–1145. https://doi.org/10.1007/BF00401058

Jbel, M., Mercier, A., & Labbé, S. (2011). Grx4 monothiol glutaredoxin is required for iron limitation-dependent inhibition of Fep1. *Eukaryotic Cell*, *10*(5), 629–645. https://doi.org/10.1128/EC.00015-11

Ježek, J., Dlasková, A., Zelenka, J., Jabůrek, M., & Ježek, P. (2015). H2O2-Activated Mitochondrial Phospholipase iPLA 2 γ Prevents Lipotoxic Oxidative Stress in Synergy with UCP2, Amplifies Signaling via G-Protein–Coupled Receptor GPR40, and Regulates Insulin Secretion in Pancreatic β-Cells. *Antioxidants & Redox Signaling*, *23*(12), 958–972. https://doi.org/10.1089/ars.2014.6195

Jiang, L., Wan, J., Ke, L. Q., Lü, Q. G., & Tong, N. W. (2010). Activation of PPARδ promotes mitochondrial energy metabolism and decreases basal insulin secretion in palmitate-treated β-cells. *Molecular and Cellular Biochemistry*, *343*(1–2), 249–256. https://doi.org/10.1007/s11010-010-0520-8

Jiang, Z., Sun, H., Miao, J., Sheng, Q., Xu, J., Gao, Z., et al. (2023). The natural flavone acacetin protects against high-fat diet-induced lipid accumulation in the liver via the endoplasmic reticulum stress/ferroptosis pathway. *Biochemical and Biophysical Research Communications*, *640*, 183–191. https://doi.org/10.1016/j.bbrc.2022.12.014

Jin, W., Fan, M., Zhang, Y., Zhang, Q., Jing, C., Jiang, R., et al. (2022). Polydatin prevents lipotoxicity-induced dysfunction in pancreatic β-cells by inhibiting endoplasmic reticulum stress and excessive autophagy. *Phytomedicine*, *106*, 154410. https://doi.org/10.1016/j.phymed.2022.154410

Johansson, C., Roos, A. K., Montano, S. J., Sengupta, R., Filippakopoulos, P., Guo, K., et al. (2011). The crystal structure of human GLRX5: iron–sulfur cluster co-ordination, tetrameric assembly and monomer activity. *Biochemical Journal*, *433*(2), 303–311. https://doi.org/10.1042/BJ20101286

Johnson, M. K., Kowal, A. T., Morningstar, J. E., Oliver, M. E., Whittaker, K., Gunsalus, R. P., et al. (1988). Subunit Location of the Iron-Sulfur Clusters in Fumarate Reductase from Escherichia coli. *Journal of Biological Chemistry*, *263*(29), 14732–14738. https://doi.org/10.1016/S0021-9258(18)68098-6

Jonsson, J., Carlsson, L., Edlund, T., & Edlund, H. (1994). Insulin-promoter-factor 1 is required for pancreas development in mice. *Nature*, *371*(6498), 606–609. https://doi.org/10.1038/371606A0

Juan-Mateu, J., Rech, T. H., Villate, O., Lizarraga-Mollinedo, E., Wendt, A., Turatsinze, J.-V., et al. (2017). Neuron-enriched RNA-binding Proteins Regulate Pancreatic Beta Cell Function and Survival. *Journal of Biological Chemistry*, *292*(8), 3466–3480. https://doi.org/10.1074/jbc.M116.748335

Jung, I.-R., Choi, S.-E., Jung, J.-G., Lee, S.-A., Han, S. J., Kim, H. J., et al. (2015). Involvement of iron depletion in palmitate-induced lipotoxicity of beta cells. *Molecular and Cellular Endocrinology*, *407*, 74–84. https://doi.org/10.1016/j.mce.2015.03.007

Jung, Y. H., & Bu, S. Y. (2020). Suppression of long chain acyl-CoA synthetase blocks intracellular fatty acid flux and glucose uptake in skeletal myotubes. *Biochimica et Biophysica Acta (BBA) - Molecular and Cell Biology of Lipids*, *1865*(7), 158678. https://doi.org/10.1016/j.bbalip.2020.158678

Kaptoge, S., Seshasai, S., Sun, L., Walker, M., Bolton, T., Spackman, S., et al. (2023). Life expectancy associated with different ages at diagnosis of type 2 diabetes in high-income countries: 23 million person-years of observation. *The Lancet Diabetes & Endocrinology*, *11*(10), 731–742. https://doi.org/10.1016/S2213-8587(23)00223-1

van Karnebeek, C. D. M., Tarailo-Graovac, M., Leen, R., Meinsma, R., Correard, S., Jansen-Meijer, J., et al. (2024). CIAO1 and MMS19 deficiency: A lethal neurodegenerative phenotype caused by cytosolic Fe-S cluster protein assembly disorders. *Genetics in Medicine*, *26*(6), 101104. https://doi.org/10.1016/J.GIM.2024.101104

Kato, I., Kasukabe, T., & Kumakura, S. (2020). Menin-MLL inhibitors induce ferroptosis and enhance the anti-proliferative activity of auranofin in several types of cancer cells. *International Journal of Oncology*, *57*(4), 1057–1071. https://doi.org/10.3892/IJO.2020.5116

Kearney, A. L., Norris, D. M., Ghomlaghi, M., Kin Lok Wong, M., Humphrey, S. J., Carroll, L., et al. (2021). Akt phosphorylates insulin receptor substrate to limit PI3K-mediated PIP3 synthesis. *ELife*, *10*, e66942. https://doi.org/10.7554/eLife.66942

Kerins, M. J., Vashisht, A. A., Liang, B. X.-T., Duckworth, S. J., Praslicka, B. J., Wohlschlegel, J. A., & Ooi, A. (2017). Fumarate Mediates a Chronic Proliferative Signal in Fumarate Hydratase-Inactivated Cancer Cells by Increasing Transcription and Translation of Ferritin Genes. *Molecular and Cellular Biology*, *37*(11). https://doi.org/10.1128/MCB.00079-17

Khan, M. A., Mohammad, T., Malik, A., Hassan, M. I., & Domashevskiy, A. V. (2023). Iron response elements (IREs)-mRNA of Alzheimer's amyloid precursor protein binding to iron regulatory protein (IRP1): a combined molecular docking and spectroscopic approach. *Scientific Reports*, *13*(1), 5073. https://doi.org/10.1038/s41598-023-32073-x

Kim, C., Lee, H., Kang, H., Shin, J. J., Tak, H., Kim, W., et al. (2016). RNA-binding protein HuD reduces triglyceride production in pancreatic β cells by enhancing the expression of insulin-induced gene 1. *Biochimica et Biophysica Acta (BBA) - Gene Regulatory Mechanisms*, *1859*(4), 675–685. https://doi.org/10.1016/j.bbagrm.2016.02.017

Kim, K.-D., Chung, W.-H., Kim, H.-J., Lee, K.-C., & Roe, J.-H. (2010). Monothiol glutaredoxin Grx5 interacts with Fe–S scaffold proteins Isa1 and Isa2 and supports Fe–S assembly and DNA integrity in mitochondria of fission yeast. *Biochemical and Biophysical Research Communications*, *392*(3), 467–472. https://doi.org/10.1016/j.bbrc.2010.01.051

Kim, K.-D., Kim, H.-J., Lee, K.-C., & Roe, J.-H. (2011). Multi-domain CGFS-type glutaredoxin Grx4 regulates iron homeostasis via direct interaction with a repressor Fep1 in fission yeast. *Biochemical and Biophysical Research Communications*, *408*(4), 609–614. https://doi.org/10.1016/j.bbrc.2011.04.069

Kim, M. K., Cheong, Y. H., Lee, S. H., Kim, T. H., Jung, I. H., Chae, Y., et al. (2021). A novel GPR119 agonist DA-1241 preserves pancreatic function via the suppression of ER stress and increased PDX1 expression. *Biomedicine & Pharmacotherapy*, *144*, 112324. https://doi.org/10.1016/J.BIOPHA.2021.112324

Kim, Y. B., Nikoulina, S. E., Ciaraldi, T. P., Henry, R. R., & Kahn, B. B. (1999). Normal insulin-dependent activation of Akt/protein kinase B, with diminished activation of phosphoinositide 3-kinase, in muscle in type 2 diabetes. *The Journal of Clinical Investigation*, *104*(6), 733–741. https://doi.org/10.1172/JCI6928

Kimita, W., Skudder-Hill, L., Shamaitijiang, X., Priya, S., & Petrov, M. S. (2024). Associations of pancreas fat content and size with markers of iron metabolism. *Obesity Research & Clinical Practice*, *18*(1), 56–63. https://doi.org/10.1016/J.ORCP.2024.01.002

King, H., Aubert, R. E., & Herman, W. H. (1998). Global Burden of Diabetes, 1995–2025: Prevalence, numerical estimates, and projections. *Diabetes Care*, *21*(9), 1414–1431. https://doi.org/10.2337/diacare.21.9.1414

Kita, K., Oya, H., Gennis, R. B., Ackrell, B. A. C., & Kasahara, M. (1990). Human complex II(succinate-ubiquinone oxidoreductase): cDNA cloning of iron sulfur(Ip) subunit of liver mitochondria. *Biochemical and Biophysical Research Communications*, *166*(1), 101–108. https://doi.org/10.1016/0006-291X(90)91916-G

Knaff, D. B., & Sutton, R. B. (2013). Utility of Synechocystis sp. PCC 6803 glutaredoxin A as a platform to study high-resolution mutagenesis of proteins. *Frontiers in Plant Science*, *4*(NOV), 66744. https://doi.org/10.3389/fpls.2013.00461

Koch, R. O., Zoller, H., Theurl, I., Obrist, P., Egg, G., Strohmayer, W., et al. (2003). Distribution of DMT 1 within the human glandular system. *Histology and Histopathology*, *18*(4), 1095–1101. https://doi.org/10.14670/HH-18.1095

Kohler, S. A., Menotti, E., & Kühn, L. C. (1999). Molecular cloning of mouse glycolate oxidase. High evolutionary conservation and presence of an iron-responsive element-like sequence in the mRNA. *Journal of Biological Chemistry*, *274*(22), 15966. https://doi.org/10.1016/S0021-9258(19)73113-5

Köhnke, D., Ludwig, B., & Kadenbach, B. (1993). A threshold membrane potential accounts for controversial effects of fatty acids on mitochondrial oxidative phosphorylation. *FEBS Letters*, *336*(1), 90–94. https://doi.org/10.1016/0014-5793(93)81616-8

Koopman, R. J., Mainous, A. G., Diaz, V. A., & Geesey, M. E. (2005). Changes in age at diagnosis or type 2 diabetes mellitus in the United States, 1988 to 2000. *Annals of Family Medicine*, *3*(1), 60–63. https://doi.org/10.1370/afm.214

Kreimer, H. (2024). *Auswirkungen von Glukose, Ölsäure und inflammatorischen Zytokinen auf Glutaredoxin 5 und den Eisenstoffwechsel von MIN6 Zellen*. Justus-Liebig-Universität Gießen. https://doi.org/10.22029/jlupub-19398

Kumar, P., Nagarajan, A., & Uchil, P. D. (2018). Analysis of Cell Viability by the MTT Assay. *Cold Spring Harbor Protocols*, *2018*(6), pdb.prot095505. https://doi.org/10.1101/pdb.prot095505

Lagou, V., Jiang, L., Ulrich, A., Zudina, L., González, K. S. G., Balkhiyarova, Z., et al. (2023). GWAS of random glucose in 476,326 individuals provide insights into diabetes pathophysiology, complications and treatment stratification. *Nature Genetics*, *55*(9), 1448–1461. https://doi.org/10.1038/s41588-023-01462-3

Lai, S., Li, Y., Kuang, Y., Cui, H., Yang, Y., Sun, W., et al. (2017). PKCδ silencing alleviates saturated fatty acid induced ER stress by enhancing SERCA activity. *Bioscience Reports*, *37*(6), 20170869. https://doi.org/10.1042/BSR20170869/57694

Lai, Y., Zhang, Y., Zhou, S., Xu, J., Du, Z., Feng, Z., et al. (2023). Structure of the human ATP synthase. *Molecular Cell*, *83*(12), 2137–2147. https://doi.org/10.1016/j.molcel.2023.04.029

Lan, X., Han, J., Wang, B., & Sun, M. (2022). Integrated analysis of transcriptome profiling of lncRNAs and mRNAs in livers of type 2 diabetes mellitus. *Physiological Genomics*, *54*(2), 86–97. https://doi.org/10.1152/physiolgenomics.00105.2021

Lan, Y., Yang, T., Yue, Q., Wang, Z., Zhong, X., Luo, X., et al. (2023). IRP1 mediated ferroptosis reverses temozolomide resistance in glioblastoma via affecting LCN2/FPN1 signaling axis depended on NFKB2. *IScience*, *26*(8), 107377. https://doi.org/10.1016/j.isci.2023.107377

Lang, A. L., Nissanka, N., Louzada, R. A., Tamayo, A., Pereira, E., Moraes, C. T., & Caicedo, A. (2023). A Defect in Mitochondrial Complex III but Not in Complexes I or IV Causes Early β-Cell Dysfunction and Hyperglycemia in Mice. *Diabetes*, *72*(9), 1262–1276. https://doi.org/10.2337/DB22-0728

Lange, H., Lisowsky, T., Gerber, J., Mühlenhoff, U., Kispal, G., & Lill, R. (2001). An essential function of the mitochondrial sulfhydryl oxidase Erv1p/ALR in the maturation of cytosolic Fe/S proteins. *EMBO Reports*, *2*(8), 715–720. https://doi.org/10.1093/embo-reports/kve161

Laurent, T. C., Moore, E. C., & Reichard, P. (1964). Enzymatic Synthesis of Deoxyribonucleotides. *Journal of Biological Chemistry*, *239*(10), 3436–3444. https://doi.org/10.1016/S0021-9258(18)97742-2

Leasher, J. L., Bourne, R. R. A., Flaxman, S. R., Jonas, J. B., Keeffe, J., Naidoo, K., et al. (2016). Global Estimates on the Number of People Blind or Visually Impaired by Diabetic Retinopathy: A Meta-analysis From 1990 to 2010. *Diabetes Care*, *39*(9), 1643–1649. https://doi.org/10.2337/dc15-2171

Lee, D., Yoon, E., Ham, S. J., Lee, K., Jang, H., Woo, D., et al. (2024). Diabetic sensory neuropathy and insulin resistance are induced by loss of UCHL1 in Drosophila. *Nature Communications*, *15*(1), 468. https://doi.org/10.1038/s41467-024-44747-9

Lee, D. W., Kaur, D., Chinta, S. J., Rajagopalan, S., & Andersen, J. K. (2009). A Disruption in Iron-Sulfur Center Biogenesis via Inhibition of Mitochondrial Dithiol Glutaredoxin 2 May Contribute to Mitochondrial and Cellular Iron Dysregulation in Mammalian Glutathione-Depleted Dopaminergic Cells: Implications for Parkinson's Disease. *Antioxidants & Redox Signaling*, *11*(9), 2083–2094. https://doi.org/10.1089/ars.2009.2489

Lee, J., You, J. H., Shin, D., & Roh, J.-L. (2020). Inhibition of Glutaredoxin 5 predisposes Cisplatin-resistant Head and Neck Cancer Cells to Ferroptosis. *Theranostics*, *10*(17), 7775–7786. https://doi.org/10.7150/thno.46903

Lee, J. H., Jung, I. R., Choi, S. E., Lee, S. M., Lee, S. J., Han, S. J., et al. (2014). Toxicity generated through inhibition of pyruvate carboxylase and carnitine palmitoyl transferase-1 is similar to high glucose/palmitate-induced glucolipotoxicity in INS-1 beta cells. *Molecular and Cellular Endocrinology*, *383*(1–2), 48–59. https://doi.org/10.1016/j.mce.2013.12.002

Lee, S., & Annes, J. P. (2020). Mitochondrial Dysfunction Promotes Diabetes via A Previously Unrecognized Mechanism: Protein Succinylation. *The FASEB Journal*, *34*(S1), 1–1. https://doi.org/10.1096/fasebj.2020.34.s1.04969

Lee, S., Xu, H., Van Vleck, A., Mawla, A. M., Li, A. M., Ye, J., et al. (2022). β-Cell Succinate Dehydrogenase Deficiency Triggers Metabolic Dysfunction and Insulinopenic Diabetes. *Diabetes*, *71*(7), 1439–1453. https://doi.org/10.2337/db21-0834

Lee, Y., Hirose, H., Ohneda, M., Johnson, J. H., McGarry, J. D., & Unger, R. H. (1994). Beta-cell lipotoxicity in the pathogenesis of non-insulin-dependent diabetes mellitus of obese rats: impairment in adipocyte-beta-cell relationships. *Proceedings of the National Academy of Sciences*, *91*(23), 10878–10882. https://doi.org/10.1073/pnas.91.23.10878

Lenzen, S. (2008). Oxidative stress: The vulnerable β-cell. *Biochemical Society Transactions*, *36*(3), 343–347. https://doi.org/10.1042/BST0360343

Lewandowski, S. L., Foster, H. R., Capozzi, M. E., Campbell, J. E., & Merrins, M. J. (2022). Pyruvate kinase and GLP-1 receptor signaling converge on cAMP production to enhance insulin secretion. *Biophysical Journal*, *121*(3), 86a. https://doi.org/10.1016/j.bpj.2021.11.2293

Li, G., Nanjaraj Urs, A. N., Dancis, A., & Zhang, Y. (2022). Genetic suppressors of Δgrx3 Δgrx4, lacking redundant multidomain monothiol yeast glutaredoxins, rescue growth and iron homeostasis. *Bioscience Reports*, *42*(6), 20212665. https://doi.org/10.1042/BSR20212665

Li, Y., Lin, Y., Han, X., Li, W., Yan, W., Ma, Y., et al. (2021). GSK3 inhibitor ameliorates steatosis through the modulation of mitochondrial dysfunction in hepatocytes of obese patients. *IScience*, *24*(3), 102149. https://doi.org/10.1016/j.isci.2021.102149

Li, Zheng, Liu, C., Zhou, Z., Hu, L., Deng, L., Ren, Q., & Qian, H. (2020). A novel FFA1 agonist, CPU025, improves glucose-lipid metabolism and alleviates fatty liver in obese-diabetic (ob/ob) mice. *Pharmacological Research*, *153*, 104679. https://doi.org/10.1016/j.phrs.2020.104679

Li, Zonghong, Zhou, M., Cai, Z., Liu, H., Zhong, W., Hao, Q., et al. (2018). RNA-binding protein DDX1 is responsible for fatty acid-mediated repression of insulin translation. *Nucleic Acids Research*, *46*(22), 12052. https://doi.org/10.1093/NAR/GKY867

Liao, P., Wang, W., Wang, W., Kryczek, I., Li, X., Bian, Y., et al. (2022). CD8+ T cells and fatty acids orchestrate tumor ferroptosis and immunity via ACSL4. *Cancer Cell*, *40*(4), 365-378.e6. https://doi.org/10.1016/j.ccell.2022.02.003

Liew, C. G., Shah, N. N., Briston, S. J., Shepherd, R. M., Khoo, C. P., Dunne, M. J., et al. (2008). PAX4 Enhances Beta-Cell Differentiation of Human Embryonic Stem Cells. *PLoS ONE*, *3*(3), e1783. https://doi.org/10.1371/journal.pone.0001783

Lill, R., Dutkiewicz, R., Freibert, S. A., Heidenreich, T., Mascarenhas, J., Netz, D. J., et al. (2015). The role of mitochondria and the CIA machinery in the maturation of cytosolic and nuclear iron–sulfur proteins. *European Journal of Cell Biology*, *94*(7–9), 280–291. https://doi.org/10.1016/j.ejcb.2015.05.002

Lillig, C. H., Berndt, C., Vergnolle, O., Lönn, M. E., Hudemann, C., Bill, E., & Holmgren, A. (2005). Characterization of human glutaredoxin 2 as iron–sulfur protein: A possible role as redox sensor. *Proceedings of the National Academy of Sciences*, *102*(23), 8168–8173. https://doi.org/10.1073/pnas.0500735102

Lillig, C. H., Berndt, C., & Holmgren, A. (2008). Glutaredoxin systems. *Biochimica et Biophysica Acta (BBA) - General Subjects*, *1780*(11), 1304–1317. https://doi.org/10.1016/j.bbagen.2008.06.003

Lin, E., Graziano, J. H., & Freyer, G. A. (2001). Regulation of the 75-kDa subunit of mitochondrial complex I by iron. *The Journal of Biological Chemistry*, *276*(29), 27685–27692. https://doi.org/10.1074/JBC.M100941200

Lingvay, I., Sumithran, P., Cohen, R. V., & le Roux, C. W. (2022). Obesity management as a primary treatment goal for type 2 diabetes: time to reframe the conversation. *The Lancet*, *399*(10322), 394–405. https://doi.org/10.1016/S0140-6736(21)01919-X

Lipper, C. H., Paddock, M. L., Onuchic, J. N., Mittler, R., Nechushtai, R., & Jennings, P. A. (2015). Cancer-Related NEET Proteins Transfer 2Fe-2S Clusters to Anamorsin, a Protein Required for Cytosolic Iron-Sulfur Cluster Biogenesis. *PLoS ONE*, *10*(10), e0139699. https://doi.org/10.1371/journal.pone.0139699

Liu, G., Guo, S., Anderson, G. J., Camaschella, C., Han, B., & Nie, G. (2014). Heterozygous missense mutations in the GLRX5 gene cause sideroblastic anemia in a Chinese patient. *Blood*, *124*(17), 2750–2751. https://doi.org/10.1182/blood-2014-08-598508

Liu, H., Wu, X., Yang, T., Wang, C., Huang, F., Xu, Y., & Peng, J. (2023). NARFL deficiency caused mitochondrial dysfunction in lung cancer cells by HIF-1α–DNMT1 axis. *Scientific Reports*, *13*(1), 17176. https://doi.org/10.1038/s41598-023-44418-7

Liu, S., Fu, H., Jiang, J., Chen, Z., Gao, J., Shu, H., et al. (2019). Overexpression of a CPYC-Type Glutaredoxin, OsGrxC2.2, Causes Abnormal Embryos and an Increased Grain Weight in Rice. *Frontiers in Plant Science*, *10*, 454960. https://doi.org/10.3389/fpls.2019.00848

Liu, W., Zhu, M., Liu, J., Su, S., Zeng, X., Fu, F., et al. (2024). Comparison of the effects of monounsaturated fatty acids and polyunsaturated fatty acids on the lipotoxicity of islets. *Frontiers in Endocrinology*, *15*, 1368853. https://doi.org/10.3389/fendo.2024.1368853

Liu, Yanting, Wang, Y., Yang, M., Luo, J., Zha, J., Geng, S., & Zeng, W. (2024). Exosomes from hypoxic pretreated ADSCs attenuate ultraviolet light-induced skin injury via GLRX5 delivery and ferroptosis inhibition. *Photochemical & Photobiological Sciences*, *23*(1), 55–63. https://doi.org/10.1007/s43630-023-00498-y

Liu, Yuanbin. (1999). Understanding the biological activity of amyloid proteins in vitro: From inhibited cellular mtt reduction to altered cellular cholesterol homeostatis. *Progress in Neuro-Psychopharmacology and Biological Psychiatry*, *23*(3), 377–395. https://doi.org/10.1016/S0278-5846(99)00003-2

Liu, Yuanbin, Peterson, D. A., Kimura, H., & Schubert, D. (1997). Mechanism of Cellular 3-(4,5-Dimethylthiazol-2-yl)-2,5-Diphenyltetrazolium Bromide (MTT) Reduction. *Journal of Neurochemistry*, *69*(2), 581–593. https://doi.org/10.1046/J.1471-4159.1997.69020581.X

Loots, D. T., Adeniji, A. A., Van Reenen, M., Ozturk, M., Brombacher, F., & Parihar, S. P. (2022). The metabolomics of a protein kinase C delta (PKCδ) knock-out mouse model. *Metabolomics*, *18*(11), 92. https://doi.org/10.1007/s11306-022-01949-w

Loza-Rodríguez, H., Estrada-Soto, S., Alarcón-Aguilar, F. J., Huang, F., Aquino-Jarquín, G., Fortis-Barrera, Á., et al. (2020). Oleanolic acid induces a dual agonist action on PPARγ/α and GLUT4 translocation: A pentacyclic triterpene for dyslipidemia and type 2 diabetes. *European Journal of Pharmacology*, *883*, 173252. https://doi.org/10.1016/j.ejphar.2020.173252

Lu, H., Koshkin, V., Allister, E. M., Gyulkhandanyan, A. V., & Wheeler, M. B. (2010). Molecular and metabolic evidence for mitochondrial defects associated with β-cell dysfunction in a mouse model of type 2 diabetes. *Diabetes*, *59*(2), 448–459. https://doi.org/10.2337/db09-0129

Luikenhuis, S., Perrone, G., Dawes, I. W., & Grant, C. M. (1998). The Yeast Saccharomyces cerevisiae Contains Two Glutaredoxin Genes That Are Required for Protection against Reactive Oxygen Species. *Molecular Biology of the Cell*, *9*(5), 1081. https://doi.org/10.1091/MBC.9.5.1081

Luo, H., Wang, X., Song, S., Wang, Y., Dan, Q., & Ge, H. (2022). Targeting stearoyl-coa desaturase enhances radiation induced ferroptosis and immunogenic cell death in esophageal squamous cell carcinoma. *OncoImmunology*, *11*(1). https://doi.org/10.1080/2162402X.2022.2101769

Luo, M., Jiang, Y. L., Ma, X. X., Tang, Y. J., He, Y. X., Yu, J., et al. (2010). Structural and biochemical characterization of yeast monothiol glutaredoxin Grx6. *Journal of Molecular Biology*, *398*(4), 614–622. https://doi.org/10.1016/J.JMB.2010.03.029

Ma, X. M., Geng, K., Law, B. Y.-K., Wang, P., Pu, Y. L., Chen, Q., et al. (2023). Lipotoxicity-induced mtDNA release promotes diabetic cardiomyopathy by activating the cGAS-STING pathway in obesity-related diabetes. *Cell Biology and Toxicology*, *39*(1), 277–299. https://doi.org/10.1007/s10565-021-09692-z

Maestre, I., Jordán, J., Calvo, S., Reig, J. A., Ceña, V., Soria, B., et al. (2003). Mitochondrial dysfunction is involved in apoptosis induced by serum withdrawal and fatty acids in the β-cell line INS-1. *Endocrinology*, *144*(1), 335–345. https://doi.org/10.1210/en.2001-211282

Magtanong, L., Ko, P.-J., To, M., Cao, J. Y., Forcina, G. C., Tarangelo, A., et al. (2019). Exogenous Monounsaturated Fatty Acids Promote a Ferroptosis-Resistant Cell State. *Cell Chemical Biology*, *26*(3), 420-432.e9. https://doi.org/10.1016/j.chembiol.2018.11.016

Maio, N., Singh, A., Uhrigshardt, H., Saxena, N., Tong, W.-H., & Rouault, T. A. (2014). Cochaperone Binding to LYR Motifs Confers Specificity of Iron Sulfur Cluster Delivery. *Cell Metabolism*, *19*(3), 445–457. https://doi.org/10.1016/j.cmet.2014.01.015

Maio, N., Saneto, R. P., Steet, R., Sotero de Menezes, M. A., Skinner, C., & Rouault, T. A. (2022). Disruption of cellular iron homeostasis by IREB2 missense variants causes severe neurodevelopmental delay, dystonia and seizures. *Brain Communications*, *4*(3). https://doi.org/10.1093/braincomms/fcac102

Mann, J., Reznik, E., Santer, M., Fongheiser, M. A., Smith, N., Hirschhorn, T., et al. (2024). Ferroptosis inhibition by oleic acid mitigates iron-overload-induced injury. *Cell Chemical Biology*, *31*(2), 249-264.e7. https://doi.org/10.1016/j.chembiol.2023.10.012

Mao, X., Chen, H., Tang, J., Wang, L., & Shu, T. (2017). Hepcidin links gluco-toxicity to pancreatic beta cell dysfunction by inhibiting Pdx-1 expression. *Endocrine Connections*, *6*(3), 121–128. https://doi.org/10.1530/EC-16-0115

Maris, M., Robert, S., Waelkens, E., Derua, R., Hernangomez, M. H., D'Hertog, W., et al. (2013). Role of the saturated nonesterified fatty acid palmitate in beta cell dysfunction. *Journal of Proteome Research*, *12*(1), 347–362. https://doi.org/10.1021/pr300596g

Martelli, A., Wattenhofer-donzé, M., Schmucker, S., Bouvet, S., Reutenauer, L., & Puccio, H. (2007). Frataxin is essential for extramitochondrial Fe–S cluster proteins in mammalian tissues. *Human Molecular Genetics*, *16*(22), 2651–2658. https://doi.org/10.1093/HMG/DDM163

Martin, J. L. (1995). Thioredoxin - a fold for all reasons. *Structure*, *3*(3), 245–250. https://doi.org/10.1016/S0969-2126(01)00154-X

McCotter, S. W., Kretschmer, M., Lee, C. W. J., Heimel, K., & Kronstad, J. W. (2023). The Monothiol Glutaredoxin Grx4 Influences Iron Homeostasis and Virulence in Ustilago maydis. *Journal of Fungi*, *9*(11), 1112. https://doi.org/10.3390/jof9111112

McDonagh, B., Padilla, C. A., Pedrajas, J. R., & Barcena, J. A. (2011). Biosynthetic and iron metabolism is regulated by thiol proteome changes dependent on glutaredoxin-2 and mitochondrial peroxiredoxin-1 in Saccharomyces cerevisiae. *The Journal of Biological Chemistry*, *286*(17), 15565–15576. https://doi.org/10.1074/JBC.M110.193102

McNally, B. D., Ashley, D. F., Hänschke, L., Daou, H. N., Watt, N. T., Murfitt, S. A., et al. (2022). Long-chain ceramides are cell non-autonomous signals linking lipotoxicity to endoplasmic reticulum stress in skeletal muscle. *Nature Communications*, *13*(1), 1748. https://doi.org/10.1038/s41467-022-29363-9

Mei, J., Park, M., York, D. A., & Erlanson-Albertsson, C. (2007). Fatty acids and glucose in high concentration down-regulates ATP synthase β-subunit protein expression in INS-1 cells. *Nutritional Neuroscience*, *10*(5–6), 273–278. https://doi.org/10.1080/10284150701745910

Meier, D. T., Rachid, L., Wiedemann, S. J., Traub, S., Trimigliozzi, K., Stawiski, M., et al. (2022). Prohormone convertase 1/3 deficiency causes obesity due to impaired proinsulin processing. *Nature Communications*, *13*(1), 4761. https://doi.org/10.1038/s41467-022-32509-4

Meli, R., Mattace Raso, G., Irace, C., Simeoli, R., Di Pascale, A., Paciello, O., et al. (2013). High Fat Diet Induces Liver Steatosis and Early Dysregulation of Iron Metabolism in Rats. *PLoS ONE*, *8*(6), e66570. https://doi.org/10.1371/journal.pone.0066570

Meng, F., Fleming, B. A., Jia, X., Rousek, A. A., Mulvey, M. A., & Ward, D. M. (2022). Lysosomal iron recycling in mouse macrophages is dependent upon both LcytB and Steap3 reductases. *Blood Advances*, *6*(6), 1692–1707. https://doi.org/10.1182/bloodadvances.2021005609

Menga, A., Infantino, V., Iacobazzi, F., Convertini, P., Palmieri, F., & Iacobazzi, V. (2013). Insight into mechanism of in vitro insulin secretion increase induced by antipsychotic clozapine: Role of FOXA1 and mitochondrial citrate carrier. *European Neuropsychopharmacology*, *23*(8), 978–987. https://doi.org/10.1016/j.euroneuro.2012.08.015

Mercier, A., & Labbé, S. (2009). Both Php4 Function and Subcellular Localization Are Regulated by Iron via a Multistep Mechanism Involving the Glutaredoxin Grx4 and the Exportin Crm1. *Journal of Biological Chemistry*, *284*(30), 20249–20262. https://doi.org/10.1074/JBC.M109.009563

Miao, R., Fang, X., Zhang, Y., Wei, J., Zhang, Y., & Tian, J. (2023). Iron metabolism and ferroptosis in type 2 diabetes mellitus and complications: mechanisms and therapeutic opportunities. *Cell Death & Disease*, *14*(3), 186. https://doi.org/10.1038/s41419-023-05708-0

Mir, S. U. R., George, N. M., Zahoor, L., Harms, R., Guinn, Z., & Sarvetnick, N. E. (2015). Inhibition of autophagic turnover in β-cells by fatty acids and glucose leads to apoptotic cell death. *Journal of Biological Chemistry*, *290*(10), 6071–6085. https://doi.org/10.1074/jbc.M114.605345

Mise, K., Long, J., Galvan, D. L., Ye, Z., Fan, G., Sharma, R., et al. (2024). NDUFS4 regulates cristae remodeling in diabetic kidney disease. *Nature Communications*, *15*(1), 1965. https://doi.org/10.1038/s41467-024-46366-w

Mishra, B. K., Banerjee, B. D., Agrawal, V., & Madhu, S. V. (2020). Association of PPARγ gene expression with postprandial hypertriglyceridaemia and risk of type 2 diabetes mellitus. *Endocrine*, *68*(3), 549–556. https://doi.org/10.1007/s12020-020-02257-w

Misslinger, M., Scheven, M. T., Hortschansky, P., López-Berges, M. S., Heiss, K., Beckmann, N., et al. (2019). The monothiol glutaredoxin GrxD is essential for sensing iron starvation in Aspergillus fumigatus. *PLOS Genetics*, *15*(9), e1008379. https://doi.org/10.1371/journal.pgen.1008379

Miyazaki, J. I., Araki, K., Yamato, E., Ikegami, H., Asano, T., Shibasaki, Y., et al. (1990). Establishment of a pancreatic β cell line that retains glucose-inducible insulin secretion: Special reference to expression of glucose transporter isoforms. *Endocrinology*, *127*(1), 126–132. https://doi.org/10.1210/endo-127-1-126

Mleczko-Sanecka, K., Roche, F., Rita da Silva, A., Call, D., D'Alessio, F., Ragab, A., et al. (2014). Unbiased RNAi screen for hepcidin regulators links hepcidin suppression to proliferative Ras/RAF and nutrient-dependent mTOR signaling. *Blood*, *123*(10), 1574–1585. https://doi.org/10.1182/blood-2013-07-515957

Moirand, R., Kerdavid, F., Loréal, O., Hubert, N., Leroyer, P., Brissot, P., & Lescoat, G. (1995). Regulation of ferritin expression by alcohol in a human hepatoblastoma cell line and in rat hepatocyte cultures. *Journal of Hepatology*, *23*(4), 431–439. https://doi.org/10.1016/0168-8278(95)80202-9

Montes-Cortes, D. H., Hicks, J. J., Ceballos-Reyes, G. M., Garcia-Sanchez, J. R., Medina-Navarro, R., & Olivares-Corichi, I. M. (2010). Chemical and functional changes of human insulin by in vitro incubation with blood from diabetic patients in oxidative stress. *Metabolism*, *59*(7), 935–942. https://doi.org/10.1016/j.metabol.2009.10.013

Moon, J. S., Karunakaran, U., Suma, E., Chung, S. M., & Won, K. C. (2020). The Role of CD36 in Type 2 Diabetes Mellitus: β-Cell Dysfunction and Beyond. *Diabetes & Metabolism Journal*, *44*(2), 222. https://doi.org/10.4093/dmj.2020.0053

Morgan, K. L., Estevez, A. O., Mueller, C. L., Cacho-Valadez, B., Miranda-Vizuete, A., Szewczyk, N. J., & Estevez, M. (2010). The Glutaredoxin GLRX-21 Functions to Prevent Selenium-Induced Oxidative Stress in Caenorhabditis elegans. *Toxicological Sciences*, *118*(2), 530–543. https://doi.org/10.1093/toxsci/kfq273

Mori, K., Miyanohara, I., Moteki, H., Nishio, S., Kurono, Y., & Usami, S. (2015). Novel Mutations in GRXCR1 at DFNB25 Lead to Progressive Hearing Loss and Dizziness. *Annals of Otology, Rhinology & Laryngology*, *124*(1_suppl), 129S-134S. https://doi.org/10.1177/0003489415575061

Morita, M., & Imanaka, T. (2012). Peroxisomal ABC transporters: Structure, function and role in disease. *Biochimica et Biophysica Acta (BBA) - Molecular Basis of Disease*, *1822*(9), 1387–1396. https://doi.org/10.1016/j.bbadis.2012.02.009

Moseler, A., Aller, I., Wagner, S., Nietzel, T., Przybyla-Toscano, J., Mühlenhoff, U., et al. (2015). The mitochondrial monothiol glutaredoxin S15 is essential for iron-sulfur protein maturation in Arabidopsis thaliana. *Proceedings of the National Academy of Sciences*, *112*(44), 13735–13740. https://doi.org/10.1073/pnas.1510835112

Mosmann, T. (1983). Rapid colorimetric assay for cellular growth and survival: Application to proliferation and cytotoxicity assays. *Journal of Immunological Methods*, *65*(1–2), 55–63. https://doi.org/10.1016/0022-1759(83)90303-4

Moss, N. D., Wells, K. L., Theis, A., Kim, Y.-K., Spigelman, A. F., Liu, X., et al. (2023). Modulation of insulin secretion by RBFOX2-mediated alternative splicing. *Nature Communications*, *14*(1), 7732. https://doi.org/10.1038/s41467-023-43605-4

Muche, A. A., Olayemi, O. O., & Gete, Y. K. (2019). Prevalence and determinants of gestational diabetes mellitus in Africa based on the updated international diagnostic criteria: a systematic review and meta-analysis. *Archives of Public Health*, *77*(1), 36. https://doi.org/10.1186/s13690-019-0362-0

Mühlenhoff, U. (2003). Components involved in assembly and dislocation of iron-sulfur clusters on the scaffold protein Isu1p. *The EMBO Journal*, *22*(18), 4815–4825. https://doi.org/10.1093/emboj/cdg446

Mühlenhoff, U., Braymer, J. J., Christ, S., Rietzschel, N., Uzarska, M. A., Weiler, B. D., & Lill, R. (2020). Glutaredoxins and iron-sulfur protein biogenesis at the interface of redox biology and iron metabolism. *Biological Chemistry*, *401*(12), 1407–1428. https://doi.org/10.1515/hsz-2020-0237

Murataliev, M. B., Feyereisen, R., & Walker, F. A. (2004). Electron transfer by diflavin reductases. *Biochimica et Biophysica Acta (BBA) - Proteins and Proteomics*, *1698*(1), 1–26. https://doi.org/10.1016/j.bbapap.2003.10.003

Nagaraju, R., & Rajini, P. S. (2016). Adaptive response of rat pancreatic β-cells to insulin resistance induced by monocrotophos: Biochemical evidence. *Pesticide Biochemistry and Physiology*, *134*, 39–48. https://doi.org/10.1016/j.pestbp.2016.04.009

Nakamura, M. (2024). Lipotoxicity as a therapeutic target in obesity and diabetic cardiomyopathy. *Journal of Pharmacy & Pharmaceutical Sciences*, *27*, 12568. https://doi.org/10.3389/jpps.2024.12568

Nathan, D. M., Davidson, M. B., DeFronzo, R. A., Heine, R. J., Henry, R. R., Pratley, R., & Zinman, B. (2007). Impaired Fasting Glucose and Impaired Glucose Tolerance. *Diabetes Care*, *30*(3), 753–759. https://doi.org/10.2337/dc07-9920

Navarro-Sastre, A., Tort, F., Stehling, O., Uzarska, M. A., Arranz, J. A., Del Toro, M., et al. (2011). A fatal mitochondrial disease is associated with defective NFU1 function in the maturation of a subset of mitochondrial Fe-S proteins. *American Journal of Human Genetics*, *89*(5), 656–67. https://doi.org/10.1016/j.ajhg.2011.10.005

Netz, D. J. A., Stith, C. M., Stümpfig, M., Köpf, G., Vogel, D., Genau, H. M., et al. (2012). Eukaryotic DNA polymerases require an iron-sulfur cluster for the formation of active complexes. *Nature Chemical Biology*, *8*(1), 125–132. https://doi.org/10.1038/nchembio.721

Nicolas, E., Golemis, E. A., & Arora, S. (2016). POLD1: Central mediator of DNA replication and repair, and implication in cancer and other pathologies. *Gene*, *590*(1), 128–141. https://doi.org/10.1016/j.gene.2016.06.031

Ning, X., Sun, Y., Wang, C., Zhang, W., Sun, M., Hu, H., et al. (2018). A Rice CPYC-Type Glutaredoxin OsGRX20 in Protection against Bacterial Blight, Methyl Viologen and Salt Stresses. *Frontiers in Plant Science*, *9*, 291207. https://doi.org/10.3389/fpls.2018.00111

Nishizawa, H., Matsumoto, M., Shindo, T., Saigusa, D., Kato, H., Suzuki, K., et al. (2020). Ferroptosis is controlled by the coordinated transcriptional regulation of glutathione and labile iron metabolism by the transcription factor BACH1. *Journal of Biological Chemistry*, *295*(1), 69–82. https://doi.org/10.1074/jbc.RA119.009548

Ogata, F. T., Branco, V., Vale, F. F., & Coppo, L. (2021). Glutaredoxin: Discovery, redox defense and much more. *Redox Biology*, *43*, 101975. https://doi.org/10.1016/j.redox.2021.101975

Ojeda, L., Keller, G., Mühlenhoff, U., Rutherford, J. C., Lill, R., & Winge, D. R. (2006). Role of Glutaredoxin-3 and Glutaredoxin-4 in the Iron Regulation of the Aft1 Transcriptional Activator in Saccharomyces cerevisiae. *Journal of Biological Chemistry*, *281*(26), 17661–17669. https://doi.org/10.1074/jbc.M602165200

Olson, L. K., Sharma, A., Peshavaria, M., Wright, C. V. E., Towle, H. C., Rodertson, R. P., & Stein, R. (1995). Reduction of insulin gene transcription in HIT-T15 beta cells chronically exposed to a supraphysiologic glucose concentration is associated with loss of STF-1 transcription factor expression. *Proceedings of the National Academy of Sciences*, *92*(20), 9127–9131. https://doi.org/10.1073/pnas.92.20.9127

Ong, K. L., Stafford, L. K., McLaughlin, S. A., Boyko, E. J., Vollset, S. E., Smith, A. E., et al. (2023). Global, regional, and national burden of diabetes from 1990 to 2021, with projections of prevalence to 2050: a systematic analysis for the Global Burden of Disease Study 2021. *The Lancet*, *402*(10397), 203–234. https://doi.org/10.1016/S0140-6736(23)01301-6

Oropeza, D., Jouvet, N., Bouyakdan, K., Perron, G., Ringuette, L. J., Philipson, L. H., et al. (2015). PGC-1 coactivators in β-cells regulate lipid metabolism and are essential for insulin secretion coupled to fatty acids. *Molecular Metabolism*, *4*(11), 811–822. https://doi.org/10.1016/j.molmet.2015.08.001

Oskarsson, G. R., Oddsson, A., Magnusson, M. K., Kristjansson, R. P., Halldorsson, G. H., Ferkingstad, E., et al. (2020). Predicted loss and gain of function mutations in ACO1 are associated with erythropoiesis. *Communications Biology*, *3*(1), 189. https://doi.org/10.1038/s42003-020-0921-5

Ouyang, J., Zhou, L., & Wang, Q. (2023). Spotlight on iron and ferroptosis: research progress in diabetic retinopathy. *Frontiers in Endocrinology*, *14*, 1234824. https://doi.org/10.3389/fendo.2023.1234824

Ozer, H. K., Dlouhy, A. C., Thornton, J. D., Hu, J., Liu, Y., Barycki, J. J., et al. (2015). Cytosolic Fe-S cluster protein maturation and iron regulation are independent of the mitochondrial Erv1/Mia40 Import System. *Journal of Biological Chemistry*, *290*(46), 27829–27840. https://doi.org/10.1074/jbc.M115.682179

Palomera-Avalos, V., Griñán-Ferré, C., Puigoriol-Illamola, D., Camins, A., Sanfeliu, C., Canudas, A. M., & Pallàs, M. (2017). Resveratrol Protects SAMP8 Brain Under Metabolic Stress: Focus on Mitochondrial Function and Wnt Pathway. *Molecular Neurobiology*, *54*(3), 1661–1676. https://doi.org/10.1007/S12035-016-9770-0

Pandey, A. K., Pain, J., Dancis, A., & Pain, D. (2019). Mitochondria export iron–sulfur and sulfur intermediates to the cytoplasm for iron–sulfur cluster assembly and tRNA thiolation in yeast. *Journal of Biological Chemistry*, *294*(24), 9489–9502. https://doi.org/10.1074/jbc.RA119.008600

Pandey, A. K., Pain, J., J, B., Dancis, A., & Pain, D. (2023). Essential mitochondrial role in iron-sulfur cluster assembly of the cytoplasmic isopropylmalate isomerase Leu1 in Saccharomyces cerevisiae. *Mitochondrion*, *69*, 104–115. https://doi.org/10.1016/j.mito.2023.02.006

Paul, V. D., Mühlenhoff, U., Stümpfig, M., Seebacher, J., Kugler, K. G., Renicke, C., et al. (2015). The deca-GX3 proteins Yae1-Lto1 function as adaptors recruiting the ABC protein Rli1 for iron-sulfur cluster insertion. *ELife*, *4*(JULY2015). https://doi.org/10.7554/eLife.08231

Paulo, M. S., Abdo, N. M., Bettencourt-Silva, R., & Al-Rifai, R. H. (2021). Gestational Diabetes Mellitus in Europe: A Systematic Review and Meta-Analysis of Prevalence Studies. *Frontiers in Endocrinology*, *12*. https://doi.org/10.3389/fendo.2021.691033

Peggion, C., Lopreiato, R., Casanova, E., Ruzzene, M., Facchin, S., Pinna, L. A., et al. (2008). Phosphorylation of the Saccharomyces cerevisiae Grx4p glutaredoxin by the Bud32p kinase unveils a novel signaling pathway involving Sch9p, a yeast member of the Akt / PKB subfamily. *The FEBS Journal*, *275*(23), 5919–5933. https://doi.org/10.1111/J.1742-4658.2008.06721.X

Peng, X., Ren, H., Yang, L., Tong, S., Zhou, R., Long, H., et al. (2024). Readily releasable β cells with tight Ca2+–exocytosis coupling dictate biphasic glucose-stimulated insulin secretion. *Nature Metabolism*, *6*(2), 238–253. https://doi.org/10.1038/s42255-023-00962-0

Pérez-García, A., Torrecilla-Parra, M., Fernández-de Frutos, M., Martín-Martín, Y., Pardo-Marqués, V., & Ramírez, C. M. (2022). Posttranscriptional Regulation of Insulin Resistance: Implications for Metabolic Diseases. *Biomolecules*, *12*(2), 208. https://doi.org/10.3390/biom12020208

Petry, S. F., Sharifpanah, F., Sauer, H., & Linn, T. (2017). Differential expression of islet glutaredoxin 1 and 5 with high reactive oxygen species production in a mouse model of diabesity. *PLoS ONE*, *12*(5), 1–17. https://doi.org/10.1371/journal.pone.0176267

Petry, S. F., Sun, L. M., Knapp, A., Reinl, S., & Linn, T. (2018). Distinct shift in beta-cell glutaredoxin 5 expression is mediated by hypoxia and lipotoxicity both in vivo and in vitro. *Frontiers in Endocrinology*, *9*(MAR), 1–11. https://doi.org/10.3389/fendo.2018.00084

Petry, S. F., Römer, A., Rawat, D., Brunner, L., Lerch, N., Zhou, M., et al. (2022). Loss and Recovery of Glutaredoxin 5 Is Inducible by Diet in a Murine Model of Diabesity and Mediated by Free Fatty Acids In Vitro. *Antioxidants*, *11*(4), 788. https://doi.org/10.3390/antiox11040788

Phelps, N. H., Singleton, R. K., Zhou, B., Heap, R. A., Mishra, A., Bennett, J. E., et al. (2024). Worldwide trends in underweight and obesity from 1990 to 2022: a pooled analysis of 3663 population-representative studies with 222 million children, adolescents, and adults. *The Lancet*, *403*(10431), 1027–1050. https://doi.org/10.1016/S0140-6736(23)02750-2

Plecitá-Hlavatá, L., Engstová, H., Holendová, B., Tauber, J., Špaček, T., Petrásková, L., et al. (2020). Mitochondrial Superoxide Production Decreases on Glucose-Stimulated Insulin Secretion in Pancreatic β Cells Due to Decreasing Mitochondrial Matrix NADH/NAD + Ratio. *Antioxidants & Redox Signaling*, *33*(12), 789–815. https://doi.org/10.1089/ars.2019.7800

Plötz, T., von Hanstein, A. S., Krümmel, B., Laporte, A., Mehmeti, I., & Lenzen, S. (2019). Structure-toxicity relationships of saturated and unsaturated free fatty acids for elucidating the lipotoxic effects in human EndoC-βH1 beta-cells. *Biochimica et Biophysica Acta (BBA) - Molecular Basis of Disease*, *1865*(11), 165525. https://doi.org/10.1016/j.bbadis.2019.08.001

Pourcelot, E., Lénon, M., Mobilia, N., Cahn, J.-Y., Arnaud, J., Fanchon, E., et al. (2015). Iron for proliferation of cell lines and hematopoietic progenitors: Nailing down the intracellular functional iron concentration. *Biochimica et Biophysica Acta (BBA) - Molecular Cell Research*, *1853*(7), 1596–1605. https://doi.org/10.1016/j.bbamcr.2015.03.009

Prentki, M., Corkey, B. E., & Madiraju, S. R. M. (2020). Lipid-associated metabolic signalling networks in pancreatic beta cell function. *Diabetologia*, *63*(1), 10–20. https://doi.org/10.1007/s00125-019-04976-w

Quehenberger, O., Armando, A. M., Brown, A. H., Milne, S. B., Myers, D. S., Merrill, A. H., et al. (2010). Lipidomics reveals a remarkable diversity of lipids in human plasma1. *Journal of Lipid Research*, *51*(11), 3299–3305. https://doi.org/10.1194/jlr.M009449

Quinlan, C. L., Orr, A. L., Perevoshchikova, I. V., Treberg, J. R., Ackrell, B. A., & Brand, M. D. (2012). Mitochondrial complex II can generate reactive oxygen species at high rates in both the forward and reverse reactions. *The Journal of Biological Chemistry*, *287*(32), 27255–27264. https://doi.org/10.1074/JBC.M112.374629

Rah, B., Shafarin, J., Karim, A., Bajbouj, K., Hamad, M., & Muhammad, J. S. (2024). Iron Overloading Potentiates the Antitumor Activity of 5-Fluorouracil by Promoting Apoptosis and Ferroptosis in Colorectal Cancer Cells. *Cell Biochemistry and Biophysics*, *82*(4), 3763–3780. https://doi.org/10.1007/s12013-024-01463-x

Rahul, R., Stinchcombe, A. R., Joseph, J. W., & Ingalls, B. (2023). Kinetic modelling of β -cell metabolism reveals control points in the insulin-regulating pyruvate cycling pathways. *IET Systems Biology*, *17*(6), 303–315. https://doi.org/10.1049/syb2.12077

Rakhshandehroo, M., Knoch, B., Müller, M., & Kersten, S. (2010). Peroxisome Proliferator-Activated Receptor Alpha Target Genes. *PPAR Research*, *2010*, 1–20. https://doi.org/10.1155/2010/612089

Ramachandran, D., Roy, U., Garg, S., Ghosh, S., Pathak, S., & Kolthur-Seetharam, U. (2011). Sirt1 and mir-9 expression is regulated during glucose-stimulated insulin secretion in pancreatic β-islets. *The FEBS Journal*, *278*(7), 1167–1174. https://doi.org/10.1111/J.1742-4658.2011.08042.X

Ramzan, R., Vogt, S., & Kadenbach, B. (2020). Stress-mediated generation of deleterious ROS in healthy individuals - role of cytochrome c oxidase. *Journal of Molecular Medicine*, *98*(5), 651–657. https://doi.org/10.1007/s00109-020-01905-y

Ramzy, A., & Kieffer, T. J. (2022). Altered islet prohormone processing: a cause or consequence of diabetes? *Physiological Reviews*, *102*(1), 155–208. https://doi.org/10.1152/physrev.00008.2021

Rauen, U., Petrat, F., Sustmann, R., & De Groot, H. (2004). Iron-induced mitochondrial permeability transition in cultured hepatocytes. *Journal of Hepatology*, *40*(4), 607–615. https://doi.org/10.1016/j.jhep.2003.12.021

Ravassard, P., Hazhouz, Y., Pechberty, S., Bricout-Neveu, E., Armanet, M., Czernichow, P., & Scharfmann, R. (2011). A genetically engineered human pancreatic β cell line exhibiting glucose-inducible insulin secretion. *The Journal of Clinical Investigation*, *121*(9), 3589–3597. https://doi.org/10.1172/JCI58447

Read, A. D., Bentley, R. E., Archer, S. L., & Dunham-Snary, K. J. (2021). Mitochondrial iron–sulfur clusters: Structure, function, and an emerging role in vascular biology. *Redox Biology*, *47*, 102164. https://doi.org/10.1016/J.REDOX.2021.102164

Reddy, N. G., Venkatesh, R., Jayadev, C., Gadde, S. G. K., Agrawal, S., Mishra, P., et al. (2022). Diabetic Retinopathy and Diabetic Macular Edema in People With Early-Onset Diabetes. *Clinical Diabetes*, *40*(2), 222–232. https://doi.org/10.2337/CD21-0110

Reinier, F., Zoledziewska, M., Hanna, D., Smith, J. D., Valentini, M., Zara, I., et al. (2015). Mandibular hypoplasia, deafness, progeroid features and lipodystrophy (MDPL) syndrome in the context of inherited lipodystrophies. *Metabolism*, *64*(11), 1530–1540. https://doi.org/10.1016/J.METABOL.2015.07.022

Rey, P., Becuwe, N., Tourrette, S., & Rouhier, N. (2017). Involvement of Arabidopsis glutaredoxin S14 in the maintenance of chlorophyll content. *Plant, Cell & Environment*, *40*(10), 2319–2332. https://doi.org/10.1111/pce.13036

Rizzollo, F., More, S., Vangheluwe, P., & Agostinis, P. (2021). The lysosome as a master regulator of iron metabolism. *Trends in Biochemical Sciences*, *46*(12), 960–975. https://doi.org/10.1016/J.TIBS.2021.07.003

Rochira, A., Damiano, F., Marsigliante, S., Gnoni, G. V., & Siculella, L. (2013). 3,5-Diiodo-l-thyronine induces SREBP-1 proteolytic cleavage block and apoptosis in human hepatoma (Hepg2) cells. *Biochimica et Biophysica Acta (BBA) - Molecular and Cell Biology of Lipids*, *1831*(12), 1679–1689. https://doi.org/10.1016/J.BBALIP.2013.08.003

Rodríguez-Manzaneque, M. T., Ros, J., Cabiscol, E., Sorribas, A., & Herrero, E. (1999). Grx5 Glutaredoxin Plays a Central Role in Protection against Protein Oxidative Damage in Saccharomyces cerevisiae. *Molecular and Cellular Biology*, *19*(12), 8180–8190. https://doi.org/10.1128/MCB.19.12.8180

Rodríguez-Manzaneque, M. T., Tamarit, J., Bellí, G., Ros, J., & Herrero, E. (2002). Grx5 is a mitochondrial glutaredoxin required for the activity of iron/sulfur enzymes. *Molecular Biology of the Cell*, *13*(4), 1109–1121. https://doi.org/10.1091/mbc.01-10-0517

Roduit, R., Morin, J., Massé, F., Segall, L., Roche, E., Newgard, C. B., et al. (2000). Glucose Down-regulates the Expression of the Peroxisome Proliferator-activated Receptor-α Gene in the Pancreatic β-Cell. *Journal of Biological Chemistry*, *275*(46), 35799–35806. https://doi.org/10.1074/jbc.M006001200

Römer, A., Linn, T., & Petry, S. F. (2021). Lipotoxic Impairment of Mitochondrial Function in β-Cells: A Review. *Antioxidants*, *10*(2), 293. https://doi.org/10.3390/antiox10020293

Römer, A., Rawat, D., Linn, T., & Petry, S. F. (2022). Preparation of fatty acid solutions exerts significant impact on experimental outcomes in cell culture models of lipotoxicity. *Biology Methods and Protocols*, *7*(1), bpab023. https://doi.org/10.1093/biomethods/bpab023

Romsang, A., Leesukon, P., Duangnkern, J., Vattanaviboon, P., & Mongkolsuk, S. (2015). Mutation of the gene encoding monothiol glutaredoxin (GrxD) in Pseudomonas aeruginosa increases its susceptibility to polymyxins. *International Journal of Antimicrobial Agents*, *45*(3), 314–318. https://doi.org/10.1016/j.ijantimicag.2014.10.024

Rouault, T. A. (2006a). If the RNA fits, use it. *Science*, *314*(5807), 1886–1887. https://doi.org/10.1126/science.1137174

Rouault, T. A. (2006b). The role of iron regulatory proteins in mammalian iron homeostasis and disease. *Nature Chemical Biology*, *2*(8), 406–414. https://doi.org/10.1038/nchembio807

Rouault, T. A. (2019). The indispensable role of mammalian iron sulfur proteins in function and regulation of multiple diverse metabolic pathways. *BioMetals*, *32*(3), 343–353. https://doi.org/10.1007/s10534-019-00191-7

Rouault, T. A., & Tong, W.-H. (2005). Iron–sulphur cluster biogenesis and mitochondrial iron homeostasis. *Nature Reviews Molecular Cell Biology*, *6*(4), 345–351. https://doi.org/10.1038/nrm1620

Roy Chowdhury, S., Mittal, R., Yadav, R., & Guglany, V. (2024). Teaching NeuroImage: Glutaredoxin-5–Associated Variant Nonketotic Hyperglycinemia. *Neurology*, *102*(3), e208105. https://doi.org/10.1212/WNL.0000000000208105

Saitoh, Y., Hongwei, W., Ueno, H., Mizuta, M., & Nakazato, M. (2010). Candesartan attenuates fatty acid-induced oxidative stress and NAD(P)H oxidase activity in pancreatic β-cells. *Diabetes Research and Clinical Practice*, *90*(1), 54–59. https://doi.org/10.1016/j.diabres.2010.06.005

Samuel, V. T., & Shulman, G. I. (2019). Nonalcoholic Fatty Liver Disease, Insulin Resistance, and Ceramides. *New England Journal of Medicine*, *381*(19), 1866–1869. https://doi.org/10.1056/NEJMcibr1910023

Sasaki, H., Yanagi, K., Ugi, S., Kobayashi, K., Ohkubo, K., Tajiri, Y., et al. (2018). Definitive diagnosis of mandibular hypoplasia, deafness, progeroid features and lipodystrophy (MDPL) syndrome caused by a recurrent *de novo* mutation in the *POLD1* gene. *Endocrine Journal*, *65*(2), 227–238. https://doi.org/10.1507/endocrj.EJ17-0287

Schägger, H. (2006). Tricine-SDS-PAGE. *Nature Protocols*, *1*(1), 16–22. https://doi.org/10.1038/NPROT.2006.4

Schalinske, K. L., & Eisenstein, R. S. (1996). Phosphorylation and activation of both iron regulatory proteins 1 and 2 in HL-60 cells. *The Journal of Biological Chemistry*, *271*(12), 7168–7176. https://doi.org/10.1074/JBC.271.12.7168

Scharfmann, R., Pechberty, S., Hazhouz, Y., Bülow, M. von, Bricout-Neveu, E., Grenier-Godard, M., et al. (2014). Development of a conditionally immortalized human pancreatic β cell line. *The Journal of Clinical Investigation*, *124*(5), 2087–2098. https://doi.org/10.1172/JCI72674

Schreurs, M., Kuipers, F., & van der Leij, F. R. (2010). Regulatory enzymes of mitochondrial β-oxidation as targets for treatment of the metabolic syndrome. *Obesity Reviews*, *11*(5), 380–388. https://doi.org/10.1111/j.1467-789X.2009.00642.x

Schulz, V., Steinhilper, R., Oltmanns, J., Freibert, S.-A., Krapoth, N., Linne, U., et al. (2024). Mechanism and structural dynamics of sulfur transfer during de novo [2Fe-2S] cluster assembly on ISCU2. *Nature Communications*, *15*(1), 3269. https://doi.org/10.1038/s41467-024-47310-8

Sergeant, S., Ruczinski, I., Ivester, P., Lee, T. C., Morgan, T. M., Nicklas, B. J., et al. (2016). Impact of methods used to express levels of circulating fatty acids on the degree and direction of associations with blood lipids in humans. *British Journal of Nutrition*, *115*(2), 251–61. https://doi.org/10.1017/S0007114515004341

Shao, J., Bai, Z., Zhang, L., & Zhang, F. (2022). Ferrostatin-1 alleviates tissue and cell damage in diabetic retinopathy by improving the antioxidant capacity of the Xc--GPX4 system. *Cell Death Discovery*, *8*(1), 426. https://doi.org/10.1038/s41420-022-01141-y

Sharifi, S., Yamamoto, T., Zeug, A., Elsner, M., Avezov, E., & Mehmeti, I. (2024). Non-esterified fatty acid palmitate facilitates oxidative endoplasmic reticulum stress and apoptosis of β-cells by upregulating ERO-1α expression. *Redox Biology*, *73*, 103170. https://doi.org/10.1016/J.REDOX.2024.103170

Sharma, L., Lu, J., & Bai, Y. (2009). Mitochondrial respiratory complex I: structure, function and implication in human diseases. *Current Medicinal Chemistry*, *16*(10), 1266–1277. https://doi.org/10.2174/092986709787846578

Sharp, P. (2007). Molecular mechanisms involved in intestinal iron absorption. *World Journal of Gastroenterology*, *13*(35), 4716. https://doi.org/10.3748/wjg.v13.i35.4716

Sheftel, A. D., Stehling, O., Pierik, A. J., Netz, D. J. A., Kerscher, S., Elsässer, H.-P., et al. (2009). Human Ind1, an Iron-Sulfur Cluster Assembly Factor for Respiratory Complex I. *Molecular and Cellular Biology*, *29*(22), 6059–6073. https://doi.org/10.1128/MCB.00817-09

Sheftel, A. D., Stehling, O., Pierik, A. J., Elsässer, H.-P., Mühlenhoff, U., Webert, H., et al. (2010). Humans possess two mitochondrial ferredoxins, Fdx1 and Fdx2, with distinct roles in steroidogenesis, heme, and Fe/S cluster biosynthesis. *Proceedings of the National Academy of Sciences*, *107*(26), 11775–11780. https://doi.org/10.1073/pnas.1004250107

Sheftel, A. D., Wilbrecht, C., Stehling, O., Niggemeyer, B., Elsässer, H.-P., Mühlenhoff, U., & Lill, R. (2012). The human mitochondrial ISCA1, ISCA2, and IBA57 proteins are required for [4Fe-4S] protein maturation. *Molecular Biology of the Cell*, *23*(7), 1157–1166. https://doi.org/10.1091/mbc.e11-09-0772

Sheftel, A. D., Mason, A. B., & Ponka, P. (2012). The long history of iron in the Universe and in health and disease. *Biochimica et Biophysica Acta (BBA) - General Subjects*, *1820*(3), 161–187. https://doi.org/10.1016/j.bbagen.2011.08.002

Shen, M., Goforth, J. B., & Eisenstein, R. S. (2023). Iron-dependent post transcriptional control of mitochondrial aconitase expression. *Metallomics*, *15*(1), 99. https://doi.org/10.1093/MTOMCS/MFAC099

Shiao, M.-S., Liao, B.-Y., Long, M., & Yu, H.-T. (2008). Adaptive Evolution of the Insulin Two-Gene System in Mouse. *Genetics*, *178*(3), 1683–1691. https://doi.org/10.1534/genetics.108.087023

Shu, T., Lv, Z., Xie, Y., Tang, J., & Mao, X. (2019). Hepcidin as a key iron regulator mediates glucotoxicity-induced pancreatic β-cell dysfunction. *Endocrine Connections*, *8*(3), 150. https://doi.org/10.1530/EC-18-0516

Sidarala, V., & Kowluru, A. (2017). The Regulatory Roles of Mitogen-Activated Protein Kinase (MAPK) Pathways in Health and Diabetes: Lessons Learned from the Pancreatic β-Cell. *Recent Patents on Endocrine, Metabolic & Immune Drug Discovery*, *10*(2), 76–84. https://doi.org/10.2174/1872214810666161020154905

Sies, H., & Jones, D. P. (2020). Reactive oxygen species (ROS) as pleiotropic physiological signalling agents. *Nature Reviews Molecular Cell Biology*, *21*(7), 363–383. https://doi.org/10.1038/s41580-020-0230-3

Signes, A., & Fernandez-Vizarra, E. (2018). Assembly of mammalian oxidative phosphorylation complexes I–V and supercomplexes. *Essays in Biochemistry*, *62*(3), 255. https://doi.org/10.1042/EBC20170098

Da Silva Xavier, G. (2018). The Cells of the Islets of Langerhans. *Journal of Clinical Medicine*, *7*(3), 54. https://doi.org/10.3390/jcm7030054

Silvestri, L., Nai, A., Pagani, A., & Camaschella, C. (2014). The extrahepatic role of TFR2 in iron homeostasis. *Frontiers in Pharmacology*, *5*, 90885. https://doi.org/10.3389/fphar.2014.00093

Skelin, M., Rupnik, M., & Cencic, A. (2010). Pancreatic beta cell lines and their applications in diabetes mellitus research. *ALTEX*, *27*(2), 105–113. https://doi.org/10.14573/ALTEX.2010.2.105

Sobczak, A. I. S., Blindauer, C. A., & Stewart, A. J. (2019). Changes in Plasma Free Fatty Acids Associated with Type-2 Diabetes. *Nutrients*, *11*(9), 2022. https://doi.org/10.3390/nu11092022

Sokolowska, E., & Blachnio-Zabielska, A. (2019). The Role of Ceramides in Insulin Resistance. *Frontiers in Endocrinology*, *10*, 577. https://doi.org/10.3389/fendo.2019.00577

Song, J., Li, N., Hu, R., Yu, Y., Xu, K., Ling, H., et al. (2022). Effects of PPARD gene variants on the therapeutic responses to exenatide in chinese patients with type 2 diabetes mellitus. *Frontiers in Endocrinology*, *13*, 949990. https://doi.org/10.3389/fendo.2022.949990

Song, Z., Wang, W., Li, N., Yan, S., Rong, K., Lan, T., & Xia, P. (2019). Sphingosine kinase 2 promotes lipotoxicity in pancreatic β-cells and the progression of diabetes. *The FASEB Journal*, *33*(3), 3636–3646. https://doi.org/10.1096/fj.201801496R

Srinivasan, V., Pierik, A. J., & Lill, R. (2014). Crystal Structures of Nucleotide-Free and Glutathione-Bound Mitochondrial ABC Transporter Atm1. *Science*, *343*(6175), 1137–1140. https://doi.org/10.1126/science.1246729

Srivastava, A. K., Reutovich, A. A., Hunter, N. J., Arosio, P., & Bou-Abdallah, F. (2023). Ferritin microheterogeneity, subunit composition, functional, and physiological implications. *Scientific Reports*, *13*(1), 19862. https://doi.org/10.1038/s41598-023-46880-9

Srivastava, S., & Chan, C. (2008). Application of metabolic flux analysis to identify the mechanisms of free fatty acid toxicity to human hepatoma cell line. *Biotechnology and Bioengineering*, *99*(2), 399–410. https://doi.org/10.1002/bit.21568

Stancill, J. S., Broniowska, K. A., Oleson, B. J., Naatz, A., & Corbett, J. A. (2019). Pancreatic β-cells detoxify H2O2 through the peroxiredoxin/thioredoxin antioxidant system. *The Journal of Biological Chemistry*, *294*(13), 4843–4853. https://doi.org/10.1074/jbc.RA118.006219

Stehling, O., Vashisht, A. A., Mascarenhas, J., Jonsson, Z. O., Sharma, T., Netz, D. J. A., et al. (2012). MMS19 Assembles Iron-Sulfur Proteins Required for DNA Metabolism and Genomic Integrity. *Science*, *337*(6091), 195–199. https://doi.org/10.1126/science.1219723

Stehling, O., Mascarenhas, J., Vashisht, A. A., Sheftel, A. D., Niggemeyer, B., Rösser, R., et al. (2013). Human CIA2A-FAM96A and CIA2B-FAM96B integrate iron homeostasis and maturation of different subsets of cytosolic-nuclear iron-sulfur proteins. *Cell Metabolism*, *18*(2), 187–198. https://doi.org/10.1016/j.cmet.2013.06.015

Stehling, O., Wilbrecht, C., & Lill, R. (2014). Mitochondrial iron–sulfur protein biogenesis and human disease. *Biochimie*, *100*(1), 61–77. https://doi.org/10.1016/j.biochi.2014.01.010

Stehling, O., Jeoung, J.-H., Freibert, S. A., Paul, V. D., Bänfer, S., Niggemeyer, B., et al. (2018). Function and crystal structure of the dimeric P-loop ATPase CFD1 coordinating an exposed [4Fe-4S] cluster for transfer to apoproteins. *Proceedings of the National Academy of Sciences*, *115*(39), E9085–E9094. https://doi.org/10.1073/pnas.1807762115

Sumi, K., Hatanaka, Y., Takahashi, R., Wada, N., Ono, C., Sakamoto, Y., et al. (2022). Citrate Synthase Insufficiency Leads to Specific Metabolic Adaptations in the Heart and Skeletal Muscles Upon Low-Carbohydrate Diet Feeding in Mice. *Frontiers in Nutrition*, *9*. https://doi.org/10.3389/fnut.2022.925908

Sun, H., Saeedi, P., Karuranga, S., Pinkepank, M., Ogurtsova, K., Duncan, B. B., et al. (2022). IDF Diabetes Atlas: Global, regional and country-level diabetes prevalence estimates for 2021 and projections for 2045. *Diabetes Research and Clinical Practice*, *183*, 109119. https://doi.org/10.1016/j.diabres.2021.109119

Sun, L.-L., Jiang, B.-G., Li, W.-T., Zou, J.-J., Shi, Y.-Q., & Liu, Z.-M. (2011). MicroRNA-15a positively regulates insulin synthesis by inhibiting uncoupling protein-2 expression. *Diabetes Research and Clinical Practice*, *91*(1), 94–100. https://doi.org/10.1016/j.diabres.2010.11.006

Taddeo, E. P., Alsabeeh, N., Baghdasarian, S., Wikstrom, J. D., Ritou, E., Sereda, S., et al. (2020). Mitochondrial proton leak regulated by Cyclophilin D elevates insulin secretion in islets at nonstimulatory glucose levels. *Diabetes*, *69*(2), 131–145. https://doi.org/10.2337/db19-0379

Tam, E., Sung, H. K., & Sweeney, G. (2023). MitoNEET prevents iron overload-induced insulin resistance in H9c2 cells through regulation of mitochondrial iron. *Journal of Cellular Physiology*, *238*(8), 1867–1875. https://doi.org/10.1002/JCP.31044

Tamayo, E., Benabdellah, K., & Ferrol, N. (2016). Characterization of Three New Glutaredoxin Genes in the Arbuscular Mycorrhizal Fungus Rhizophagus irregularis: Putative Role of RiGRX4 and RiGRX5 in Iron Homeostasis. *PLoS ONE*, *11*(2), e0149606. https://doi.org/10.1371/journal.pone.0149606

Tan, G., Liu, D., Pan, F., Zhao, J., Li, T., Ma, Y., et al. (2016). His-87 ligand in mitoNEET is crucial for the transfer of iron sulfur clusters from mitochondria to cytosolic aconitase. *Biochemical and Biophysical Research Communications*, *470*(1), 226–232. https://doi.org/10.1016/J.BBRC.2016.01.040

Tang, S., Fuß, A., Fattahi, Z., & Culmsee, C. (2024). Drp1 depletion protects against ferroptotic cell death by preserving mitochondrial integrity and redox homeostasis. *Cell Death & Disease*, *15*(8), 626. https://doi.org/10.1038/s41419-024-07015-8

Tang, W., Liang, H., Cheng, Y., Yuan, J., Huang, G., Zhou, Z., & Yang, L. (2021). Diagnostic value of combined islet antigen-reactive T cells and autoantibodies assays for type 1 diabetes mellitus. *Journal of Diabetes Investigation*, *12*(6), 963–969. https://doi.org/10.1111/jdi.13440

Tang, Y., Majewska, M., Leß, B., Mehmeti, I., Wollnitzke, P., Semleit, N., et al. (2024). The fate of intracellular S1P regulates lipid droplet turnover and lipotoxicity in pancreatic beta-cells. *Journal of Lipid Research*, *65*(8), 100587. https://doi.org/10.1016/J.JLR.2024.100587

Terzi, E. M., Sviderskiy, V. O., Alvarez, S. W., Whiten, G. C., & Possemato, R. (2021). Iron-sulfur cluster deficiency can be sensed by IRP2 and regulates iron homeostasis and sensitivity to ferroptosis independent of IRP1 and FBXL5. *Science Advances*, *7*(22). https://doi.org/10.1126/sciadv.abg4302

Tolosa, L., Donato, M. T., & Gómez-Lechón, M. J. (2015). General Cytotoxicity Assessment by Means of the MTT Assay. In *Methods in Molecular Biology* (Vol. 1250, pp. 333–348). Humana Press, New York, NY. https://doi.org/10.1007/978-1-4939-2074-7_26

Trnka, D., Engelke, A. D., Gellert, M., Moseler, A., Hossain, M. F., Lindenberg, T. T., et al. (2020). Molecular basis for the distinct functions of redox-active and FeS-transfering glutaredoxins. *Nature Communications*, *11*(1), 3445. https://doi.org/10.1038/s41467-020-17323-0

Tuttle, K. R., Bosch-Traberg, H., Cherney, D. Z. I., Hadjadj, S., Lawson, J., Mosenzon, O., et al. (2023). Post hoc analysis of SUSTAIN 6 and PIONEER 6 trials suggests that people with type 2 diabetes at high cardiovascular risk treated with semaglutide experience more stable kidney function compared with placebo. *Kidney International*, *103*(4), 772–781. https://doi.org/10.1016/J.KINT.2022.12.028

Uhrigshardt, H., Singh, A., Kovtunovych, G., Ghosh, M., & Rouault, T. A. (2010). Characterization of the human HSC20, an unusual DnaJ type III protein, involved in iron–sulfur cluster biogenesis. *Human Molecular Genetics*, *19*(19), 3816–3834. https://doi.org/10.1093/hmg/ddq301

Upadhyay, A. S., Stehling, O., Panayiotou, C., Rösser, R., Lill, R., & Överby, A. K. (2017). Cellular requirements for iron-sulfur cluster insertion into the antiviral radical SAM protein viperin. *The Journal of Biological Chemistry*, *292*(33), 13879–13889. https://doi.org/10.1074/JBC.M117.780122

Urzica, E., Pierik, A. J., Mühlenhoff, U., & Lill, R. (2009). Crucial Role of Conserved Cysteine Residues in the Assembly of Two Iron−Sulfur Clusters on the CIA Protein Nar1. *Biochemistry*, *48*(22), 4946–4958. https://doi.org/10.1021/bi900312x

Usui, R., Yabe, D., Fauzi, M., Goto, H., Botagarova, A., Tokumoto, S., et al. (2019). GPR40 activation initiates store-operated Ca2+ entry and potentiates insulin secretion via the IP3R1/STIM1/Orai1 pathway in pancreatic β-cells. *Scientific Reports*, *9*(1), 15562. https://doi.org/10.1038/s41598-019-52048-1

Uzarska, M. A., Nasta, V., Weiler, B. D., Spantgar, F., Ciofi-Baffoni, S., Saviello, M. R., et al. (2016). Mitochondrial Bol1 and Bol3 function as assembly factors for specific iron-sulfur proteins. *ELife*, *5*(AUGUST). https://doi.org/10.7554/eLife.16673

Vachon, P., Mercier, A., Jbel, M., & Labbé, S. (2012). The Monothiol Glutaredoxin Grx4 Exerts an Iron-Dependent Inhibitory Effect on Php4 Function. *Eukaryotic Cell*, *11*(6), 806–819. https://doi.org/10.1128/EC.00060-12

Vallon, V., & Thomson, S. C. (2020). The tubular hypothesis of nephron filtration and diabetic kidney disease. *Nature Reviews Nephrology*, *16*(6), 317–336. https://doi.org/10.1038/s41581-020-0256-y

Vatier, C., Bidault, G., Briand, N., Guénantin, A. C., Teyssières, L., Lascols, O., et al. (2013). What the genetics of lipodystrophy can teach us about insulin resistance and diabetes. *Current Diabetes Reports*, *13*(6), 757–767. https://doi.org/10.1007/S11892-013-0431-7

Venezia, O., Islam, S., Cho, C., Timme-Laragy, A. R., & Sant, K. E. (2021). Modulation of PPAR signaling disrupts pancreas development in the zebrafish, Danio rerio. *Toxicology and Applied Pharmacology*, *426*, 115653. https://doi.org/10.1016/j.taap.2021.115653

Verma, Pankaj K., Verma, S., Pande, V., Mallick, S., Deo Tripathi, R., Dhankher, O. P., & Chakrabarty, D. (2016). Overexpression of Rice Glutaredoxin OsGrx_C7 and OsGrx_C2.1 Reduces Intracellular Arsenic Accumulation and Increases Tolerance in Arabidopsis thaliana. *Frontiers in Plant Science*, *7*(7), 597–604. https://doi.org/10.3389/fpls.2016.00740

Verma, Pankaj Kumar, Verma, S., Tripathi, R. D., Pandey, N., & Chakrabarty, D. (2021). CC-type glutaredoxin, OsGrx_C7 plays a crucial role in enhancing protection against salt stress in rice. *Journal of Biotechnology*, *329*, 192–203. https://doi.org/10.1016/j.jbiotec.2021.02.008

Walden, W. E., Selezneva, A. I., Dupuy, J., Volbeda, A., Fontecilla-Camps, J. C., Theil, E. C., & Volz, K. (2006). Structure of Dual Function Iron Regulatory Protein 1 Complexed with Ferritin IRE-RNA. *Science*, *314*(5807), 1903–1908. https://doi.org/10.1126/science.1133116

Walters, L. A., & Escobar, M. A. (2016). The AtGRXS3/4/5/7/8 glutaredoxin gene cluster on Arabidopsis thaliana chromosome 4 is coordinately regulated by nitrate and appears to control primary root growth. *Plant Signaling & Behavior*, *11*(4), e1171450. https://doi.org/10.1080/15592324.2016.1171450

Wan, J., Jiang, L., Lü, Q., Ke, L., Li, X., & Tong, N. (2010). Activation of PPARδ up-regulates fatty acid oxidation and energy uncoupling genes of mitochondria and reduces palmitate-induced apoptosis in pancreatic β-cells. *Biochemical and Biophysical Research Communications*, *391*(3), 1567–1572. https://doi.org/10.1016/j.bbrc.2009.12.127

Wang, B., Thompson, M. S., & Adkins, K. M. (2021). Characteristics of the Iron-responsive Element (IRE) Stems in the Untranslated Regions of Animal mRNAs. *The Open Biochemistry Journal*, *15*(1), 26–37. https://doi.org/10.2174/1874091X02115010026

Wang, Jian, & Pantopoulos, K. (2011). Regulation of cellular iron metabolism. *The Biochemical Journal*, *434*(3), 365–381. https://doi.org/10.1042/BJ20101825

Wang, Jing, Jiang, M., Yue, G., Zhu, L., Wang, X., Liang, M., et al. (2022). ISCA2 deficiency leads to heme synthesis defects and impaired erythroid differentiation in K562 cells by indirect ROS-mediated IRP1 activation. *Biochimica et Biophysica Acta (BBA) - Molecular Cell Research*, *1869*(10), 119307. https://doi.org/10.1016/J.BBAMCR.2022.119307

Wang, L. R., Radonjic, A., Dilliott, A. A., McIntyre, A. D., & Hegele, R. A. (2018). A De Novo POLD1 Mutation Associated With Mandibular Hypoplasia, Deafness, Progeroid Features, and Lipodystrophy Syndrome in a Family With Werner Syndrome. *Journal of Investigative Medicine High Impact Case Reports*, *6*, 232470961878677. https://doi.org/10.1177/2324709618786770

Wang, X., Zhang, X., Cao, K., Zeng, M., Fu, X., Zheng, A., et al. (2022). Cardiac disruption of SDHAF4-mediated mitochondrial complex II assembly promotes dilated cardiomyopathy. *Nature Communications*, *13*(1), 3947. https://doi.org/10.1038/s41467-022-31548-1

Wang, Yinu, Situ, X., Cardenas, H., Siu, E., Alhunayan, S. A., Keathley, R., et al. (2024). Preclinical Evaluation of NTX-301, a Novel DNA Hypomethylating Agent in Ovarian Cancer. *Clinical Cancer Research*, *30*(6), 1175–1188. https://doi.org/10.1158/1078-0432.CCR-23-2368

Wang, Yubo, Protchenko, O., Huber, K. D., Shakoury-Elizeh, M., Ghosh, M. C., & Philpott, C. C. (2023). The iron chaperone poly(rC)-binding protein 1 regulates iron efflux through intestinal ferroportin in mice. *Blood*, *142*(19), 1658–1671. https://doi.org/10.1182/BLOOD.2023020504

Wang, Z., Yang, T., & Fu, H. (2021). Prevalence of diabetes and hypertension and their interaction effects on cardio-cerebrovascular diseases: a cross-sectional study. *BMC Public Health*, *21*(1), 1224. https://doi.org/10.1186/s12889-021-11122-y

Watt, N. T., McGrane, A., & Roberts, L. D. (2023). Linking the unfolded protein response to bioactive lipid metabolism and signalling in the cell non-autonomous extracellular communication of ER stress. *BioEssays*, *45*(8), 2300029. https://doi.org/10.1002/bies.202300029

Webert, H., Freibert, S.-A., Gallo, A., Heidenreich, T., Linne, U., Amlacher, S., et al. (2014). Functional reconstitution of mitochondrial Fe/S cluster synthesis on Isu1 reveals the involvement of ferredoxin. *Nature Communications*, *5*(1), 5013. https://doi.org/10.1038/ncomms6013

Wehinger, S., Ortiz, R., Díaz, M. I., Aguirre, A., Valenzuela, M., Llanos, P., et al. (2015). Phosphorylation of caveolin-1 on tyrosine-14 induced by ROS enhances palmitate-induced death of beta-pancreatic cells. *Biochimica et Biophysica Acta (BBA) - Molecular Basis of Disease*, *1852*(5), 693–708. https://doi.org/10.1016/j.bbadis.2014.12.021

Weidemann, B. J., Marcheva, B., Kobayashi, M., Omura, C., Newman, M. V., Kobayashi, Y., et al. (2024). Repression of latent NF-κB enhancers by PDX1 regulates β cell functional heterogeneity. *Cell Metabolism*, *36*(1), 90-102.e7. https://doi.org/10.1016/j.cmet.2023.11.018

Weijiao, Y., Fuchun, L., Mengjie, C., Xiaoqing, Q., Hao, L., Yuan, L., & Desheng, Y. (2021). Immune infiltration and a ferroptosis-associated gene signature for predicting the prognosis of patients with endometrial cancer. *Aging*, *13*(12), 16713–16732. https://doi.org/10.18632/AGING.203190

Wen, Q., Chowdhury, A. I., Aydin, B., Shekha, M., Stenlid, R., Forslund, A., & Bergsten, P. (2023). Metformin restores prohormone processing enzymes and normalizes aberrations in secretion of proinsulin and insulin in palmitate-exposed human islets. *Diabetes, Obesity and Metabolism*, *25*(12), 3757–3765. https://doi.org/10.1111/DOM.15270

Wenz, C., Faust, D., Linz, B., Turmann, C., Nikolova, T., Bertin, J., et al. (2018). t-BuOOH induces ferroptosis in human and murine cell lines. *Archives of Toxicology*, *92*(2), 759–775. https://doi.org/10.1007/s00204-017-2066-y

White, C. L., Weisberg, A. S., & Moss, B. (2000). A glutaredoxin, encoded by the G4L gene of vaccinia virus, is essential for virion morphogenesis. *Journal of Virology*, *74*(19), 9175–9183. https://doi.org/10.1128/JVI.74.19.9175-9183.2000

Witte, S., Villalba, M., Bi, K., Liu, Y., Isakov, N., & Altman, A. (2000). Inhibition of the c-Jun N-terminal kinase/AP-1 and NF-kappaB pathways by PICOT, a novel protein kinase C-interacting protein with a thioredoxin homology domain. *The Journal of Biological Chemistry*, *275*(3), 1902–1909. https://doi.org/10.1074/JBC.275.3.1902

Wu, S., Yin, S., & Zhou, B. (2022). Molecular physiology of iron trafficking in Drosophila melanogaster. *Current Opinion in Insect Science*, *50*, 100888. https://doi.org/10.1016/j.cois.2022.100888

Wu, T., Wan, J., Qu, X., Xia, K., Wang, F., Zhang, Z., et al. (2023). Nodal promotes colorectal cancer survival and metastasis through regulating SCD1-mediated ferroptosis resistance. *Cell Death & Disease*, *14*(3), 229. https://doi.org/10.1038/s41419-023-05756-6

Xia, H., Li, B., Zhang, Z., Wang, Q., Qiao, T., & Li, K. (2015). Human glutaredoxin 3 can bind and effectively transfer [4Fe–4S] cluster to apo-iron regulatory protein 1. *Biochemical and Biophysical Research Communications*, *465*(3), 620–624. https://doi.org/10.1016/j.bbrc.2015.08.073

Xia, Q., Wu, F., Wu, W., Dong, H., Huang, Z., Xu, L., et al. (2022). Berberine reduces hepatic ceramide levels to improve insulin resistance in HFD-fed mice by inhibiting HIF-2α. *Biomedicine & Pharmacotherapy*, *150*, 112955. https://doi.org/10.1016/j.biopha.2022.112955

Xiao, Q., Lan, Z., Zhang, S., Ren, H., Wang, S., Wang, P., et al. (2023). Overexpression of ZNF488 supports pancreatic cancer cell proliferation and tumorigenesis through inhibition of ferroptosis via regulating SCD1-mediated unsaturated fatty acid metabolism. *Biology Direct*, *18*(1), 77. https://doi.org/10.1186/s13062-023-00421-6

Xie, X., Tian, L., Zhao, Y., Liu, F., Dai, S., Gu, X., et al. (2023). BACH1-induced ferroptosis drives lymphatic metastasis by repressing the biosynthesis of monounsaturated fatty acids. *Cell Death & Disease*, *14*(1), 48. https://doi.org/10.1038/s41419-023-05571-z

Xie, Y., Wang, B., Zhao, Y., Tao, Z., Wang, Y., Chen, G., & Hu, X. (2022). Mammary adipocytes protect triple-negative breast cancer cells from ferroptosis. *Journal of Hematology & Oncology*, *15*(1), 72. https://doi.org/10.1186/s13045-022-01297-1

Xing, S., & Zachgo, S. (2008). ROXY1 and ROXY2, two Arabidopsis glutaredoxin genes, are required for anther development. *The Plant Journal*, *53*(5), 790–801. https://doi.org/10.1111/j.1365-313X.2007.03375.x

Xu, J., Tian, H., Ji, Y., Dong, L., Liu, Y., Wang, Y., et al. (2023). Urolithin C reveals anti-NAFLD potential via AMPK-ferroptosis axis and modulating gut microbiota. *Naunyn-Schmiedeberg's Archives of Pharmacology*, *396*(10), 2687–2699. https://doi.org/10.1007/s00210-023-02492-8

Xu, L., Wen, B., Wu, Q., Lu, S., Liao, J., Mo, L., et al. (2024). Long non-coding RNA KB-1460A1.5 promotes ferroptosis by inhibiting mTOR/SREBP-1/SCD1-mediated polyunsaturated fatty acid desaturation in glioma. *Carcinogenesis*, *45*(7), 487–499. https://doi.org/10.1093/carcin/bgae016

Xu, S., Nam, S. M., Kim, J.-H., Das, R., Choi, S.-K., Nguyen, T. T., et al. (2015). Palmitate induces ER calcium depletion and apoptosis in mouse podocytes subsequent to mitochondrial oxidative stress. *Cell Death & Disease*, *6*(11), e1976–e1976. https://doi.org/10.1038/cddis.2015.331

Xu, W., Zhang, D., Ma, Y., Gaspar, R. C., Kahn, M., Nasiri, A., et al. (2024). Ceramide synthesis inhibitors prevent lipid-induced insulin resistance through the DAG-PKCε-insulin receptorT1150 phosphorylation pathway. *Cell Reports*, *43*(10), 114746. https://doi.org/10.1016/j.celrep.2024.114746

Xue, Q., Yan, D., Chen, X., Li, X., Kang, R., Klionsky, D. J., et al. (2023). Copper-dependent autophagic degradation of GPX4 drives ferroptosis. *Autophagy*, *19*(7), 1982–1996. https://doi.org/10.1080/15548627.2023.2165323

Yagoda, N., von Rechenberg, M., Zaganjor, E., Bauer, A. J., Yang, W. S., Fridman, D. J., et al. (2007). RAS–RAF–MEK-dependent oxidative cell death involving voltage-dependent anion channels. *Nature*, *447*(7146), 865–869. https://doi.org/10.1038/nature05859

Yamada, H., Yoshida, M., Ito, K., Dezaki, K., Yada, T., Ishikawa, S., & Kakei, M. (2016). Potentiation of Glucose-stimulated Insulin Secretion by the GPR40–PLC–TRPC Pathway in Pancreatic β-Cells. *Scientific Reports*, *6*(1), 25912. https://doi.org/10.1038/srep25912

Yamada, M., Suzuki, J., Sato, S., Zenimaru, Y., Saito, R., Konoshita, T., et al. (2022). Hormone-sensitive lipase protects adipose triglyceride lipase-deficient mice from lethal lipotoxic cardiomyopathy. *Journal of Lipid Research*, *63*(5), 100194. https://doi.org/10.1016/j.jlr.2022.100194

Yan, H. fa, Tuo, Q. zhang, & Lei, P. (2024). Cell density impacts the susceptibility to ferroptosis by modulating IRP1-mediated iron homeostasis. *Journal of Neurochemistry*, *168*(7), 1359–1373. https://doi.org/10.1111/JNC.16085

Yaney, G. C., & Corkey, B. E. (2003). Fatty acid metabolism and insulin secretion in pancreatic beta cells. *Diabetologia*, *46*(10), 1297–1312. https://doi.org/10.1007/s00125-003-1207-4

Yang, H., Liu, M., Sheng, Y., Zhu, L., Jin, M., Jiang, T., et al. (2022). All-trans retinoic acid impairs glucose-stimulated insulin secretion by activating the RXR/SREBP-1c/UCP2 pathway. *Acta Pharmacologica Sinica*, *43*(6), 1441–1452. https://doi.org/10.1038/s41401-021-00740-2

Yang, Q., Liu, W., Zhang, S., & Liu, S. (2020). The cardinal roles of ferroportin and its partners in controlling cellular iron in and out. *Life Sciences*, *258*, 118135. https://doi.org/10.1016/J.LFS.2020.118135

Yang, W. S., & Stockwell, B. R. (2008). Synthetic Lethal Screening Identifies Compounds Activating Iron-Dependent, Nonapoptotic Cell Death in Oncogenic-RAS-Harboring Cancer Cells. *Chemistry & Biology*, *15*(3), 234–245. https://doi.org/10.1016/j.chembiol.2008.02.010

Yang, W. S., Sriramaratnam, R., Welsch, M. E., Shimada, K., Skouta, R., Viswanathan, V. S., et al. (2014). Regulation of Ferroptotic Cancer Cell Death by GPX4. *Cell*, *156*(0), 317. https://doi.org/10.1016/J.CELL.2013.12.010

Yang, X., Liu, Q., Li, Y., Tang, Q., Wu, T., Chen, L., et al. (2020). The diabetes medication canagliflozin promotes mitochondrial remodelling of adipocyte via the AMPK-Sirt1-Pgc-1α signalling pathway. *Adipocyte*, *9*(1), 484–494. https://doi.org/10.1080/21623945.2020.1807850

Yang, Y., Chen, J., Gao, Q., Shan, X., Wang, J., & Lv, Z. (2020). Study on the attenuated effect of Ginkgolide B on ferroptosis in high fat diet induced nonalcoholic fatty liver disease. *Toxicology*, *445*, 152599. https://doi.org/10.1016/j.tox.2020.152599

Yao, F., Cui, X., Zhang, Y., Bei, Z., Wang, H., Zhao, D., et al. (2021). Iron regulatory protein 1 promotes ferroptosis by sustaining cellular iron homeostasis in melanoma. *Oncology Letters*, *22*(3), 657. https://doi.org/10.3892/ol.2021.12918

Ye, H., Jeong, S. Y., Ghosh, M. C., Kovtunovych, G., Silvestri, L., Ortillo, D., et al. (2010). Glutaredoxin 5 deficiency causes sideroblastic anemia by specifically impairing heme biosynthesis and depleting cytosolic iron in human erythroblasts. *Journal of Clinical Investigation*, *120*(5), 1749–1761. https://doi.org/10.1172/JCI40372

Ye, Z., Chen, H., Ji, S., Hu, Y., Lou, X., Zhang, W., et al. (2022). MEN1 promotes ferroptosis by inhibiting mTOR-SCD1 axis in pancreatic neuroendocrine tumors. *Acta Biochimica et Biophysica Sinica*, *54*(11), 1599–1609. https://doi.org/10.3724/ABBS.2022162

Yook, J.-S., You, M., Kim, J., Toney, A. M., Fan, R., Puniya, B. L., et al. (2021). Essential role of systemic iron mobilization and redistribution for adaptive thermogenesis through HIF2-α/hepcidin axis. *Proceedings of the National Academy of Sciences*, *118*(40). https://doi.org/10.1073/pnas.2109186118

Yoon, H., Shaw, J. L., Haigis, M. C., & Greka, A. (2021). Lipid metabolism in sickness and in health: Emerging regulators of lipotoxicity. *Molecular Cell*, *81*(18), 3708–3730. https://doi.org/10.1016/j.molcel.2021.08.027

Yu, E. A., Hu, P. J., & Mehta, S. (2018). Plasma fatty acids in de novo lipogenesis pathway are associated with diabetogenic indicators among adults: NHANES 2003–2004. *The American Journal of Clinical Nutrition*, *108*(3), 622–632. https://doi.org/10.1093/ajcn/nqy165

Yu, H., Yang, J., Shi, Y., Donelson, J., Thompson, S. M., Sprague, S., et al. (2017). Arabidopsis Glutaredoxin S17 Contributes to Vegetative Growth, Mineral Accumulation, and Redox Balance during Iron Deficiency. *Frontiers in Plant Science*, *8*, 274897. https://doi.org/10.3389/fpls.2017.01045

Yuan, S., & Larsson, S. C. (2020). Association of genetic variants related to plasma fatty acids with type 2 diabetes mellitus and glycaemic traits: a Mendelian randomisation study. *Diabetologia*, *63*(1), 116–123. https://doi.org/10.1007/s00125-019-05019-0

Yusuf, R. Z., Saez, B., Sharda, A., van Gastel, N., Yu, V. W. C., Baryawno, N., et al. (2020). Aldehyde dehydrogenase 3a2 protects AML cells from oxidative death and the synthetic lethality of ferroptosis inducers. *Blood*, *136*(11), 1303–1316. https://doi.org/10.1182/BLOOD.2019001808

Zhai, K., Gu, L., Yang, Z., Mao, Y., Jin, M., Chang, Y., et al. (2016). RNA-binding protein CUGBP1 regulates insulin secretion via activation of phosphodiesterase 3B in mice. *Diabetologia*, *59*(9), 1959–1967. https://doi.org/10.1007/S00125-016-4005-5

Zhang, B., Bandyopadhyay, S., Shakamuri, P., Naik, S. G., Huynh, B. H., Couturier, J., et al. (2013). Monothiol glutaredoxins can bind linear [Fe3S4]+ and [Fe4S4]2+ clusters in addition to [Fe2S2]2+ clusters: spectroscopic characterization and functional implications. *Journal of the American Chemical Society*, *135*(40), 15153–15164. https://doi.org/10.1021/JA407059N

Zhang, D., Dong, Y., Yu, Q., Kai, Z., Zhang, M., Jia, C., et al. (2017). Function of glutaredoxin 3 (Grx3) in oxidative stress response caused by iron homeostasis disorder in Candida albicans. *Future Microbiology*, *12*(15), 1397–1412. https://doi.org/10.2217/FMB-2017-0098

Zhang, G.-F., Jensen, M. V., Gray, S. M., El, K., Wang, Y., Lu, D., et al. (2021). Reductive TCA cycle metabolism fuels glutamine- and glucose-stimulated insulin secretion. *Cell Metabolism*, *33*(4), 804-817.e5. https://doi.org/10.1016/j.cmet.2020.11.020

Zhang, Jie, Cheng, P., Dai, W., Ji, J., Wu, L., Feng, J., et al. (2021). Fenofibrate Ameliorates Hepatic Ischemia/Reperfusion Injury in Mice: Involvements of Apoptosis, Autophagy, and PPAR-α Activation. *PPAR Research*, *2021*(1), 1–16. https://doi.org/10.1155/2021/6658944

Zhang, Jin, Gao, X., Yuan, Y., Sun, C., Zhao, Y., Xiao, L., et al. (2019). Perilipin 5 alleviates HCV NS5A-induced lipotoxic injuries in liver. *Lipids in Health and Disease*, *18*(1), 87. https://doi.org/10.1186/s12944-019-1022-7

Zhang, K., Bao, R., Huang, F., Yang, K., Ding, Y., Lauterboeck, L., et al. (2022). ATP synthase inhibitory factor subunit 1 regulates islet β-cell function via repression of mitochondrial homeostasis. *Laboratory Investigation*, *102*(1), 69–79. https://doi.org/10.1038/s41374-021-00670-x

Zhang, T., Sun, L., Hao, Y., Suo, C., Shen, S., Wei, H., et al. (2022). ENO1 suppresses cancer cell ferroptosis by degrading the mRNA of iron regulatory protein 1. *Nature Cancer*, *3*(1), 75–89. https://doi.org/10.1038/S43018-021-00299-1

Zhang, W., Wang, J., Liu, Z., Zhang, L., Jing, J., Han, L., & Gao, A. (2022). Iron-dependent ferroptosis participated in benzene-induced anemia of inflammation through IRP1-DHODH-ALOX12 axis. *Free Radical Biology and Medicine*, *193*(Pt 1), 122–133. https://doi.org/10.1016/j.freeradbiomed.2022.10.273

Zhang, Yan, Liu, Y., Yong, V. W., & Xue, M. (2023). Omarigliptin inhibits brain cell ferroptosis after intracerebral hemorrhage. *Scientific Reports*, *13*(1), 14339. https://doi.org/10.1038/s41598-023-41635-y

Zhang, Ying, Jia, X.-B., Liu, Y.-C., Yu, W.-Q., Si, Y.-H., & Guo, S.-D. (2022). Fenofibrate enhances lipid deposition via modulating PPARγ, SREBP-1c, and gut microbiota in ob/ob mice fed a high-fat diet. *Frontiers in Nutrition*, *9*, 971581. https://doi.org/10.3389/fnut.2022.971581

Zhang, Yuan, Liu, Y., Liu, X., Yuan, X., Xiang, M., Liu, J., et al. (2022). Exercise and Metformin Intervention Prevents Lipotoxicity-Induced Hepatocyte Apoptosis by Alleviating Oxidative and ER Stress and Activating the AMPK/Nrf2/HO-1 Signaling Pathway in db/db Mice. *Oxidative Medicine and Cellular Longevity*, *2022*(1), 1–13. https://doi.org/10.1155/2022/2297268

Zhao, Y., Wang, L., Qiu, J., Zha, D., Sun, Q., & Chen, C. (2013). Linoleic Acid Stimulates [Ca2+]i Increase in Rat Pancreatic Beta-Cells through Both Membrane Receptor- and Intracellular Metabolite-Mediated Pathways. *PLoS ONE*, *8*(4), e60255. https://doi.org/10.1371/journal.pone.0060255

Zheng, X., Baker, H., Hancock, W. S., Fawaz, F., McCaman, M., & Pungor, E. (2006). Proteomic Analysis for the Assessment of Different Lots of Fetal Bovine Serum as a Raw Material for Cell Culture. Part IV. Application of Proteomics to the Manufacture of Biological Drugs. *Biotechnology Progress*, *22*(5), 1294–1300. https://doi.org/10.1021/BP060121O

Zhou, J., Zhe, R., Guo, X., Chen, Y., Zou, Y., Zhou, L., & Wang, Z. (2020). The Role of PPARδ Agosnist GW501516 in Rats with Gestational Diabetes Mellitus. *Diabetes, Metabolic Syndrome and Obesity: Targets and Therapy*, *13*, 2307–2316. https://doi.org/10.2147/DMSO.S251491

Zhou, L., Lv, Z., Tian, X., Zhang, Y., & Xu, Z. (2022). Eye pain and blurred vision as main complaints in a new case with MDPL syndrome. *European Journal of Ophthalmology*, *32*(5), NP82–NP86. https://doi.org/10.1177/11206721211009179

Zhou, S., Wang, Z., Wang, T., Peng, C., Zhang, J., Liu, C., et al. (2024). Salvia miltiorrhiza Bge. processed with porcine cardiac blood inhibited GLRX5-mediated ferroptosis alleviating cerebral ischemia-reperfusion injury. *Phytomedicine*, *129*, 155622. https://doi.org/10.1016/j.phymed.2024.155622

Zhou, X., Zhang, J., Sun, Y., Shen, J., Sun, B., & Ma, Q. (2023). Glutamine Ameliorates Liver Steatosis via Regulation of Glycolipid Metabolism and Gut Microbiota in High-Fat Diet-Induced Obese Mice. *Journal of Agricultural and Food Chemistry*, *71*(42), 15656–15667. https://doi.org/10.1021/acs.jafc.3c05566

Zhou, Z. D., & Tan, E.-K. (2017). Iron regulatory protein (IRP)-iron responsive element (IRE) signaling pathway in human neurodegenerative diseases. *Molecular Neurodegeneration*, *12*(1), 75. https://doi.org/10.1186/s13024-017-0218-4

Zhu, J., Zhang, Y., Ren, R., Sanford, L. D., & Tang, X. (2022). Blood transcriptome analysis: Ferroptosis and potential inflammatory pathways in post-traumatic stress disorder. *Frontiers in Psychiatry*, *13*. https://doi.org/10.3389/fpsyt.2022.841999

Zhu, M., Peng, L., Huo, S., Peng, D., Gou, J., Shi, W., et al. (2023). STAT3 signaling promotes cardiac injury by upregulating NCOA4-mediated ferritinophagy and ferroptosis in high-fat-diet fed mice. *Free Radical Biology and Medicine*, *201*, 111–125. https://doi.org/10.1016/j.freeradbiomed.2023.03.003

Supplementary material

Supplement 1: Sequence of Sport6-Glrx5 plasmid

GACGCGCCCTGTAGCGGCGCATTAAGCGCGGCGGGTGTGGTGGTTACGCGC
AGCGTGACCGCTACACTTGCCAGCGCCCTAGCGCCCGCTCCTTTCGCTTTCT
TCCCTTCCTTTCTCGCCACGTTCGCCGGCTTTCCCCGTCAAGCTCTAAATCGG
GGGCTCCCTTTAGGGTTCCGATTTAGTGCTTTACGGCACCTCGACCCCAAAA
AACTTGATTAGGGTGATGGTTCACGTAGTGGGCCATCGCCCTGATAGACGG
TTTTTCGCCCTTTGACGTTGGAGTCCACGTTCTTTAATAGTGGACTCTTGTTC
CAAACTGGAACAACACTCAACCCTATCTCGGTCTATTCTTTTGATTTATAAG
GGATTTTGCCGATTTCGGCCTATTGGTTAAAAAATGAGCTGATTTAACAAAA
ATTTAACGCGAATTTTAACAAAATATTAACGTTTACAATTTCAGGTGGCACT
TTTCGGGGAAATGTGCGCGGAACCCCTATTTGTTTATTTTTCTAAATACATTC
AAATATGTATCCGCTCATGCCAGGTCTTGGACTGGTGAGAACGGCTTGCTCG
GCAGCTTCGATGTGTGCTGGAGGGAGAATAAAGGTCTAAGATGTGCGATAG
AGGGAAGTCGCATTGAATTATGTGCTGTGTAGGGATCGCTGGTATCAAATA
TGTGTGCCCACCCCTGGCATGAGACAATAACCCTGATAAATGCTTCAATAAT
ATTGAAAAAGGAAGAGTATGAGTATTCAACATTTCCGTGTCGCCCTTATTCC
CTTTTTTGCGGCATTTTGCCTTCCTGTTTTTGCTCACCCAGAAACGCTGGTGA
AAGTAAAAGATGCTGAAGATCAGTTGGGTGCACGAGTGGGTTACATCGAAC
TGGATCTCAACAGCGGTAAGATCCTTGAGAGTTTTCGCCCCGAAGAACGTTT
TCCAATGATGAGCACTTTTAAAGTTCTGCTATGTGGCGCGGTATTATCCCGT
ATTGACGCCGGGCAAGAGCAACTCGGTCGCCGCATACACTATTCTCAGAAT
GACTTGGTTGAGTACTCACCAGTCACAGAAAAGCATCTTACGGATGGCATG
ACAGTAAGAGAATTATGCAGTGCTGCCATAACCATGAGTGATAACACTGCG
GCCAACTTACTTCTGACAACGATCGGAGGACCGAAGGAGCTAACCGCTTTT
TTGCACAACATGGGGGATCATGTAACTCGCCTTGATCGTTGGGAACCGGAG
CTGAATGAAGCCATACCAAACGACGAGCGTGACACCACGATGCCTGTAGCA
ATGGCAACAACGTTGCGCAAACTATTAACTGGCGAACTACTTACTCTAGCTT
CCCGGCAACAATTAATAGACTGGATGGAGGCGGATAAAGTTGCAGGACCAC
TTCTGCGCTCGGCCCTTCCGGCTGGCTGGTTTATTGCTGATAAATCTGGAGC
CGGTGAGCGTGGGTCTCGCGGTATCATTGCAGCACTGGGGCCAGATGGTAA
GCCCTCCCGTATCGTAGTTATCTACACGACGGGGAGTCAGGCAACTATGGA
TGAACGAAATAGACAGATCGCTGAGATAGGTGCCTCACTGATTAAGCATTG

GTAACTGTCAGACCAAGTTTACTCATATATACTTTAGATTGATTTAAAACTT
CATTTTTAATTTAAAAGGATCTAGGTGAAGATCCTTTTTGATAATCTCATGC
CATAACTTCGTATAATGTATGCTATACGAAGTTATGGCATGACCAAAATCCC
TTAACGTGAGTTTTCGTTCCACTGAGCGTCAGACCCCGTAGAAAAGATCAA
AGGATCTTCTTGAGATCCTTTTTTTCTGCGCGTAATCTGCTGCTTGCAAACAA
AAAAACCACCGCTACCAGCGGTGGTTTGTTTGCCGGATCAAGAGCTACCAA
CTCTTTTTCCGAAGGTAACTGGCTTCAGCAGAGCGCAGATACCAAATACTGT
CCTTCTAGTGTAGCCGTAGTTAGGCCACCACTTCAAGAACTCTGTAGCACCG
CCTACATACCTCGCTCTGCTAATCCTGTTACCAGTGGCTGCTGCCAGTGGCG
ATAAGTCGTGTCTTACCGGGTTGGACTCAAGACGATAGTTACCGGATAAGG
CGCAGCGGTCGGGCTGAACGGGGGGTTCGTGCACACAGCCCAGCTTGGAGC
GAACGACCTACACCGAACTGAGATACCTACAGCGTGAGCATTGAGAAAGCG
CCACGCTTCCCGAAGGGAGAAAGGCGGACAGGTATCCGGTAAGCGGCAGG
GTCGGAACAGGAGAGCGCACGAGGGAGCTTCCAGGGGGAAACGCCTGGTA
TCTTTATAGTCCTGTCGGGTTTCGCCACCTCTGACTTGAGCGTCGATTTTTGT
GATGCTCGTCAGGGGGGCGGAGCCTATGGAAAAACGCCAGCAACGCGGCCT
TTTTACGGTTCCTGGCCTTTTGCTGGCCTTTTGCTCACATGTTCTTTCCTGCGT
TATCCCCTGATTCTGTGGATAACCGTATTACCGCCTTTGAGTGAGCTGATAC
CGCTCGCCGCAGCCGAACGACCGAGCGCAGCGAGTCAGTGAGCGAGGAAG
CGGAAGAGCGCCCAATACGCAAACCGCCTCTCCCCGCGCGTTGGCCGATTC
ATTAATGCAGAGCTTGCAATTCGCGCGTTTTTCAATATTATTGAAGCATTTA
TCAGGGTTATTGTCTCATGAGCGGATACATATTTGAATGTATTTAGAAAAAT
AAACAAATAGGGGTTCCGCGCACATTTCCCCGAAAAGTGCCACCTGACGTC
TAAGAAACCATTATTATCATGACATTAACCTATAAAAATAGGCGTAGTACG
AGGCCCTTTCACTCATTAGATGCATGTCGTTACATAACTTACGGTAAATGGC
CCGCCTGGCTGACCGCCCAACGACCCCCGCCCATTGACGTCAATAATGACG
TATGTTCCCATAGTAACGCCAATAGGGACTTTCCATTGACGTCAATGGGTGG
AGTATTTACGGTAAACTGCCCACTTGGCAGTACATCAAGTGTATCATATGCC
AAGTACGCCCCCTATTGACGTCAATGACGGTAAATGGCCCGCCTGGCATTAT
GCCCAGTACATGACCTTATGGGACTTTCCTACTTGGCAGTACATCTACGTAT
TAGTCATCGCTATTACCATGGTGATGCGGTTTTGGCAGTACATCAATGGGCG
TGGATAGCGGTTTGACTCACGGGGATTTCCAAGTCTCCACCCCATTGACGTC
AATGGGAGTTTGTTTTGGCACCAAAATCAACGGGACTTTCCAAAATGTCGTA
ACAACTCCGCCCCATTGACGCAAATGGGCGGTAGGCGTGTACGGTGGGAGG

TCTATATAAGCAGAGCTCGTTTAGTGAACCGTCAGATCGCCTGGAGACGCC
ATCCACGCTGTTTTGACCTCCATAGAAGACACCGGGACCGATCCAGCCTCCG
GACTCTAGCCTAGGCCGCGGAGCGGATAACAATTTCACACAGGAAACAGCT
ATGACCATTAGGCCTATTTAGGTGACACTATAGAACAAGTTTGTACAAAAA
AGCAGGCTGGTACCGGTCCGGAATTCCCGGGATATCGTCGACCCACGCGTC
CGGTGGCCCGCTGTGGGCCCGGGCCGTCGTGGGCTCCGGCTTGCGTGCGGA
G(*start codon Glrx5*)ATGAGCGGGTCCCTCGGCCGAGCTGCGGCGGCTCTGCTC
CGCTGGGGGCGCGGCGCGGGCGGCGGTGGCCTTTGGGGTCCGGGCGTGCGG
GCGGCGGGCTCGGGCGCGGGCGGCGGCGGCTCGGCGGAGCAGTTGGACGC
GCTGGTGAAGAAGGACAAGGTGGTGGTCTTCCTCAAGGGGACGCCGGAGCA
GCCCCAGTGCGGCTTCAGCAACGCCGTGGTGCAGATCCTGCGGCTGCACGG
CGTCCGCGATTACGCGGCCTACAACGTGCTGGACGACCCGGAGCTCCGACA
AGGCATTAAAGACTATTCCAACTGGCCCACCATCCCGCAAGTGTACCTCAAT
GGCGAGTTTGTAGGGGGCTGTGACATTCTTCTGCAGATGCACCAGAATGGG
GACTTGGTGGAAGAACTGAAAAAGCTGGGGATCCACTCCGCCCTTTTAGAT
GAAAAGAAAGACCAAGACTCCAAGTGA(*stop codon Glrx5*)GGGCGGCCAAGT
CCTCGCTGAGCAGAGAGGGAGCCGTTCATGTCAGAGACTCACTGCCAGAAA
AGCCTTACCCATTTTGGTTTTCACTATTGAGACCGCAACTGCTTGCACTGAT
CATTTTGGTTCGTGAGCAGTTGGTGATTTTAGTTGGTCTGGTGTTCGGGCTA
AGAATATTTTATTGTGGACTTAATTACAACCACTGCACTGTAATGATTCAAT
GCTGTATTATGATATTGCTGTAAACAAAATTCATTCTTATATTGTCACTTATT
CTTTGCCTGATTCAGAAGTTAAATAGGAGCTTTGGAATCATTATTCATGACC
CCTCTGCAAATGTGTCAGTCTCCAAAGAGAGTATCTCCCCCCAAATTTTGTG
TAGCTTCTTTTGTTATGGAAAATGGTGGACAAAAAAAGAAACTGTGATAAC
TGGGGGCGTTGTTTTTTAAAATAAACTCCAGCACAGGGATGCTGTGCATGCC
TGAAAAAAAAAAAAAAAAAGGGCGGCCGCTCTAGAGTATCCCTCGAGGGG
CCCAAGCTTACGCGTACCCAGCTTTCTTGTACAAAGTGGTCCCTATAGTGAG
TCGTATTATAAGCTAGGCACTGGCCGTCGTTTTACAACGTCGTGACTGGGAA
AACTGCTAGCTTGGGATCTTTGTGAAGGAACCTTACTTCTGTGGTGTGACAT
AATTGGACAAACTACCTACAGAGATTTAAAGCTCTAAGGTAAATATAAAAT
TTTTAAGTGTATAATGTGTTAAACTAGCTGCATATGCTTGCTGCTTGAGAGT
TTTGCTTACTGAGTATGATTTATGAAAATATTATACACAGGAGCTAGTGATT
CTAATTGTTTGTGTATTTTAGATTCACAGTCCCAAGGCTCATTTCAGGCCCCT
CAGTCCTCACAGTCTGTTCATGATCATAATCAGCCATACCACATTTGTAGAG

GTTTTACTTGCTTTAAAAAACCTCCCACACCTCCCCCTGAACCTGAAACATA
AAATGAATGCAATTGTTGTTGTTAACTTGTTTATTGCAGCTTATAATGGTTA
CAAATAAAGCAATAGCATCACAAATTTCACAAATAAAGCATTTTTTTCACTG
CATTCTAGTTGTGGTTTGTCCAAACTCATCAATGTATCTTATCATGTCTGGAT
CGATCCTGCATTAATGAATCGGCCAACGCGCGGGGAGAGGCGGTTTGCGTA
TTGGCTGGCGTAATAGCGAAGAGGCCCGCACCGATCGCCCTTCCCAACAGT
TGCGCAGCCTGAATGGCGAATGG

Supplement 2: MIN6 generation time

During the cultivation of MIN6 cells in standard DMEM within T75 or T175 flasks, the generation time was calculated during passaging. This was determined based on the number of cells seeded and harvested after trypsinization, relative to duration of cultivation (Supplement Figure 1). The generation time was 3.943 ± 0.747 d.

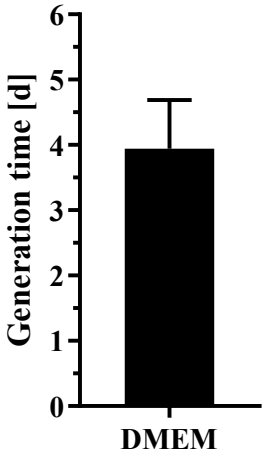

Supplement Figure 1: Generation time of MIN6 cells during regular cell culture (n = 14).

Supplement 3: DMSO and ethanol in the MTT assay

The impact of fatty acid solvents DMSO and ethanol were evaluated using the MTT assay after 24 h treatment of MIN6 cells. Highest DMSO concentration decreased MTT assay readout, whereas lower concentrations had no significant effect. The effect of ethanol was more pronounced, with a decrease in MTT readouts observed at lower concentrations compared to DMSO (0.2350 ± 0.03645, with DMEM; 0.2600 ± 0.01952, at 0.5 % DMSO; 0.2618 ± 0.02094, at 1 % DMSO; 0.2644 ± 0.01860, at 2 % DMSO; 0.2403 ± 0.01987, at 3 % DMSO; 0.1636 ± 0.01765, **** $p < 0.0001$, at 4 % DMSO; 0.2274 ± 0.01737,

at 0.5 % EtOH; 0.1952 ± 0.01526, at 1 % EtOH; 0.1611 ± 0.01255, **** p < 0.0001, at 2 % EtOH; 0.09123 ± 0.02001, **** p < 0.0001, at 3 % EtOH; 0.05780 ± 0.01938, **** p < 0.0001, at 4 % EtOH, Supplement Figure 2, significance determined by one-way ANOVA compared to DMEM). The ethanol concentration in the fatty acid protocol ranged from 0.23 % to 0.31 %, which appeared to have no significant adverse effect on the cells. Despite ethanol's relatively stronger impact on MTT readouts compared to DMSO, ethanol was selected as the solvent for fatty acid preparation. This decision was based on descriptions pointing to a limited solubility of palmitic acid in DMSO.

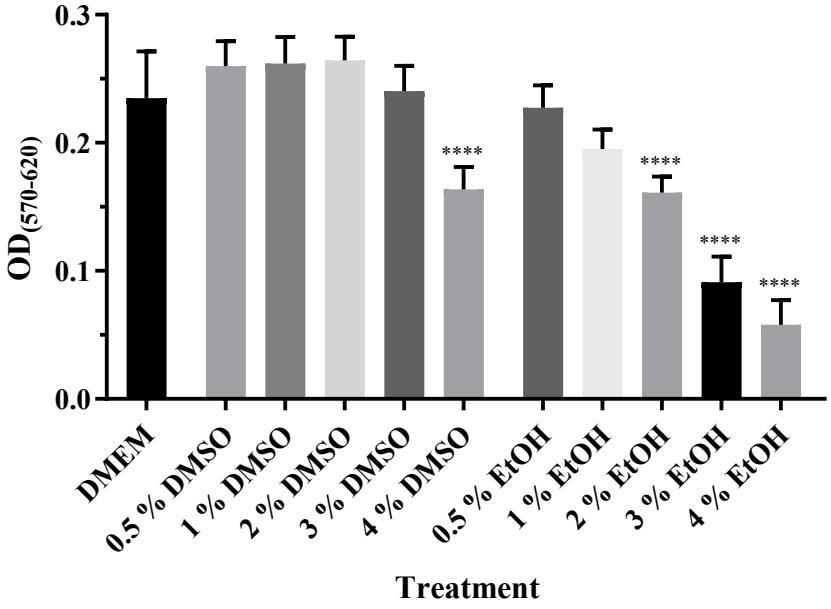

Supplement Figure 2: MTT assay readouts of MIN6 cells treated for 24 h with DMSO or ethanol (n = 5). **** p < 0.0001, significances by one-way ANOVA compared to DMEM.

Supplement 4: BSA in MTT assay

MIN6 cells were treated with albumin, which increased MTT assay readouts after 24 h, reaching a peak at a concentration of 6 %. The treatment group with 5 % ethanol was included as a control to induce a reliable cytotoxic effect (0.08828 ± 0.004427, at 0 % BSA; 0.1033 ± 0.01786, at 0.5 % BSA; 0.1232 ± 0.01544, at 1 % BSA; 0.1312 ± 0.01598, * p < 0.05, at 2 % BSA; 0.1398 ± 0.01913, ** p < 0.01, at 4 % BSA; 0.1555 ± 0.01714, *** p < 0.001, at 6 % BSA; 0.1250 ± 0.02186, at 12.5 % BSA; 0.03911 ± 0.01089, ** p < 0.01, at 5 % EtOH, Supplement Figure 3A, significance determined by one-way

ANOVA compared to 0 % BSA). Prolonged BSA treatment over 5 d did not show a remarkable increase in MTT readouts at concentrations below 6 % but resulted in a marked decrease at concentrations exceeding 6 % (1.493 ± 0.07211, at 0 % BSA; 0.1033 ± 0.01786, at 0.5 % BSA; 1.593 ± 0.1001, at 1 % BSA; 1.575 ± 0.06873, at 3 % BSA; 1.098 ± 0.05124, ** $p < 0.01$, at 6 % BSA; 0.8856 ± 0.09947, **** $p < 0.0001$, at 8 % BSA; 0.7715 ± 0.1086, **** $p < 0.0001$, at 10 % BSA, Supplement Figure 3B, significance determined by one-way ANOVA compared to 0 % BSA).

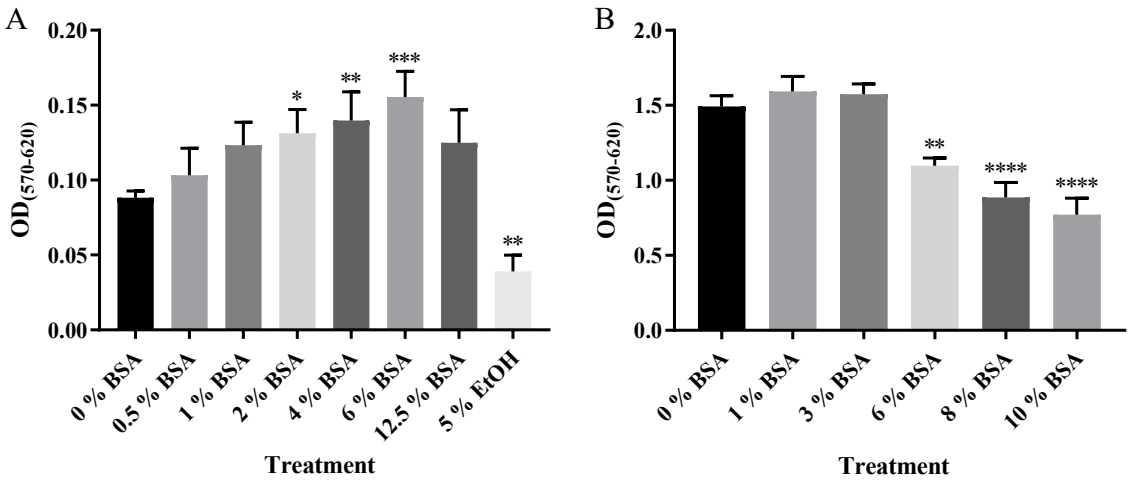

Supplement Figure 3: MIN6 cells treated with albumin or ethanol for (A) 24 h (n = 4) and (B) 5 d (n = 3). * $p < 0.05$, ** $p < 0.01$, *** $p < 0.001$, **** $p < 0.0001$, significances by one-way ANOVA compared to 0 % BSA.

To assess BSA's effect independent of cellular activity, MTT assays were conducted without cells. BSA increased OD in a concentration-dependent manner up to 10 % BSA, indicating a non-cellular effect (0.007278 ± 0.001523, at 1 % BSA; 0.006919 ± 0.007093, at 2 % BSA; 0.009667 ± 0.005905, at 4 % BSA; 0.01572 ± 0.005114, at 8 % BSA; 0.03136 ± 0.01590, * $p < 0.05$, at 10 % BSA, Supplement Figure 4, significance determined by one-way ANOVA compared to 1 % BSA). The absolute OD values remained substantially lower than those obtained in cell-containing analysis. These results highlighted the importance of including appropriate control groups in assays where albumin may interact with assay components, such as the MTT reagent.

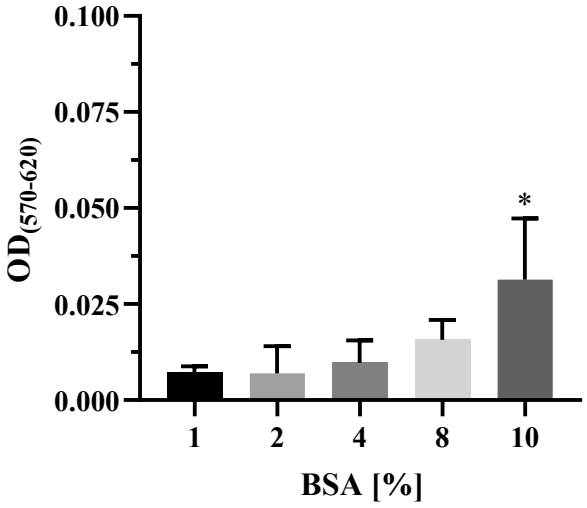

Supplement Figure 4: Applied albumin in a 96 well plate without MIN6 cells to assess cell independent effects via the MTT assay (n = 3). * $p < 0.05$, significance by one-way ANOVA compared to 1 % BSA.

Supplement 5: Analysis of GFP transfection by FACS

MIN6 cells were transfected with increasing amounts of GFP plasmid, as described in chapter 2.1.3. Living cells were identified using propidium iodide, and GFP fluorescence was analyzed via FACS. The percentage of transfected cells and GFP fluorescence intensity increased with plasmid amounts up to 1.33 µg. However, further increasing the plasmid amount to 1.77 µg or 2.22 µg decreased transfection efficiency, likely due to higher volume of JetPRIME transfection reagent exerting negative effects to the cells. The highest percentage of transfected cells was observed with 1.33 µg plasmid, which was subsequently used in the experiments (Supplement Table 1). FACS analysis of cells transfected with 1.33 µg plasmid identified GFP positive cells as population P5. The analysis was based on 10,000 counted cells (Supplement Figure 5).

Supplement Table 1: FACS analysis of transfected MIN6 cells. Amount of used GFP plasmid, percentage of transfected cells and mean intensity of GFP fluorescence by JetPRIME transfection.

Plasmid [µg]	**GFP transfected cells [%]**	**Mean FITC-A intensity of transfected MIN6 cells**
0	0.2	183
0.44	2.8	7,103
0.88	10.7	8,662
1.33	24.1	7,871
1.77	23.1	7,790
2.22	21.9	6,725

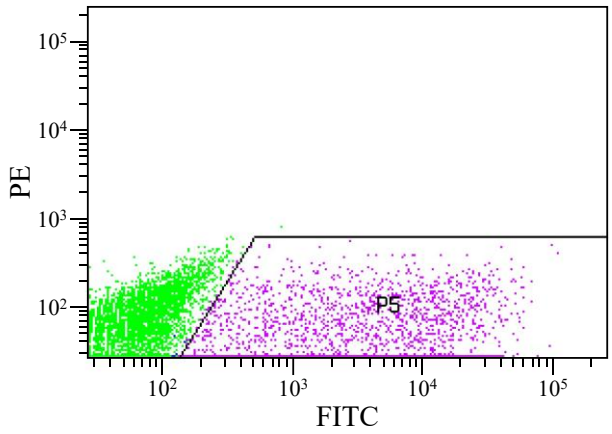

Supplement Figure 5: FACS analysis of GFP transfected MIN6 cells with 1.33 µg plasmid marked as population P5.

Supplement 6: *Glrx5* qPCR of transfected MIN6 cells

The *Glrx5* gene expression in transfected MIN6 cells was analyzed via qPCR using *Rpl32* as the reference gene. Transfection with the Glrx5 plasmid induced a 15-fold increase in *Glrx5* gene expression compared to cells transfected with the GFP plasmid (1.0 ± 0.1433, for GFP+; 14.59 ± 6.781, * $p < 0.05$, for Glrx5+, Supplement Figure 6, significance determined by t-test).

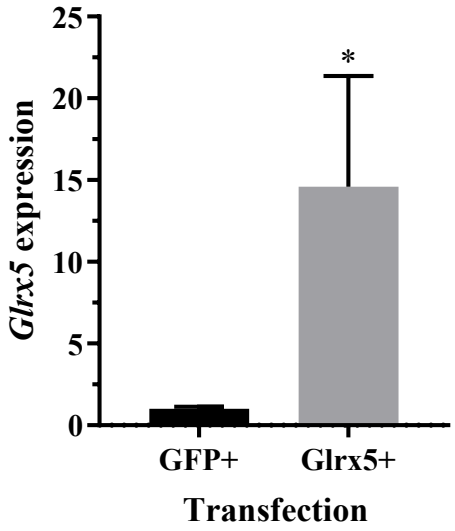

Supplement Figure 6: qPCR analysis of *Glrx5* gene expression of transfected MIN6 cells with reference gene *Rpl32* (n = 3). * $p < 0.05$, significance by t-test.

Supplement 7: Immunoblotting of Glrx5 with different antibodies

To identify suitable antibodies for Glrx5 detection, immunoblotting was performed using various samples. The gels were loaded (from left to right) with 15 µg of Glrx5+ transfected MIN6 cells, 75 ng of a recombinant human Glrx5 protein expressed in *Escherichia coli*, 50 µg of wild type MIN6 cells, and 60 µg wild type MIN6 cells.

Based on sequence information, the recombinant Glrx5 protein consisted of 157 amino acids with an additional 20 amino acid His-Tag at the N-terminus, resulting in a molecular weight of 18.8 kDa. As described in the introduction, the mature Glrx5 protein in MIN6 cells has a calculated weight of 13-14 kDa. Detection with antibodies from Novus Biologicals (Cat-No: Nbp1-89897) and Abcepta (Cat-No: AW5463) yielded strong signals for Glrx5+ cells and the recombinant protein, whereas signals for wild type MIN6 cells were weaker, but corresponded to the signal of Glrx5+ cells, appearing below 15 kDa (Supplement Figure 7A and 7B). In contrast, detection using the Glrx5 antibody from Bioss (Cat-No: bs-13395R) produced no signal for the recombinant protein (Supplement Figure 7C). Furthermore, this antibody did not yield a clear signal for Glrx5+ MIN6 cells that could be distinguished from cross-reactive bands above 15 kDa. Particularly in wild type samples with increased protein loading, strong cross-reactive bands above 15 kDa were observed, with no specific signals below 15 kDa corresponding

to the transfected cell signals detected using the Novus Biologicals or Abcepta antibodies. Tubulin served as reference protein. Based on these results, the antibody from Novus Biologicals was selected for further experiments. The antibody from Abcepta also demonstrated sufficient specificity and could potentially be used in future studies.

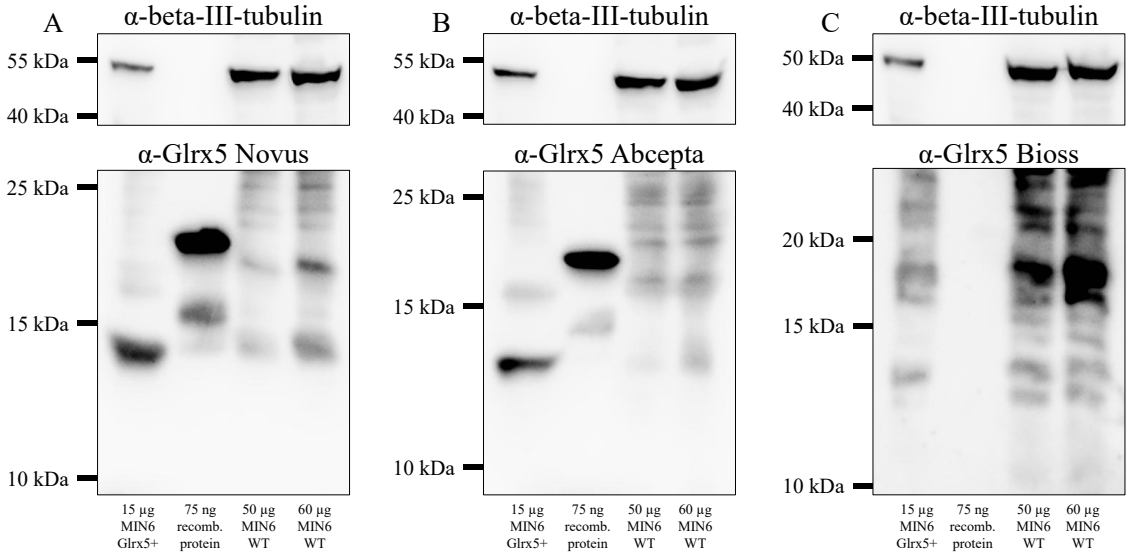

Supplement Figure 7: Detection of Glrx5+ transfected MIN6 cells, recombinant protein, and wild type MIN6 cells via immunoblotting using Glrx5 antibodies of (A) Novus Biologicals, (B) Abcepta, and (C) Bioss. Tubulin was the loading control.

Supplement 8: Immunoblotting of ACO1 with different antibodies

Various antibodies were tested for the detection of ACO1 in fractions of transfected MIN6 cells by immunoblotting. Fractions were prepared as described in chapters 2.4.3.1 and 2.4.4.2. The molecular weight of ACO1 was 98 kDa. Detection using the antibody from Biorbyt Ltd (Cat-No: orb318924) revealed no signal in the cytosolic fraction but showed a strong signal in the organelles containing fraction, below 130 kDa (Supplement Figure 8). In contrast, detection with the antibody from Proteintech Group (Cat-No: 12406-1-AP) produced a signal in the cytosolic fraction at approximately 95 kDa. The signal appeared as a double band, where the lower band likely represented ACO1. The upper band may resulted from cross-reactivity with IRP2, a homolog of ACO1/IRP1. However, definitive identification of the upper band as IRP2, with a molecular weight of 105 kDa, requires further validation. Tubulin was used as control protein.

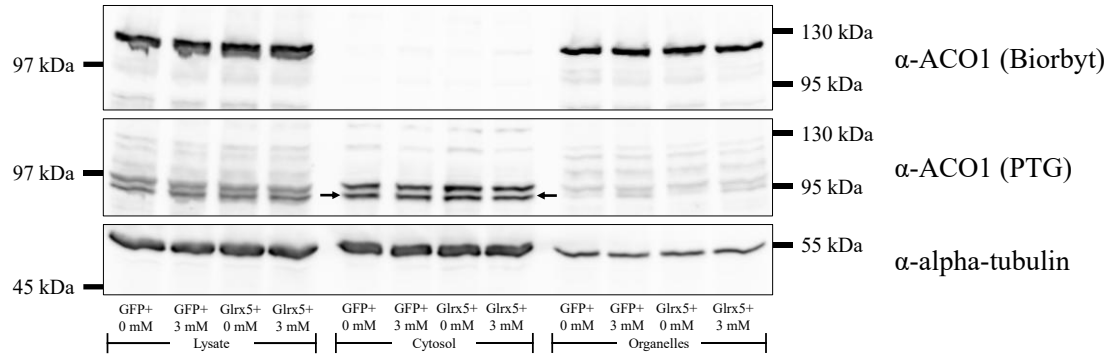

Supplement Figure 8: Detection of transfected MIN6 cell fractions via immunoblotting using different ACO1 antibodies. Tubulin was the loading control.

The detection of proteins with a varying specificity between single antibodies should raise awareness of carefully selecting antibodies for research applications. Validation using recombinant proteins or subcellular fractions can provide valuable insights into antibody reactivity and specificity.

Supplement 9: Linear correlation of chemiluminescence signals in immunoblotting

Quantitative analysis of immunoblotting signals requires a linear correlation between the amount of loaded protein and the chemiluminescence signal. In this experiment, signals for total ERK1/2 and tubulin were analyzed in two independent samples of MIN6 cells across a protein load range of 5-70 µg, using linear regression. The results demonstrated a correlation between signal intensity and protein amount with a slope significantly deviating from zero for both ERK1/2 ($y = 14631*x + 264245$, **** $p < 0.0001$, R^2 0.9841, Supplement Figure 9A) and tubulin ($y = 5292*x + 159990$, **** $p < 0.0001$, R^2 0.9335, Supplement Figure 9B).

When ERK1/2 signals were normalized to the control protein tubulin, the resulting correlation yielded a slope that was not significantly different from zero ($y = 0.01150*x + 1.787$, $p = 0.0657$, R^2 0.4041, Supplement Figure 9C). This analysis highlighted the importance of ensuring that signals remain within a linear detection range, as demonstrated by the significant correlation between signal intensity and protein amount. Notably, this significance was no longer observed when the ratio of the protein of interest to the control protein was calculated. Had this not been considered, statistical

analysis could have resulted in misleading interpretations due to the inadequacy of the measurement scale.

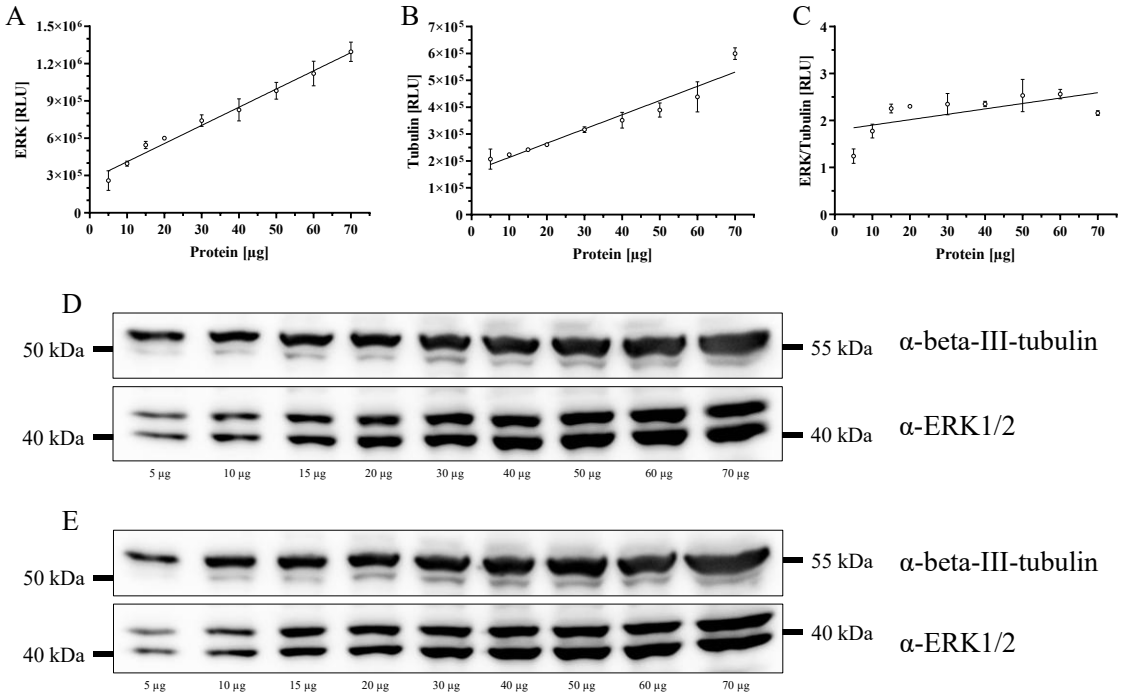

Supplement Figure 9: Intensity of MIN6 chemiluminescence signals via immunoblotting in dependence with protein amount for (A) ERK1/2, (B) tubulin, and (C) the ratio of ERK1/2 and tubulin (n = 2). (D, E) Blot images of both samples are shown.

Supplement 10: Ferritin protein expression by ethanol treatment

In several immunoblot analyses of FTL, control treatments induced a substantial increase in FTL levels compared to DMEM. Ethanol concentrations were evaluated as a possible factor contributing to the control group effect. An increase in FTL expression was observed at ethanol concentrations up to 0.3 % and 0.6 %, with no further increase at 0.9 % (0.1411 ± 0.08503, at 0 %; 0.1806 ± 0.08433, at 0.2 %; 0.2179 ± 0.1384, at 0.3 %; 0.2403 ± 0.03332, at 0.6 %; 0.1816 ± 0.0681, at 0.9 %, Supplement Figure 10A). Overall, the control group effect observed in fatty acid experiments was stronger and could not be fully explained by ethanol alone. The final ethanol concentration in the fatty acid control group ranged from 0.23 % to 0.31 %. Potential interactions between ethanol and albumin might contributed to these effects, although the literature did not describe a direct influence of albumin on FTL or synergistic effects between ethanol and albumin.

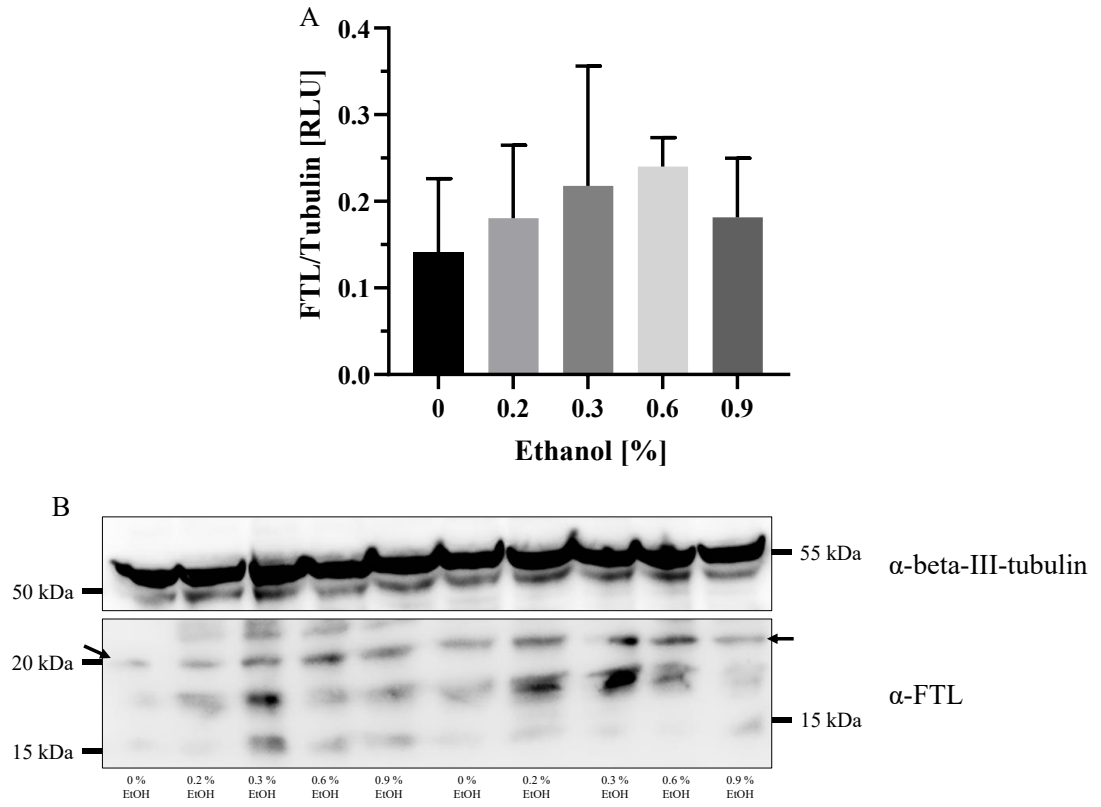

Supplement Figure 10: Ethanol effect on FTL expression via (A) quantification of protein expression (n = 4). (B) Representative image of two independent experiments with 40 µg against tubulin and FTL are shown. No significance by one-way ANOVA.

Supplement 11: Analysis of Glrx5+ mice by immunoblotting

Organs and isolated islets from Glrx5 transgenic mice were analyzed by immunoblotting, with additional samples from MIN6 cells serving as controls. GAPDH detection confirmed equal loading across organ samples, although GAPDH levels were higher in intestines than in pancreata. Despite weak GAPDH signals in islet samples, successful blotting was evident. No PDX1 signal corresponding to the 40 kDa signal in MIN6 cells was detected. Detection of beta-III-tubulin presented significant challenges, as no signal was observed in organ samples (Supplement Figure 11). Reanalysis with a different tubulin antibody yielded detectable but unevenly distributed signals, further highlighting difficulties in tubulin detection despite consistent GAPDH levels. Additionally, Glrx5 signals were absent in organ samples at the expected molecular weight matching the signal of Glrx5+ MIN6 cells below 15 kDa. The transfection of the mice would thereby need further clarification (Supplement Figure 12).

In summary, GAPDH detection confirmed successful organ preparation for immunoblotting, while PDX1, tubulin, and Glrx5 posed challenges. Although islet blotting was rarely reported in the literature, this method appeared promising, given its comparable preparation to MIN6 cells. However, extensive analyses would necessitate pooling samples from multiple mice, which is a limiting factor.

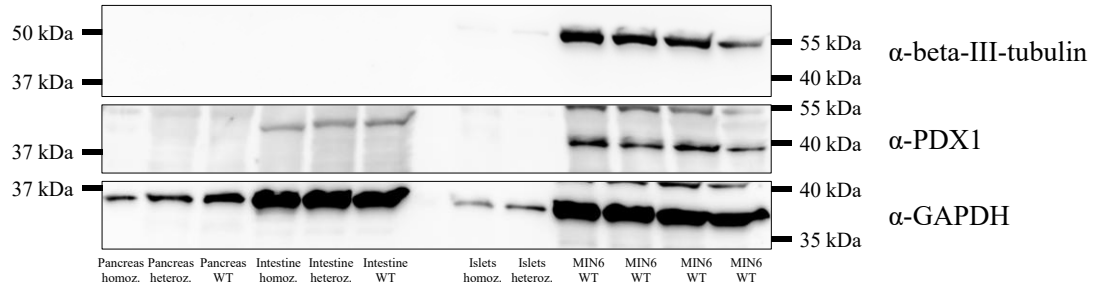

Supplement Figure 11: Immunoblotting of pancreata and intestines of heterozygous and homozygous Glrx5 transfected mice and wild type mice, isolated islets of heterozygous and homozygous Glrx5 transfected mice and MIN6 cells.

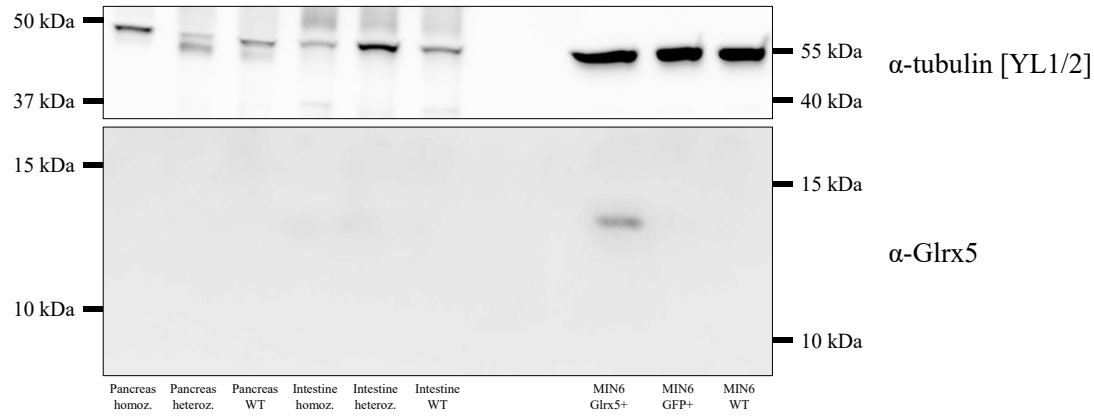

Supplement Figure 12: Immunoblotting of pancreata and intestines of heterozygous and homozygous Glrx5 transfected mice and wild type mice, and Glrx5 transfected, GFP transfected, and wild type MIN6 cells against Glrx5.

Publikationsverzeichnis

Zhou, Hanschmann, Römer, Linn & Petry (2024). The significance of glutaredoxins for diabetes mellitus and its complications. *Redox Biology*, 71, 103043. doi.org/10.1016/j.redox.2024.103043

Petry*, Römer*, Rawat, Brunner, Lerch, Zhou, Grewal, Sharifpanah, Sauer, Eckert & Linn (2022). Loss and Recovery of Glutaredoxin 5 Is Inducible by Diet in a Murine Model of Diabesity and Mediated by Free Fatty Acids In Vitro. *Antioxidants (Basel, Switzerland)*, 11, 788, doi.org/10.3390/antiox11040788
*geteilte Erstautorenschaft

Römer, Rawat, Linn & Petry (2022). Preparation of fatty acid solutions exerts significant impact on experimental outcomes in cell culture models of lipotoxicity. *Biology Methods and Protocols*, 7(1). doi.org/10.1093/biomethods/bpab023

Römer, Linn & Petry (2021). Lipotoxic Impairment of Mitochondrial Function in β-Cells: A Review. *Antioxidants (Basel, Switzerland)*, 10(2), 293. doi.org/10.3390/antiox10020293

Kongressbeitrag, Poster

Römer, Petry, Stehling, Eckert & Linn (16.-18. März 2022). Impact of lipotoxicity on mitochondrial function of the β-cell by the example of Glutaredoxin 5. 59. Wissenschaftlicher Kongress der Deutschen Gesellschaft für Ernährung e.V.

Ehrenwörtliche Erklärung

„Hiermit erkläre ich, dass ich die vorliegende Arbeit selbständig und ohne unzulässige Hilfe oder Benutzung anderer als der angegebenen Hilfsmittel angefertigt habe. Alle Textstellen, die wörtlich oder sinngemäß aus veröffentlichten oder nichtveröffentlichten Schriften entnommen sind, und alle Angaben, die auf mündlichen Auskünften beruhen, sind als solche kenntlich gemacht. Bei den von mir durchgeführten und in der Dissertation erwähnten Untersuchungen habe ich die Grundsätze guter wissenschaftlicher Praxis, wie sie in der „Satzung der Justus-Liebig-Universität Gießen zur Sicherung guter wissenschaftlicher Praxis“ niedergelegt sind, eingehalten sowie ethische, datenschutzrechtliche und tierschutzrechtliche Grundsätze befolgt. Ich versichere, dass Dritte von mir weder unmittelbar noch mittelbar geldwerte Leistungen für Arbeiten erhalten haben, die im Zusammenhang mit dem Inhalt der vorgelegten Dissertation stehen, und dass die vorgelegte Arbeit weder im Inland noch im Ausland in gleicher oder ähnlicher Form einer anderen Prüfungsbehörde zum Zweck einer Promotion oder eines anderen Prüfungsverfahrens vorgelegt wurde. Alles aus anderen Quellen und von anderen Personen übernommene Material, das in der Arbeit verwendet wurde oder auf das direkt Bezug genommen wird, wurde als solches kenntlich gemacht. Insbesondere wurden alle Personen genannt, die direkt und indirekt an der Entstehung der vorliegenden Arbeit beteiligt waren. Mit der Überprüfung meiner Arbeit durch eine Plagiatserkennungssoftware bzw. ein internetbasiertes Softwareprogramm erkläre ich mich einverstanden.“

_____ _____

Ort, Datum Unterschrift

Danksagung

Ich danke Prof. Linn und seiner Arbeitsgruppe, dass sie mir die Möglichkeit gegeben haben, meine Dissertation zu erstellen.

Ebenso danke ich Prof. Eckert und seiner Arbeitsgruppe, dass die Arbeit um die funktionalen Messungen der Mitochondrien erweitert werden konnte.

Weiterhin sei Dr. Stehling und seiner Arbeitsgruppe aus dem Institut für Zytobiologie der Philipps-Universität Marburg gedankt, die mir weitreichende Kenntnisse zur Proteinanalyse vermitteln konnten.

Curriculum Vitae

Der Lebenslauf wurde aus der veröffentlichten Version der Dissertation entfernt.